



**Detection of Highly Enriched Uranium and
Tungsten Surface Damage Studies Using a Pulsed
Inertial Electrostatic Confinement Fusion Device**

Ross F. Radel

May 2007

UWFDM-1325

Ph.D. thesis.

***FUSION TECHNOLOGY INSTITUTE
UNIVERSITY OF WISCONSIN
MADISON WISCONSIN***

**Detection of Highly Enriched Uranium and
Tungsten Surface Damage Studies Using a
Pulsed Inertial Electrostatic Confinement
Fusion Device**

Ross F. Radel

Fusion Technology Institute
University of Wisconsin
1500 Engineering Drive
Madison, WI 53706

<http://fti.neep.wisc.edu>

May 2007

UWFDM-1325

Ph.D. thesis.

**DETECTION OF HIGHLY ENRICHED URANIUM AND
TUNGSTEN SURFACE DAMAGE STUDIES USING A PULSED
INERTIAL ELECTROSTATIC CONFINEMENT FUSION DEVICE**

By

Ross F. Radel

A dissertation submitted in partial fulfillment of
the requirements for the degree of

Doctor of Philosophy

(Nuclear Engineering & Engineering Physics)

at the

UNIVERSITY OF WISCONSIN-MADISON

2007

Abstract

The research in this thesis examines two applications of a pulsed Inertial Electrostatic Confinement (IEC) fusion device: detection of highly enriched uranium (HEU) and tungsten surface damage studies. In order to complete this thesis, a pulsed IEC device was developed that is capable of generating converging ion pulses with widths ranging from 0.1 to 5 ms at frequencies between 1 and 50 Hz. This device operated at cathode voltages as high as 120 kV, and with D^+ currents in excess of 6 A and He^+ currents as high as 1 A. Pulsed D-D neutron production rates as high as 4.7×10^9 n/s were measured during 110 μ s pulses at 5 Hz, with a cathode voltage of 94 kV and pulse current of 4.8 A.

The first project used the IEC device as a pulsed D-D neutron source to detect HEU. An MCNP5 model was developed that accurately models the time-dependent behavior of pulsed IEC neutron production and the associated HEU detection hardware. This model aided in the construction of a 3He detector-based system capable of detecting delayed neutrons. Using this hardware, pulsed D-D neutron production rates as low as 4×10^8 n/s were used to detect the presence of a 10 gram sample of uranium-235. Delayed neutron production was found to increase linearly with fusion neutron rates.

The second project studied the effects of high energy He^+ and D^+ implantation on the surface morphology of high-temperature tungsten, for use as a fusion first-wall material and IEC cathodes. Irradiations were performed with 0.2-2 ms He^+ pulses of up to 1 ampere at rep rates ranging from 1-25 Hz. Pulsed helium implantation of polycrystalline tungsten was performed at 1,150°C to fluences of 1×10^{18} to 1×10^{19} He^+/cm^2 in 1 ms pulses at 25 Hz.

Micrographs of these samples revealed increased surface damage at all fluences compared to steady-state irradiation. The samples also experienced a measurable change in mass.

Steady-state irradiation experiments were also performed that extended the knowledge base for tungsten as a fusion first-wall material. Helium fluences of 10^{20} He⁺/cm² on polycrystalline tungsten at 1,100°C further degraded the surface morphology beyond the 10^{19} He⁺/cm² levels seen in previous work and extended the subsurface porous layer. Elastic Recoil Detection analysis revealed the saturated helium retention level to be 40 percent (atomic) in tungsten when exposed to 30 keV He⁺ at 1,100°C. Other factors investigated in this thesis include simultaneous implantation of deuterium and helium ions on tungsten at ~1100 °C, the effect of alloying tungsten with 25 percent rhenium, irradiating single crystal tungsten samples with He⁺ at ~1,100°C, and irradiating tungsten-coated carbide foams in the IEC device with steady-state deuterium and helium ions.

The pulsed IEC fusion device developed at the University of Wisconsin is a versatile piece of equipment. It has been used both to detect special nuclear material and as an irradiation facility for fusion first wall materials research.

Acknowledgements

I would like first to offer my thanks to Professor Gerald Kulcinski for his advice and support over the years. His passion for discovery first drew me to this field and his enthusiasm has been contagious over the years. I want to thank Bob Ashley for his guidance and teaching. His cool head and steady hands have kept me on the path forward, often without my realizing it. I also want to thank John Santarius for his knowledge and insights. His door was always open and he wouldn't quit until we'd found the answer.

I want to extend my gratitude to the many faculty members in the Engineering Physics department who provided instruction and guidance with this and other projects. In particular, I always knew that I could turn to Professors Paul Wilson, Jake Blanchard, or Mike Corradini for information, answers, or advice. I would also like to thank Rick Noll at the UW Materials Science Center for spending many hours with me capturing SEM and FIB images.

I'd like to acknowledge and thank the many students that I have worked side-by-side with on the IEC project over the years. I particularly want to thank Greg Piefer and Ben Cipiti, whose guidance, advice, and friendship have meant more to me than they could know. I also want to thank John Weidner, Alex Wehmeyer, Murali Subramanian, Kunihiro Tomiyasu, Dave Boris, Thad Heltemes, Tracy Radel, Ryan Giar, Brian Egle, Eric Alderson, Sam Zenobia, Chris Seyfert, Logan Campbell, David Donovan, and John Sorebo. It has been a pleasure working and laughing with each and every one of you.

I want to thank the staff of the Engineering Physics department and the Fusion Technology Institute for all their assistance; especially Dennis Bruggink, Joan Welc-LePain, Pat Arnold, and Rose Birzer. No problem was ever too big or too small.

I would like to thank the Greatbatch Foundation and the Grainger Foundation for their generous financial support of the IEC project. In addition, partial funding was supplied by the National Nuclear Security Administration under DOE grant DE-AC52-06NA25396 and by the Naval Research Laboratory under DOD grant N00173-03-1-G901. Tungsten samples were provided by Lance Snead at Oak Ridge National Laboratory and by Ultramet.

Finally, I want to offer my thanks to my family; to my wife Tracy, whose strength inspires me every day; to my sisters Shannon and Elizabeth, who help me keep at least one foot on the ground; and especially my parents, who provided me with the foundation that my career, and this thesis, is built upon - a strong work ethic and an unwavering dedication to the task at hand. I am truly blessed to have them.

Table of Contents

<i>Abstract</i>	<i>i</i>
<i>Acknowledgements</i>	<i>iii</i>
<i>Table of Contents</i>	<i>v</i>
<i>Table of Figures</i>	<i>vii</i>
<i>Table of Tables</i>	<i>xii</i>
Chapter 1: Introduction	1
1.1 Inertial Electrostatic Confinement	2
1.2 Highly Enriched Uranium Detection	3
1.3 Tungsten Irradiation.....	4
1.4 References.....	5
Chapter 2: Previous Work	6
2.1 Inertial Electrostatic Confinement	6
2.1.1 Pulsed IEC Research.....	10
2.1.2 University of Wisconsin IEC Research	12
2.2 Highly Enriched Uranium Detection	15
2.3 Tungsten Irradiation.....	20
2.3.1 Helium Implantation in Metals	20
2.3.2 International Thermonuclear Experimental Reactor.....	24
2.3.3 High Average Power Laser Program	26
2.4 References.....	32
Chapter 3: Theory	37
3.1 Inertial Electrostatic Confinement	37
3.2 HEU Detection.....	41
3.2.1 Fission	43
3.2.2 Delayed Neutrons.....	45
3.3 Tungsten Irradiation.....	48
3.3.1 Implantation Depth	48
3.3.2 Secondary Electron Emission	50
3.3.3 Sputtering.....	52
3.3.4 Bubble formation and growth	56
3.4 References.....	64

Chapter 4: Experimental Procedure	66
4.1 Experimental Facility.....	66
4.1.1 High Voltage Components.....	67
4.1.2 Cathode and Anode System.....	69
4.1.3 IEC Operation.....	72
4.1.4 Diagnostics.....	73
4.2 Highly Enriched Uranium Detection.....	79
4.2.1 Pulsed IEC Development.....	79
4.2.2 Delayed Neutron Detection.....	83
4.3 Tungsten Irradiation.....	86
4.3.1 IEC Modifications.....	86
4.3.2 Microscopy.....	91
4.4 References.....	95
Chapter 5: Results	96
5.1 MCNP Modeling of HEU Detection.....	96
5.1.1 Delayed Neutrons in MCNP.....	96
5.1.2 MCNP Model of the IEC.....	103
5.1.3 Neutron Scattering.....	108
5.2 Pulsed Neutron Source Development.....	110
5.2.1 Ion Source Region.....	110
5.2.2 Pulse Characteristics.....	114
5.2.3 Pulsed Neutron Production.....	119
5.3 Highly Enriched Uranium Detection.....	130
5.4 Pulsed Helium Implantation in Tungsten.....	137
5.5 Polycrystalline Tungsten.....	145
5.5.1 Simultaneous He ⁺ and D ⁺ Implantation.....	146
5.5.2 W-25%Re Alloy.....	147
5.5.3 Helium Retention.....	149
5.5.4 Expanded Fluence.....	152
5.6 Other Tungsten Forms.....	155
5.6.1 Single Crystal Tungsten.....	155
5.6.2 Tungsten-Coated Foams.....	158
5.7 References.....	168
Chapter 6: Discussion	169
6.1 Pulsed IEC.....	170
6.2 HEU Detection Approach.....	171
6.3 Helium Implantation in Tungsten.....	173
6.3.1 Implications of Helium Implantation in Tungsten.....	173
6.4 References.....	175
Chapter 7: Conclusions	176

Chapter 8: Recommendations	181
8.1 Pulsed Inertial Electrostatic Confinement	
8.2 Highly Enriched Uranium Detection	
8.3 Tungsten Implantation Studies	
Appendix A: MCNP Input Files	185

Table of Figures

Chapter 1: Introduction

Figure 1.1: Summary of tungsten irradiation experiments.	5
---	---

Chapter 2: Previous Work

Figure 2.1: Schematic of P.T. Farnsworth's early IEC design	6
Figure 2.2: Polywell concept.....	8
Figure 2.3: Illinois pulsed IEC circuit	10
Figure 2.4: Tokyo Institute of Technology pulsed IEC circuit	11
Figure 2.5: Typical waveform of short pulse at a deuterium gas pressure of 12.5 mTorr and a charging voltage of -50.0 kV	12
Figure 2.6: Timeline of UW IEC project.....	13
Figure 2.7: Photograph of active well coincidence counter setup at Savannah River	15
Figure 2.8: Sketch of ORNL lightweight neutron generator	16
Figure 2.9: Schematic of modular detector	18
Figure 2.10: Response from the portable detector at LANL	19
Figure 2.11: Blistering of molybdenum surfaces after bombardment with 36 keV He ⁺ ions at different temperature	21
Figure 2.12: An example of differing damage mechanisms occurring at different 100 keV helium doses in room temperature niobium.....	22
Figure 2.13: Vanadium implanted with 300 keV helium to 2×10^{18} He ⁺ /cm ² at 1,200°C	22
Figure 2.14: Cross-section of ARIES-RS device.....	24
Figure 2.15: ARIES-RS divertor plate with coolant channels.....	25
Figure 2.16: Cutaway schematic of ICF fusion device.....	26
Figure 2.17: D-T target	27
Figure 2.18: Helium ion energy spectra at the HAPL first wall	28
Figure 2.19: Summary of early UW-Madison experimental conditions for He ⁺ ions on tungsten	29
Figure 2.20: Typical temperature and helium ion profiles for the HEROS code	30
Figure 2.21: Time sequence of pore evolution for 730°C tungsten.....	31

Chapter 3: Theory

Figure 3.1: IEC fusion reactions and product energies	37
Figure 3.2: Potential and ion distributions in an IEC device.....	38
Figure 3.3: Fusion cross sections as a function of center-of-mass energy in a spherical IEC device	39
Figure 3.4: The three regions of neutron production in the UW-IEC	40
Figure 3.5: Fission cross-section of uranium-235	43
Figure 3.6: Fission product yield for uranium-235	44
Figure 3.7: Growth of delayed neutron population during irradiation (1 second) ...	46
Figure 3.8: Growth of delayed neutron population during irradiation (60 seconds).	46
Figure 3.9: Predicted neutron activity after irradiation	47
Figure 3.10: Projected helium range in tungsten vs. initial ion energy	48
Figure 3.11: SRIM image of 100 keV helium implantation in tungsten	49
Figure 3.12: Ideal secondary electron coefficient vs. work function.....	50
Figure 3.13: Secondary emission coefficient of tungsten vs. helium ion energy	51
Figure 3.14: Deuterium on tungsten sputtering coefficients as a function of ion energy	52
Figure 3.15: Helium on tungsten sputtering coefficients as a function of ion energy	53
Figure 3.16: Sputtering yields for molybdenum.....	54
Figure 3.17: Some sputtered atoms will redeposit on rough surfaces	55
Figure 3.18: Effect of temperature on sputtering yield.....	55
Figure 3.19: Helium re-emission during bombardment of molybdenum by 20 keV He ⁺	56
Figure 3.20: Helium and hydrogen retention in tungsten	57
Figure 3.21: Blister formation in metals	57
Figure 3.22: Blister formation by helium in molybdenum	58
Figure 3.23: 300 keV He on 1200°C Vanadium at 2×10^{18} He ⁺ /cm ²	59
Figure 3.24: Molybdenum surface damage at various temperatures	60
Figure 3.25: Increase of pore diameter and decrease of pore density with temperature in tungsten under helium implantation	61
Figure 3.26: Blister diameter as a function of He ⁺ energy	61
Figure 3.27: Fluence scan of 100 keV helium in room temperature niobium	62
Figure 3.28: Increase of pore diameter and decrease of pore density with helium fluence on tungsten	63

Chapter 4: Experimental Procedure

Figure 4.1: UW-IEC experimental setup.....	66
Figure 4.2: Schematic of ridged BN insulating stalk	67
Figure 4.3: Hipotronics 8200-75 transformer and controller	68
Figure 4.4: High-voltage buffer resistors	69
Figure 4.5: 10 cm and 20 cm diameter tungsten-rhenium inner grids.....	70
Figure 4.6: Latitude/longitude and symmetric cathode configurations.....	71

Figure 4.7: Grid construction procedure	72
Figure 4.8: Modified long counter.....	74
Figure 4.9: Efficiency of the long counter shown in Figure 4.8 versus the average energy of the source neutrons.....	74
Figure 4.10: Proton energy loss through lead foil and Si detector.....	75
Figure 4.11: Screenshot of LabVIEW data collection program	76
Figure 4.12: Tungsten filament emissivity	77
Figure 4.13: Screenshot of residual gas analyzer software.....	78
Figure 4.14: Pulsed high voltage circuit	79
Figure 4.15: Buffer resistors for high voltage pulsing circuit.....	80
Figure 4.16: Filament circuitry for pulsed IEC operation.....	81
Figure 4.17: Filament bias and cathode pulse current during a pulse.....	82
Figure 4.18: Picture of HEU detection equipment.....	83
Figure 4.19: Schematic of HEU detection equipment	84
Figure 4.20: Gate signal used in delayed neutron detection	84
Figure 4.21: Screenshot of PCA3 MCA output	85
Figure 4.22: Modified IEC fusion device	86
Figure 4.23: Tungsten sample during irradiation.....	87
Figure 4.24: High voltage circuit for pulsed IEC operation	89
Figure 4.25: Pulsed vs. steady-state irradiation current.....	90
Figure 4.27: Initial attempts to mill tungsten yielded poor results	92
Figure 4.28: Platinum layer over a tungsten substrate.....	93
Figure 4.29: Platinum layer with a milled trench intersecting it.....	93
Figure 4.30: FIB imaging allowed evaluation of subsurface pore structure.....	94

Chapter 5: Results

Figure 5.1: MCNP results with benchmarking data	97
Figure 5.2: MCNP5 spectra without delayed neutrons	98
Figure 5.3: MCNP5 counts vs. time tallies with delayed neutrons	99
Figure 5.4: Calculated delayed neutron spectra out to 30 seconds.....	100
Figure 5.5: Calculated delayed neutron spectra out to 300 seconds.....	100
Figure 5.6: Calculated fluence for a series of 5 pulses in test case	101
Figure 5.7: Calculated fluence for a series of 20 pulses in test case	102
Figure 5.8: Calculated delayed neutron spectra for 3 pulses.....	103
Figure 5.9: Side view of the HEU detection model in MCNP.....	104
Figure 5.10: Top view of the HEU detection model in MCNP	104
Figure 5.11: Calculated average neutron fluence in the ^3He detectors	106
Figure 5.12: Calculated reaction rate within the ^3He detectors	107
Figure 5.13: Calculated fusion neutron pulse decay.....	108
Figure 5.14: Thermal neutron decay for MCNP model and experimental data.....	109
Figure 5.15: Emission current increases with increasing filament temperature	110
Figure 5.16: Emission current increases linearly with filament bias	111
Figure 5.17: Emission current increases with increased deuterium pressure	112
Figure 5.18: Pulse current increases with increased deuterium pressure.....	113
Figure 5.19: Pulse current scales linearly with filament emission current	114

Figure 5.20: Pulse current scales linearly with cathode voltage	115
Figure 5.21: Shorter pulse widths yield higher average current	116
Figure 5.22: Exponential decay can be seen when pulse width is increased to 5 ms.....	117
Figure 5.23: Measured pulse shapes at various pulse currents	117
Figure 5.24: Pulse amplitude increases at lower frequencies	118
Figure 5.25: Pulsed neutron rate increases with cathode voltage in a manner similar to the steady-state neutron rate	120
Figure 5.26: Steady-state neutron rate increases linearly with cathode current	121
Figure 5.27: Measured pulsed neutron rate increases nearly linearly with cathode current at low pulse currents	122
Figure 5.28: Measured pulsed neutron rate increases with cathode current	122
Figure 5.29: Measured neutron rate of 20 cm cathode/40 cm anode configuration is nearly twice that of 10 cm cathode/50 cm anode	124
Figure 5.30: The measured instantaneous neutron production rate drops with increasing pulse width.....	125
Figure 5.31: Neutron production rate versus cathode voltage at optimum conditions for neutron production.....	126
Figure 5.32: Using a Ti coating on the inner chamber surface increases the measured steady-state neutron production rate.....	127
Figure 5.33: Measured steady-state neutron rate without filaments increases rapidly as cathode voltage is increased.....	128
Figure 5.34: Measured steady-state neutron rate without filaments increases as deuterium pressure is increased	129
Figure 5.35: Delayed neutron counts after steady-state IEC operation	130
Figure 5.36: Modified HEU detection module shields detector while allowing neutrons into HEU sample	131
Figure 5.37: Increased levels of neutrons are measured when HEU is present.....	132
Figure 5.38: Delayed neutron production measured as a function of IEC neutron rate	133
Figure 5.39: Delayed neutron production as a function of IEC neutron flux at the HEU	134
Figure 5.40: Maximum detectable distance from the IEC device to the HEU sample	135
Figure 5.41: Signal to noise ratio of HEU counts taken between 50 kV and 90 kV	136
Figure 5.42: Pulse capabilities of selected HAPL experimental facilities.....	137
Figure 5.43: Pulsed and steady-state tungsten samples (1×10^{18} He ⁺ /cm ²)	139
Figure 5.44: Pulsed and steady-state tungsten samples (6×10^{18} He ⁺ /cm ²)	140
Figure 5.45: Pulsed and steady-state tungsten samples (1×10^{19} He ⁺ /cm ²)	141
Figure 5.46: FIB images of tungsten irradiated with pulsed helium fluence.....	142
Figure 5.47: FIB images of tungsten irradiated with steady-state helium fluence ...	143
Figure 5.48: Tungsten samples irradiated at 1150 °C with He and He + D at 1×10^{18} and 1×10^{19} ions/cm ²	146

Figure 5.49: Pure tungsten and W-25%Re alloy samples irradiated with 30 keV He ⁺ at 1,150°C.....	148
Figure 5.50: Elastic Recoil Detection is used to determine He concentrations	149
Figure 5.51: Helium concentration depth profile for 1x10 ¹⁹ He ⁺ /cm ² sample	150
Figure 5.52: Helium retention saturates by 1x10 ¹⁸ He ⁺ /cm ²	151
Figure 5.53: Helium retention ratio versus incident fluence.....	152
Figure 5.54: Polycrystalline tungsten samples irradiated with 30 keV He ⁺ at 1,150°C to 10 ¹⁸ , 10 ¹⁹ , and 10 ²⁰ He ⁺ /cm ² , respectively.....	153
Figure 5.55: Polycrystalline tungsten sample irradiated with 30 keV He ⁺ at 1,150°C to 10 ²⁰ He ⁺ /cm ²	154
Figure 5.56: Tungsten sample irradiated at ~1,100°C to with 30 keV helium at ~1,100°C to 1x10 ¹⁸ He ⁺ /cm ²	156
Figure 5.57: As-received and irradiated single crystal	157
Figure 5.58: Polycrystalline and single crystal W samples irradiated with 30 keV helium to 3x10 ¹⁸ He ⁺ /cm ²	158
Figure 5.59: As-received foam samples.....	159
Figure 5.60: Cross section of TaC sample	159
Figure 5.61: SEM micrographs of HfC foam samples coated with tungsten	160
Figure 5.62: Large grain W-coated TaC before and after vacuum annealing	162
Figure 5.63: Large Grain W-coated TaC Sample (D ⁺ irradiation)	163
Figure 5.64: Large grain W-coated HfC before and after vacuum annealing	164
Figure 5.65: Large-grain W-coated HfC sample (He ⁺ irradiated)	164
Figure 5.66: Medium-grain side of the “High ε” sample before and after vacuum annealing	165
Figure 5.67: Fine-grain W side of the “High ε” sample before and after vacuum annealing	166
Figure 5.68: Medium grain side of the “High ε” sample (He ⁺ irradiated).....	167
Figure 5.69: Fine grain side of the “High ε” sample (He ⁺ irradiated).....	167

Chapter 6: Discussion

Figure 6.1: The pulsed D-D neutron production rate of the UW-IEC has increased by a factor of 500 in the past two years	170
---	-----

Table of Tables

Chapter 2: Previous Work

Table 2.1: Major parameters that can affect radiation blistering	23
--	----

Chapter 3: Theory

Table 3.1: Natural Radiation from U and Pu isotopes	42
Table 3.2: Half-life and relative abundance for the six delayed neutron groups	45

Chapter 4: Experimental Procedure

Table 4.1: Summary of helium ion irradiation experiments in tungsten	88
--	----

Chapter 5: Results

Table 5.1: Mass loss for pulsed samples (1 ms pulse width, 25 Hz, 1,150°C).....	144
Table 5.2: Summary of irradiation history and pore density	145
Table 5.3: Summary of experiments on alternative tungsten materials.....	161

Chapter 6: Discussion

Table 6.1: Comparison of UW-IEC to other known pulsed IEC systems operated with deuterium fuels.....	171
---	-----

Chapter 1: Introduction

The research discussed in this thesis follows the development of a pulsed Inertial Electrostatic Confinement (IEC) fusion device for use in a diverse set of applications, including the detection of highly enriched uranium (HEU) and as a tungsten irradiation facility. Due to the flexible nature of the IEC device, the technology development required for the two projects was very similar and diverged only in the latest stages of research. This device was ultimately used to accomplish research goals in two distinct fields.

The first project used the IEC device as a pulsed D-D neutron source to detect HEU. The primary accomplishments for this research track included the characterization of previously existing IEC technology, the development of a pulsed IEC neutron source capable of providing up to 4.7×10^9 D-D neutron/s in 0.1 to 5 ms long pulses at 1 to 50 Hz, and the construction of a system capable of detecting delayed neutrons generated by a uranium target being irradiated by a pulsed IEC neutron source.

The second project studied the effects of high energy He^+ and D^+ implantation on the surface morphology of high-temperature tungsten for use as a fusion first-wall material and IEC cathodes. The primary objectives of this research track included the evaluation of surface morphology changes of polycrystalline tungsten and tungsten alloys, single crystal tungsten, and tungsten-coated carbide foams after high-temperature irradiation at fluences as high as $10^{20} \text{ He}^+/\text{cm}^2$. This work also required the development of both steady-state and pulsed IEC technology to perform these irradiations.

1.1 Inertial Electrostatic Confinement

There are numerous ways to produce neutrons. Fission reactors produce large numbers of neutrons, but are kept far from public areas, due to safety and security concerns, and are large, expensive facilities. Radioactive sources, utilizing either spontaneous fission or (α,n) reactions can also produce a high neutron flux in a small volume, but cannot be turned off when not in use, and pose a risk themselves for nuclear terrorism. A third way to produce neutrons is through nuclear fusion. This potential source can be turned on and off as needed, requires no radioactive fuel, and can be constructed in small, inexpensive configurations.

Fusion, the energy source of the sun, is the process by which two low-mass nuclei are combined to form a larger nucleus. This larger nucleus can be inherently unstable and immediately break into smaller products. The total mass of these products is less than the mass of the initial nuclei, and this lost mass is converted to kinetic energy according to Einstein's famous equation, $E=mc^2$, where m is the mass difference and c is the speed of light. Various concepts exist that will generate fusion reactions. Each of these mechanisms creates a combination of high energy, density, and confinement time to encourage fusion reactions to occur. The Inertial Electrostatic Confinement (IEC) fusion device sacrifices density to achieve high energies and long confinement time.

The sole purpose of most fusion experiments is the development of energy producing reactors. While variants of IEC technology may one day produce electricity, the primary focus of the research described in this paper is development of near-term, non-electric applications.

1.2 Highly Enriched Uranium Detection

In September 2002, an ABC News crew smuggled a 6.8-kilogram cylinder of depleted uranium metal into a New York port, and televised the story on the first anniversary of the September 2001 terrorist attacks [1]. In September 2003, the network did it again, this time in Los Angeles. Just last year, a Russian man attempted to sell weapons-grade uranium on the Georgian black market [2]. These news stories revealed a weak point in this nation's defense against terrorist activities—the trafficking of special nuclear material for use in weapons of mass destruction.

The smuggling of illicit nuclear material has been an issue of serious concern for U.S. officials since the early 1990s, and has gained increased attention in the wake of September 11, 2001. In the past decade, there have been over 150 confirmed incidents of smuggling of nuclear material in the International Atomic Energy Agency's (IAEA) Illicit Trafficking Database [3]. Of these, nearly half involved enriched uranium or plutonium. In the wrong hands, these materials could represent a serious threat to national security in the United States, and preventing this from occurring has become a high priority for the newly formed Department of Homeland Security.

The development of a cheap, reliable means to detect fissile and other nuclear materials will allow the U.S. and other countries to inspect cargo as it enters their borders. This thesis overviews the work that has been done toward the development of a pulsed IEC fusion device for the detection of HEU and other fissile materials.

1.3 Tungsten Irradiation

The durability and lifetime of thin tungsten or refractory metal coatings on the first walls of inertial and magnetic confinement fusion reactors is a key issue for the feasibility of such devices. Work as early as 1974 by Thomas and Bauer showed blistering in vanadium as the result of helium implantation at high temperature [4]. Past studies at the University of Wisconsin-Madison [5] and the Oak Ridge National Laboratory [6] have shown that when tungsten is subjected to low energy (20-50 keV) He^+ fluences in excess of $4 \times 10^{17} \text{He}^+/\text{cm}^2$, it exhibits extensive surface pore formation at 1,100°C. The current study has investigated alternative forms of tungsten for future use in both magnetic and inertial fusion reactors.

Scientists working in the High Average Power Laser (HAPL) program [7] are studying tungsten as a potential material to act as a shield to protect the first structural wall from light ions, such as helium, whose energy ranges from tens of keV to a few MeV. This study examines the lower portion of that spectrum.

Both steady-state and pulsed irradiations have been performed to evaluate the effectiveness of tungsten as a first wall. Figure 1.1 summarizes the experiments that have been performed on polycrystalline and single crystal tungsten and tungsten-coated carbide foams.

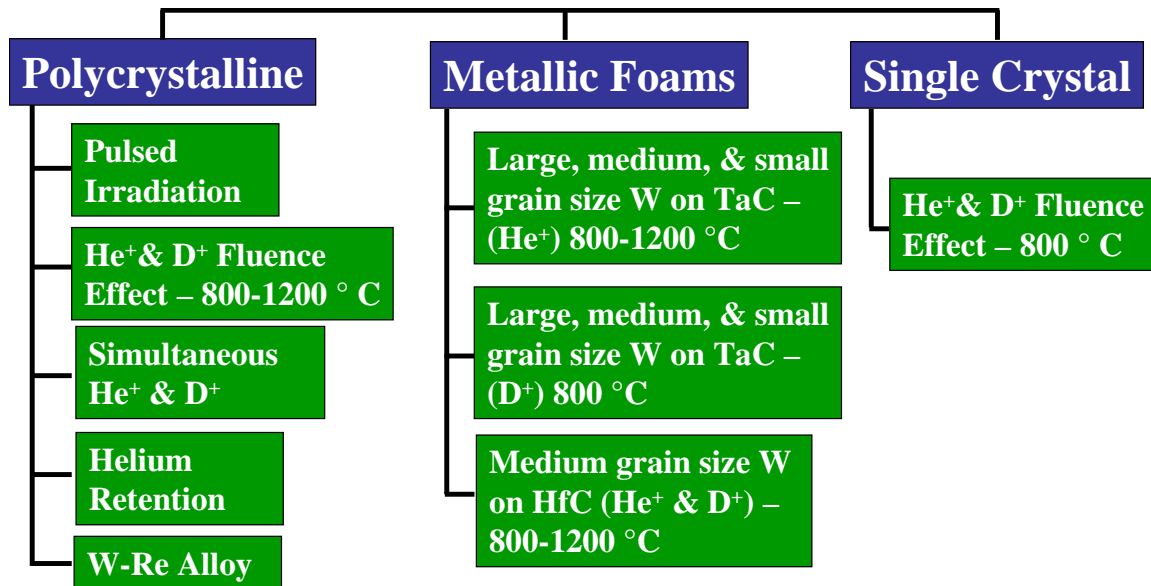


Figure 1.1: Summary of tungsten irradiation experiments.

1.4 References

- [1] Ross, Brian. “New Report Reveals Gaps in Port Safety: Federal Investigation Shows ABC News Nuclear Smuggling Test Exposed Homeland Security Flaws” ABC News Report- October 13, 2004
- [2] Meyer, H, Wisconsin State Journal, “Foiled Uranium Sale Raises Security Concerns” Jan 24, 2007
- [3] Orlov, V.A. “Illicit Nuclear Trafficking & the New Agenda,” IAEA Bulletin, Issue 46/1; June 2004
- [4] G.J. Thomas and W. Bauer, “Surface Deformation in He and H Implanted Metals,” *Journal of Nuclear Materials*, Vol. 53, p. 134-141, 1974
- [5] B.B. Cipiti and G.L. Kulcinski, “Helium and Deuterium Implantation in Tungsten at Elevated Temperatures,” *Journal of Nuclear Materials*, Vol. 347(3), p. 298, 2005
- [6] S.B. Gilliam, et al, “Retention and Surface Blistering of Helium Irradiated Tungsten as a First Wall Material,” *Journal of Nuclear Materials*, Vol. 347(3), p 289-297, 2005
- [7] J.D. Sethian, “An Overview of the Development of the First Wall and other Principal Components of a Laser Fusion Power Plant,” *Journal of Nuclear Materials*, 347 (3), p. 161–177, 2005

Chapter 2: Previous Work

2.1 Inertial Electrostatic Confinement

Inertial electrostatic confinement fusion, as it is called today, was born through the theoretical efforts of Elmore, Tuck, and Watson [1] and the experimental efforts of Farnsworth, and later Hirsch, through the late 1960s. Philo Farnsworth's patent, "Electric Discharge Device for Producing Interactions Between Nuclei" was filed in 1966 [2]. An example of one of Farnsworth's later concepts is shown in Figure 2.1 [3]. Ultimately, Hirsch was able to produce 3×10^9 n/s steady-state using the D-T reaction at a cathode voltage of 150 kV in a tabletop experiment [4].

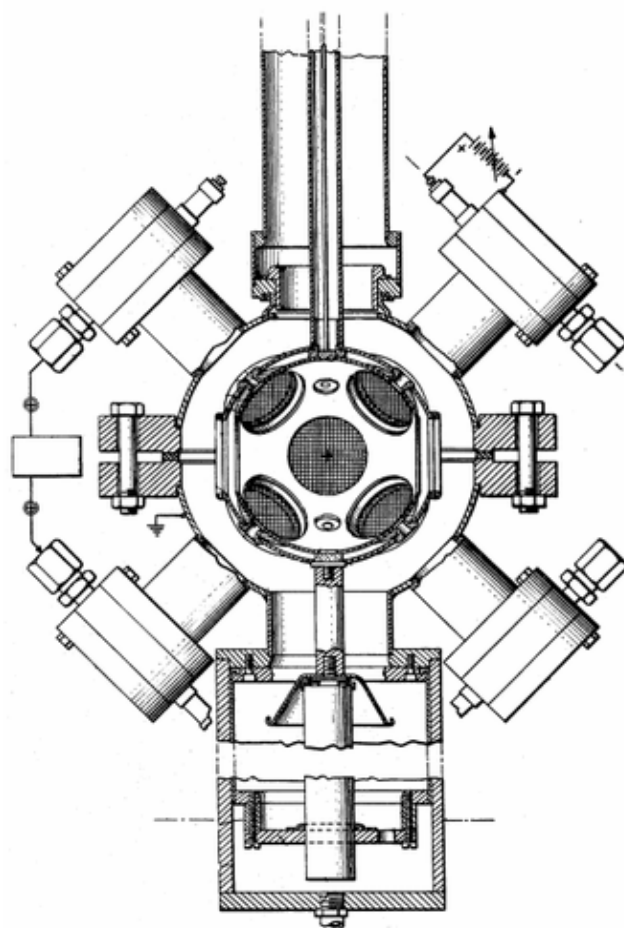


Figure 2.1: Schematic of P.T. Farnsworth's early IEC design [3].

Hirsch's initial success generated interest in the IEC concept. Numerous researchers, including G. Miley, D.A Swanson [5], and T. Dolan [6] at the University of Illinois and W.M. Black at George Mason University [7], studied IEC potential profiles. A team of researchers at Brigham Young University, led by A.L. Gardner, attempted to repeat Hirsch's experiments, but was unable to achieve the same neutron rates [8]. During this time, physicists were also looking more closely at IEC theory. It was ultimately concluded that IEC cathode grids would become too hot at high power levels to be feasible for electricity production.

It was not until Bussard began work on the grid-less Polywell™ concept (pictured in Figure 2.2) in the late 1980s that the scientific community once again considered the IEC device as a viable alternative for fusion power. This device uses cusp magnetic fields to generate an electron cloud that acts as the IEC cathode [9]. The electron cloud then is able to accelerate and confine ions as in the conventional concept. The Polywell™ concept was investigated by an experimental facility at Directed Technologies, Inc. (DTI). The experiment began in 1990, and was able to demonstrate the production of a virtual cathode. The cathode voltages were low in initial experiments, and β was $\ll 1$, so the parameters were far below those required to fully demonstrate the Polywell™ concept. Work continued to improve these parameters. However, the project was shut down prematurely during a DARPA restructuring.

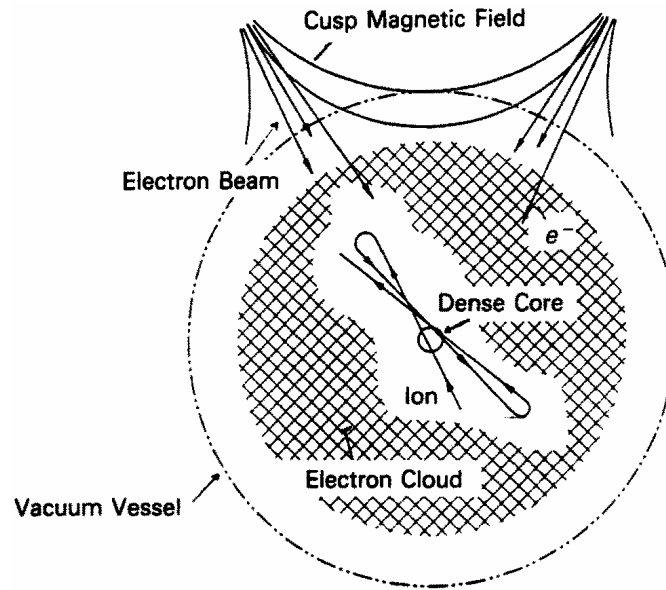


Figure 2.2: Polywell™ concept [12].

With the cancellation of the DTI project, attention turned back to small, gridded IEC systems. However, the primary focus was now on near-term applications, such as landmine detection and medical isotope generation, instead of power production. Over the past decade, there have been a growing number of IEC projects around the world. In the U.S., the University of Illinois [10,11], along with Daimler-Benz [12], first attempted to develop the IEC concept for use as a low-power commercial neutron generator. Researchers at the Marshall Space Flight Center have investigated using the gridded IEC concept for space propulsion [13]. Nebel and Barnes at Los Alamos National Laboratory have developed a unique approach to the IEC concept called the Periodically Oscillating Plasma Sphere (POPS) [14]. The University of Wisconsin IEC experiment began operation in 1994. Researchers at the UW have conducted near-term application experiments using fusion products from both the D-D and D-³He reactions [15].

More recently, numerous IEC projects have been established internationally, including four in Japan, one in South Korea, and one in Australia. The Tokyo Institute of Technology [16], Kyoto University [17], Kansai University [18], and Kyushu University [19] are all focusing primarily on the D-D reaction, with a particular interest in landmine detection. However, Kyoto University has recently begun studying the D-³He reaction as well [20]. Seoul National University and Hanyang University have started work on an IEC project in South Korea [21]. The University of Sydney also has a small IEC research effort focusing on core spectroscopy [22].

2.1.1 Pulsed IEC Operation

There are currently only a small number of active research groups pursuing IEC fusion. In the United States, the primary groups are located at Los Alamos National Laboratory [23], University of Illinois [24], and the University of Wisconsin [25]. There is also a similarly sized research effort in Japan, principally at Kyoto University [26] and the Tokyo Institute of Technology [27]. At this time, the majority of research activity is focused on developing steady-state IEC devices, particularly for use in near-term applications.

Initial investigations into pulsed IEC behavior began in the early 1990s at the University of Illinois. John Nadler and George Miley developed a pulsed IEC device capable of 43 kV and 17 Ampere operation [24]. As shown in Figure 2.3, their design utilized high voltage switches and capacitors to directly pulse the device cathode. Voltage limitations in the high voltage circuit and power supply limited them to 50 kV operation during these

investigations. However, even at these relatively modest voltages, they detected a peak of 10^9 D-D n/s during $100\mu\text{s}$ pulses at a 10 Hz repetition rate.

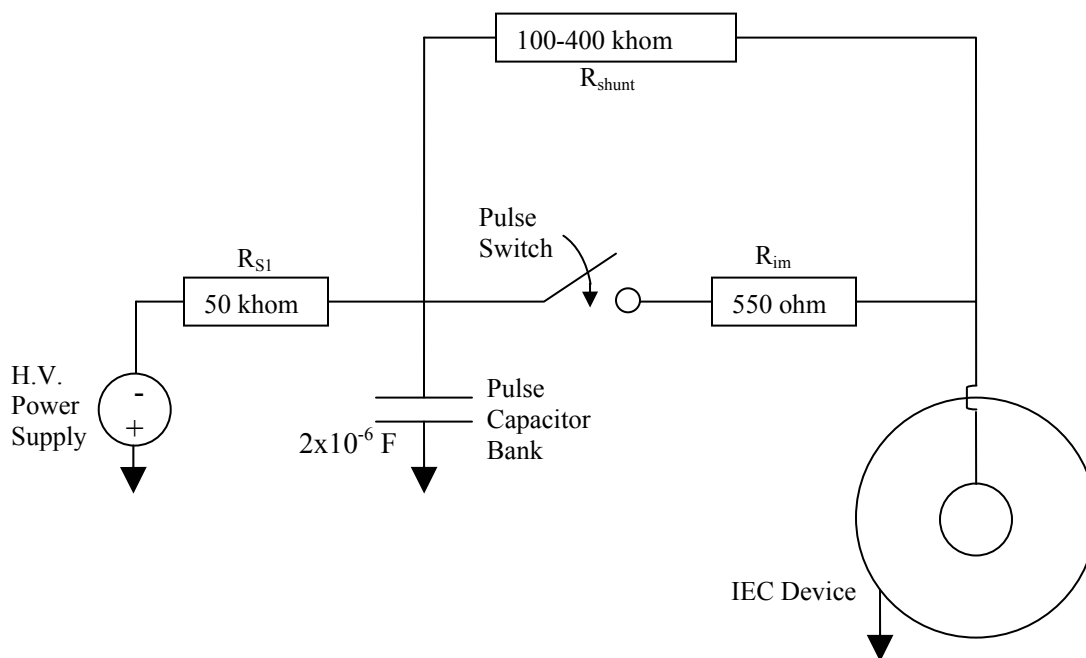


Figure 2.3: Illinois pulsed IEC circuit [from 23].

More recently, a research team at the Tokyo Institute of Technology led by Kunihiro Yamauchi has begun work on a similar device [27]. As shown in Figure 2.4, their concept again relies on high voltage switches and capacitors to directly pulse the voltage on the IEC cathode. This device was typically operated at 100 Hz with a pulse width of 50-100 μs . When operating at pulse discharges of -51 kV and 7.3 A, a maximum neutron production rate of 2×10^8 D-D n/s was achieved. However, the discharge shape appears to be fairly

uncontrolled, even at -50 kV cathode potential. Figure 2.5 shows typical waveforms of a ~ 10 ms pulse at deuterium gas pressure of 12.5 mTorr and a charging voltage of -50 kV.

A cylindrical pulsed IEC device has also been constructed at the Tokyo Institute of Technology. This device operates at pulse frequency and pulse rate of 4 Hz and 20 μ s, respectively [28]. The optimum operating conditions in this IEC device were -70 kV and 10 A, with a maximum neutron production rate of 6.8×10^9 n/s during the pulse.

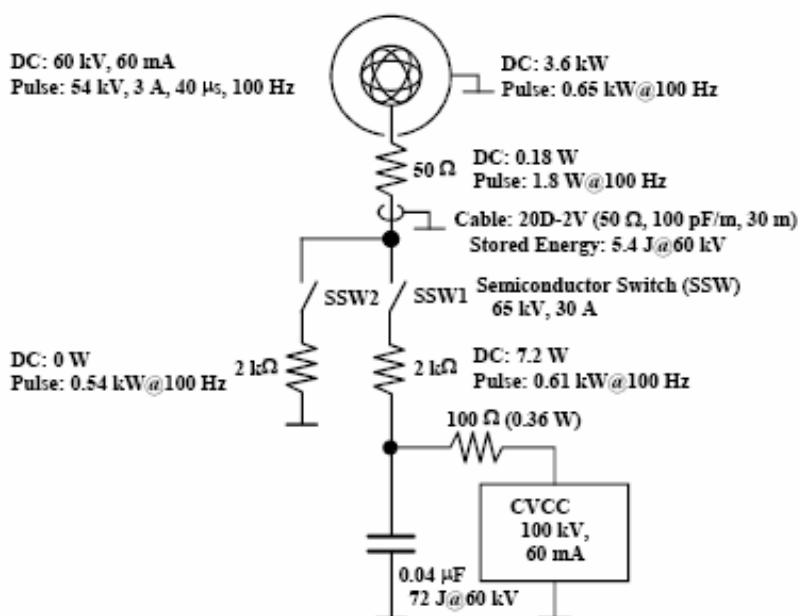


Figure 2.4: Tokyo Institute of Technology pulsed IEC circuit [27].

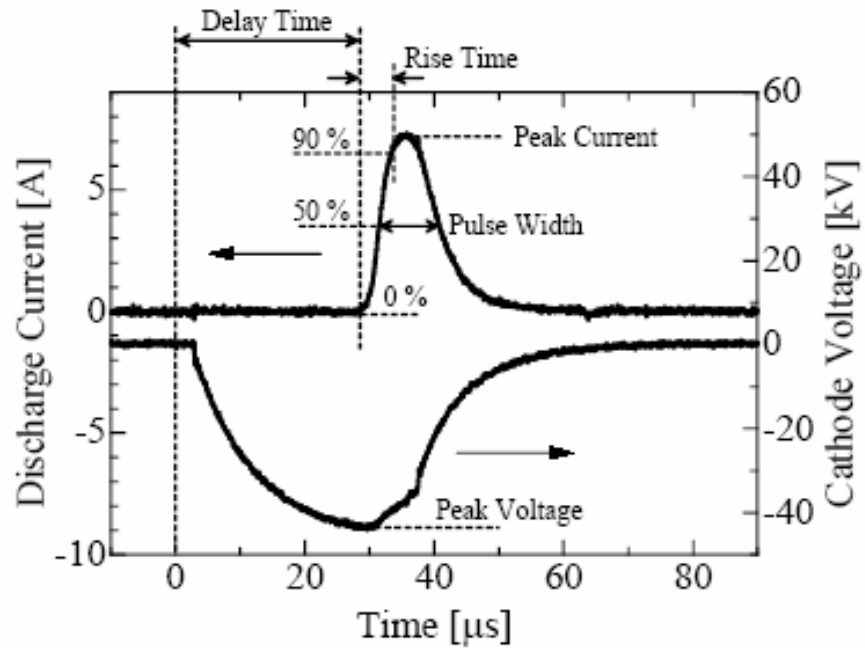


Figure 2.5: Typical waveform of short pulse at a deuterium gas pressure of 12.5 mTorr and a charging voltage of -50.0 kV [27].

2.1.2 University of Wisconsin IEC Research

As seen in Figure 2.6, the first IEC device at the University of Wisconsin was constructed in 1994. Early experiments performed by Thorson [29] focused on determining the ion flow and potential structure within the IEC. By 1999, the Wisconsin team, led by Kulcinski and Santarius, had turned its attention to improving both D-D and D- 3 He fusion rates in the IEC, with hopes of performing proof-of-principle studies on numerous bootstrapping technologies [30]. As fusion neutron and proton rates increased to $\sim 10^8$ /s, many of these technologies were explored. Experiments with medical isotope production by Weidner [31] and Cipiti [32] showed that while proof-of-principle experiments were possible

for isotope generation with an IEC device, it would be very difficult for an IEC device to compete with current isotope production technologies at existing fusion output levels.

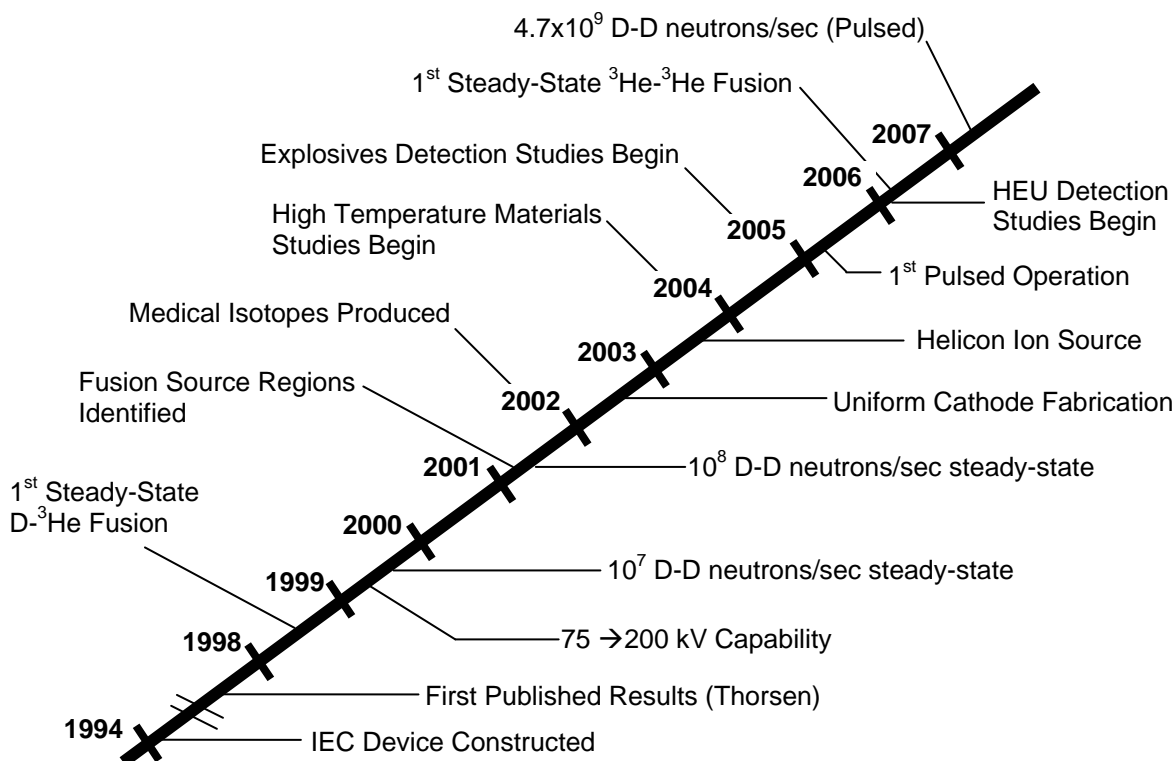


Figure 2.6: Timeline of UW IEC project.

Wehmeyer developed a demonstration experiment for the detection of explosives using D-D neutrons [33]. His project was used as a proof-of-principle experiment for the detection of landmines. During these experiments, steady-state D-D neutron rates as high as 1.8×10^8 n/s were achieved, and NaI(Tl) detectors were used to examine characteristic radiation emitted by explosives during neutron irradiation. Cipiti [34], Radel [35, 36], and Zenobia [37] have used the Wisconsin IEC device as a spherical accelerator to study the effects of low energy ion irradiation on refractory alloys and silicon carbide. Although these

experiments do not generate fusion, they do demonstrate the flexibility of an IEC system, and provide additional resources to the project.

Currently, a large team of researchers and students continues to investigate IEC physics and applications at the University of Wisconsin. Santarius and Emmert continue their efforts to model IEC reaction rates and core physics [38, 39]. Recent work by Piefer has expanded IEC research into lower pressure operating regimes using a helicon ion source [40]. He has also demonstrated the ^3He - ^3He reaction using an IEC device [40]. Boris is working to couple solid-state direct energy conversion technology with the IEC concept and has introduced Langmuir probes and ion-acoustic wave diagnostics into the ion source region of the UW IEC device [41]. Experiments also continue on near-term applications of IEC, including explosives detection, medical isotope production with a cylindrical IEC device [42], and helium implantation studies.

2.2 Highly Enriched Uranium Detection

A number of research groups are currently developing active interrogation systems for the detection of special nuclear material. Most of these detection systems utilize pulsed or steady-state neutrons and gammas to induce fission reactions within the test material, and then employ various detection schemes to detect the prompt or delayed fission products. The European SAfeguards Research and Development Association (ESARDA) Working Group for Standards and Non Destructive Assay Techniques (WGNDATA) summarized many of these techniques in their 2002 evaluation [43]. They have come to the conclusion that only active interrogation is suitable for HEU analysis in most practical situations. Since this working group focuses on existing commercial technologies, they only look at evaluating samples in known locations, not in trafficking situations. They do not evaluate the effectiveness of utilizing pulsed sources of neutrons and so have concluded that coincidence counting of fission neutrons is the most effective means of detection.



Figure 2.7: Photograph of active well coincidence counter setup at Savannah River [44].

An example of a steady-state means of active interrogation was performed by the Savannah River Technology Center (SRTC) to determine the quantity of fissile material in two drums [44]. For this application, an active well coincidence counter (AWCC) was first used to search for spontaneous fission events and then was used in active mode with a ^{252}Cf source placed near the drums, as seen in Figure 2.7. The detection assembly consisted of 42 ^3He -detector tubes mounted in two concentric circles in polyethylene blocks. The signals were then summed and run through a coincidence processor to find fission events. This technology was successfully used to characterize the contents of the two drums.

Another such system under development at Oak Ridge National Laboratory (pictured in Figure 2.8) utilizes a steady-state DT fusion generator to produce 10^7 n/s [45]. This system uses a set of proton recoil scintillation detectors on either side of the sample to again search for prompt fission events with a coincidence circuit. One advantage of looking for prompt neutrons is that there is a factor of ~ 500 more particles available for detection than when looking for delayed neutrons. However, for shipping port security, larger and more complicated detection systems will be required for coincidence techniques.

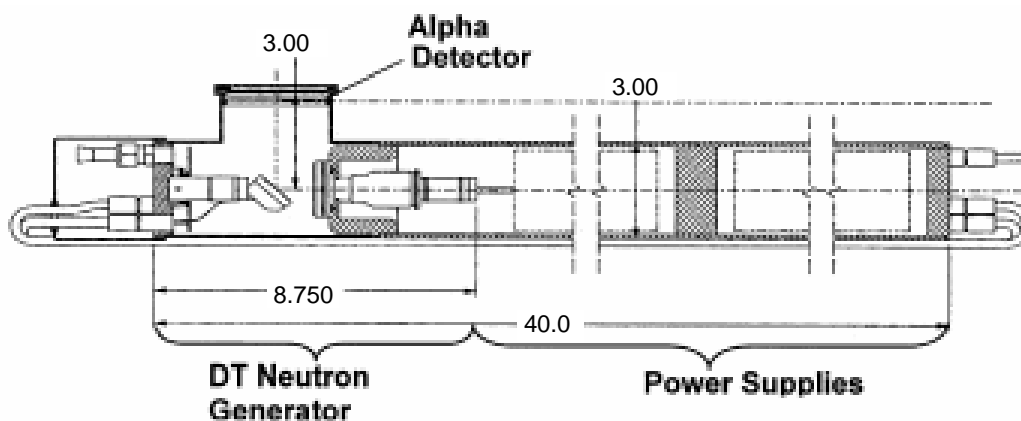


Figure 2.8: Sketch of ORNL lightweight neutron generator [45].

Pulsed sources are also being investigated for active interrogation of special nuclear material (SNM). The Advanced Nuclear Technology Group (NIS-6) at Los Alamos National Laboratory (LANL) has developed a linear accelerator-based technique for HEU detection [46]. A pulsed 10 MV linac was used to induce photofission in shielded HEU. This setup was used to study the effects of both lead and polyethylene shielding, as well as effects of varying the distance to the HEU for several configurations. For comparison in some measurements, a beryllium block was inserted into the beam to produce a pulsed neutron source for interrogation.

Brown and Gozani are developing another system using Pulsed Fast Neutron Analysis (PFNA) for active non-destructive cargo inspection [47]. It uses a Pelletron tandem Van de Graaff accelerator to produce 1 ns Full Width Half Maximum (FWHM) pulses of 5 MeV deuterons. This beam enters a deuteron gas target and produces D-D fusion neutrons with an energy spectrum centered around 8 MeV. The neutrons are then collimated and used to assay various illicit materials, including high explosives and illegal drugs. However, they have not used this setup for HEU or other nuclear material detection.

One of the most relevant experiments currently being studied in this research area is being performed at LANL [48]. In addition to the linear accelerator work mentioned earlier, the NIS-6 group has also spent a great deal of effort developing high-efficiency neutron detectors for HEU detection. An MF Physics model CC A-210 device operating at 50 Hz was used to generate 14 MeV interrogating neutrons. This device operated with ~ 10 μ s pulses to produce 10^6 n/pulse, at a time-averaged rate of 5×10^7 n/s. HEU samples ranging from 5-22 kg were interrogated and the resulting delayed fission neutrons counted using one of three detection systems.

The first detector used a large (122 cm × 244 cm) polyethylene box to achieve high efficiency. The moderating box contained four ^3He detectors, 5 cm diameter × 183 cm long, each pressurized to 2 atm. The box was then completely surrounded by cadmium and 5 percent boron-loaded polyethylene to prevent room-scattered neutrons from adding to the background counts. This system was able to detect ~10 percent of the fission neutrons incident on its front face.

Another system was constructed of modules that could be configured for more diverse applications. The basic construction of an individual module was similar to that of the large detector. Each module was constructed of a 13 cm × 25 cm × 117 cm box of cadmium-covered polyethylene. It then contained three ^3He tubes, as configured in Figure 2.9. The group at LANL constructed 16 of these modules, and used them to assay large objects.

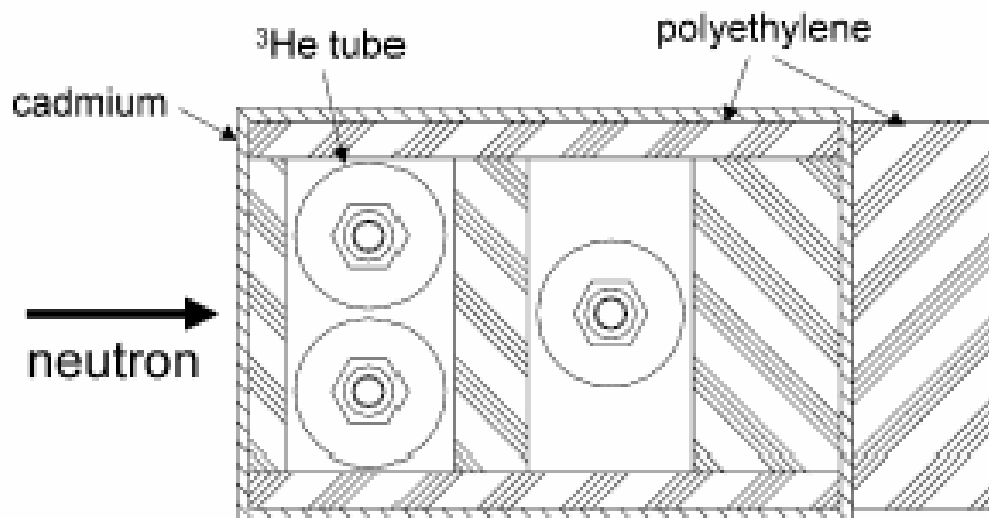


Figure 2.9: Schematic of modular detector [48].

The third detector was a portable system that utilized fifteen ^3He tubes pressurized to 10 atm inserted in a 10 cm \times 43 cm \times 51 cm polyethylene block. This block was again surrounded by cadmium and weighed 25 kg. This detector system was then tested by placing it next to a pulsed neutron generator to analyze a 5 kg HEU sample placed 50 cm from both of them. Figure 2.10 shows the detector response for 8,000 integrated interrogating pulses.

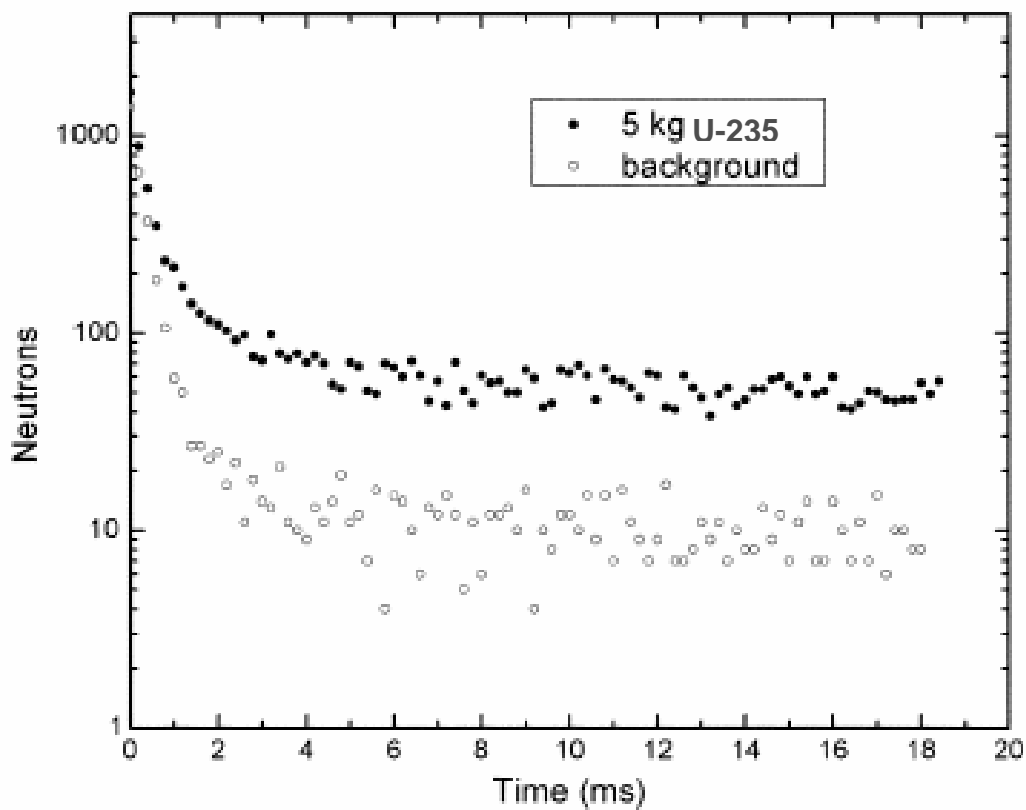


Figure 2.10: Response from the portable detector at LANL. Data acquired for 8,000 pulses from a 5×10^7 D-T n/s (time averaged) generator operating at 50 Hz [48].

2.3 Tungsten Irradiation

There is a long history of investigations on the effects of helium bombardment to fusion first-wall materials. Early research focused primarily on refractory metals, such as niobium, vanadium, and molybdenum [49]. These researchers discovered dramatic changes in surface morphology due to helium implantation. This work slowed down for a period in the 1980-90s, but gained new momentum as the construction of higher power tokamaks, such as ITER, was planned [50]. The creation of the High Average Power Laser (HAPL) conceptual ICF reactor design program has generated renewed interest in this work as well [51].

2.3.1 Helium Implantation in Metals

Research into radiation damage on fusion first walls grew out of earlier research of more general material science. By the early 1960s, Kaminsky [49] and others had developed a significant database of material properties, such as work functions, ionization potentials, sputtering coefficients, and secondary electron yield. Many of these researchers went on to investigate radiation damage of fusion first walls.

Significant work was performed through the 1970s examining the effects of radiation damage on refractory metals. Helium ion implantation was of particular interest due to the relatively large amount of damage it causes. It was observed that helium bombardment typically resulted in one of three damage mechanisms, depending on the ion fluence [52] and energy, and the sample composition and temperature [53]. The first mechanism, as seen in Figure 2.11, is the blistering of the metal surface. The second is surface exfoliation (Figure

2.12), and the third is the development of a porous surface structure (Figures 2.12 and 2.13) [54].

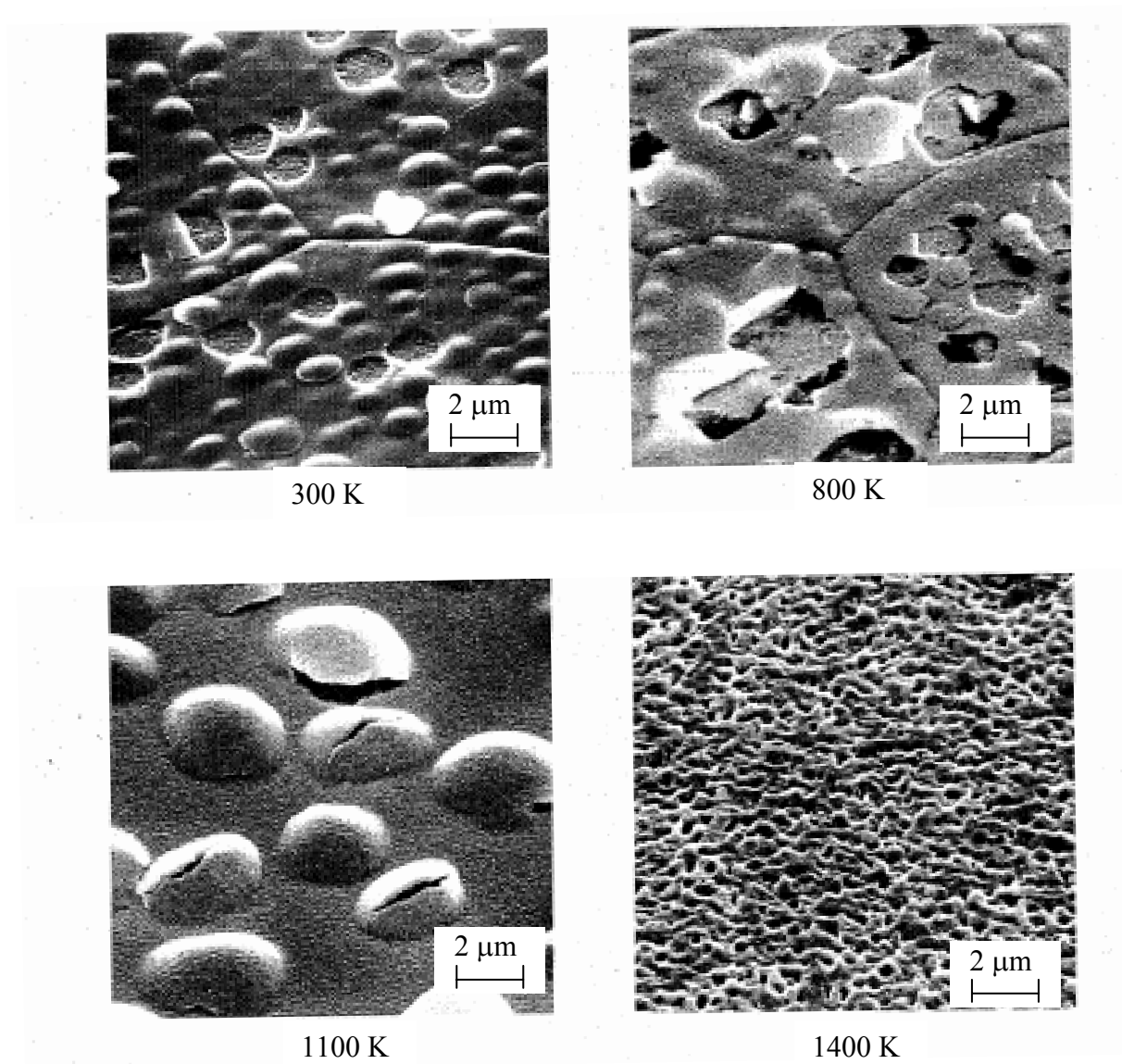
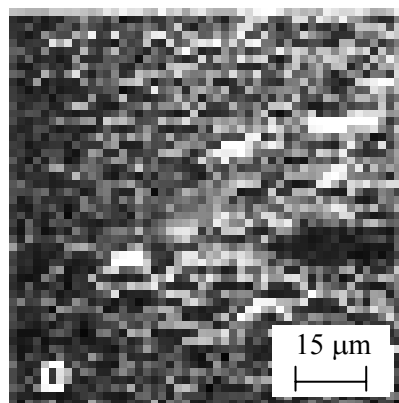
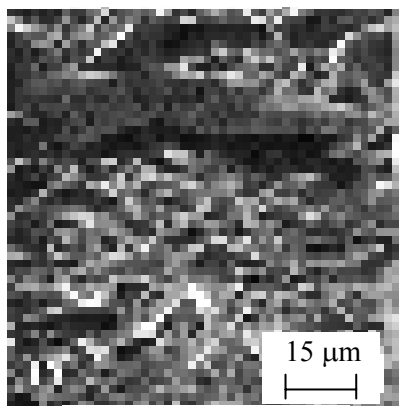


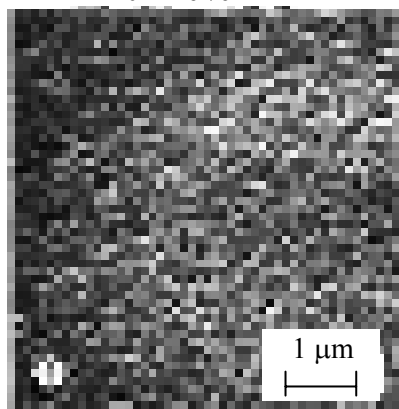
Figure 2.11: Blistering of molybdenum surfaces after bombardment with 36 keV He⁺ ions at different temperatures [53].



$2 \times 10^{18} \text{ He}^+/\text{cm}^2 \perp$



$1 \times 10^{19} \text{ He}^+/\text{cm}^2 \perp$



$1.2 \times 10^{20} \text{ He}^+/\text{cm}^2 \perp$

Figure 2.12: An example of differing damage mechanisms occurring at different 100 keV helium doses in room temperature niobium[52].

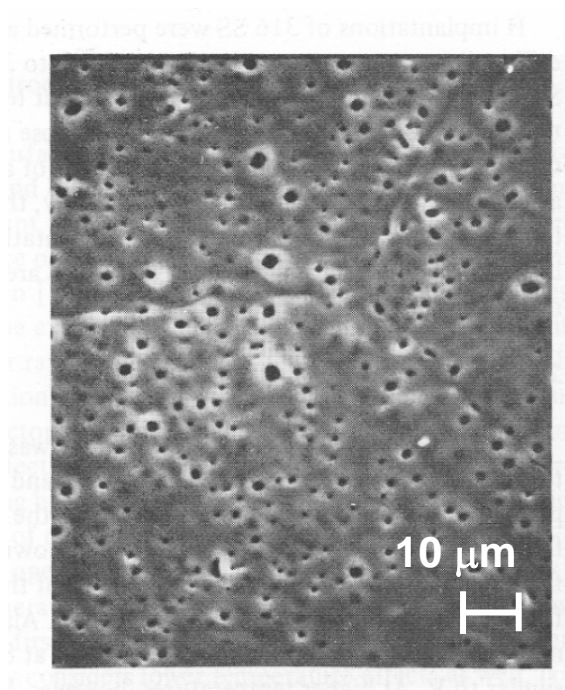


Figure 2.13: Vanadium implanted with 300 keV helium to $2 \times 10^{18} \text{ He}^+/\text{cm}^2$ at $1,200^\circ\text{C}$ [54].

A summary of the factors found to affect radiation blistering is found in Table 2.1 below [55].

<p><u>A. Target-Related Parameters</u></p> <ol style="list-style-type: none"> 1. Type of target metal or alloy 2. Target temperature 3. Target microstructure: <ol style="list-style-type: none"> a. Grain size b. Initial defect density (i.e. cold worked vs. annealed structures) c. Effects of precipitates: size distribution, volume fraction, and type 4. Yield strength and rupture strength of target material 5. Crystallographic orientation of irradiated surface 6. Target surface finish <p><u>B. Projectile-Related Parameters</u></p> <ol style="list-style-type: none"> 1. Type of projectile 2. Projectile energy 3. Total dose (fluence) 4. Dose rate (flux) 5. Channeling condition of projectile 6. Angle of incidence of projectile <p><u>C. Parameters Affected by Target-Projectile Combinations</u></p> <ol style="list-style-type: none"> 1. Diffusivity and solubility of projectile in metals and alloys 2. Critical dose for blister appearance

Table 2.1: Major parameters that can affect radiation blistering [55].

Over time, these studies led to a firm experimental understanding of the surface damage and changes in bulk properties caused by helium bombardment. The campaign to model the blistering damage mechanism did not have the same success. No single model was developed that could predict the full evolution of blister formation. However, a series of models were developed that together provided modest predictive capability. Brice and others

developed a series of codes to predict ion range and energy deposition [56]. Results from this code were imported into numerous gas pressure models, most notably Evans' interbubble fracture code [57]. A unique extension of this type of code was also developed by Bauer [58]. This code coupled the effects of sputtering with a blistering model. In all, this work provided a strong base that later modelers would build upon.

2.3.2 International Thermonuclear Experimental Reactor

Tungsten damage again became an important issue as reactor designs such as ARIES and ITER were developed. These designs required the development of divertor material capable of withstanding high heat flux generated by ion bombardment. An example of one such design, the ARIES-RS, is shown in Figure 2.14 [59].

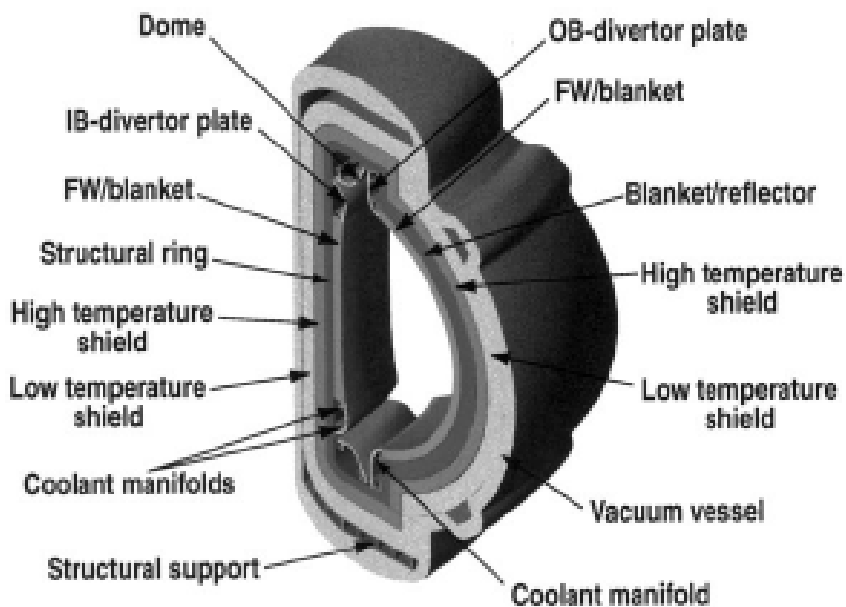


Figure 2.14: Cross-section of ARIES-RS device [59].

Two notable differences between these studies and previous work are the energy and flux of the incoming ions on the divertor surface. While previous experiments had focused on helium energies in the tens of keV, the advanced tokamak research looked at energies under 100 eV. One such experiment exposed multiple materials (carbon, beryllium, vanadium, and tungsten) to a 60-70 eV ion flux of 3×10^{18} ions/cm²s, with a heat flux of about 0.7 MW/m² [59]. For a coating thickness of 2 mm, the corresponding divertor lifetime due to erosion for carbon, beryllium, vanadium and tungsten are 139, 617, 1112, and 5560 h, respectively.

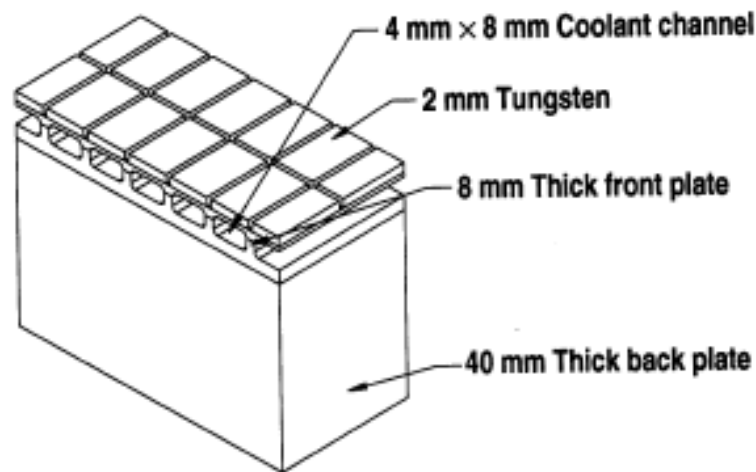


Figure 2.15: ARIES-RS divertor plate with coolant channels [59].

When extrapolated to the operating conditions of the ARIES or ITER divertor designs (such as that shown in Figure 2.15), with the possible exception of tungsten, these erosion rates are unacceptably high. This lifetime can possibly be increased by a factor of ten to about 2 years when the redeposition effect is included [60]. Research to engineer tungsten surfaces that can act as an acceptable divertor material continues. However, the low energy

and high flux operating regime of some types of divertors ensures that the tungsten surface is eroded away prior to the development of the type of surface deformation seen in previous work. Research for these types of divertors, therefore, is not directly linked to the type of surface damage discussed in this thesis.

2.3.3 High Average Power Laser Program

Scientists and engineers from across the country are working on the HAPL program to develop technologies for inertial confinement fusion energy and defense applications. An important aspect of this project is the ongoing effort to develop fusion chamber first-wall technology [50]. Due to its high melting point and the resilience seen in previous studies, tungsten has been identified as a material of particular interest.

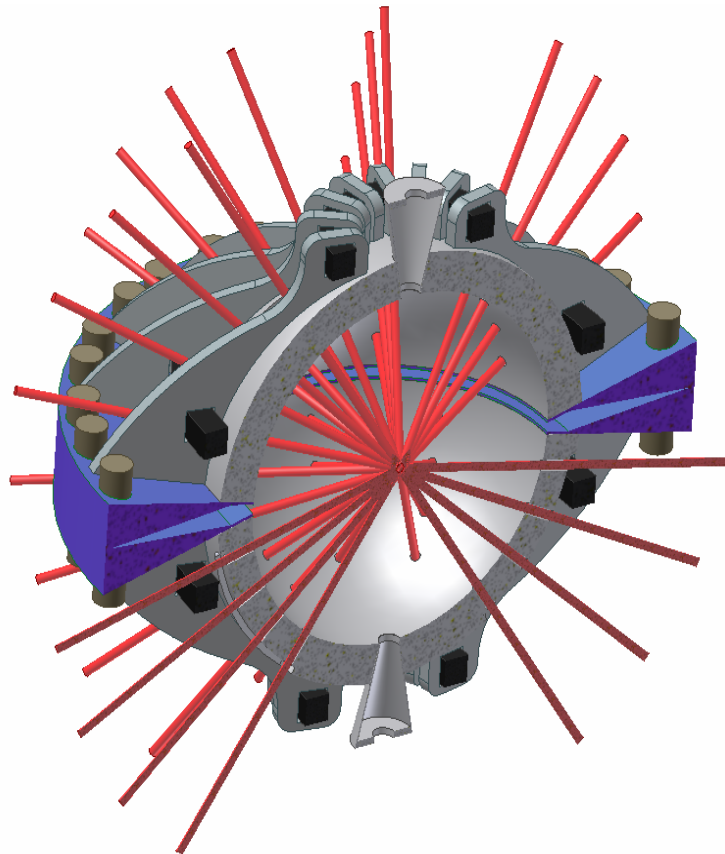


Figure 2.16: Cutaway schematic of ICF fusion device [61].

Inertial Confinement Fusion (ICF) utilizes high-energy beams, such as lasers or ion beams, to heat and compress solid fuel targets. The laser beams are generated externally and reflected off a series of mirrors to produce the converging pattern seen in Figure 2.16. The target is injected into the chamber from the top and is hit by lasers in the chamber center. One example of a Deuterium-Tritium (D-T) target is shown in Figure 2-17. It is composed of a shell of D-T ice with a layer of ablator and an outer coating.

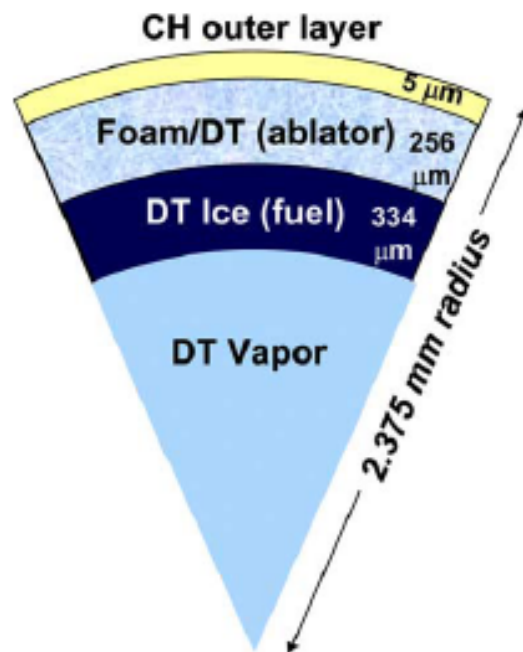


Figure 2.17: D-T target [50].

When the lasers strike the target, it is rapidly heated. The outer layers ablate and expand, compressing the fuel. The heating and compression initiates a fusion burn within the fuel. The energy released vaporizes the remaining target, sending x-rays, unburned fuel ions, neutrons, and other fusion products toward the chamber walls. The ion debris is composed primarily of hydrogen and helium species whose energy ranges from tens of keV to a few MeV. A typical helium energy spectrum at the first wall with no internal gas in the chamber is shown in Figure 2.18 [62].

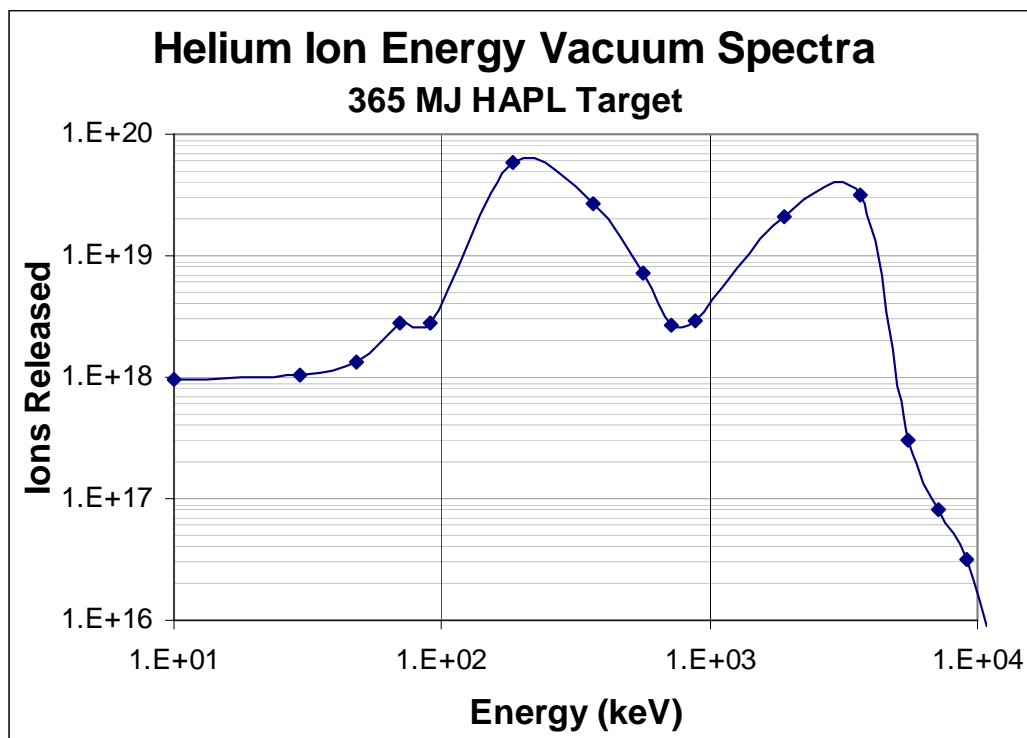


Figure 2.18: Helium ion energy spectra at the HAPL first wall [62].

The HAPL project has pulled together teams of experimental and computational scientists to understand the effects of these threat spectra on the first wall. Several research groups are looking at the effects of helium ions on tungsten. The Repetitive High-Energy Pulsed Power (RHEPP) experiment at the Sandia National Laboratory is investigating the effects of high flux, short duration ion pulses to simultaneously simulate ICF heating and damage [63]. Groups at the University of North Carolina [64] and the University of Wisconsin-Madison [34] are also investigating surface morphology and helium retention of steady-state helium bombardments. Scientists at UNC have focused on high-energy (> 1 MeV) helium implantation, while UW-Madison researchers are focusing on low-energy

(<100 keV) implantation. A summary of the fluence, temperature, and voltage (ion energy) for initial experiments performed by Cipiti and Kulcinski is found in Figure 2.19.

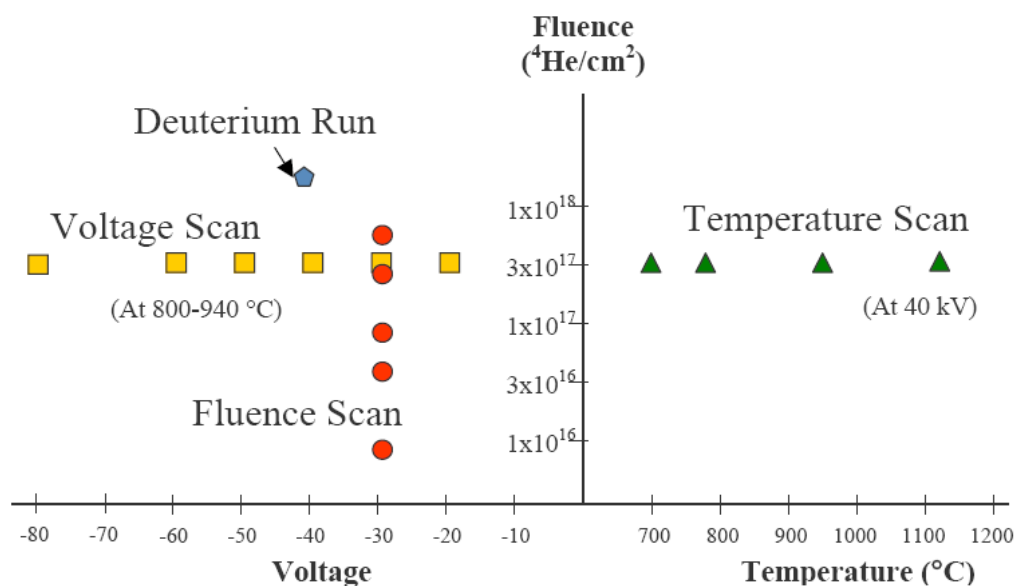


Figure 2.19: Summary of early UW-Madison experimental conditions for He^+ ions on tungsten [34].

The HAPL program is also working to model the effects of helium implantation in tungsten. These modeling efforts have been lead by Sharafat and Ghoniem at UCLA [65]. Their approach has been to first model the initial helium implantation, and then model the helium migration and bubble formation. The first portion of this task is performed using HEROS, a numerical code that evaluates the reaction-diffusion rate equation [65]. The temperature and helium implantation profiles for a typical test can be seen in Figure 2.20. The code then breaks the tungsten sample into variable-size bins and determines the initial bubble density and average bubble radii throughout the sample.

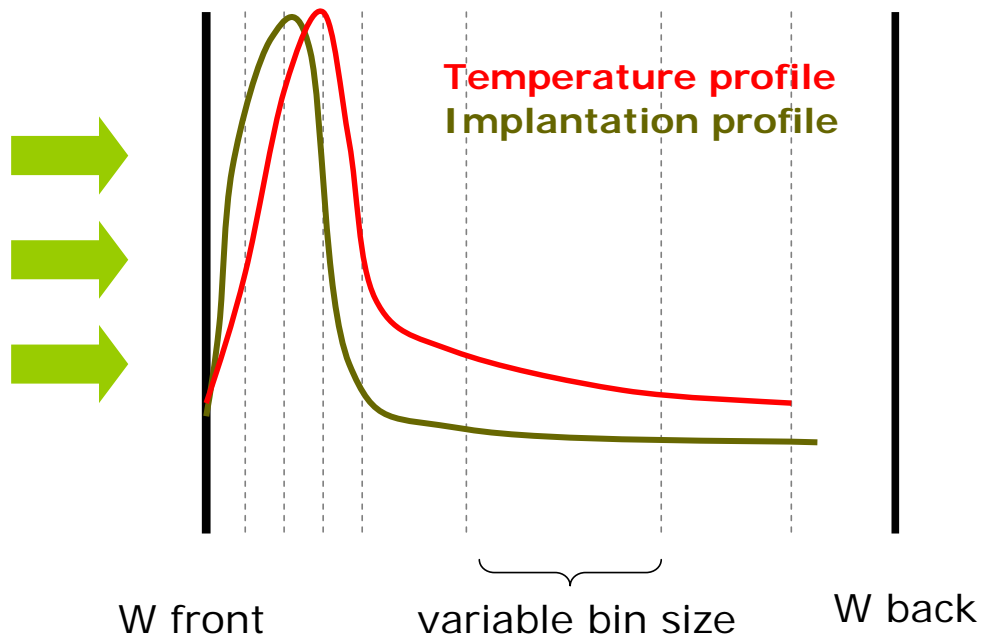


Figure 2.20: Typical temperature and helium ion profiles for the HEROS code [65].

Once these initial conditions are determined, a second code is used to evaluate the migration and coalescence of helium bubbles within the tungsten matrix as a function of time [66]. Figure 2.21 shows the time progression of helium bubbles collecting to form larger and larger bubbles. The sample is originally loaded with a helium atom distribution consistent with a 40 keV helium irradiation to 1×10^{19} ions/cm². Note that red circles represent matrix bubbles, while blue circles represent surface pores. The coupling of these codes has resulted in good agreement with experimental results, particularly with those of the University of Wisconsin group, as will be shown in Chapter 5.

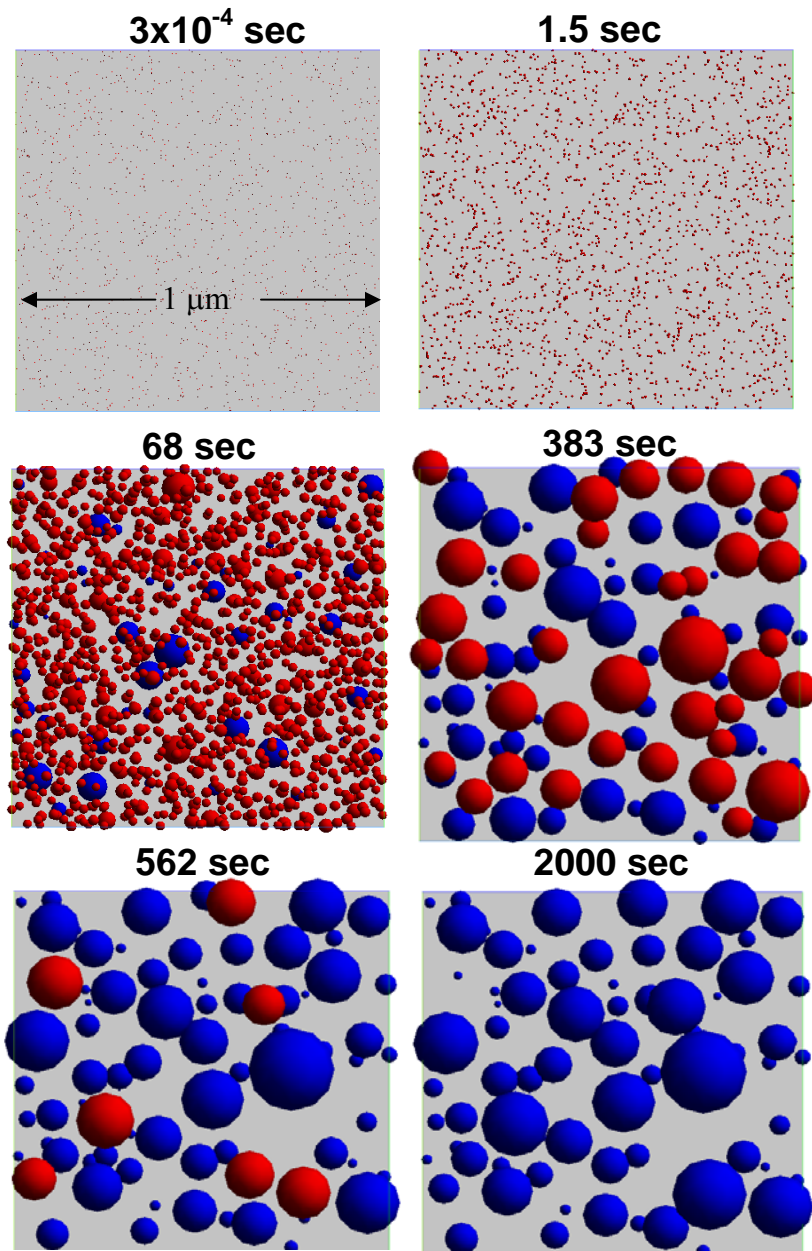


Figure 2.21: Time sequence of pore evolution for 730°C tungsten. Blue circles represent surface pores, while red circles represent matrix bubbles [66].

2.4 References

- [1] W.C. Elmore, J.L. Tuck, and K.M. Watson, "On the Inertial-Electrostatic Confinement of a Plasma," *Physics of Fluids*, Vol. 2, p. 239, 1959
- [2] P.T. Farnsworth, "Electric Discharge Device for Producing Interaction Between Nuclei," U.S. Patent #3,258,402, patented June 28, 1966
- [3] P.T. Farnsworth, "Method and Apparatus for Producing Nuclear-Fusion Reactions" U.S. Patent #3,386,883, patented June 4, 1986
- [4] R.L. Hirsch, "Inertial-Electrostatic Confinement of Ionized Fusion Gases," *Journal of Applied Physics*, Vol. 38, p. 4522, 1967
- [5] D.A. Swanson et al., "Potential Well Structure in an Inertial Electrostatic Plasma Confinement Device," *The Physics of Fluids*, Vol. 16, No. 11, November 1963
- [6] T.J. Dolan, J.T. Verdeyen, D.J. meeker, and B.E. Cherrington, "Electrostatic-Inertial Plasma Confinement," *Journal of Applied Physics*, Vol. 43, p. 1590, 1972
- [7] W.M. Black and J.W. Robinson, "Measuring Rotationally Symmetric Potential Profiles with an Electron-Beam Probe," *Journal of Applied Physics*, Vol. 45, No. 6, June 1974
- [8] A.L. Gardner et al., "Measurements on a Spherical Electrostatic Confinement System Employing Six Ion Guns," *Annals New York Academy of Sciences*, Vol. 251, 1975
- [9] R.W. Bussard, "Method and Apparatus for Creating and Controlling Nuclear Fusion Reactions," U.S. Patent #4,826,646, patented May 2, 1989
- [10] G.H. Miley, "A Portable Neutron/Tunable X-Ray Source Based on Inertial Electrostatic Confinement," *Nuclear Instruments and Methods in Physics Research A*, Vol. 422, No. 16, 1999
- [11] G.H. Miley et al., "Inertial Electrostatic Confinement: An Approach to Burning Advanced Fuels," *Fusion Technology*, Vol. 19, p. 840, 1991
- [12] G.H. Miley & J. Sved, "The IEC Star-Mode Fusion Neutron Source for NAA: Status and Next-Step Designs," *Applied Radiation and Isotopes*, Vol. 53(4-5), p. 779, 2000
- [13] I. Hrbud, "IEC Research Status at MSFS," presented at The 3rd U.S.-Japan Exchange on IEC, March 22-23, 2001, Huntsville, Alabama
- [14] R.A. Nebel & D.C. Barnes, "The Periodically Oscillating Plasma Sphere," *Fusion Technology*, Vol. 34, p. 28-45, 1998

- [15] R.P. Ashley et al., "D-³He Fusion in an Inertial Electrostatic Confinement Device," 18th IEEE/NPSS Symposium on Fusion Engineering, IEEE #99CH37050, p. 35, October 25-29, 1999
- [16] H. Matsuura et al., "Ion Distribution Function and Radial Profile of Neutron Production Rate in Spherical Inertial Electrostatic Confinement Plasmas," *Nuclear Fusion*, Vol. 40(12), p. 1951, 2000
- [17] M. Ohnishi et al., "Correlation Between Potential Well Structure and Neutron Production in Inertial Electrostatic Confinement Fusion," *Institute of Advanced Energy Research Report*, Kyoto University, ISSN 1342-3185, October 21, 1996
- [18] M. Ohnishi et al., "Beam Optics in Inertial Electrostatic Confinement Fusion," *Review of Scientific Instruments*, Vol. 71(2), p. 1210, 2000
- [19] K. Yamauchi et al., "Neutron Production Characteristics and Emission Properties of Spherically Convergent Beam Fusion," *Fusion Technology*, Vol. 39(3), p. 1182, 2001
- [20] K. Masuda et al., "Simultaneous Neutron and Proton Measurements of D-D and D-³He Fusion Reaction in an Inertial Electrostatic Confinement Fusion Device," (to be published in *Fusion Science and Technology*)
- [21] M.J. Park, "RF Plasma Ion Sources of Compact Neutron Generators," presented at the 6th U.S.-Japan Workshop on IEC, October 20-21, 2003, Tokyo, Japan.
- [22] J. Khachan, et. al., "Spatial Distribution of Ion Energies in an Electrostatic Confinement Device," *Physics of Plasmas*, Vol. 10, No. 3, 2003
- [23] R.A. Nebel and D.C. Barnes, "The Periodically Oscillating Plasma Sphere," *Fusion Technology*, Vol. 34, p. 28-45, 1998
- [24] Y. Gu, G. Miley, S. DelMedico, "Pulsed IEC Neutron Generator," Digest of Technical Papers. Tenth IEEE Trans., Volume 2, p. 1500 – 1505, 1995
- [25] R.P. Ashley, G.L. Kulcinski, J.F. Santarius, S. Krupakar Murali, G.R. Piefer, B.B. Cipiti, R.F. Radel, and J.W. Weidner, "Recent Progress in Steady State Fusion Using D-3He," *Fusion Science and Technology*, Vol. 44, p. 564, 2003
- [26] Y. Iwamoto et. Al. "Preliminary Results of Cylindrical Electrostatic Confinement Experiment" *Fusion Technology*, Vol. 39, Number 2, Part 2, p. 552-556, 2001
- [27] K. Yamauchi et al., "Pulsed Operation of a Compact Fusion Neutron Source Using a High-Voltage Pulse Generator Developed for Landmine Detection" (to be published in *Fusion Science and Technology*)

- [28] K. Yamauchi et al., "Performance of Neutron/Proton Source Based on Ion-Source-Assisted Cylindrical Radially Convergent Beam Fusion," *IEEE Trans. FM*, Vol. 126, No. 8, 2006
- [29] T. A. Thorson, "Ion Flow and Fusion Reactivity Characterization of a Spherically Convergent Ion Focus," PhD thesis, University of Wisconsin—Madison, 1994
- [30] G.L. Kulcinski, "Near Term Commercial Opportunities from Long Range Fusion Research," *Fusion Technology*, Vol. 30, Issue 3, p. 411-420, 1996
- [31] J.W. Weidner, "The Production of ^{13}N from Inertial Electrostatic Confinement Fusion," Master's Thesis, University of Wisconsin-Madison (2003)
- [32] B.B. Cipiti & G.L. Kulcinski, "Embedded $\text{D}-^3\text{He}$ Fusion Reactions and Medical Isotope Production in an Inertial Electrostatic Confinement Device," *Fusion Science and Technology*, Vol. 44, p. 534, 2003
- [33] A.L. Wehmeyer, "The Detection of Explosives Using an Inertial Electrostatic Confinement D-D Fusion Device," Master's Thesis, University of Wisconsin-Madison, 2005
- [34] B.B. Cipiti and G.L. Kulcinski, "Helium and Deuterium Implantation in Tungsten at Elevated Temperatures," *Journal of Nuclear Materials*, Vol. 347(3), p. 298, 2005
- [35] R.F. Radel and G.L. Kulcinski, "Implantation of He^+ in Candidate Fusion First Wall Materials" (accepted for publication in *Journal of Nuclear Materials*)
- [36] R.F. Radel and G.L. Kulcinski, "Implantation of D and He in W-coated Refractory Carbides," *Fusion Science and Technology*, Vol. 47(4), p. 1250, 2005
- [37] S.J. Zenobia, "Effects of He^+ Implantation on CVD SiC Surface Morphology," (to be published in *Fusion Science and Technology*)
- [38] G.A. Emmert and J.F. Santarius, "A Charge-Exchange Based Model for the Performance of Gridded, Spherical IEC Devices; Part I: single species atomic ions" (in preparation, 2007)
- [39] G.A. Emmert and J.F. Santarius, "A Charge-Exchange Based Model for the Performance of Gridded, Spherical IEC Devices; Part II: molecular ions" (in preparation, 2007)
- [40] G.R. Piefer, "Performance of a Low-Pressure, Helicon Driven IEC ^3He Fusion Device" PhD Thesis, University of Wisconsin-Madison, 2006
- [41] D.R. Boris, "Direct Conversion of High Energy Protons to Electricity using a Solid State PIN junction diode," (to be published in *Fusion Science and Technology*)

- [42] B.J. Egle, J.F. Santarius, and G.L. Kulcinski, "Comparison of Spherical and Cylindrical Cathode Geometries in Inertial Electrostatic Confinement Devices" (to be published in *Fusion Science and Technology*)
- [43] S. Guardini et al., "*Performance Values for Non-Destructive Assay (NDA) Techniques Applied to Safeguards: The 2002 Evaluation by the ESARDA NDA Working Group*". ESARDA Publication, 2002
- [44] Dewberry, R. and Salaymeh, S. "Assay of Drums with Unknown Content Stored in 247-41F" WSRC-TR-2002-00168, 2002
- [45] J.T. Mihalczko, J.K. Mattingly, J.S. Neal, J. A. Mullens, "NMIS plus Gamma Spectroscopy for Attributes of HEU, PU and HE Detection," *Nuclear Instruments and Methods in Physics Research B*, Vol. 213 (2004) 378-384
- [46] C.E. Moss, C.A. Goulding, C.L. Hollas, and W.L. Myers, "Linear Accelerator-Based Active Interrogation For Detection of Highly Enriched Uranium," in Proc. 17th Int. Conf. Application Accelerators Research and Industry, vol. 680, Denton TX, Nov. 12-16, 2002, pp. 900-904
- [47] D.R. Brown and T.Gozani, "Cargo Inspection System Based on Pulsed Fast Neutron Analysis" *Nuclear Instruments and Methods in Physics Research B*, Vol. 99, p. 753 – 756, 1995
- [48] C.A. Moss et al, "Neutron Detectors for Active Interrogation of Highly Enriched Uranium" *IEEE Transactions on Nuclear Science*, Vol. 45, No. 4, August 2004
- [49] M. Kaminsky, Atomic and Ionic Impact Phenomena on Metal Surfaces. Springer-Verlag, New York, 1965
- [50] Y. Shimomura, "ITER Overview," *Nuclear Fusion*, Vol. 39, No. 9Y, 1999
- [51] J.D. Sethian, "An Overview of the Development of the First Wall and other Principal Components of a Laser Fusion Power Plant," *Journal of Nuclear Materials*, Vol. 347, p. 161–177, 2005
- [52] H. Ullmaier, "The Influence of Helium on the Bulk Properties of Fusion Reactor Structural Materials," *Nuclear Fusion*, Vol. 24, No. 8, 1984
- [53] S.K. Erents and G.M. McCracken, "Blistering of Molybdenum under Helium Ion Bombardment," *Radiation Effects*, Vol. 18, p. 191, 1973
- [54] G.J. Thomas and W. Bauer, "Surface Deformation in He and H Implanted Metals," *Journal of Nuclear Materials*, Vol. 53, p. 134-141, 1974

- [55] S.K. Das and M. Kaminsky, "Radiation Blistering in Metals and Alloys," Proceedings of the "Symposium on Radiation Effects on Solid Surfaces," Advances in Chemistry Series, 1975
- [56] D.K. Brice, "Ion Implantation Rand and Energy Deposition Codes COREL, RASE4 and DAMG2," SAND75-0622, 1975
- [57] J.H. Evans, "The Role of Implanted Gas and Lateral Stress in Blister Formation Mechanisms," *Journal of Nuclear Materials*, Vol. 76/77, p. 228-234, 1978
- [58] W. Bauer et. al, "Helium Induced Blistering During Simultaneous Sputtering," *Journal of Nuclear Materials*, Vol. 76/77 p. 396-401, 1978
- [59] C.P.C. Wong et al, "ARIES-RS Divertor System Selection and Analysis," *Fusion Engineering and Design*, Vol. 38, p. 115–137, 1997
- [60] J.N. Brooks, "Assessment of Erosion and Surface Tritium Inventory Issue for the ITER Divertor," *Journal of Nuclear Materials*, Vol. 241–243 p. 294–298, 1997
- [61] A. Raffray et al, "Progress Towards Realization of a Laser IFE Solid Wall Chamber," *Fusion Engineering and Design*, Vol. 81, Issues 8-14, p. 1627, 2006
- [62] L.J. Perkins, Lawrence Livermore National Laboratory, personal communication, 2005
- [63] T.J. Renk, "Chamber Wall Materials Response to Pulsed Ions at Power-Plant Level Fluences," *Journal of Nuclear Materials*, Vol. 347, Issue 3, p 266-288, 2005
- [64] S.B. Gilliam, et al, "Retention and Surface Blistering of Helium Irradiated Tungsten as a First Wall Material," *Journal of Nuclear Materials*, Vol. 347, Issue 3, p 289-297, 2005
- [65] Q. Hu, "Modeling Space-Time Dependent Helium Bubble Evolution in Tungsten Armor under IFE Conditions," to be published in *Fusion Science and Technology*
- [66] A. Takahashi, et al, "MC Simulation of Tungsten Surface Pores Formed by Low-Energy Helium Implantation," to be published in *Fusion Science and Technology*

Chapter 3: Theory

3.1 Inertial Electrostatic Confinement

The three primary fusion reactions of interest for IEC systems are D-T, D-D, and D- ^3He . As seen in Figure 3.1, the D-T, or deuterium-tritium, reaction yields a 14.1 MeV neutron. As shown in Figure 3.1, the D-D, or deuterium-deuterium, reaction has two possible reaction paths, each of which is approximately equally likely to occur. Half of the D-D reactions, therefore, yield a 2.45 MeV neutron, while the other half will produce a 3.02 MeV proton. The D- ^3He , or deuterium-helium-3, reaction produces a 14.68 MeV proton, as shown in Figure 3.1.

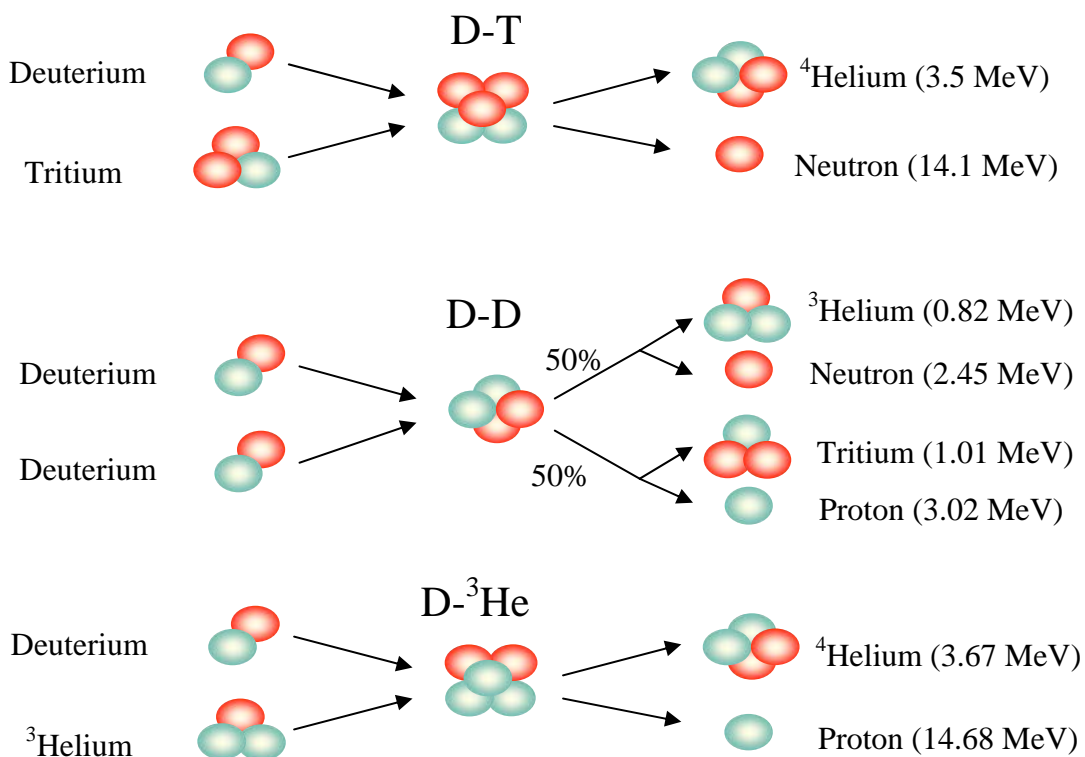


Figure 3.1: IEC fusion reactions and product energies. Blue circles represent protons and red circles represent neutrons [1].

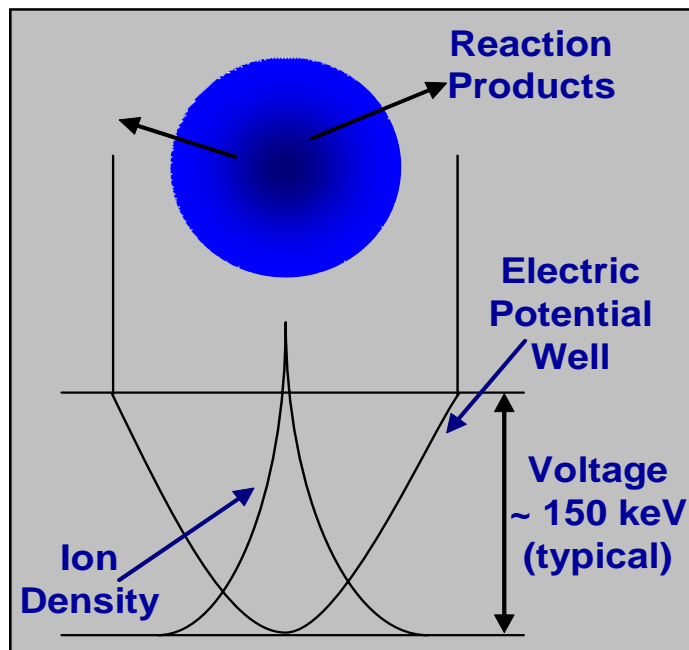


Figure 3.2: Potential and ion distributions in an IEC device. Ion density rapidly increases as the potential well deepens in the center of an IEC device. From [2].

During operation of a typical IEC device, negative voltage is applied to the inner grid cathode, and the anode is grounded, so the positively charged ions are attracted to the center of the grid. As seen in Figure 3.2, the ions will accelerate down this potential well to the cathode potential, pass through the center of the device, and decelerate back to ground potential as they reach the outer anode [2]. Though an individual ion will not spend much time there, a high steady-state ion density will be created at the center of the inner grid.

There are numerous potential fates for an individual ion traveling toward the inner grid. First, it could hit nothing, as described above, decelerate back to ground potential, and begin its journey back down the “potential hill”. Second, it could hit a background gas particle or ion, elastically scatter or become neutral in a process known as charge exchange,

and continue out to the wall of the device as a neutral particle. If the ion is energetic enough when it collides to overcome the Coulomb forces generated by their nuclei, it will fuse with its target and generate fusion products. Finally, the ion could simply collide with a grid wire.

Fusion cross-sections for the reactions of interest in an IEC system vary quite a bit between 0-200keV of IEC well depth. Figure 3.3 shows a plot of fusion cross-sections of interest for a typical IEC device. The cross-sections are plotted as function of center-of-mass energy in keV. The D-T reaction has the highest cross-section over this energy range. The cross section of D-D is greater than D-³He below about 80 keV, but then D-³He takes over.

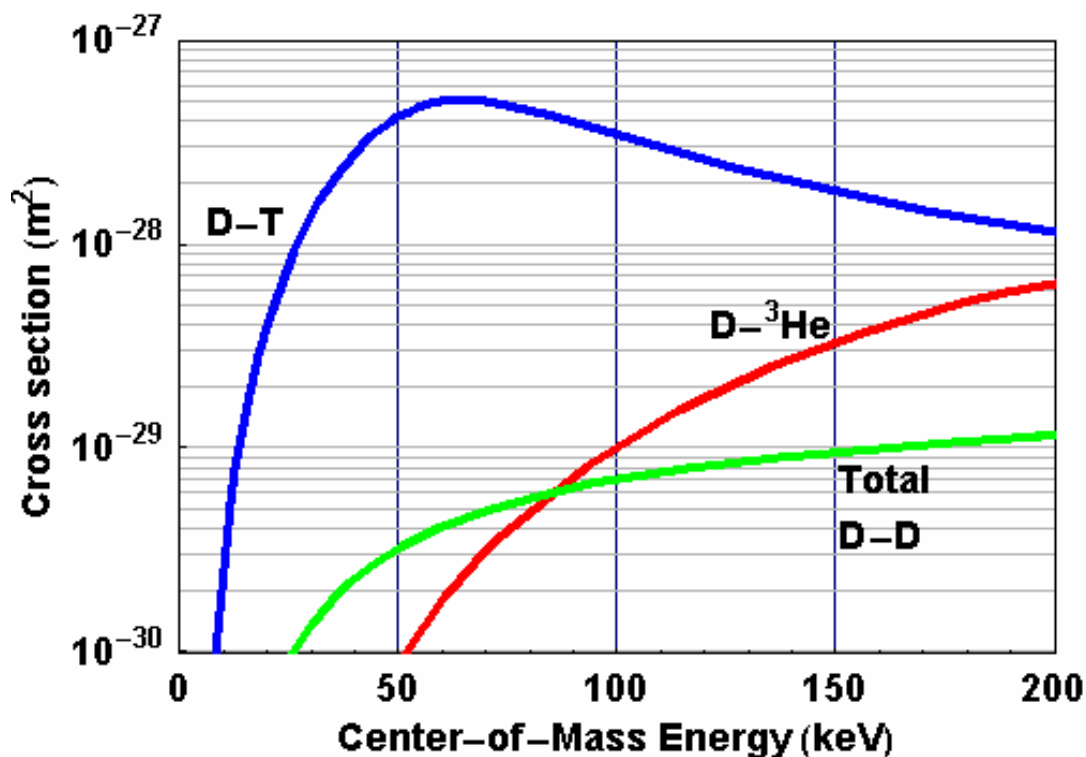


Figure 3.3: Fusion cross sections as a function of center-f-mass energy in a spherical IEC device [3].

Recent work at the UW-Madison has suggested that there are actually three sources of fusion reactions within an IEC device, as depicted in Figure 3.4 [4]. The first is

“converging core” regime as described above. These reactions essentially all take place within the inner grid of the device, predominately as a result of beam-background fusion at cathode potential. The second source, referred to as a “volume source”, of fusion neutrons is a result of the high-energy charge exchange neutrals.

When these particles collide with the background gas with sufficient energy, they can induce fusion as well. These fusion reactions will be found throughout the volume of the vacuum chamber, but the fusion density will be higher toward the center of the device.

The final source of fusion within the IEC device results from high-energy deuterium particles embedding in the grid wires, particularly in the cathode. As other ions hit the grid, it will become a source of beam-target fusion. This regime is known as a “surface source”. These three sources - “converging core”, “volume source”, and “surface source” – combine to generate the total fusion rate being produced in the UW IEC device. Cipiti’s results indicated that the volume source is dominant for D-D reactions and the surface source is dominant for D-³He reactions [4].

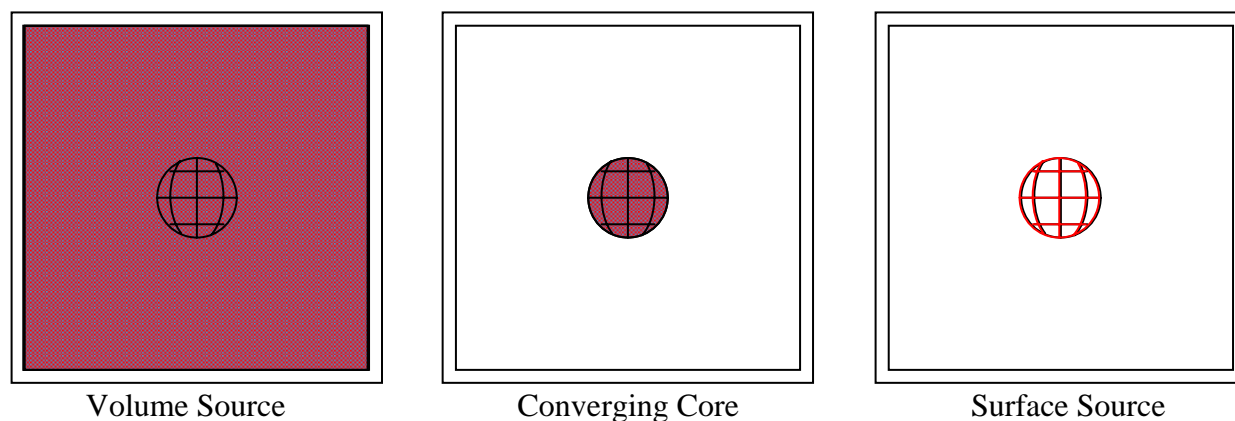


Figure 3.4: The three regions of neutron production in the UW-IEC. Red represents the predominant region of fusion reactions [4].

3.2 Highly Enriched Uranium Detection

There are two fundamental nondestructive methods of detecting highly enriched uranium (HEU) or other forms of special nuclear material (SNM) – active and passive interrogation. Passive assay relies on the emission of either photons or neutrons from the HEU, either by decay or spontaneous fission. Gozani summarizes the spontaneous radiation observed from many isotopes of interest, as shown in Table 3.1 [5]. Note that some of these decay modes result in particles that are highly penetrating, and could be detected through a cargo container or other vehicle. It is, however, relatively easy to shield these photons using a small volume of material. In addition, all of these decay modes have long half-lives resulting in low count rates, which can reduce detection efficiency or require excessive interrogation times. Calorimetric techniques can also be used as a passive interrogation scheme, but it is again relatively easy to deceive such a system, particularly when low quantities of SNM are present [5].

Active interrogation utilizes either a neutron or a gamma ray source to irradiate the nuclear material. Each of these will then initiate fissions within the material, releasing two to three prompt fast neutrons and approximately eight prompt gamma rays. In addition to the prompt radiation, fission product nuclei will continue to emit delayed neutrons and gammas for several minutes after the initiating event. Detection schemes have been developed to target either the prompt or the delayed spectra. Active interrogation offers a number of advantages over its passive counterpart. Neutrons and high-energy gammas are both very penetrating radiation sources. The fission neutrons and resulting gammas are also highly penetrating and difficult to shield. In addition, the source strength – and therefore signal strength – can be tuned to appropriate levels for various applications. Active interrogation is

also more universally applicable, as passive interrogation is ineffective for plutonium and uranium-235.

Radiation Observed in Non-Destructive Analysis

Nuclide	Decay Mode	Radiation, Type	Intensity (s ⁻¹ , g ⁻¹)	Specific Power (W/g)	Thermal Fission Cross Section (b)
²³⁵ U	α	185.7 keV γ	4.3x10 ⁴		577 (fissile)
²³⁸ U	α	1001.1 keV γ	1.0x10 ²		<0.5
		766.4 keV γ	3.9x10 ¹		
	fission	fission neutrons	1.7x10 ⁻²		
²³⁸ Pu	α	766.4 keV γ	1.5x10 ⁵	5.67x10 ⁻¹	18.4
		152.7 keV γ	6.5x10 ⁻⁶		
		(α,n) neutrons, PuO ₂	1.4x10 ⁴		
	fission	fission neutrons	2.6x10 ³		
²³⁹ Pu	α	413.7 keV γ	3.4x10 ⁴	1.93x10 ⁻³	741 (fissile)
		129.3 keV γ	1.4x10 ⁵		
		(α,n) neutrons, PuO ₂	4.5x10 ²		
²⁴⁰ Pu	α	no useful γ's	--	7.10x10 ⁻³	0.03
		(α,n) neutrons, PuO ₂	1.7x10 ³		
	fission	fission neutrons	1.0x10 ³		
²⁴¹ Pu	β	208.0 keV γ	2.0x10 ⁷	3.39x10 ⁻³	950 (fissile)
		164.6 keV γ	1.8x10 ⁶		
		148.6 keV γ	7.5x10 ⁶		
²⁴² Pu	α	no useful γ's	--	1.15x10 ⁻⁴	--
		(α,n) neutrons, PuO ₂	1.0x10 ¹		
	fission	fission neutrons	1.7x10 ³		

Table 3.1: Natural Radiation from U and Pu isotopes (after [5]).

3.2.1 Fission

Active detection of SNM relies primarily on inducing fission reactions within the materials to be detected. Fission cross-sections (σ_f) of fissile material are relatively large, particularly at thermal energies. The fission cross-section for uranium-235 is shown in Figure 3.5 [6]. At low energy, σ_f approximates the inverse of the neutron velocity; this is followed by a region of resonances; and, finally, smooth and rolling above the resonance region.

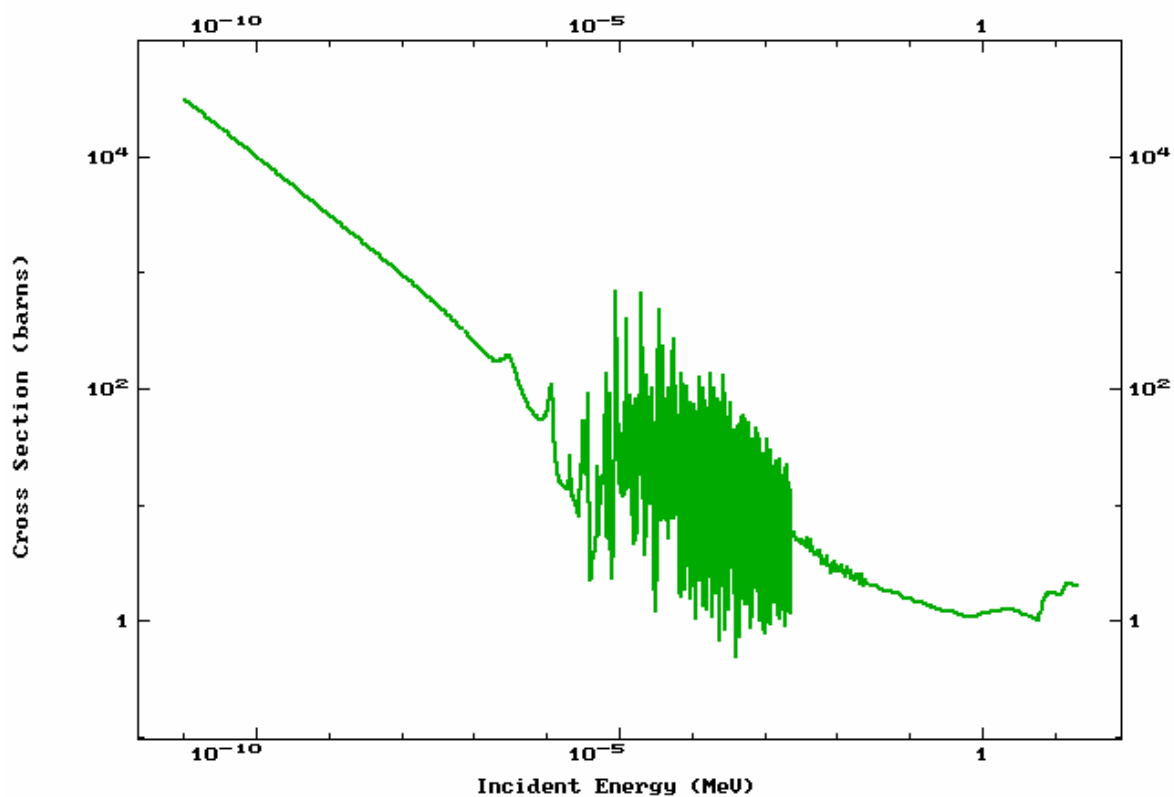


Figure 3.5: Fission cross-section of uranium-235 [6].

Fission reactions result in the production of fission products. The types of fission products generated will vary depending on the fissile material and the energy of the neutrons generating the reactions. Figure 3.6 shows fission product yields for thermal and 14 MeV fissions in uranium-235 [7]. These fission products are, on average, excessively neutron rich. As a result, they undergo a series of beta emissions. Of particular interest are the fission

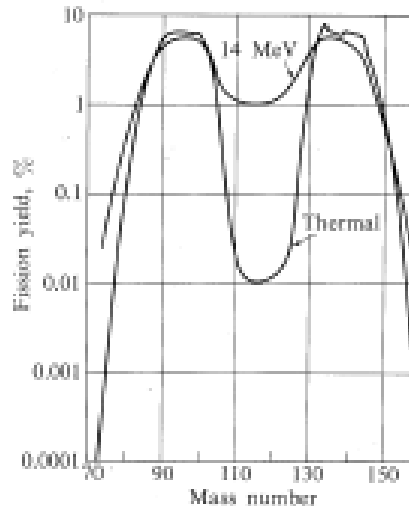
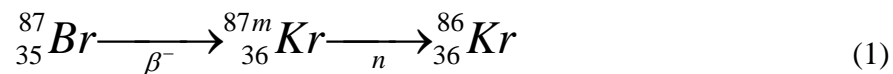


Figure 3.6: Fission product yield for ^{235}U [7].

products known as delayed neutron precursors. For example, when the fission product bromine-87 beta decays to krypton-87, the latter is sometimes formed in an excited state. In this case, the least bound neutron in the krypton-87 is ejected from the nucleus with an energy of approximately 0.3 MeV. Since this neutron is released when the excited state is formed, it appears to be emitted with the 54.5-second half-life of the bromine-87. This reaction is shown in equation 1 below.



A complete list of delayed neutron precursors, half-lives, and neutron-emission probabilities can be found in Pfeiffer [8].

3.2.2 Delayed Neutrons

Delayed fission neutrons represent only 0.65 percent of the total number of neutrons produced in the fission of uranium-235, and a similarly small fraction in other materials. Although there are dozens of isotopes contributing to the total delayed neutron population, the half-lives of these isotopes can be described using the six groups shown in Table 3.2 [9]. Each group has a characteristic half-life and a corresponding relative probability of emission.

Group Index	Half-Life (sec)	Relative Abundance (%)
1	54.51+/- 0.94	3.8+/- 0.3
2	21.84+/- 0.54	21.3+/- 0.5
3	6.00+/- 0.17	18.8+/- 1.6
4	2.23+/- 0.06	40.7+/- 0.7
5	0.50+/- 0.03	12.8+/-0.8
6	0.18+/- 0.02	2.6+/- 0.3

Table 3.2: Half-life and relative abundance for the six delayed neutron groups [9].

These data points were then used to calculate the growth and decay of the delayed neutron population during irradiation. Figures 3.7 and 3.8 show the growth of delayed neutrons during neutron irradiation. After one second, the total population has reached over 25 percent of its steady-state value. However, it requires another 60 seconds of irradiation before reaching 95 percent of its maximum value. When irradiation is stopped, the activity of the delayed neutrons quickly drops off, as shown in Figure 3.9.

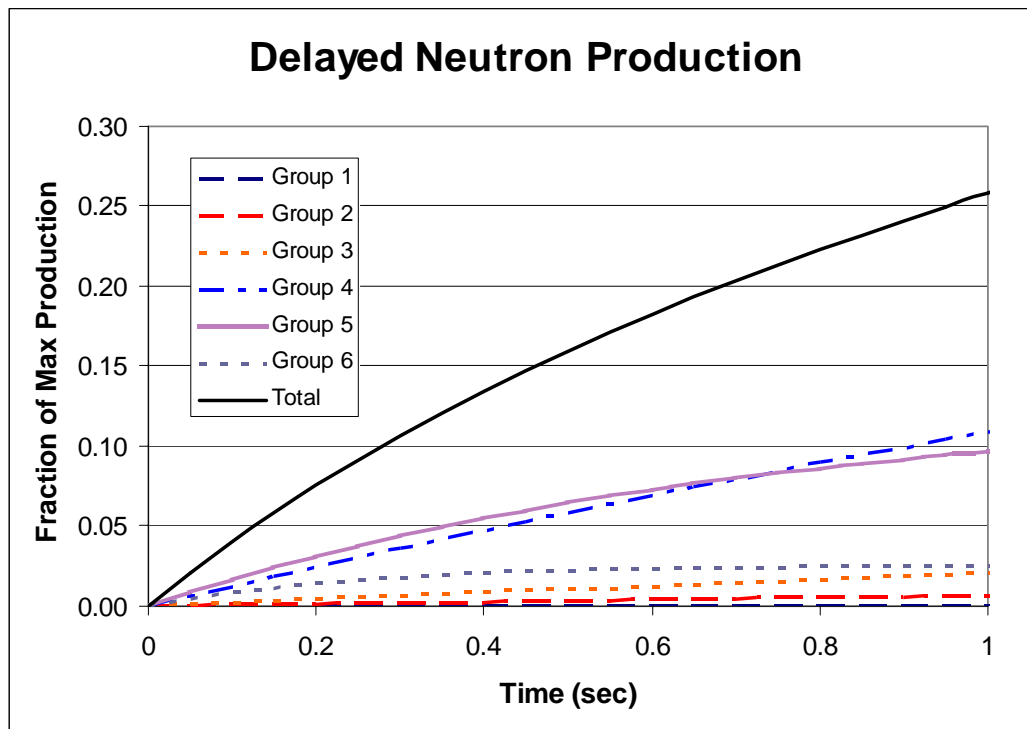


Figure 3.7: Growth of delayed neutron population during irradiation (1 second).

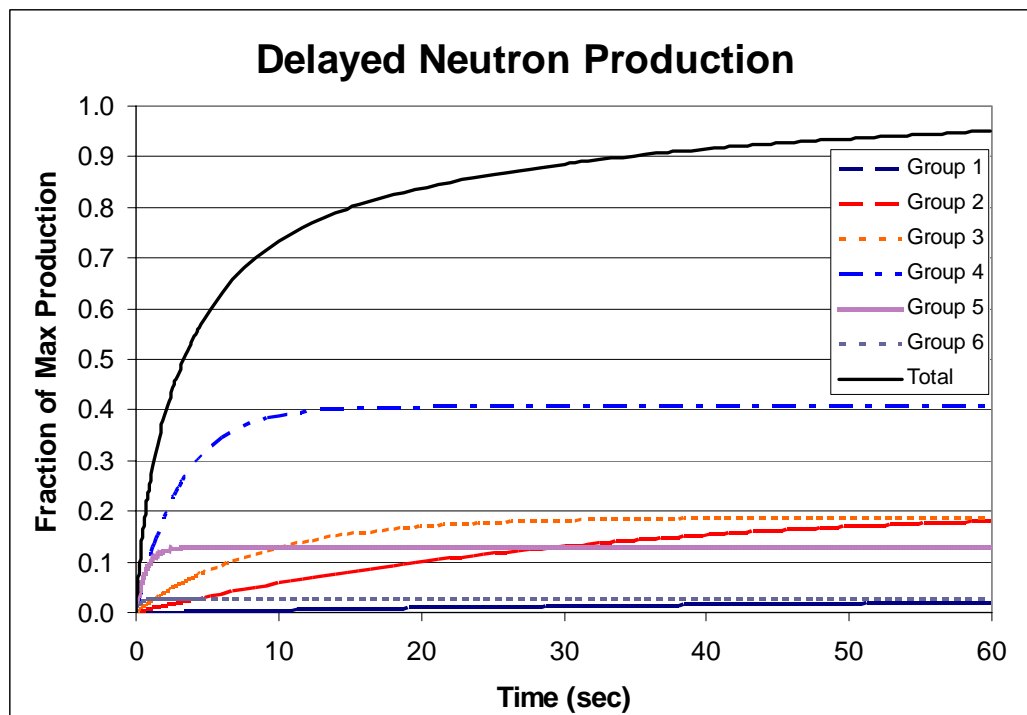


Figure 3.8: Growth of delayed neutron population during irradiation (60 seconds).

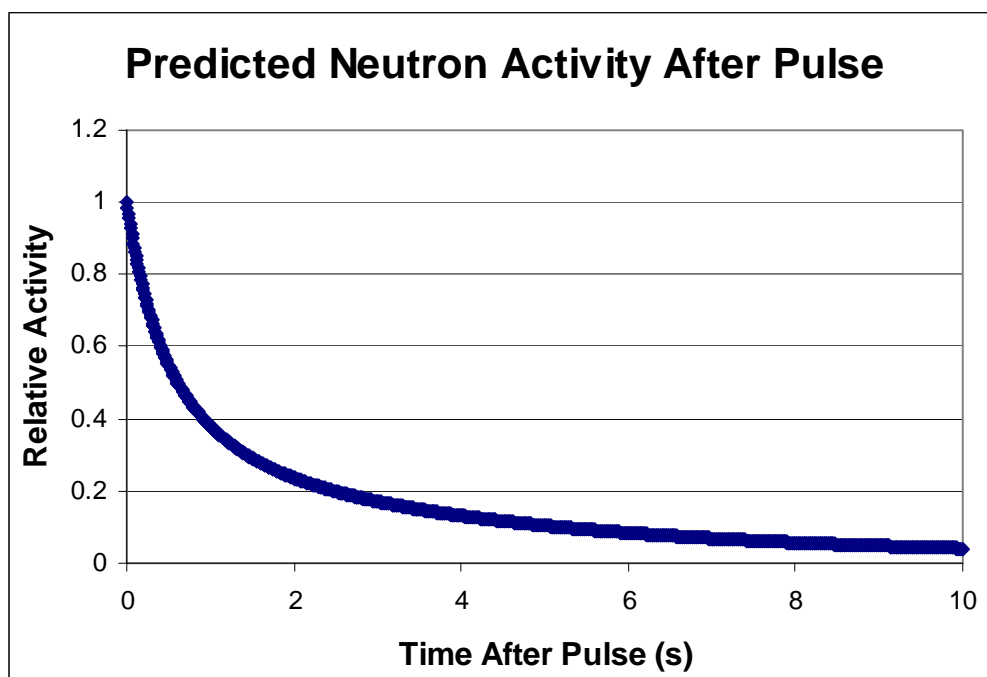


Figure 3.9: Predicted neutron activity after irradiation.

3.3 Tungsten Implantation Theory

3.3.1 Implantation Depth

The deposition depth of helium ions plays an important role during irradiation. It has a direct role in the formation of various types of damage structures. The average depth that a helium ion will penetrate into the tungsten surface, or projected range, is straightforward to predict. The National Institute of Standards and Technology has developed an extensive database of stopping-power and range tables for helium ions in various materials [10]. The projected range of helium ions for energies from 10 keV to 10 MeV is plotted in Figure 3.10.

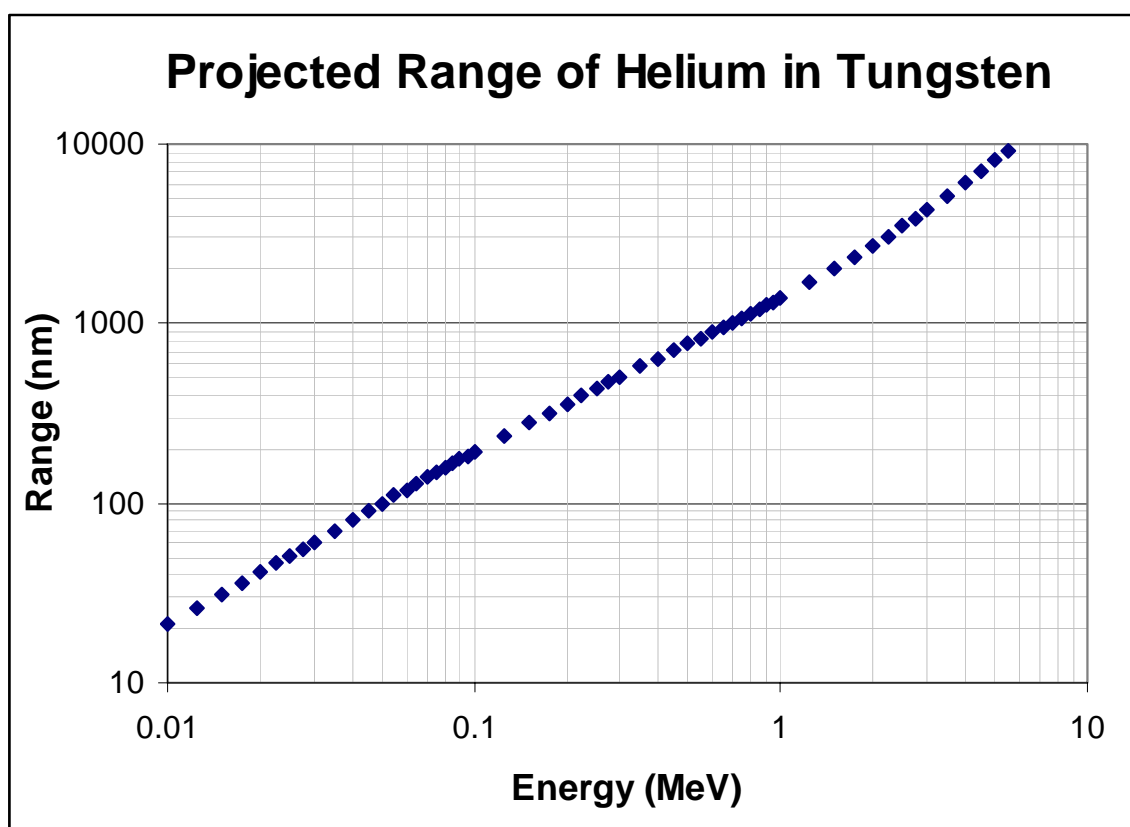


Figure 3.10: Projected helium range in tungsten vs. initial ion energy [10].

However, the projected range is only an indication of the average deposition depth of helium ions in tungsten. Collisions and large-angle scattering of the helium ions result in a wide depth distribution of helium within the tungsten matrix. This can be illustrated using TRIM, a particle-tracking model that determines the range of ions in matter [11]. Figure 3.11 shows a screenshot of 100 keV helium ions bombarding a tungsten target at a 90° angle.

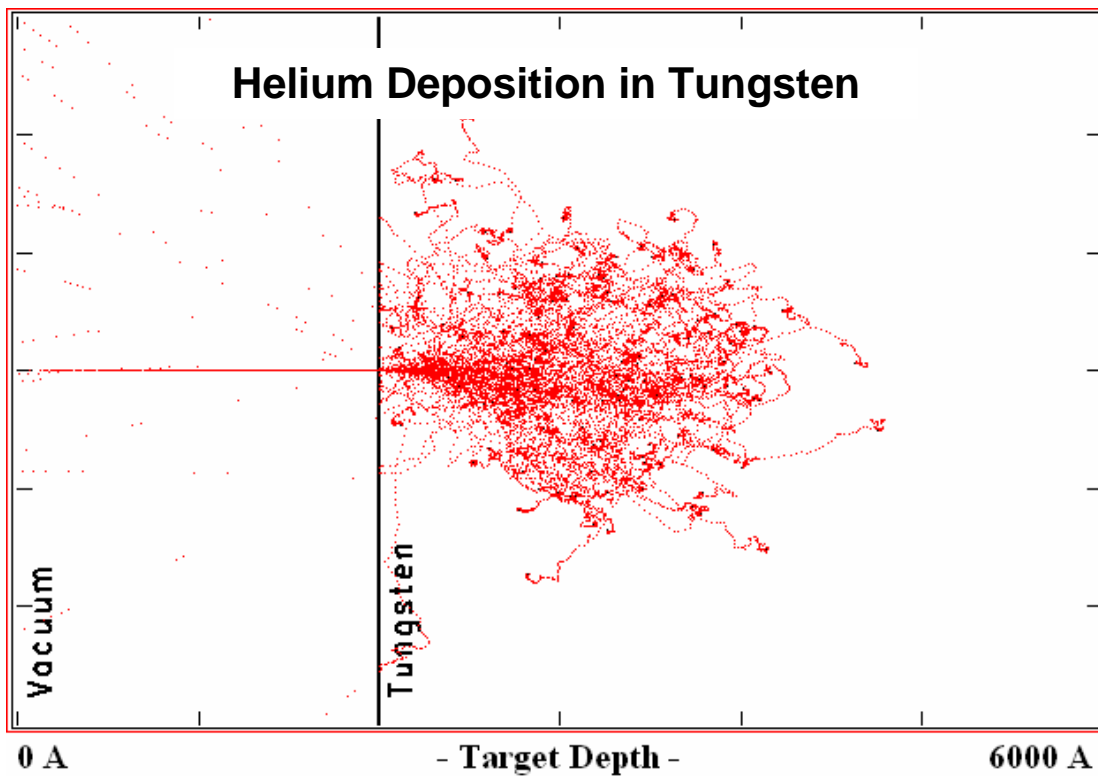


Figure 3.11: SRIM image of 100 keV helium implantation in tungsten [11].

3.3.2 Secondary Electron Emission

Ion bombardment of metal surfaces induces the emission of electrons, and this electron emission reduces the net ion current and plays an important role in helium implantation studies in the IEC device. The electron emission from the target cathode must be known to get an accurate measure of the ion current hitting the cathode. The high voltage power supply measures the current, but it includes both the ion and electron components. The actual ion current must be known to determine helium ion fluences accurately.

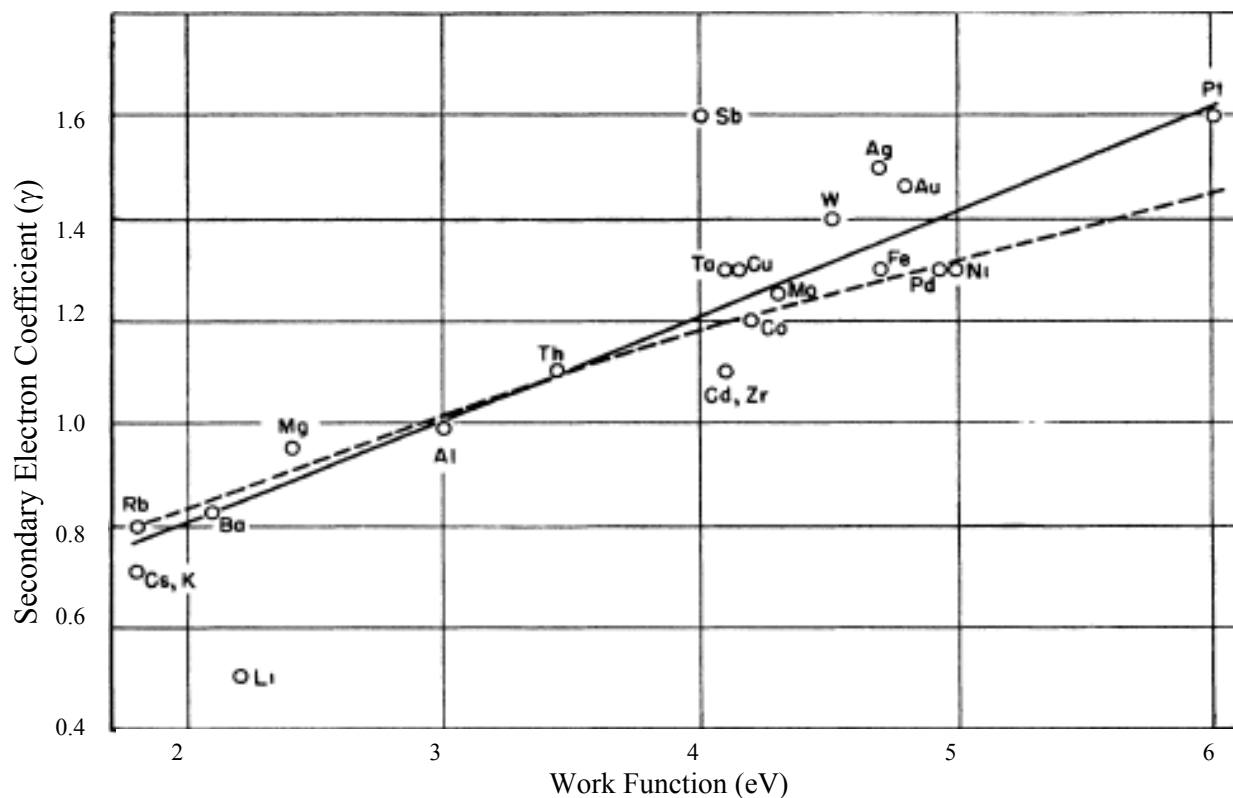


Figure 3.12: Ideal secondary electron coefficient vs. work function [12].

The secondary electron emission coefficient (γ) is defined as the number of electrons emitted per incident ion. Numerous experimental data sets are available for secondary electron coefficients, but it varies depending on the ion type, target work function (see Figure 3.12), surface finish, angle of incidence, temperature, and other variables. The experimental setup is also important in evaluating any data.

As seen in Figure 3.13, helium ions on tungsten produce secondary electron emission values ranging from 2-3 at energies in the 50-100 keV range [13]. These experiments were performed with an ion beam impinging a clean, smooth tungsten surface normal (0° to perpendicular) to the surface. Increasing angle of incidence can increase the secondary electron yield. Experiments with 250 keV deuterium ions on zirconium report γ as 5 at 0° (perpendicular) incidence, and up to 12 at 60° incidence [14].

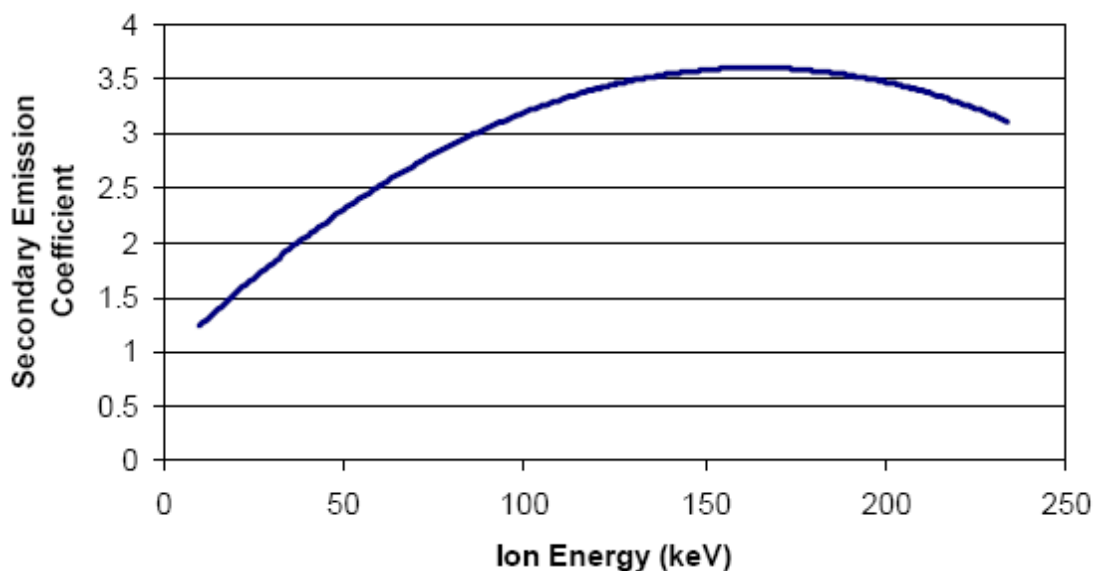


Figure 3.13: Secondary emission coefficient of tungsten vs. helium ion energy [13].

3.3.3 Sputtering

When evaluating mass loss on the tungsten samples, one must account for sputtering losses. Sputtering coefficients, like secondary electron coefficients, are dependent upon numerous factors, including ion energy, target species, and angle of incidence. Sputtering coefficients of tungsten (in sputtered atoms per incident ion) are plotted in Figures 3.14 and 3.15 as a function of energy for deuterium and helium, respectively.

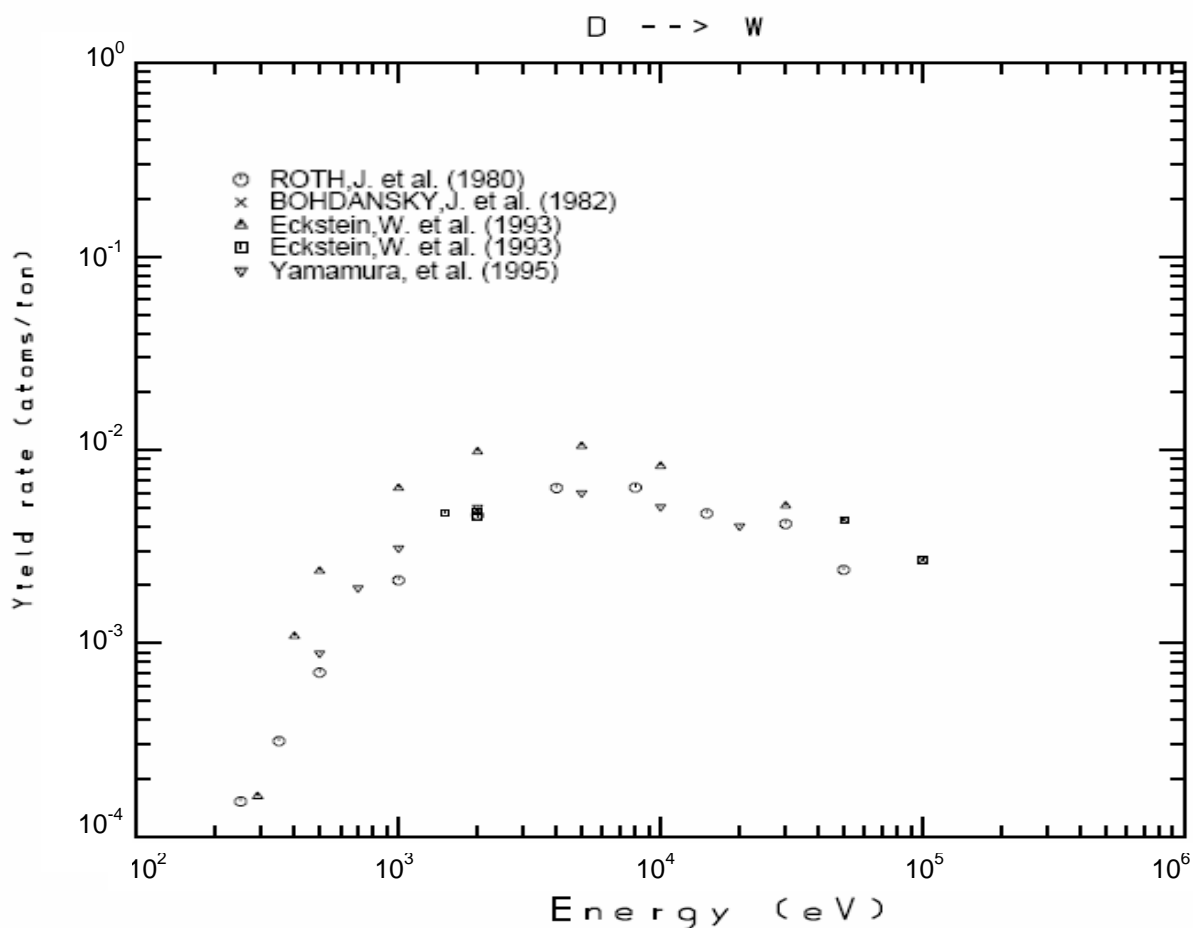


Figure 3.14: Deuterium on tungsten sputtering coefficients as a function of ion energy [15].

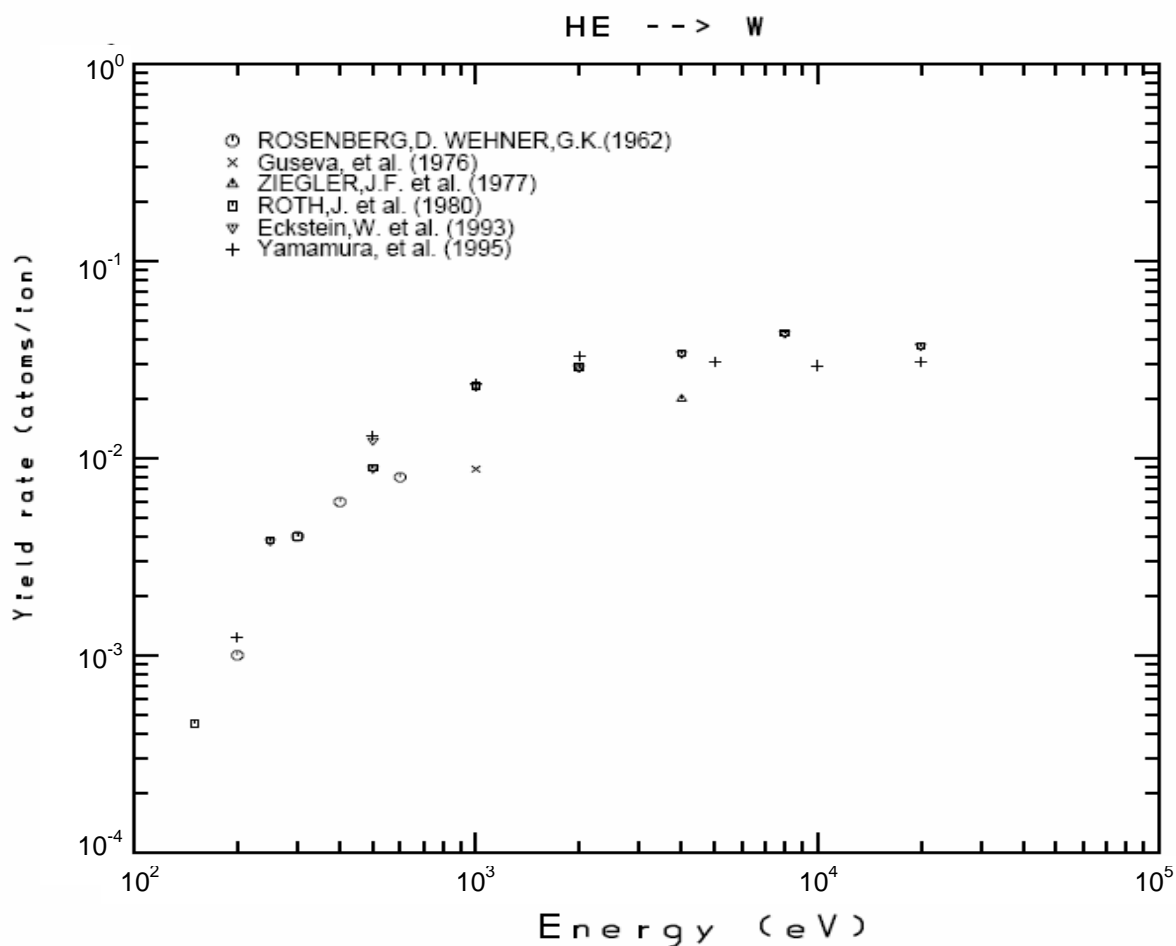


Figure 3.15: Helium on tungsten sputtering coefficients as a function of ion energy [15].

One of the most significant factors to consider when determining sputtering coefficients is the ion angle of incidence. Figure 3.16 plots the sputtering coefficient for a molybdenum target as a function of incident ion angle for H^+ , D^+ , and He^+ at three ion energies [16]. For 4 keV helium ions, the sputtering coefficient increased by nearly a factor of 5 for large-angle irradiations. The effect of increased incident angle was even more pronounced for lighter ions and higher energies.

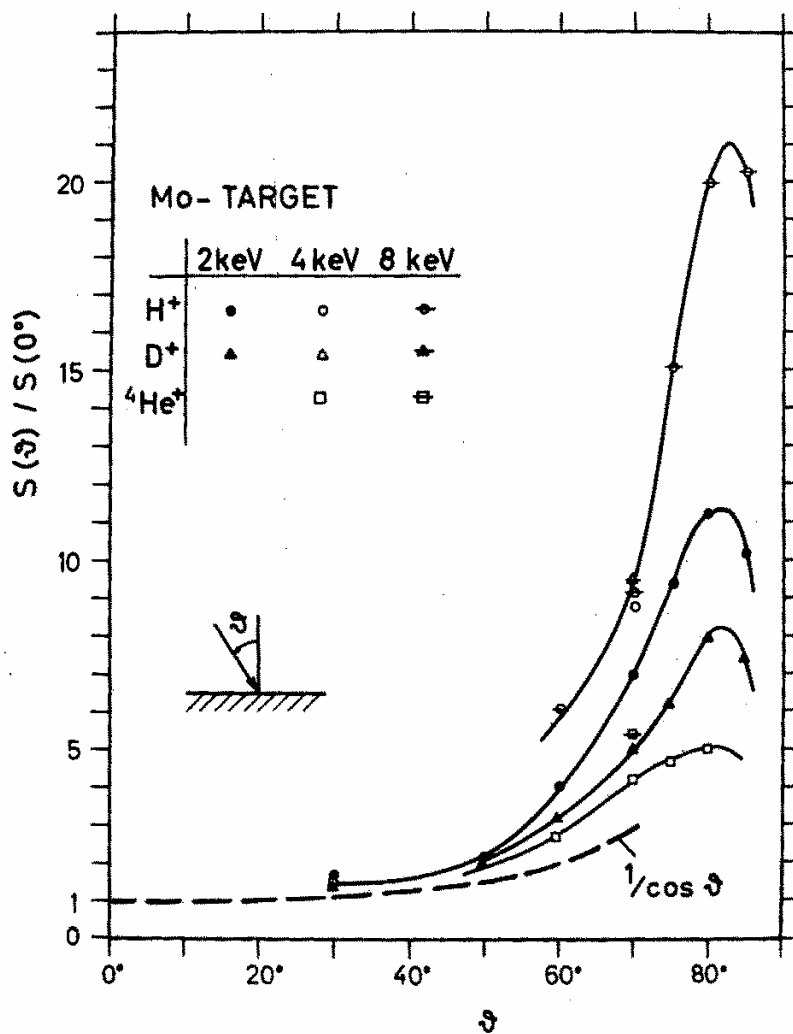


Figure 3.16: Sputtering yields for molybdenum [16].

In addition to the angle of the incident helium ions, the surface roughness of the target will also play a role in determining the overall angle of incidence. However, a rough surface will also provide a means for sputtered material to re-deposit back on the sample, as shown in Figure 3.17. This will effectively reduce the sputtering yield on the sample. Therefore, when calculating sputtering rates it is necessary to know the surface roughness of the target material.

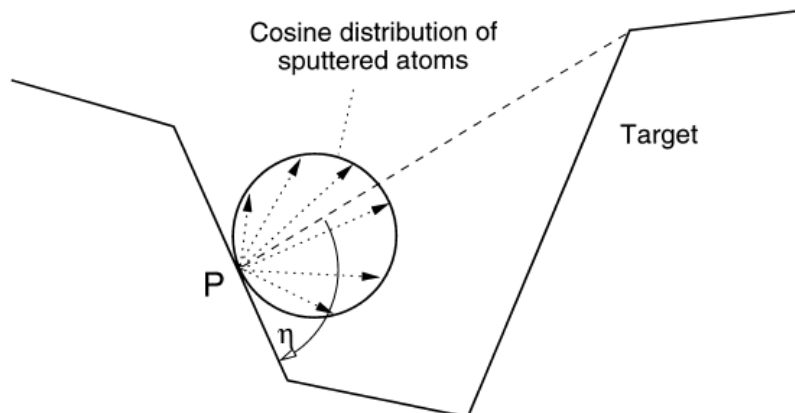


Figure 3.17: Some sputtered atoms will redeposit on rough surfaces [17].

Interestingly, one parameter that does not appear to affect the sputtering rate of a material is temperature, except near the melting point. Figure 3.18 shows the sputtering yield for 25 keV helium on tungsten as a function of temperature. For the temperature range of 350-1150 K, there appears to be no effect on sputtering yield [18].

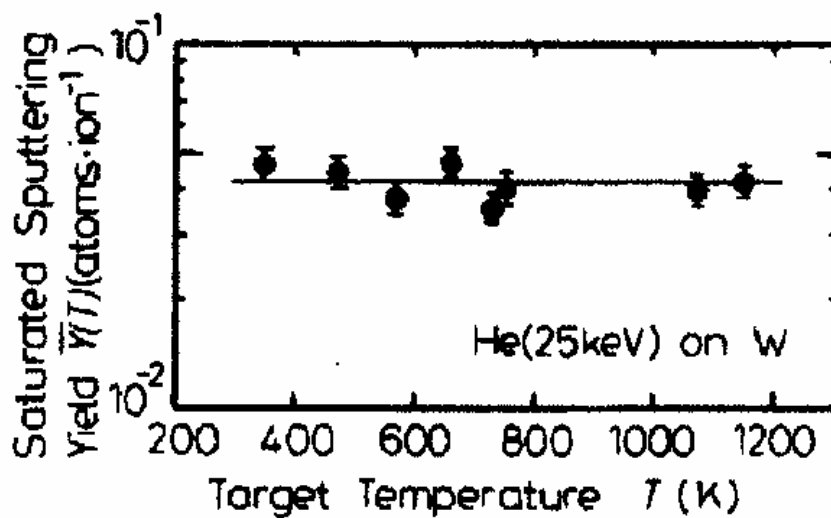


Figure 3.18: Effect of temperature on sputtering yield [18].

3.3.4 Bubble Formation and Growth

As described above, high-energy helium ions generated in ICF fusion devices will embed themselves deep into tungsten first-wall surfaces. However, once they are implanted, the low mobility of helium in tungsten will cause them to become trapped in the metal. Helium atoms in a metal may occupy either substitutional or interstitial sites. As interstitials, they are very mobile, but they will be trapped at lattice vacancies, impurities, and vacancy-impurity complexes [19]. Helium trapping results in low helium re-emission during early stages of irradiation, as shown in Figure 3.19 [20]. A plot of retained helium as a function of fluence at two temperatures is shown in Figure 3.20 [21]. However, once critical helium saturation has been reached, these tiny bubbles will coalesce to form surface blisters or micron-size subsurface bubbles, depending on helium range in metal and the material temperature. There is therefore a critical total fluence of helium ions before blistering can occur. For molybdenum, this fluence is $\sim 5 \times 10^{17}$ ions/cm² [22]. For rhenium, it is $\sim 3 \times 10^{17}$ ions/cm² [23]. A schematic summary of this process is shown in Figure 3.21 [24].

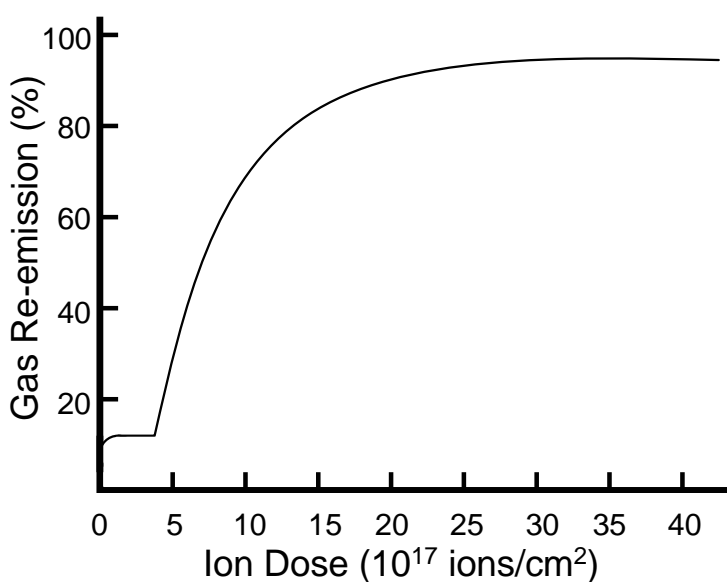


Figure 3.19: Helium re-emission during bombardment of molybdenum by 20 keV He⁺ [20].

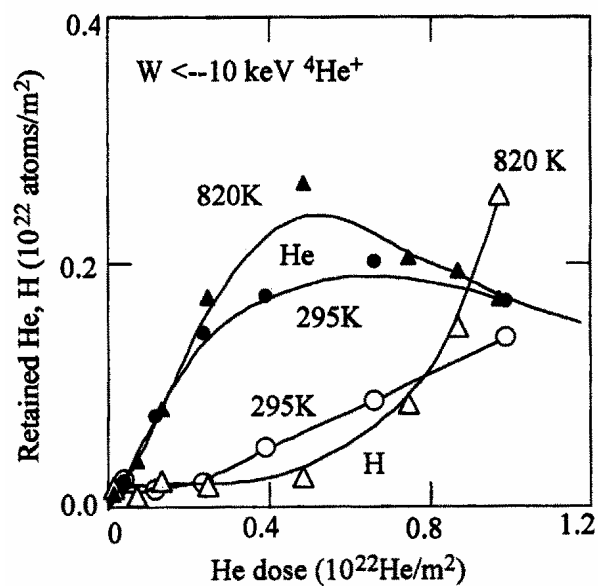


Figure 3.20: Helium (filled shapes) and hydrogen (open shapes) retention in tungsten [21].

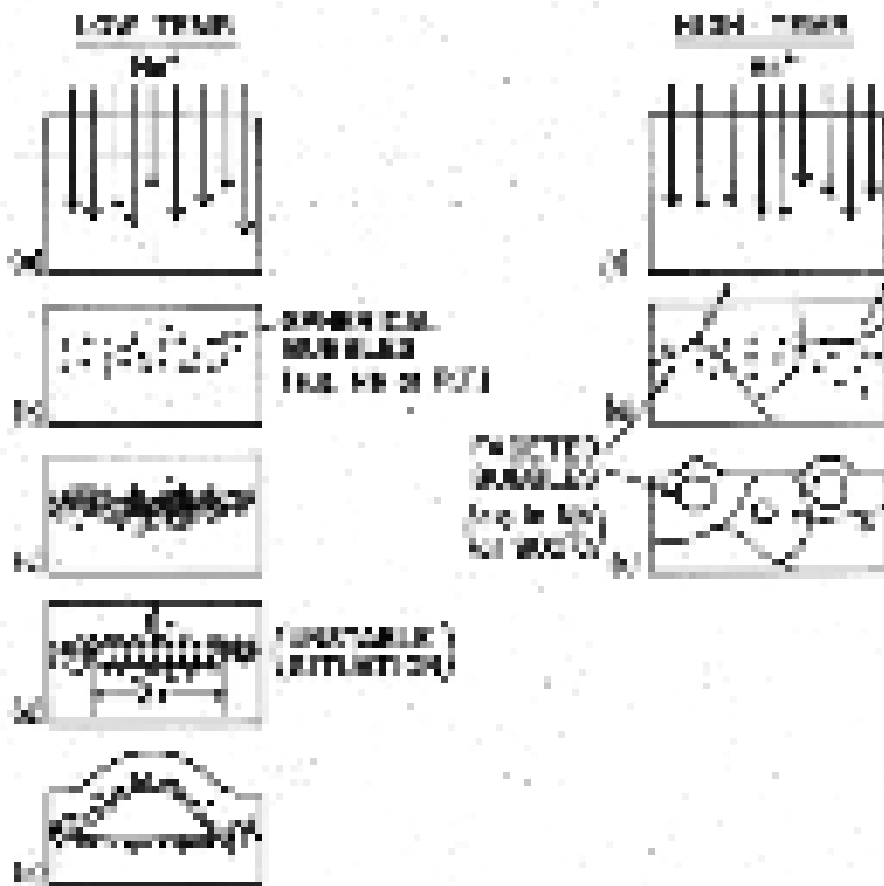


Figure 3.21: Blister formation in metals [24].

An example of this type of blister formation is shown in Figure 3.22. Erents and McCracken performed room-temperature helium irradiation experiments on molybdenum at ion energies ranging from 7 to 80 keV [20]. These experiments were coupled with helium re-emission measurements and were used to help develop initial blister formation theories.

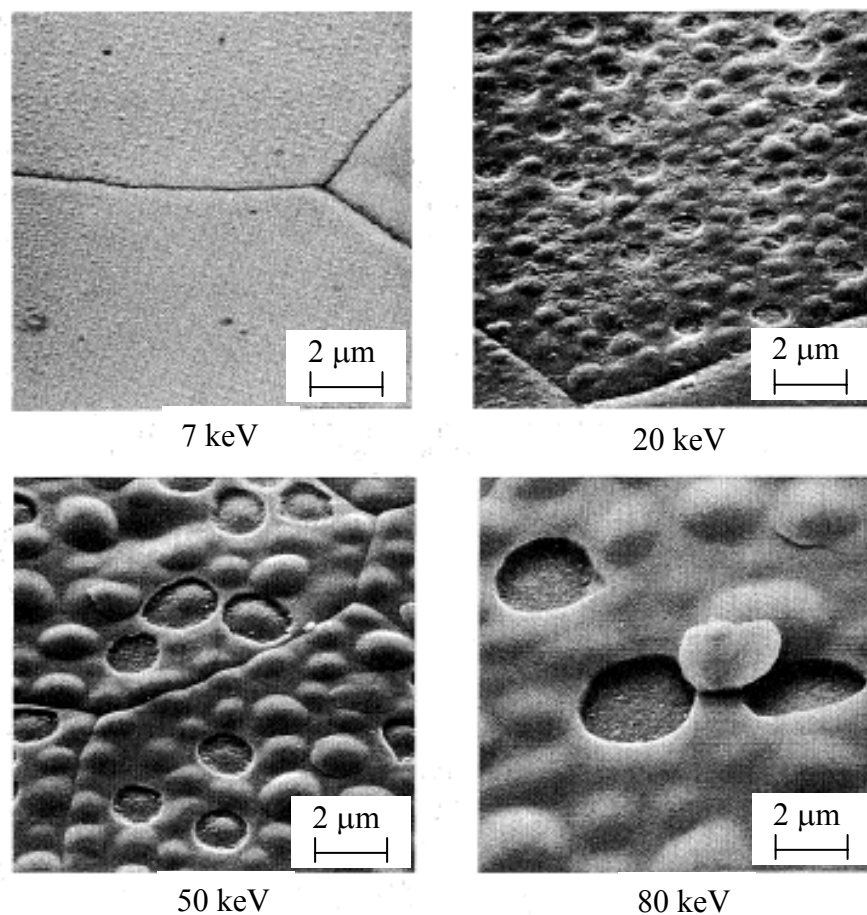


Figure 3.22: Blister formation by helium in molybdenum [20].

An experiment by Thomas and Bauer in 1974 showed the results of 300 keV helium implantation on Vanadium at 1,200°C [25]. At these conditions, the surface structure developed a porous surface morphology, as seen in Figure 3.23. The authors felt that the helium bubbles migrated to the surface to form the pores rather than breaking the surface like

in the case of low temperature implantation. It was the conclusion of the authors that this structure results in 100 percent helium re-emission during subsequent implantation, which agrees with the plot shown in Figure 3.19.

Material temperature, helium fluence, and ion energy all play important roles in determining the type of blistering that will occur. The micrographs in Figure 3.24 show varying effects of 36 keV helium

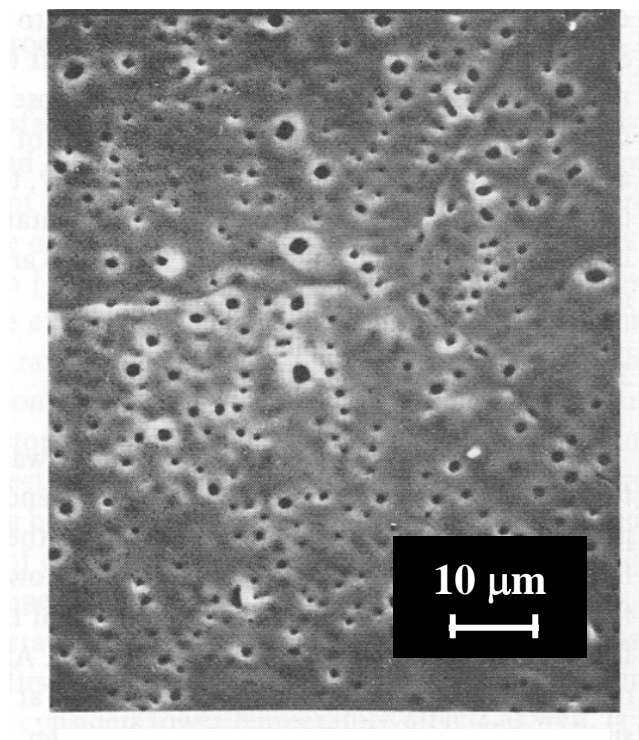


Figure 3.23: 300 keV He on 1200 °C Vanadium at 2×10^{18} He⁺/cm² [25]

implantation in molybdenum at different temperatures [20]. Lower temperature irradiation produced surface blistering, while high temperature ($2/3 T_m$) irradiation resulted in an extremely porous surface structure. Constant fluence temperature scans performed on tungsten by Cipiti showed an increased average pore diameter and a decreased pore density with increased temperature [26]. See Figure 3.25. As seen in Figure 3.26, experiments performed on room temperature niobium and molybdenum also show a clear relationship between helium ion energy and blister diameter [24].

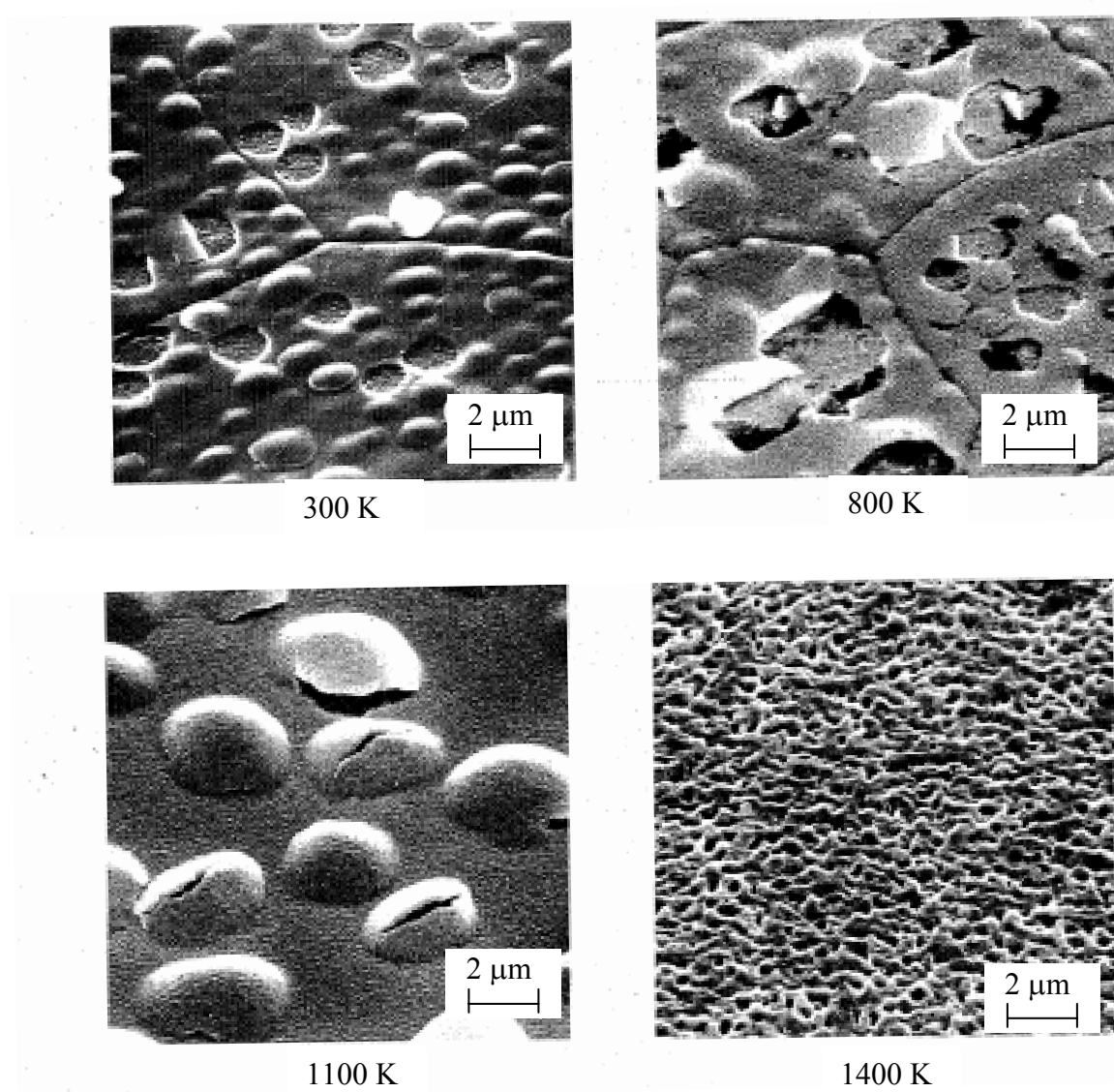


Figure 3.24: Molybdenum surface damage at various temperatures [20].

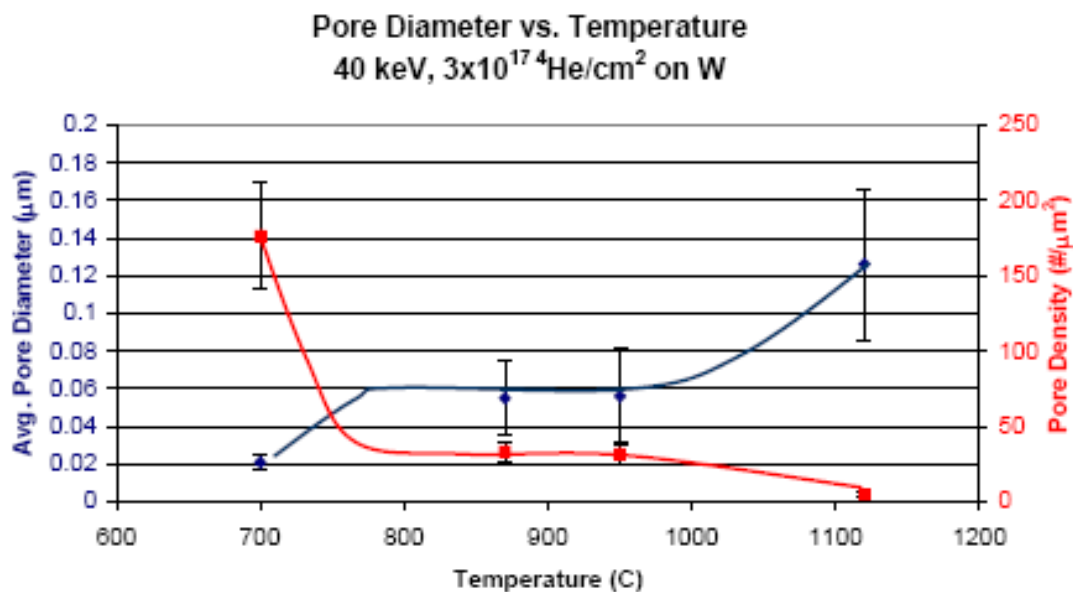


Figure 3.25: Increase of pore diameter and decrease of pore density with temperature in tungsten under helium implantation [26].

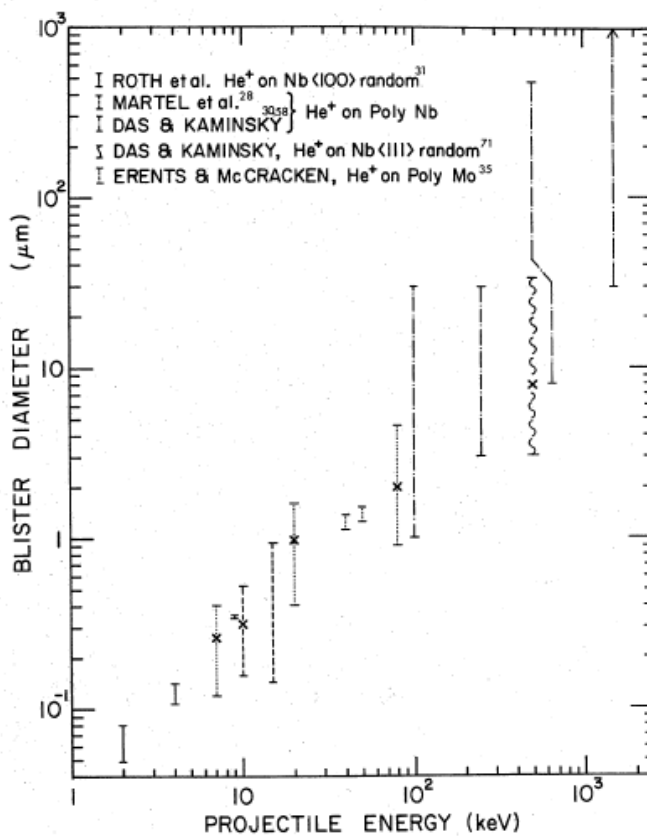


Figure 3.26: Blister diameter as a function of He⁺ energy (room temp. irradiation) [24].

Fluence plays a significant role in determining the type of surface deformation that will occur under helium irradiation. The micrographs in Figure 3.27 shows a fluence scan of 100 keV helium ions on room temperature niobium [27]. Surface blistering is seen at a fluence of $2 \times 10^{18} \text{ He}^+/\text{cm}^2$. By $1 \times 10^{19} \text{ He}^+/\text{cm}^2$, surface exfoliation has become the primary damage mechanism. Finally, at $1.2 \times 10^{20} \text{ He}^+/\text{cm}^2$, the damage mechanism has become surface pore formation. Note the different scale in this micrograph. Helium fluence scans on tungsten performed by Cipiti showed an increased average pore diameter and a decreased pore density with increased fluence [26]. See Figure 3.28.

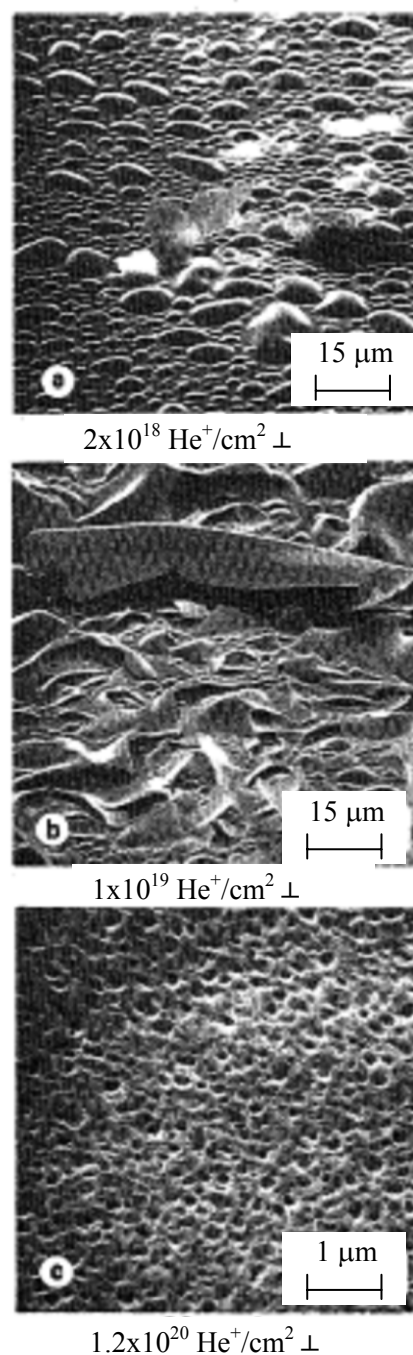


Figure 3.27: Fluence scan of 100 keV helium in room temperature niobium [27].

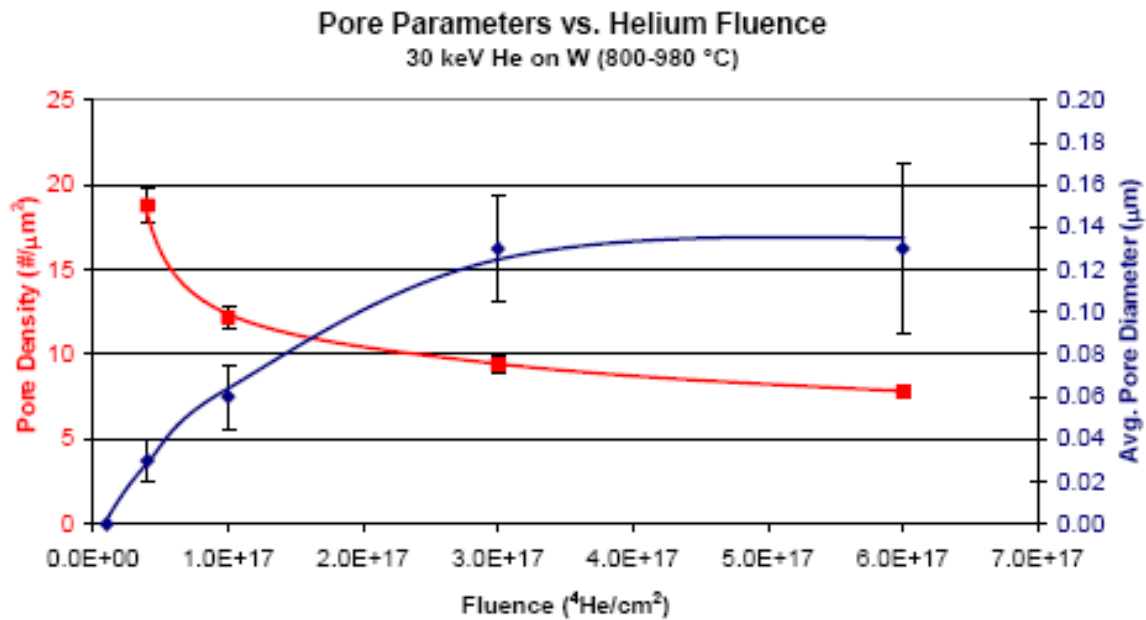


Figure 3.28: Increase of pore diameter and decrease of pore density with helium fluence on tungsten [26].

3.4 References

- [1] Ashley, R.P., Kulcinski, G.L., Santarius, J.F., Krupakar Murali S., Piefer, G. “*D-3He fusion in an inertial electrostatic confinement device*,” Proceedings of the 18th IEEE Symposium on Fusion Engineering, IEEE Publication 99CH37050, pg. 35-37, 1999
- [2] R. Hirsch, “Inertial-Electrostatic Confinement of ionized fusion gases,” *Journal of Applied Physics*, Vol. 38, p. 4522, 1967
- [3] S.S. Bosch and G.M. Hale, “Improved Formulas for Fusion Cross-Sections and Thermal Reactivities,” *Nuclear Fusion*, Vol. 32, No. 4, 1992
- [4] R.P. Ashley, G.L. Kulcinski, J.F. Santarius, S. Krupakar Murali, G.R. Piefer, B.B. Cipiti, R.F. Radel, and J.W. Weidner, “*Recent Progress in Steady State Fusion Using D-3He*,” *Fusion Science and Technology*, Vol. 44, p. 564, 2003
- [5] T. Gozani, “Active Nondestructive Assay of Nuclear Materials – Principles and Applications,” Mondanto Reseach Corporation; Contract No. FIN A-10766, January 1981
- [6] M.B. Chadwick, et al, “ENDF/B-VII.0: Next Generation Nuclear Data Library for Nuclear Science and Technology Applications,” *Nuclear Data Sheets*, 2006
- [7] J.R. Lamarsh, “Introduction to Nuclear Engineering, 2nd Edition” Addison-Wesley Publishing Company, Reading, MA, 1983
- [8] B. Pfeiffer, K.L. Kratz, and P. Möller, “Status of Delayed-Neutron Precursor Data: Half-Lives and Neutron Emission Probabilities“ *Progress in Nuclear Energy*, Vol. 41, No. 1-4, p.39-69, 2002
- [9] G.R. Keepin, T.F. Wimett, and R.K. Zeigler, “Delayed Neutrons from Fissionable Isotopes of Uranium, Plutonium, and Thorium,” *Physical Review*, Vol. 107, No. 4, 1957
- [10] ASTAR (Stopping-power and range tables for helium ions) Database, National Institute of Standards and Technology
- [11] Figure created with SRIM-2006 software: J. F. Ziegler, J. P. Biersack and U. Littmark, “The Stopping and Range of Ions in Solids,” Pergamon Press, New York, 1985
- [12] E.M. Baroody, “A Theory of Secondary Electron Emission from Metals,” *Physical Review*, Vol. 78, No. 6, 1950
- [13] L. N. Large, “Secondary Electron Emission from a Clean Tungsten Surface Bombarded by Various Positive Ions,” *Proceedings Phys. Soc.*, Vol. 81, p.1101, 1963

- [14] M. Kaminsky, *Atomic and Ionic Impact Phenomena on Metal Surfaces*, Springer-Verlag: Berlin, Germany, 1965
- [15] SPUTY (Sputtering Yields of Solids by Ions) Database, Maintained by National Institute for Fusion Science, Data and Planning Center
- [16] H.L. Bay and J. Bohdansky, "Sputtering Yields for Light Ions as a Function of Angle of Incidence," *Applied Physics*, Vol. 19, p. 421-426, 1979
- [17] M. Kustner, et al, "The Influence of Surface Roughness on the Angular Dependence of the Sputter Yield," *Nuclear Instruments and Methods in Physics Research B*, Vol. 145, p. 320-331, 1998
- [18] M. Tomita & K. Masumori, *Nuclear Instruments & Methods in Physics Research*, Vol. B39, 95, 1989
- [19] M. S. Abd El Keriem, D. P. van der Werf and F. Pleiter, "Helium-vacancy interactions in tungsten," *Physical Review B*, Vol. 47, No. 22, p. 14771-14777, 1993
- [20] S.K. Erents and G.M. McCracken, "Blistering of Molybdenum under Helium Ion Bombardment," *Radiation Effects*, Vol. 18, 191, 1973
- [21] S. Nagata, et al, "Ion Beam Analysis of a Helium and its Irradiation Effect on Hydrogen Trapping in W Single Crystals," *Nuclear Instruments and Methods in Physics Research B*, Vol. 190, p. 652-656, 2002
- [22] C.R. Fahlstrom & M.K. Sinha, "Surface Blistering of Molybdenum Irradiated with 75-350 keV Helium Ions," *Journal of Vacuum Science Technology*, Vol. 15(2), p. 675, 1978
- [23] J. Van Guysse et al., "Blistering of Rhenium Irradiated with 21 keV Helium Ions," *Applied Physics*, Vol. 17, 89, 1978
- [24] S.K. Das and M. Kaminsky, "Radiation Blistering in Metals and Alloys," Proceedings of the "Symposium on Radiation Effects on Solid Surfaces," *Advances in Chemistry Series*, 1975
- [25] G.L. Thomas & W. Bauer, "Helium and Hydrogen Re-emission During Implantation of Molybdenum, Vanadium and Stainless steel," *Journal of Nuclear Materials*, Vol. 53, 134, 1974
- [26] B.B. Cipiti, "The Fusion of Advanced Fuels to Produce Medical Isotopes Using Inertial Electrostatic Confinement" PhD Thesis, University of Wisconsin-Madison, 2004
- [27] R. Behrisch, M. Risch, J. Roth, B.M.U. Scherzer. *Fusion Technology*, 1976

Chapter 4: Experimental Procedure

4.1 Experimental Facility

As shown in Figure 4.1, the UW-Madison IEC chamber consists of a cylindrical aluminum vacuum chamber measuring 65 cm high and 91 cm in diameter. The pumping system consists of a Leybold Trivac[®] rotary vane roughing pump and Varian[®] turbo pump (500 L/s). Base pressures in the low 10^{-6} torr range are measured using an MKS[®] ion gauge.

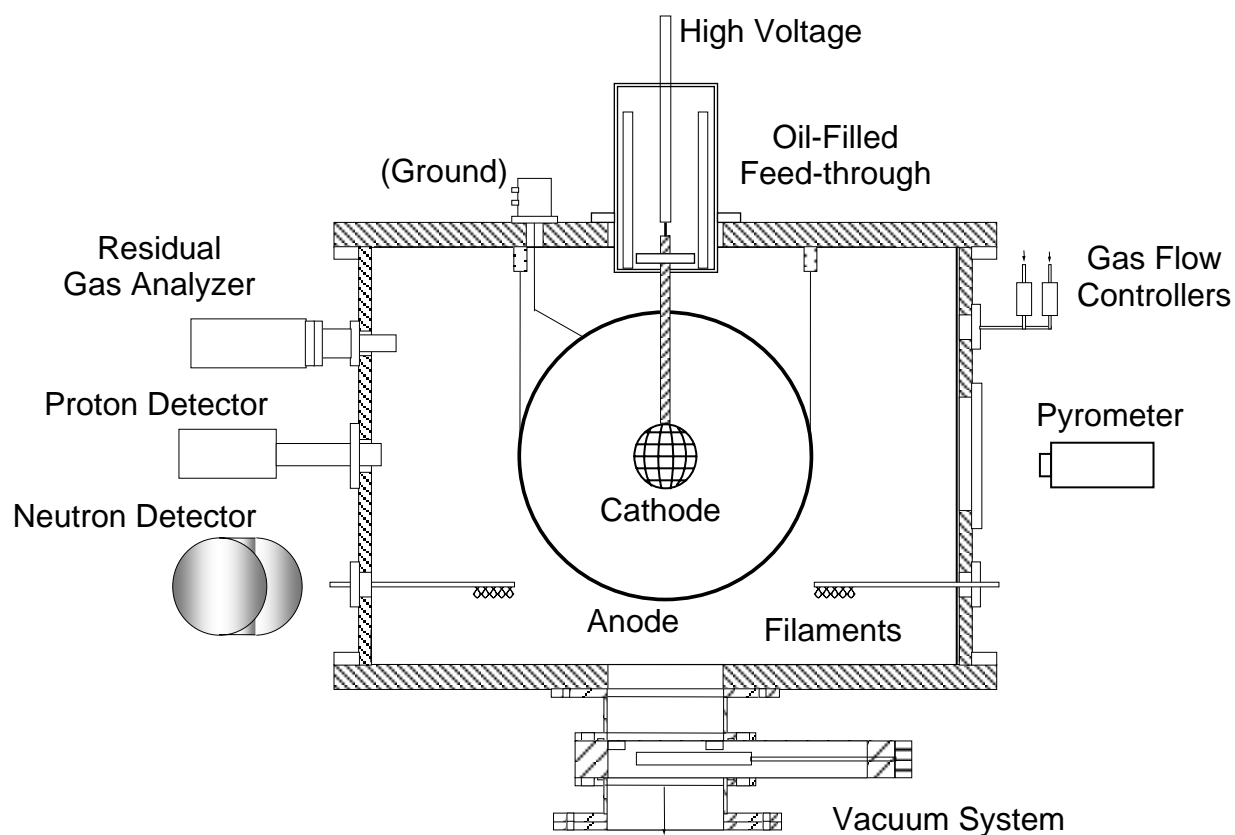


Figure 4.1: UW-IEC experimental setup.

4.1.1 High Voltage Components

A high voltage insulator carries the large negative potential to the inner grid. The present stalk design consists of a 0.48 cm diameter molybdenum rod inside a 2.5 cm diameter cylinder of boron nitride (BN). The 35 cm long BN stalk is ridged along its surface to increase the arc length from the cathode to ground, as shown in Figure 4.2.

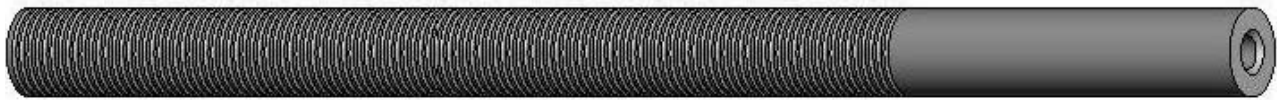


Figure 4.2: Schematic of ridged BN insulating stalk [1].

High voltage is supplied to the cathode from a Hipotronics[®] Model 8200-75 HV power supply with maximum capability of 200 kV and 75 mA. The supply is fed by a large step-up transformer which is controlled by a 480 V 3-phase variac. It is oil cooled and insulated by 218 gallons of Diala AX high voltage oil and is rated for continuous duty. The 8200-75 is protected by a high-speed current sensing circuit that will shut the system off by disconnecting a three-phase contactor in between the variac and the transformer. The trip current is adjustable from 10-110 percent of the supply's rated current. A photograph of the Hipotronics[®] control unit and transformer/rectifier unit is shown in Figure 4.3:



Figure 4.3: Hipotronics 8200-75 transformer (left) and controller (right).

Before reaching the cathode, voltage is run through a set of 250 k Ω resistors in an oil bath to limit current transients during voltage surges and spikes, as pictured in Figure 4.4. This buffer circuit allows uninterrupted operation of the IEC device during small arcs and protects the power supply from large arcs.



Figure 4.4: High-voltage buffer resistors.

4.1.2 Cathode and Anode System

Within the vacuum chamber are two highly transparent concentric grids. The inner cathode grid is held at very low negative potential during operation, while the outer anode grid is held at ground potential. For many years, the UW-IEC experiments used a 10 cm diameter W-25%Re grid with a latitude/longitude configuration. Recent experiments have evaluated the effects of varying the size, geometry, and material of the cathode grid, with the goal of maximizing fusion production rates.

Both a 10 cm and a 20 cm diameter latitude/longitude-type W-25%Re cathode grid are pictured in Figure 4.5. These grids were both used to produce D-D neutrons in the IEC device under identical conditions, and the neutron production rate was compared. It was

found that the 20 cm diameter grid produced D-D neutron rates approximately 25 percent higher than the 10 cm diameter grid at 100 kV in the 2-3 mtorr range. This work was later expanded upon to produce even greater neutron rates, as described in Section 5.2.

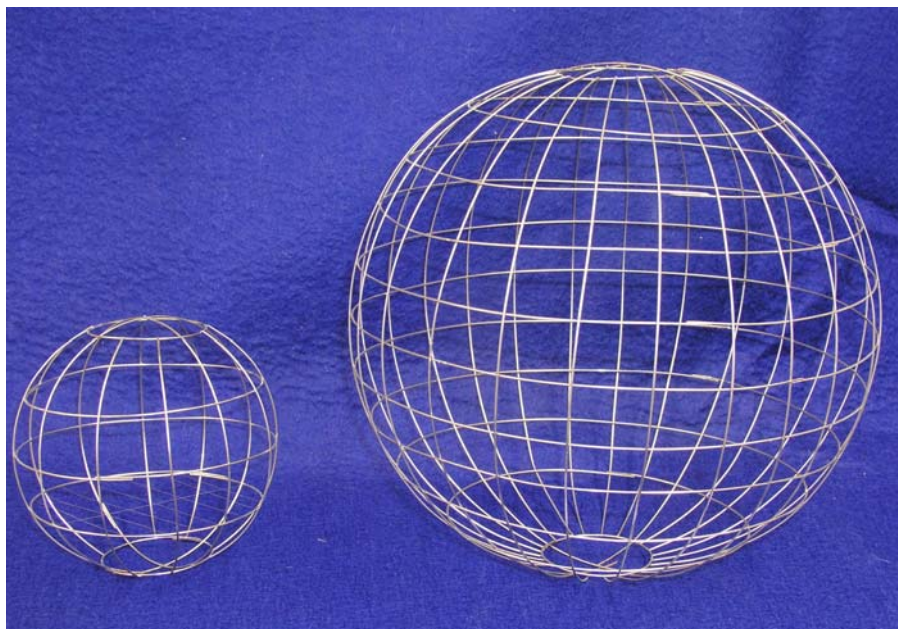


Figure 4.5: 10 cm and 20 cm diameter tungsten-rhenium inner grids.

University of Wisconsin IEC cathodes are typically fabricated from 0.75 mm diameter W-25%Re wire. This alloy's $\sim 3,200^{\circ}\text{C}$ melting point allows for high temperature operation. As a further optimization experiment, identical 10 cm diameter cathodes were constructed of W-25%Re and pure Re wire and were compared during operation with ~ 2 mtorr of deuterium. It was found that at lower voltages (< 90 kV), the pure rhenium grid produced ~ 10 percent higher neutron rates. However, as the cathode voltage was increased to 120 kV, the neutron rate was the same for both grids. This difference may be a result of the varying secondary-electron coefficients of the two materials.

The final optimization study evaluated the effects of varying the geometry of the cathode. Two geometries with identical transparencies were compared for this study. The first is the traditional latitude/longitude configuration, as shown on the left in Figure 4.6 below. The second is a 9-ring symmetric design, shown on the right in Figure 4.6. Each triangular segment made by the wires in this geometry have equal area, providing a more uniform grid surface.

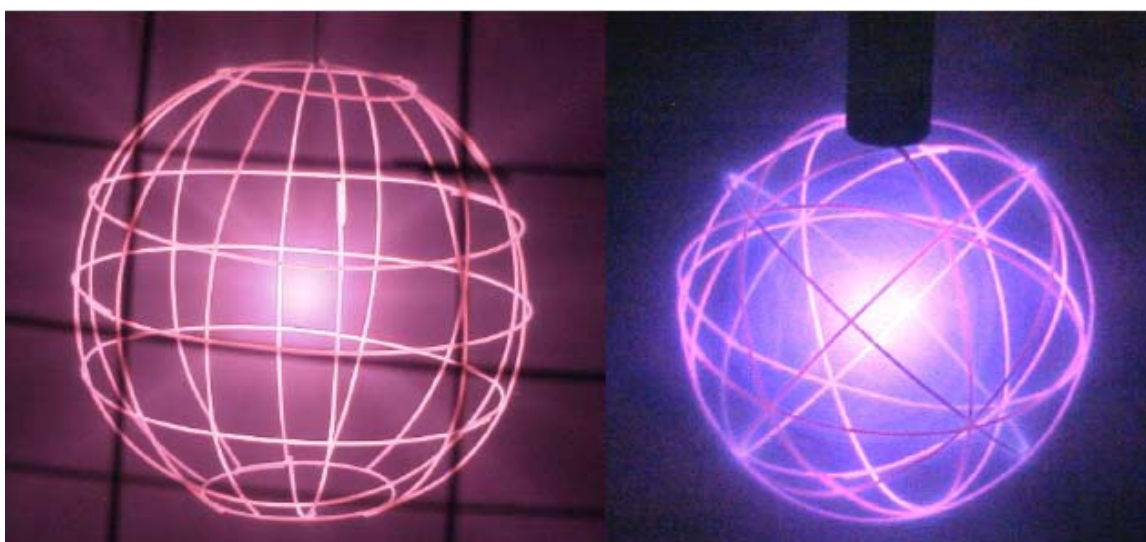


Figure 4.6: Latitude/longitude and symmetric cathode configurations.

While neither geometry produced a higher neutron production rate, the symmetric cathode grids provide an additional benefit. While the latitude/longitude grids were constructed by hand and were therefore difficult to reproduce, a new fabrication system was developed for the symmetric grids. This new system is not only simpler and faster, but it results in identical grids being produced each time. As pictured in Figures 4.7 (a-f), a mold was constructed that is then filled with wax, producing a grooved sphere. This sphere is then used to spot-weld together a new grid, and the wax is melted away.



Figure 4.7: Grid construction procedure, (a) Mold produced from rapid prototype model, (b) Wax poured into mold, (c) Wires wound around wax form, (d) Wires spot-welded at junctions, (e) Wax form melted away at $\sim 80^{\circ}\text{C}$, (f) Completed cathode.

The 40 and 50 cm diameter outer anode grids are fabricated from stainless steel wire and remain at ground potential during operation. Fine wire mesh is spot-welded to the outer grid in front of the filaments to provide additional voltage shielding.

4.1.3 IEC Operation

When running an experiment, deuterium gas is fed into the system at 5-20 sccm (standard cubic centimeters per second) using MKS Mass-Flo[®] controllers to produce a background pressure of 2-3 mtorr. An MKS Baratron[®] pressure transducer measures the neutral gas pressure in the chamber. A Stanford Research Systems CIS 200[®] residual gas analyzer (RGA) monitors gas impurities during operation. The RGA is also used to determine ratios when running two gases and helps to determine if there are leaks in the system.

Six standard 200 W light bulb filaments are positioned in the region between the anode grid and the vacuum chamber wall. During steady-state operation, these filaments are heated to generate electrons that ionize the deuterium gas. The intensity of the filaments can be varied during an experiment using a variac. The filaments are rectified, and a negative bias is added to more effectively force electrons into the source region. This also allows for more control of the current during high voltage operation.

High voltage is then applied to the cathode using the equipment described in Section 3.1.1. The potential well that is generated pulls in ions and generates fusion reactions, as described in detail in Chapter 2.

4.1.4 Diagnostics

The UW-IEC device relies on a modified long counter for neutron diagnostics. The counter consists of an aluminum cylinder filled with paraffin wax, as pictured in Figure 4.8 [2]. A single ^3He proportional counter is placed inside this device to capture the moderated neutrons. In addition to the holes left for the neutron detectors, there are an additional 12 smaller holes in the center of the cylinder. These holes are designed to produce an overall flat response to different energy neutrons. A plot of the neutron detection efficiency vs. neutron energy is shown in Figure 4.9 [2]. This is a particularly useful feature of this detector, as it is calibrated with a plutonium-beryllium source, which emits a full spectrum of energies peaked at ~ 4 MeV, and we are interested in the 2.45 MeV D-D fusion neutrons.

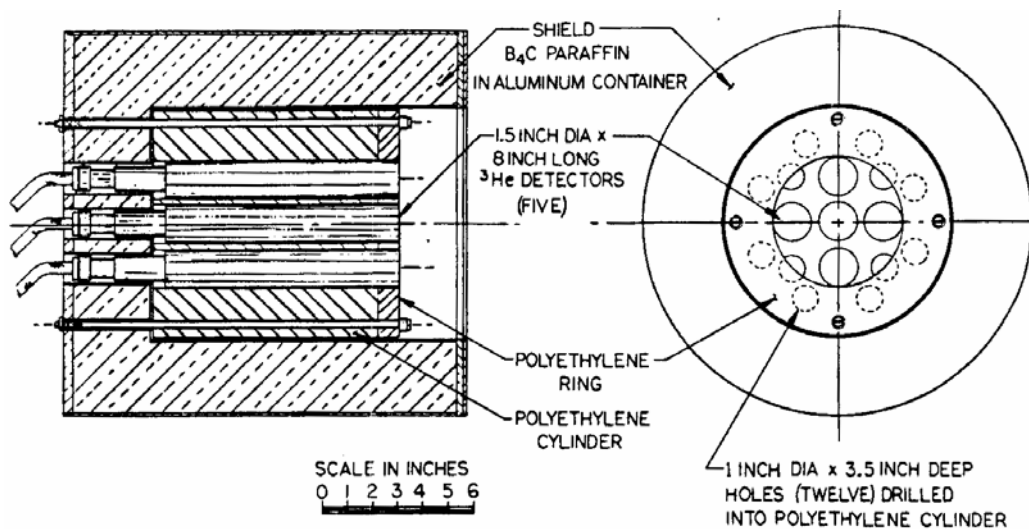


Figure 4.8: Modified long counter [2].

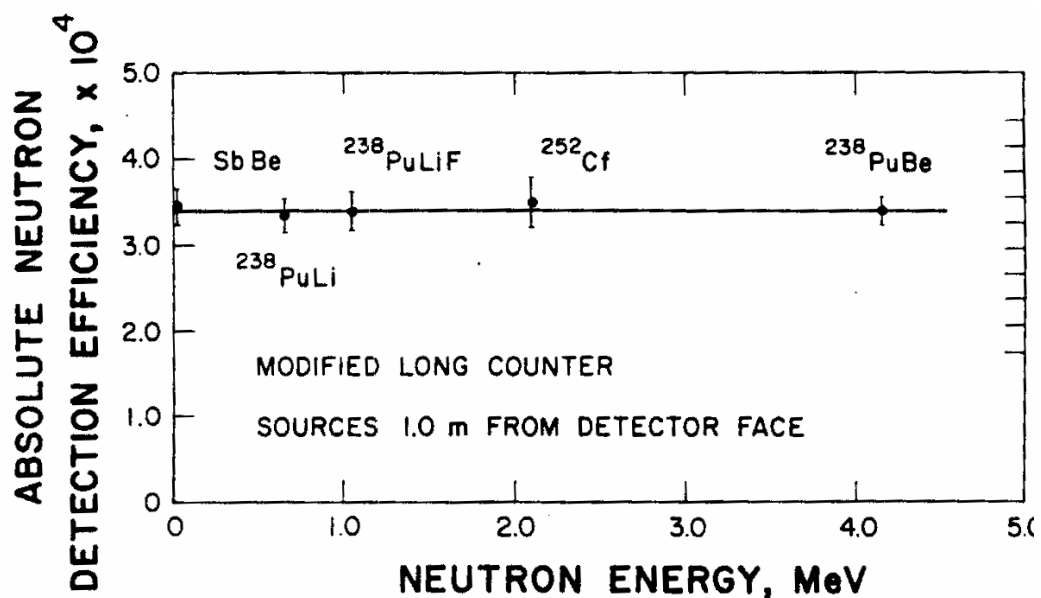


Figure 4.9: Efficiency of the long counter shown in Figure 4.8 versus the average energy of the source neutrons [2].

Fusion protons are detected with a Canberra® 1,200 mm² face area, 700 μm thick silicon detector on a port facing the center of the vacuum chamber. Signal from this detector is then fed through a pre-amp and amplifier before being displayed on a multi-channel analyzer (MCA). The MCA allows for the simultaneous detection of D-D and D-³He protons, as they each deposit a different amount of energy in the detector. A 25 μm lead foil protects the detector from some x-ray noise.

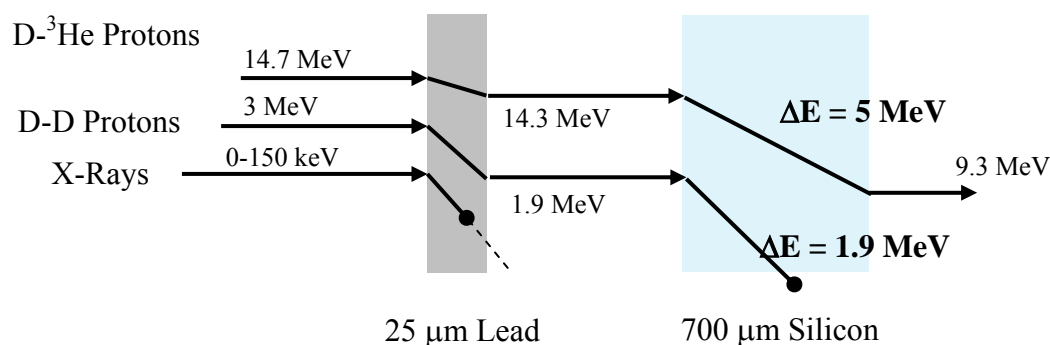


Figure 4.10: Proton energy loss through lead foil and Si detector [3].

Figure 4.10 is a schematic of the energy loss through the foil and detector [3]. Approximately 1.9 MeV is deposited in the silicon from the D-D protons, and about 5 MeV is deposited from the D-³He protons, allowing for easy differentiation on the MCA spectrum.

Initial proton detector calibrations were performed using MCNP with a volume source assumed for proton production. However, recent work by Cipiti resulted in drastically modified calibration factors [4]. Additionally, the factor is different for the D-D and D-³He reactions. These new factors are based on the percentages of reactions that occur in the plasma core, the overall volume, and the grid wires themselves.



Figure 4.11: Screenshot of LabVIEW data collection program.

Neutron and proton rates, along with cathode voltage, cathode current, and pressure, are monitored continuously during operation with a LabVIEW program developed in-house (shown in Figure 4.11). The top plot and the digital readouts provide real-time information about experimental conditions, while the lower plot makes it easy to see trends that occur in the data over the course of the experiment. The program also allows all data to be saved for future study.

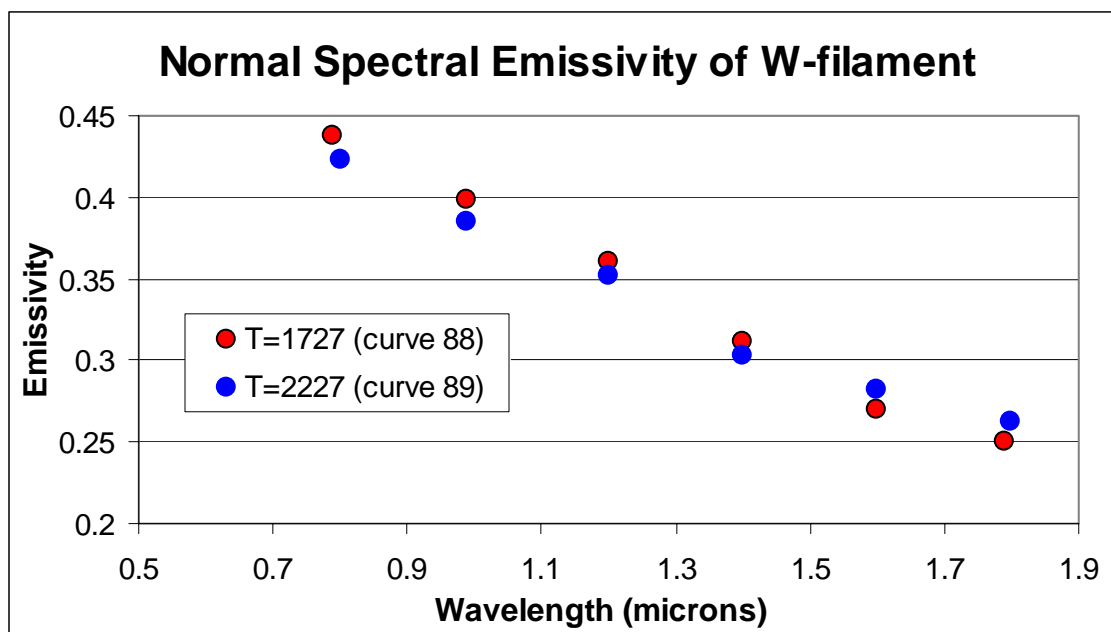


Figure 4.12: Tungsten filament emissivity [from 5].

Other diagnostics are used to monitor the IEC operating conditions during experiments. One is a Chino IR-CAQ2CS pyrometer that can be aimed at various parts of the cathode or filaments to measure surface temperatures. This model's 400°C to 3,100°C temperature range is ideally suited to cover the wide breadth of applications performed with the IEC device. Since surface emissivity at each wavelength changes as a function of temperature (see Figure 4.12), the slopes of the emissivity are first found at known temperatures and used to generate data that are more accurate at all temperatures [5]. A digital video camera, connected via USB cable to a computer in the control room, allows for visual monitoring of the stalk and cathode grid during operation. Thermocouples are also placed on the IEC chamber to monitor temperature during operation so that critical vacuum connections are not overheated.

As mentioned above, a Stanford Research Systems CIS 200[®] RGA is used to monitor gas impurities during operation. A screenshot of an RGA trace during a typical run is shown in Figure 4.13. Large peaks in the 2-6 AMU range represent various deuterium ions, while the smaller peaks are impurities such as deuterated water, nitrogen, and oxygen.

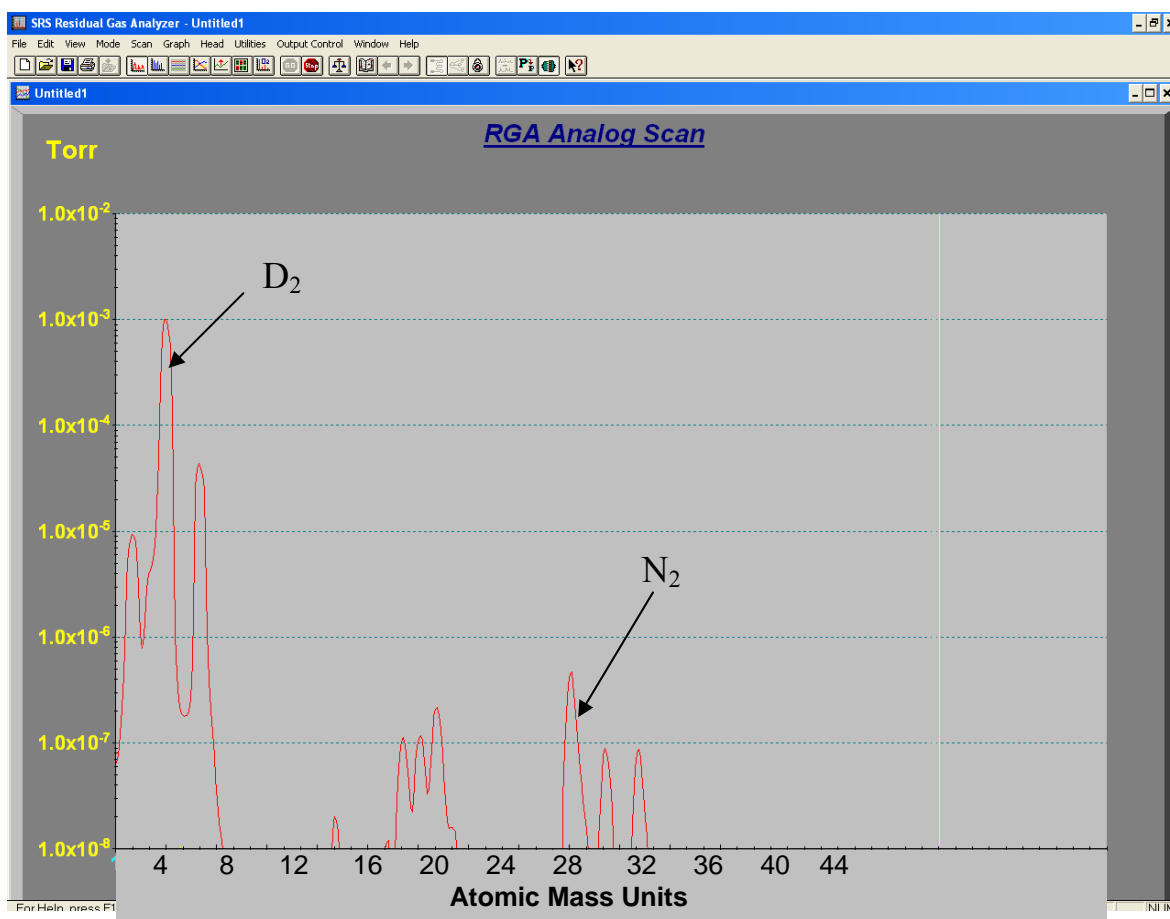


Figure 4.13: Screenshot of residual gas analyzer software.

4.2 Highly Enriched Uranium Detection

The construction of an IEC experiment capable of detecting delayed fission neutrons required the development of two additional systems in the UW-IEC laboratory. The first was the pulsing system, which is composed of two primary components. One component is the high voltage circuitry that maintains a constant cathode voltage both during and between pulses and the second is the filament biasing system that generates the ion pulses. The other system is the detection hardware that allows delayed fission neutrons to be discriminated from the IEC fusion neutrons.

4.2.1 Pulsed IEC Development

The development of a pulsed IEC system required the engineering of two unique systems, both of which went through numerous iterations to reach the conditions described in this thesis. Figure 4.14 shows the high voltage components of the pulsed IEC experiment.

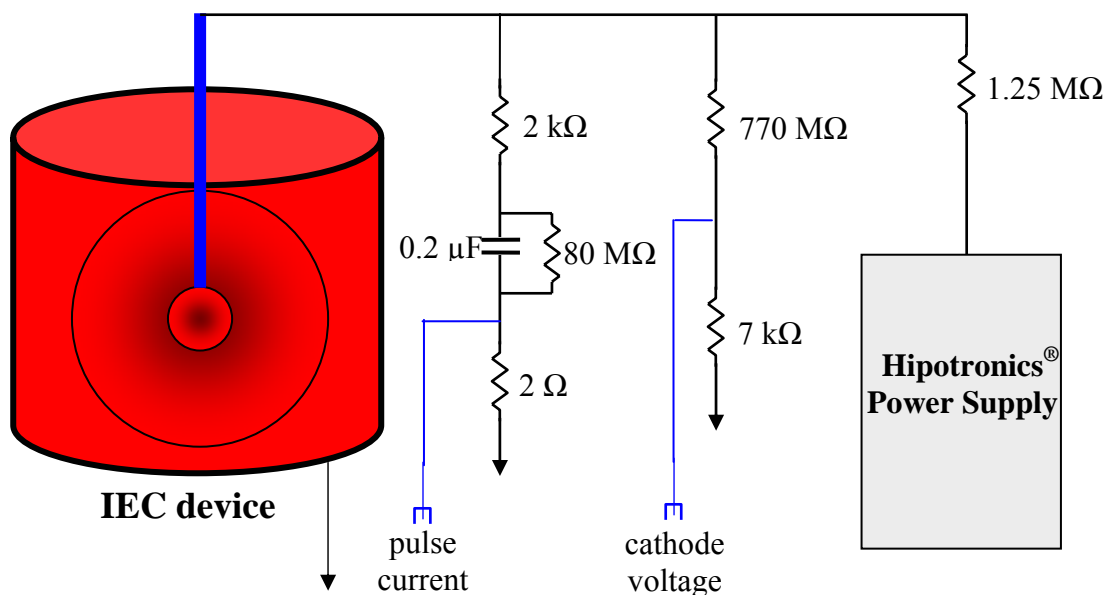


Figure 4.14: Pulsed high voltage circuit.

High voltage for pulsing experiments is provided by the Hipotronics® power supply described above. Before reaching the cathode, voltage is run through a set of ten 1,250 k Ω resistors in an oil bath to stabilize the system during voltage surges and spikes. The resistors are shown in Figure 4.15. This buffer circuit allows uninterrupted operation of the IEC device during large arcs that are driven by the capacitor and protects the power supply from them. A low-impedance voltage divider allows the cathode voltage to be measured independently of the power supply.



Figure 4.15: Buffer resistors for high voltage pulsing circuit.

The pulsing circuitry is connected in parallel with the IEC cathode. A 0.2 μ F capacitor stores charge between pulses and provides amps of current to the cathode during pulses. To act as a safety feature, an 80 M Ω resistor is connected across the capacitor to discharge it after shutdown. A 2 k Ω resistor is placed between the capacitor and the IEC device to limit current surges during arcing. Finally, a 2 Ω resistor is placed between the capacitor and ground to allow pulse current to be measured.

While the circuit described above is used to maintain a constant voltage on the cathode, it does not actually generate ion pulses. Pulses are generated by biasing the electron filaments housed in the ion source region. See Figure 4.16. Hot tungsten light-bulb

results in negative bias on the filaments until the MOSFET is switched back off. This negative bias forces the electrons to be emitted into the IEC chamber, ionizing the fuel gas and initiating the IEC discharge. An example of this filament bias during a pulse and the resulting IEC cathode current is shown in Figure 4.17. The slope of the current trace during the pulse is due to the capacitor discharging during the pulse.

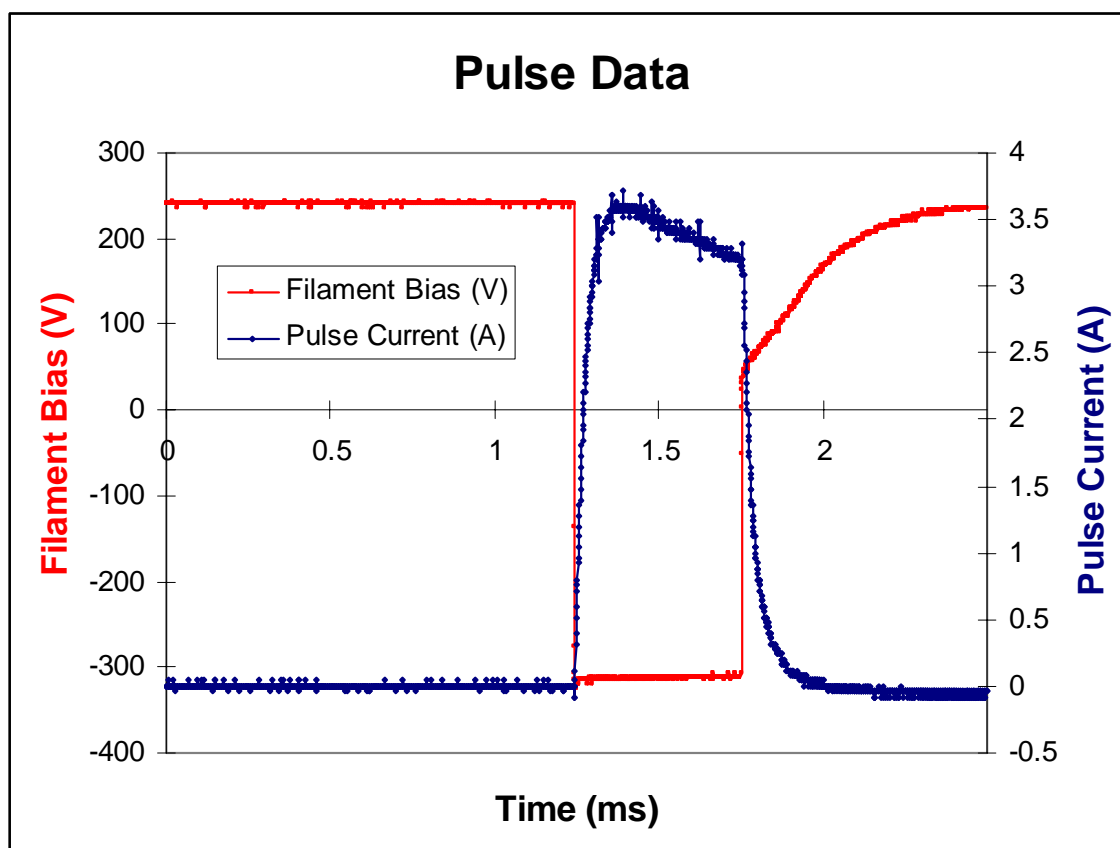


Figure 4.17: Filament bias and cathode pulse current during a pulse.

4.2.2 Delayed Neutron Detection

Helium-3 detectors were used to detect the delayed fission neutrons generated in the IEC laboratory. Figures 4.18 and 4.19 provide pictorial and schematic views of the detector hardware. These detectors rely on the reaction of He-3 with thermal neutrons to produce charged particles (see equation 4.1).



These charged particles ionize the gas in the detector, and electrons are attracted to a center wire that is held at high voltage. The generated signal is sent to pre-amplifiers that produce pulses proportional to the signal strength. The three pre-amplifier outputs are combined and fed into an amplifier. Finally, the amplifier output is sent to a multi-channel analyzer (MCA).

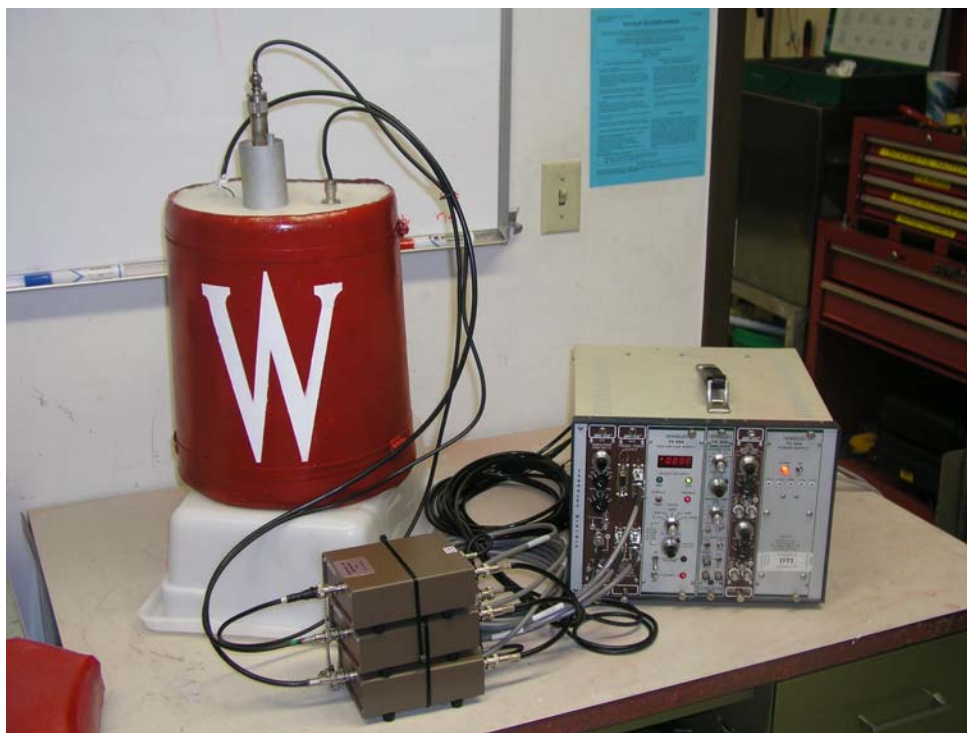


Figure 4.18: Picture of HEU detection equipment.

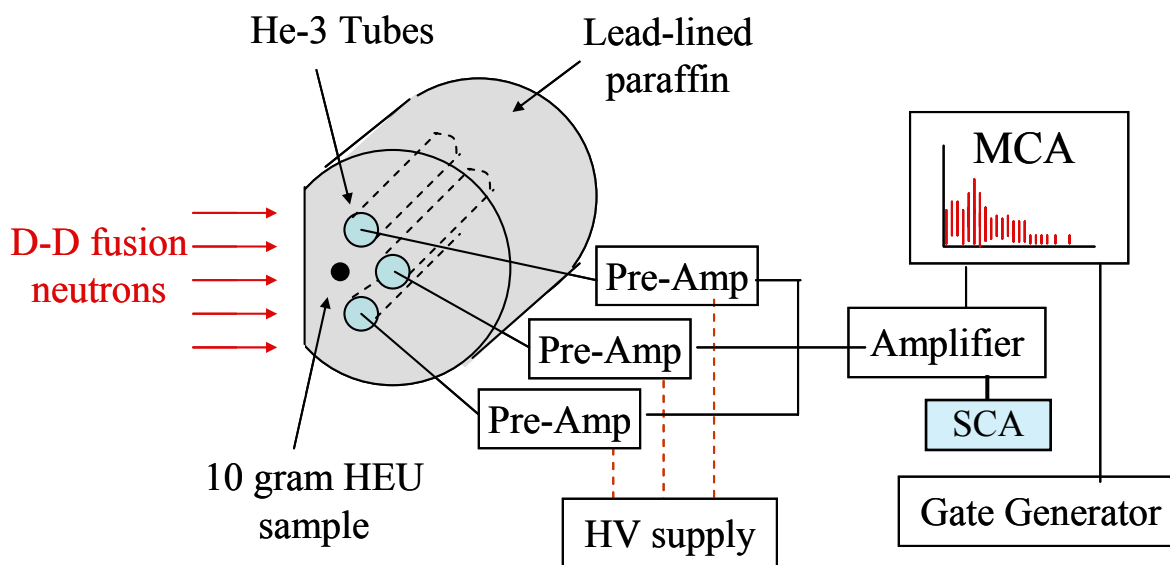
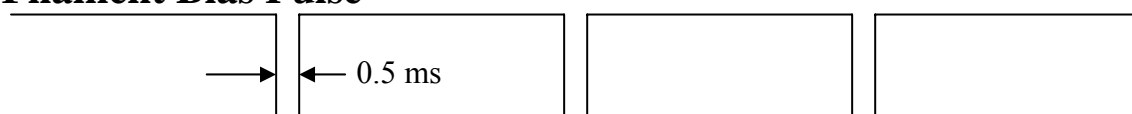


Figure 4.19: Schematic of HEU detection equipment.

In order to prevent pulsed fusion neutrons from being detected, a gate generator is used to block all neutron counts that occur during the IEC pulse and for an additional 5-10 ms after the pulse. See Figure 4.20. To ensure accurate timing, the same bias pulse that initiates the IEC pulse is also used to generate the gate signal for the neutron detector. By blocking counts for a few milliseconds after the pulse, the room-scattered fusion neutrons are not counted.

Filament Bias Pulse



Gate Signal

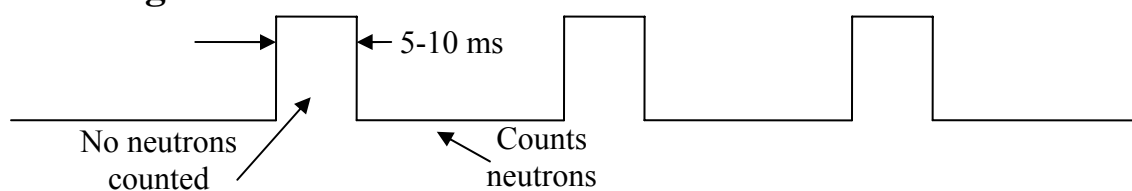


Figure 4.20: Gate signal used in delayed neutron detection.

The same circuitry is also used to generate time-dependent data. The amplifier output is also sent to a single channel analyzer (SCA) that is then sent to a Canberra PCA3 MCA card. This card takes the continuous data stream from the SCA and converts it to neutron time-dependent neutron data. An example of pulsed IEC neutron data captured with this card is shown in Figure 4.21. The 10 Hz pulses are visible in the upper screen, and the details of a single pulse can be seen in the close-up view provided in the lower screen. Single counts occurring between the pulses (circled) can also be seen in this figure. External synchronization can also be used with this MCA in order to add numerous pulses together and get better statistics.

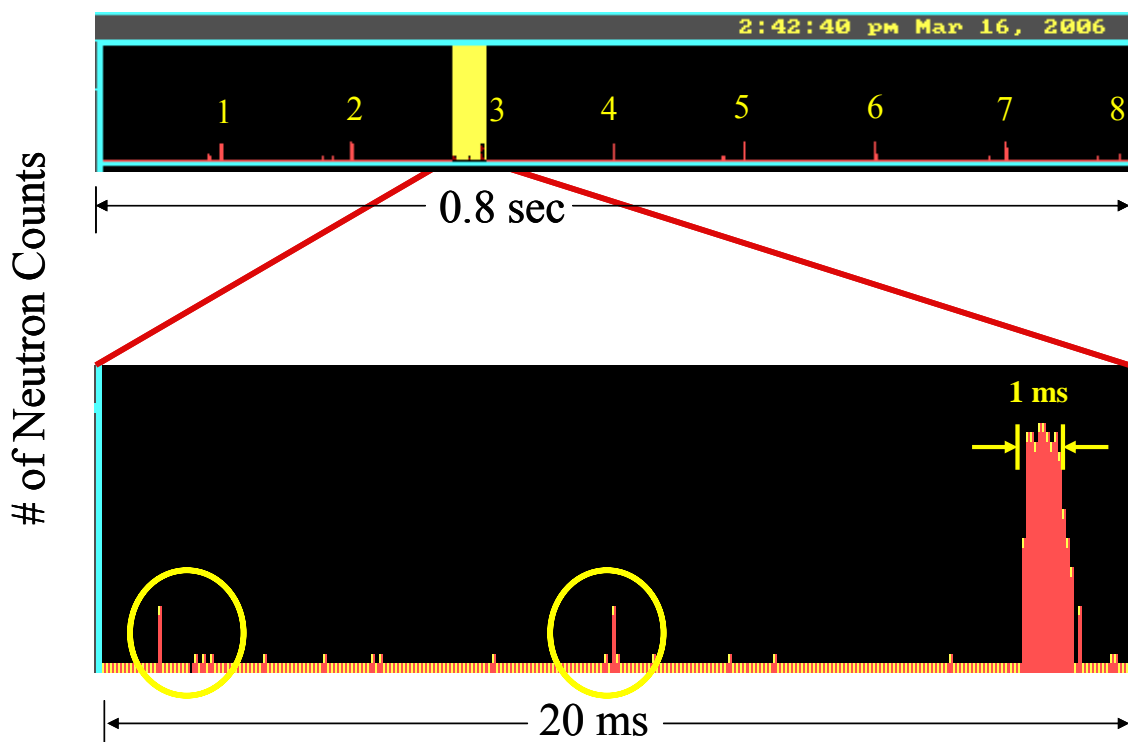


Figure 4.21: Screenshot of PCA3 MCA output. The lower portion of the figure shows a 1 ms wide neutron pulse, plus two neutron counts (circled) occurring between pulses.

4.3 Tungsten Irradiation

4.3.1 IEC Modifications

The IEC device described earlier in this chapter was modified to perform high-temperature tungsten irradiation experiments. The device used in this study (see Figure 4.22) is an aluminum chamber 65 cm tall and 91 cm in diameter. A base pressure of $\sim 10^{-6}$ torr is maintained in the device using a 500 L/s turbo pump. The outer stainless steel anode grid is 50 cm in diameter and is kept at ground potential. The inner target is the tungsten sample and it is connected to a 200 kV power supply through a high voltage feed-through.

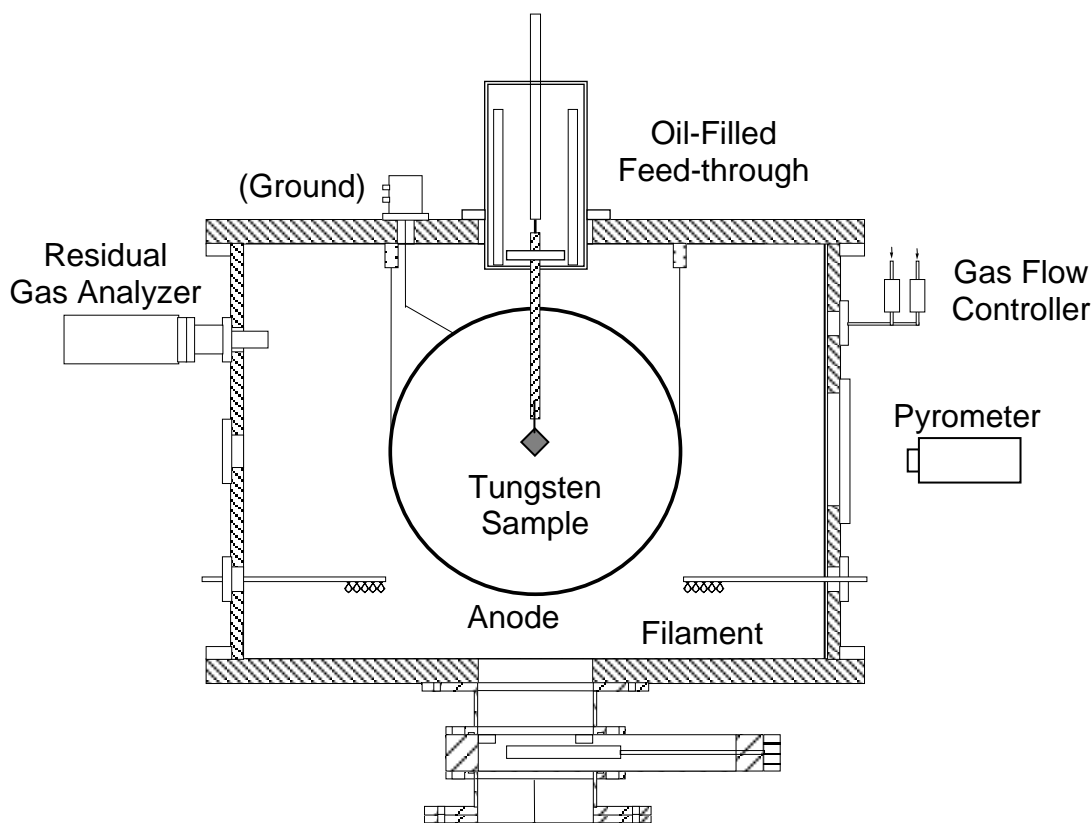


Figure 4.22: Modified IEC fusion device. The cathode has been replaced with a tungsten sample.

During steady-state operation, deuterium or helium gas is fed into the chamber to produce a background pressure of 0.5 mTorr. This gas is then ionized using electron bombardment from standard light bulb filaments. A negative voltage is applied to the target (cathode), and the positively charged ionized gas is attracted to the target. In addition to damaging the target, these ions also heat the sample to temperatures relevant to fusion first-walls, as seen in Figure 4.23. It is assumed that target cooling is due entirely to radiation losses.

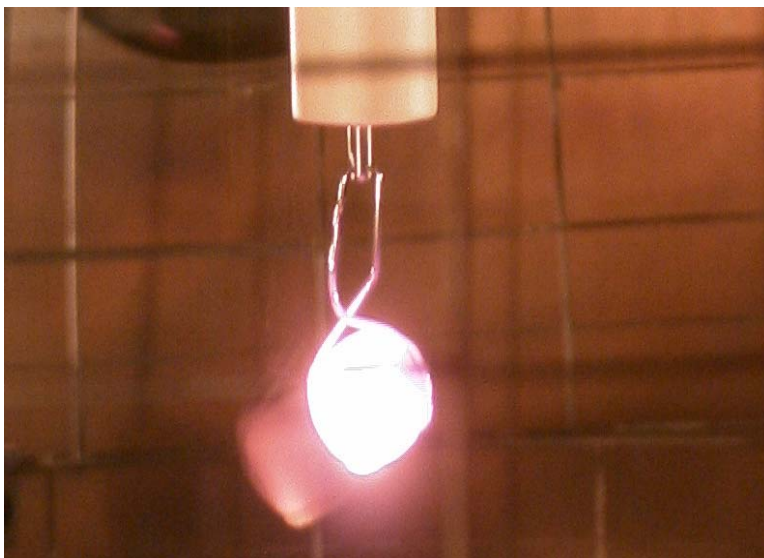


Figure 4.23: Tungsten sample during irradiation.

The polycrystalline and single crystal samples were obtained from ORNL and from ESPI, a high-purity metal alloy supplier. The tungsten-coated metal carbides were obtained from Ultramet, a manufacturer of tungsten-coated foam. SEM micrographs were taken of all samples before irradiation in the IEC device. Each of the samples was then mounted in the IEC device and irradiated to various fluence levels at temperatures ranging from 700-1,200°C. Temperatures were measured using a Raytek[®] Marathon MR pyrometer. A summary of the fluence, temperature, and pore density of the samples used in these sets of

experiments is found in Table 4.1. Irradiation times in the IEC device ranged from roughly 20 seconds to 6 hours. Temperature, pressure, voltage, and current were constantly monitored during the irradiation to ensure constant fluxes. After irradiation samples were again imaged on a LEO 1530 Field Emission Scanning Electron Microscope. Select samples were also imaged with a Zeiss crossbeam focused ion beam (FIB) mill.

Sample	Ions	Fluence (#/cm ²)	Mode	Temp (C)	Pore Density (pores/cm ²)
Poly-11	⁴ He ⁺	1x10 ²⁰	DC	~1150	2.8x10 ⁹
Poly-1	⁴ He ⁺	1x10 ¹⁹	DC	~1150	1.9x10 ⁹
Poly-2	⁴ He ⁺	6x10 ¹⁸	DC	~1120	3.7x10 ⁹
Poly-3	⁴ He ⁺	3x10 ¹⁸	DC	~1125	7.7x10 ⁹
Poly-4	⁴ He ⁺	1x10 ¹⁸	DC	~1150	1.2x10 ⁹
Poly-5	⁴ He ⁺	6x10 ¹⁷	DC	~1130	8.9x10 ⁷
Single-4	⁴ He ⁺	1x10 ¹⁹	DC	~1100	1.7x10 ⁹
Single-2	⁴ He ⁺	6x10 ¹⁸	DC	~1100	1.6x10 ⁹
Single-3	⁴ He ⁺	3x10 ¹⁸	DC	~1100	2.4x10 ⁹
Single-5	⁴ He ⁺	1x10 ¹⁸	DC	~1100	2.5x10 ⁷
Single-6	⁴ He ⁺	6x10 ¹⁷	DC	~1100	0
Poly-6	⁴ He ⁺ and D ⁺	1x10 ¹⁹	DC	~1150	2.5x10 ⁹
Poly-7	⁴ He ⁺ and D ⁺	6x10 ¹⁸	DC	~1150	1.7x10 ⁹
Poly-9	⁴ He ⁺ and D ⁺	3x10 ¹⁸	DC	~1150	1.2x10 ⁹
Poly-10	⁴ He ⁺ and D ⁺	1x10 ¹⁸	DC	~1150	3.2x10 ⁸
W-Re-1	⁴ He ⁺	1x10 ¹⁹	DC	~1100	1.3x10 ⁹
W-Re-2	⁴ He ⁺	6x10 ¹⁸	DC	~1100	1.5x10 ⁹
W-Re-3	⁴ He ⁺	3x10 ¹⁸	DC	~1100	2.5x10 ⁹
W-Re-4	⁴ He ⁺	1x10 ¹⁸	DC	~1100	1.7x10 ⁹
W-Re-5	⁴ He ⁺	6x10 ¹⁷	DC	~1100	5.9x10 ⁷
Poly-13	⁴ He ⁺	1x10 ¹⁹	pulsed	~1150	1.2x10 ⁹
Poly-14	⁴ He ⁺	6x10 ¹⁸	pulsed	~1150	1.7x10 ⁹
Poly-15	⁴ He ⁺	1x10 ¹⁸	pulsed	~1150	1.4x10 ⁹

Table 4.1: Summary of helium ion irradiation experiments on tungsten. Samples were irradiated at cathode voltages of 30-40 keV.

Helium implantation experiments were also performed using pulsed operation. IEC current is nominally suppressed during pulsed operation by applying a positive bias to the electron filaments. Cathode current pulses are then generated by adding a large negative bias to the filaments. The cathode voltage is held constant during the pulse via a 100 nF parallel capacitor.

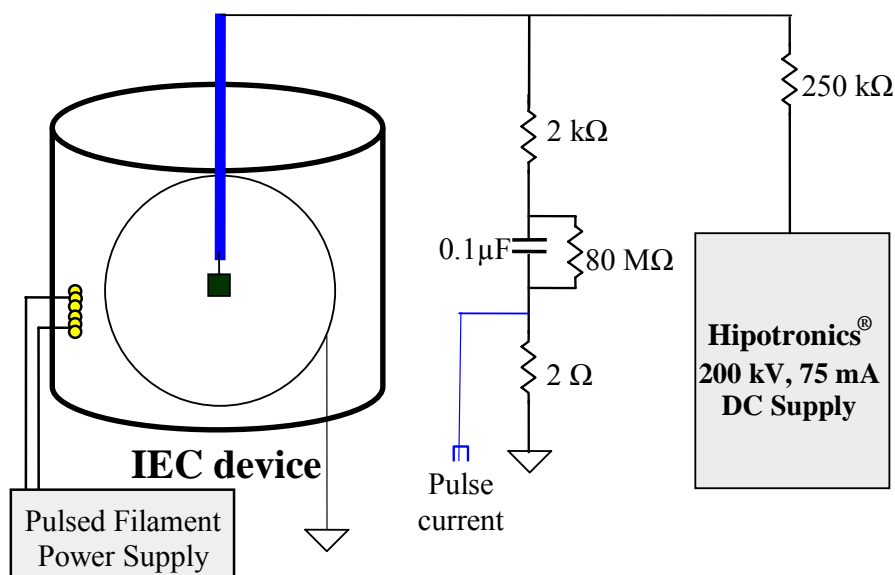


Figure 4.24: High voltage circuit for pulsed IEC operation.

The configuration shown in Figure 4.24 allows the creation of high-flux helium ion pulses at relatively constant voltages. The time-dependent current observed during the initial pulsed irradiation experiments is shown in Figure 4.25. Helium ion currents of 60 mA were pulsed at 25 Hz with a 1 ms pulse width. This resulted in a time-averaged current that was one-fourth of a typical steady-state irradiation, as shown in Figure 4.25.

Although the ion current was pulsed, the sample temperature was calculated to be nearly steady-state during irradiation. This calculation was based on the semi-infinite solid

surface radiation approximation found in Carslaw and Jaegers [6]. The equation used to compute the temperature rise during a single pulse is:

$$\Delta T = \frac{2P}{Ak} \sqrt{\frac{kt}{\pi\rho c_p}} \quad (4.2)$$

where P is the total power into the sample, A is the total surface area, k is thermal conductivity, ρ is density, t is the pulse width, and c_p is the specific heat. Substituting in typical values for a pulsed implantation experiment yields a temperature change of only 8°C during a pulse.

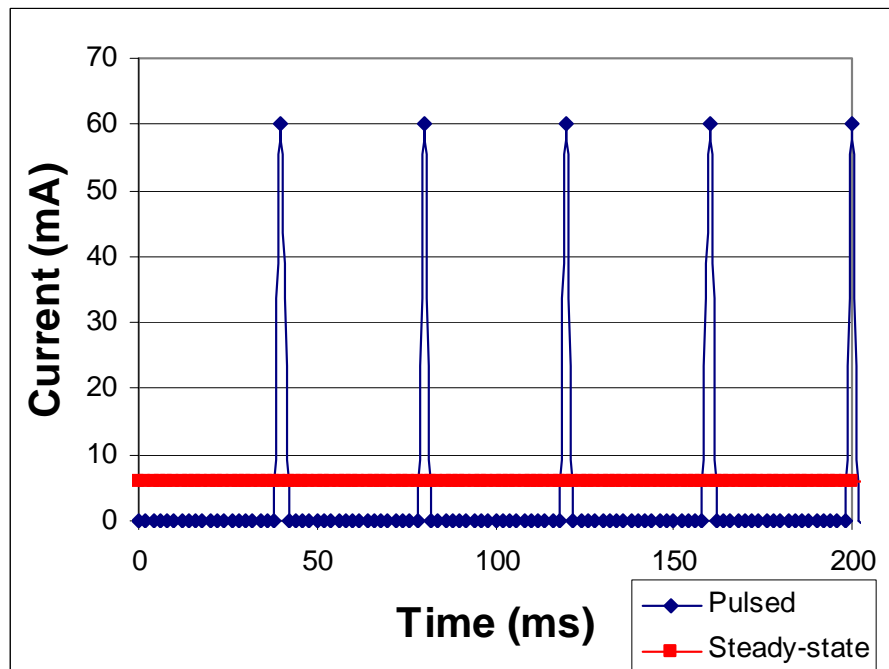


Figure 4.25: Pulsed vs. steady-state irradiation current.

4.3.2 Microscopy

The LEO 1530 is a state-of-the-art Scanning Electron Microscope (SEM) which uses a Schottky-type field-emission electron source [7]. A beam booster is used to maintain optimum electron optical performance at all accelerating voltages. In addition to conventional SEM imaging, the LEO 1530 also incorporates an Energy Dispersive Analysis System (EDS). The EDS detector has a resolution of 129 eV at manganese and a light element detection limit of boron, allowing impurity detection in the tungsten samples.

The Focused Ion Beam (FIB) in operation at the University of Wisconsin Materials Science Center uses a 30 keV gallium beam to mill samples for numerous applications. It can be used to complete modifications and rewiring on integrated circuits. Micro-machining and constructing STM probes is also possible. Another common application is the preparation of thin samples for use in Transmission Electron Microscope (TEM) imaging. A final application for the FIB is the analysis of sample cross sections, such as the ones discussed in Chapter 5. The Zeiss CrossBeam used for this project is capable of 100 nm accuracy when placing the beam location. This accuracy made it simple to image the most interesting features of the tungsten samples. Ion images can be taken directly with the device, and have a resolution of 7 nm. This device also contained a separate SEM column, making it possible to image either with primary electrons or with secondary electrons from the ion beam.

Prior to this project, no one at the University of Wisconsin had attempted to image and mill tungsten with the FIB device. Initial attempts to mill trenches in the samples with a 300 pA beam barely scratched the surface. After increasing the current to 20 nA, milling the sample was possible, but two new problems were encountered. First, there was significant

channeling of the ions going into the sample, resulting in non-uniform erosion as seen in Figure 4.27. Additionally, the high current created a “blast pattern” all around the sample, which obscured the surfaces we were interested in. One solution for this problem was to add a layer of platinum on the surface with a gas injector, as seen in Figures 4.28 and 4.29. The platinum acted as an ablation layer during the FIB milling. It was thought that the boundary between the tungsten and the platinum would be clear enough that adequate images could be taken with the platinum present.

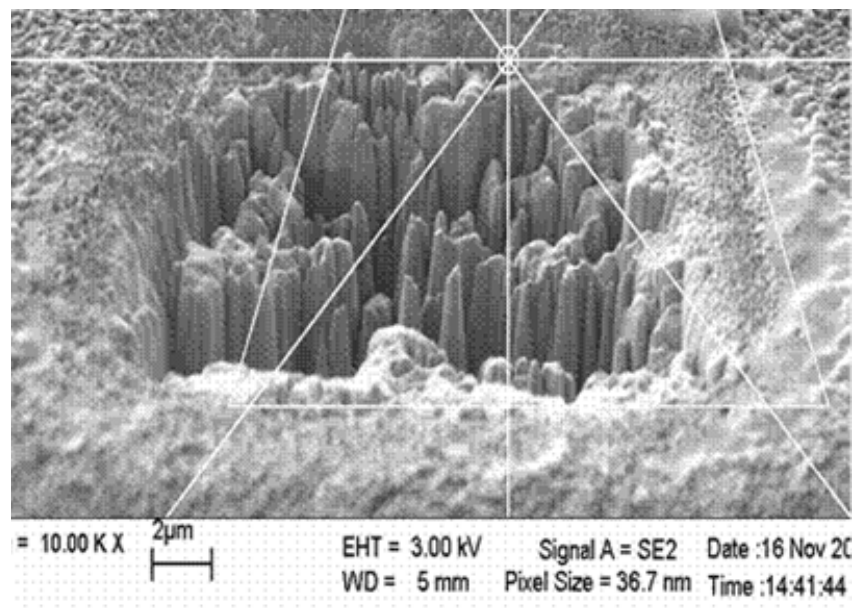


Figure 4.27: Initial attempts to mill tungsten yielded poor results.

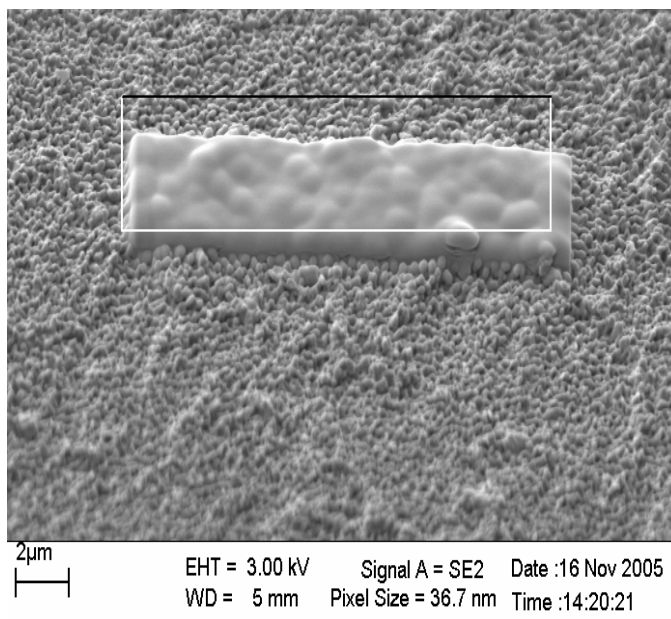


Figure 4.28: Platinum layer over a tungsten substrate. Imaged with the SEM column.

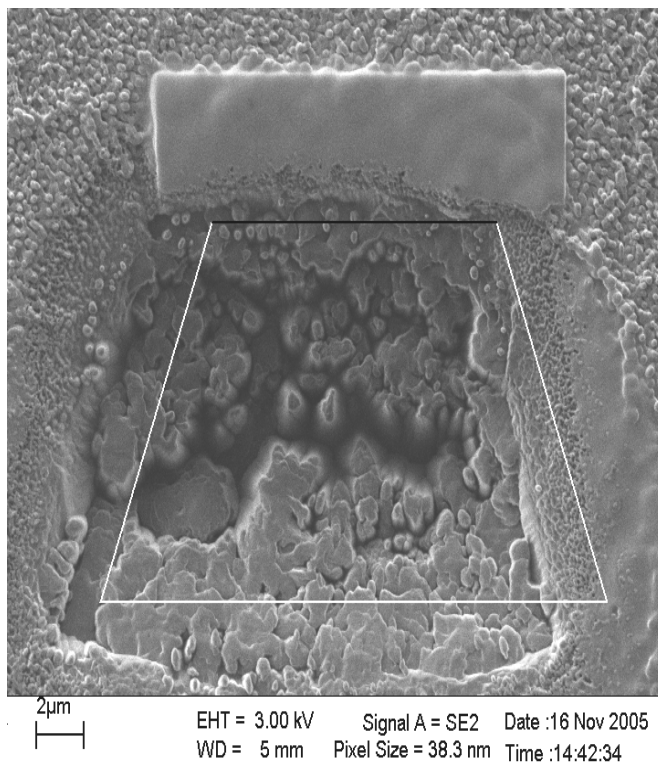


Figure 4.29: Platinum layer with a milled trench intersecting it. Imaged with the FIB column.

The leading edge was now protected, but significant channeling still occurred. Through a process of trial-and-error, it was found that water injection during the milling process significantly reduced ion channeling. Once water injection was used, the ion beam was run at 20 nA without too much of the “blasting” effect. While there was still some material ejected and redeposited on the surface of interest, this was easily removed with a second pass of a lower current (2 nA) beam. Ultimately, very clean cuts were achieved in the tungsten samples, revealing a subsurface porous structure, as shown in Figure 4.30 and described in Chapter 5.

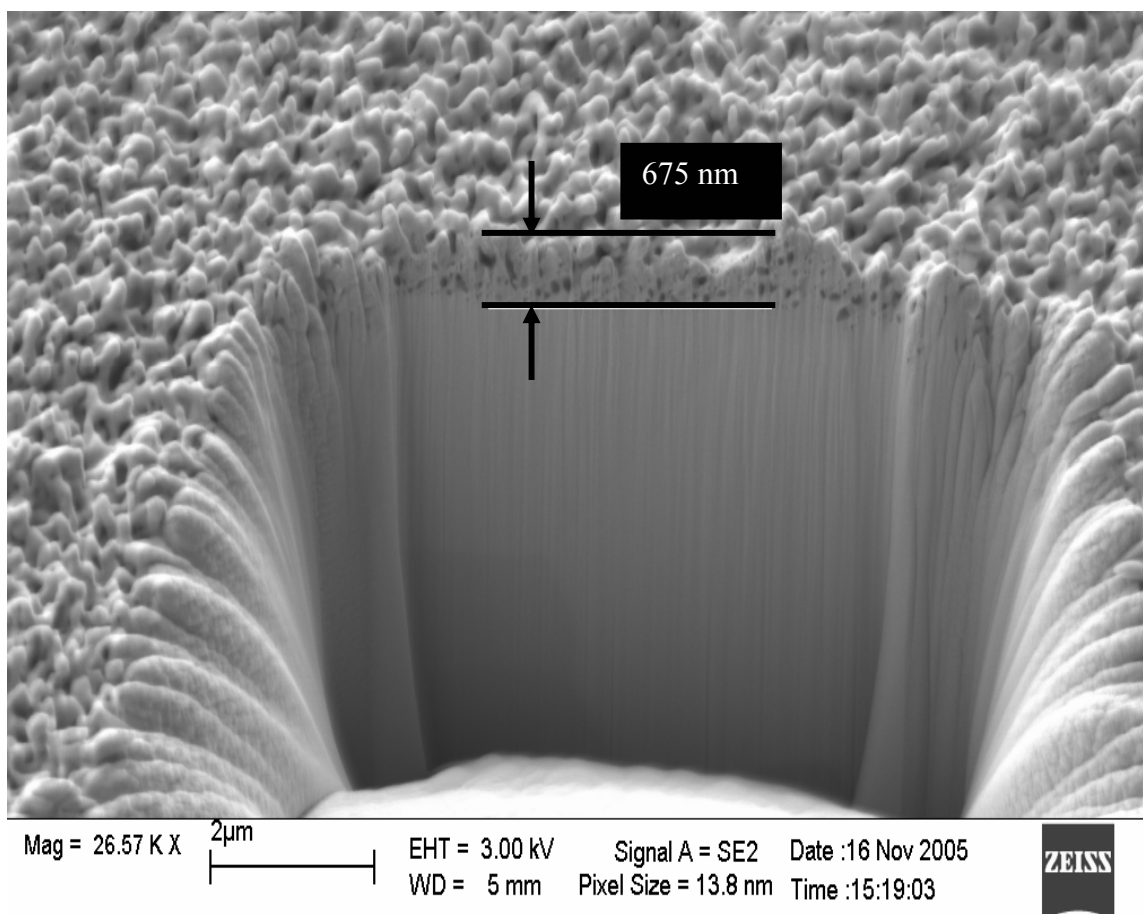


Figure 4.30: FIB imaging allowed evaluation of subsurface pore structure.

4.4 References

- [1] G.R. Piefer, "Performance of a Low-Pressure, Helicon Driven IEC ^3He Fusion Device," PhD Thesis, University of Wisconsin-Madison, 2006
- [2] Knoll, G.F. (2000). "Radiation Detection and Measurement, 3rd Edition" John Wiley and Sons, New York: 2000
- [3] R.P. Ashley et al., "Recent Progress in Steady State Fusion using D- ^3He ," *Fusion Technology*, 44(2), 564, 2003
- [4] B.B. Cipiti, "The Fusion of Advanced Fuels to Produce Medical Isotopes Using Inertial Electrostatic Confinement," PhD Thesis, University of Wisconsin-Madison, 2005
- [5] Y.S. Touloukian, "Thermo-physical Properties of Matter, Vol. 7: Thermal Radiative Properties," IFI/Plenum, New York, 1970
- [6] H.S. CARSLAW and J.C. JAEGER, *Conduction of Heat in Solids*, 2nd Ed; pp 73-76, Clarendon Press, Oxford, 2001
- [7] Rick Noll (University of Wisconsin), Private communication, 2005

Chapter 5: Results

5.1 MCNP Modeling of HEU Detection

To determine the feasibility of active HEU detection utilizing a pulsed IEC fusion device, the concept was first modeled using MCNP5; a Monte Carlo based particle-tracking code [1]. Initially, a series of test modules were developed to test the validity of the code for this specific task. Then, a detailed model of the IEC and detection hardware was constructed to determine the minimum amount of HEU needed for valid detection statistics.

5.1.1 *Delayed Neutrons in MCNP*

Proper accounting for delayed neutrons was not incorporated into the MCNP program until version MCNP4C [2]. Previous versions had represented all secondary production of neutrons created in the fission process as prompt neutrons. This deficiency has been corrected by adding delayed neutron data to the MCNP data libraries and modifying the MCNP code to sample delayed neutron time of emission and energy. Werner [2] verified the delayed neutron effects in the code both analytically and experimentally. Figure 5.1 shows a plot of delayed neutrons as a function of time for both experimental data and an MCNP4C model of the same apparatus.

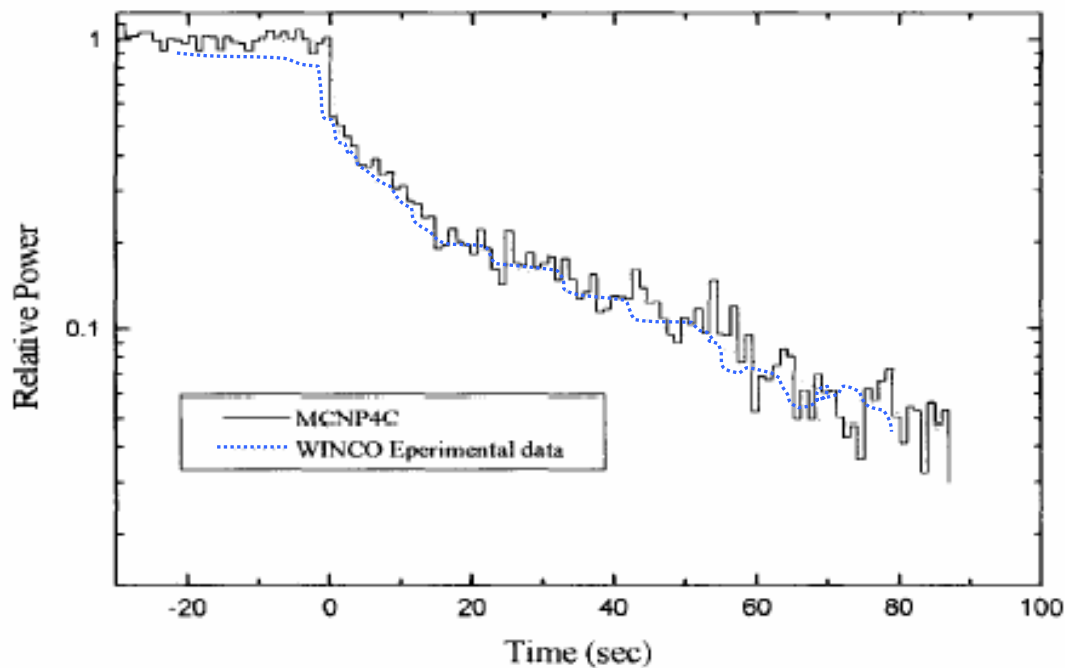


Figure 5.1: MCNP results with benchmarking data [2].

Before designing a realistic model of the IEC and HEU detection system, an effort was first made to verify that MCNP was capable of correctly modeling the time-dependent behavior of delayed neutrons produced from the fission of ^{235}U and ^{239}Pu in a pulsed system. A model of a bare sub-critical metal sphere of fissile material was used to perform this verification. A pulsed source of thermal neutrons was introduced at the center of the sphere, and a volume tally was taken within the sphere to observe the time-dependent neutron flux during and after the pulse. MCNP5 is capable of running in modes with and without delayed neutrons, so the model was first run with the delayed neutrons shut off. As seen in Figure 5.2, there are almost no neutrons present within the sphere 10 ms after the 30 ms pulse is complete, and those present are due only to scattering. Error bars are included on the graph, but are generally smaller than the data points. Also note that the counts represent a fluence

averaged over the volume of the sphere, per source neutron. Therefore to calculate actual fluences, the values must be multiplied by the total number of source neutrons in the system.

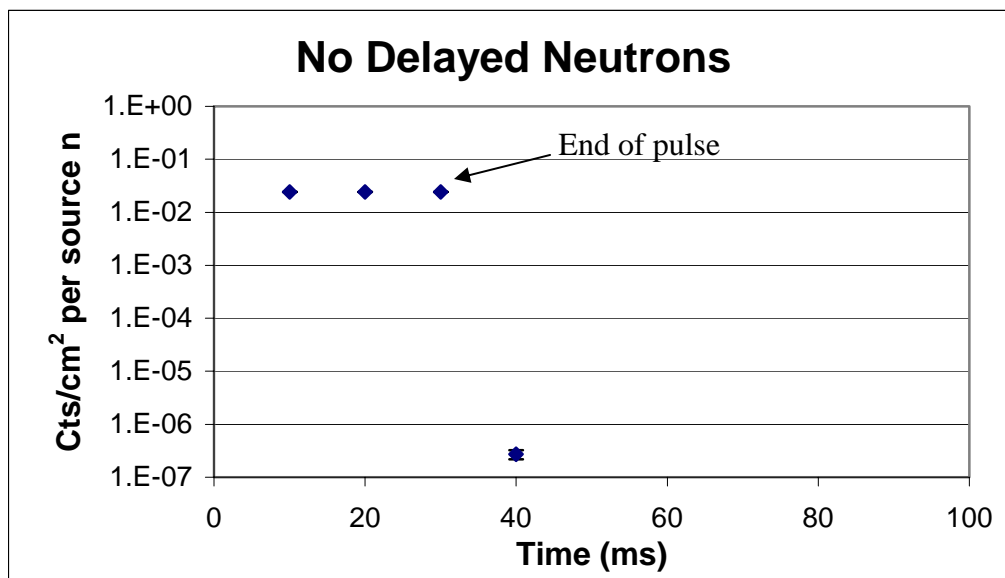


Figure 5.2: MCNP5 spectra without delayed neutrons. Counts are normalized per source neutron and are taken in 10 ms bins.

This calculation was then repeated with the delayed neutron feature turned on for both ^{235}U and ^{239}Pu spheres of 4 cm radius. Figure 5.3 shows the two spectra plotted on top of each other. Error bars are present, but are smaller than the data points. In both cases, the source neutrons were stopped at 30 ms, but tallies were extended out to 100 ms to observe the delayed neutrons. The higher cross section for thermal neutrons is reflected in the higher counts in the plutonium sample.

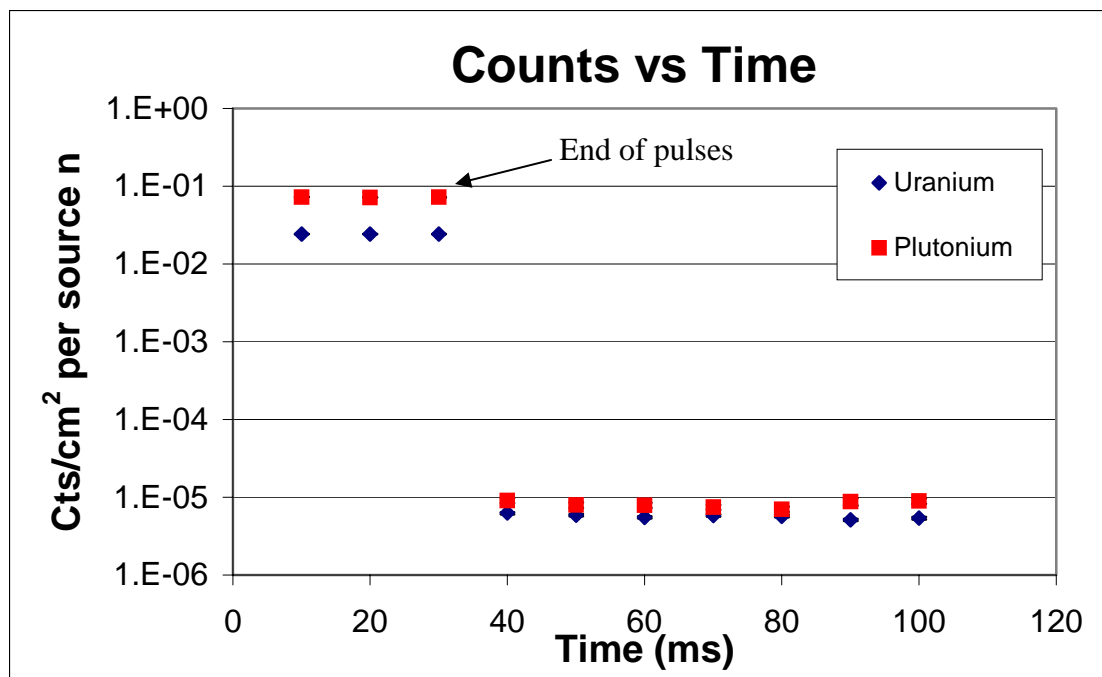


Figure 5.3: MCNP5 counts vs. time tallies with delayed neutrons. Counts are normalized per source neutron and are taken in 10 ms bins.

In addition to the delayed neutrons being created in the first few milliseconds, the longer-term behavior was observed for the HEU sample. In this case, the tallies were extended out to 30 and 300 seconds, respectively, after the 30 ms pulse. Error bars are present in both graphs, but are generally smaller than the data points. Again, these results match the expected behavior of delayed neutrons for ^{235}U , and are consistent with the experimental data in Figure 5.1.

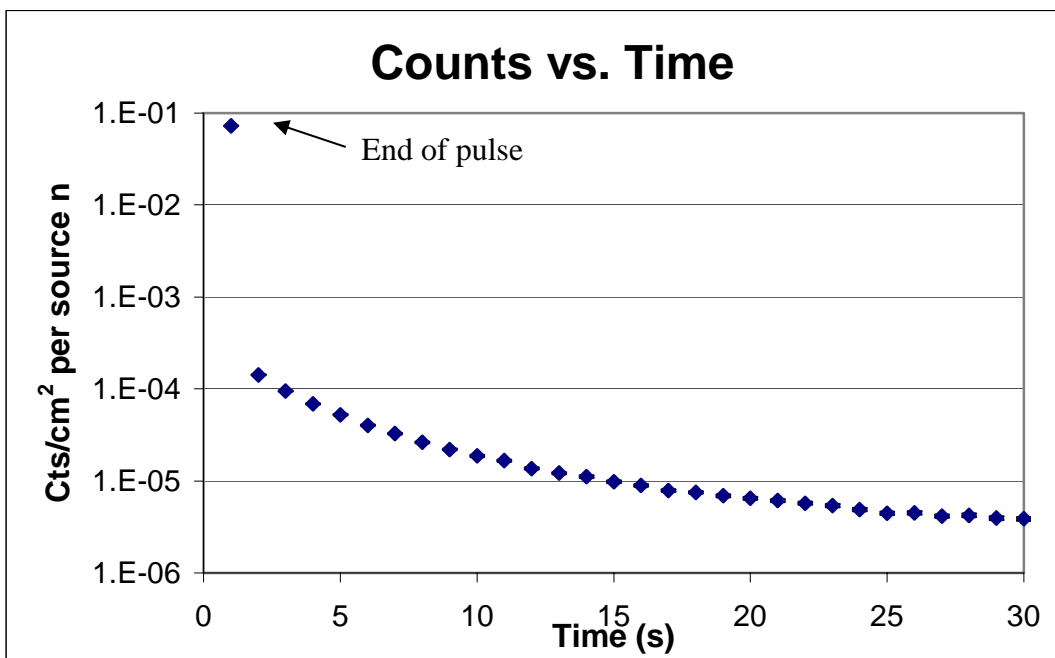


Figure 5.4: Calculated delayed neutron spectra out to 30 seconds. Counts are normalized per source neutron and are taken in 1-second bins.

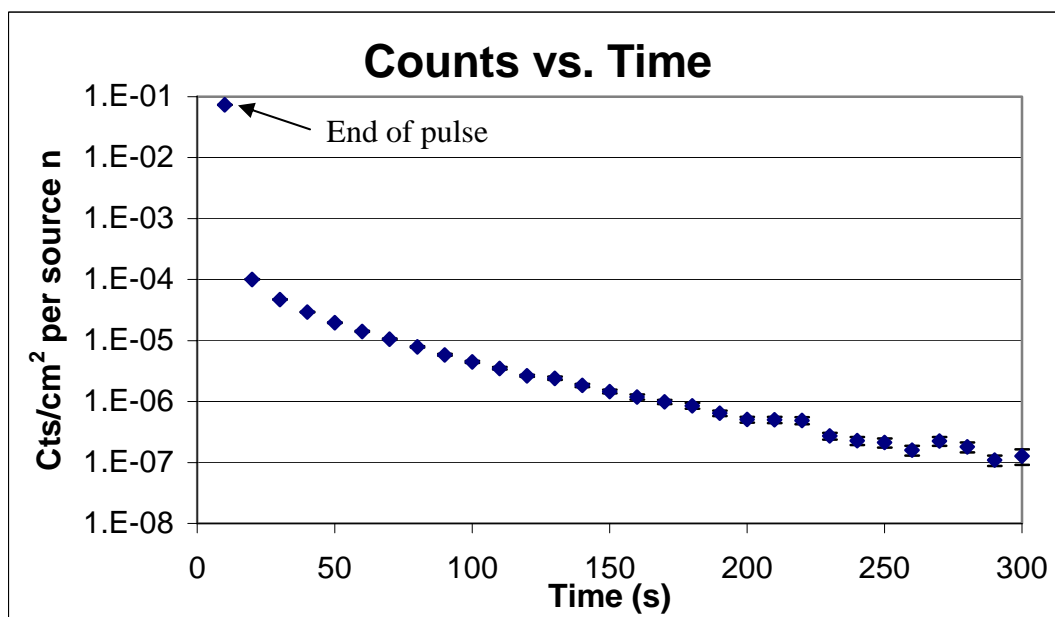


Figure 5.5: Calculated delayed neutron spectra out to 300 seconds. Counts are normalized per source neutron and are taken in 10-second bins.

The next step in the validation process was to develop a model in which the source exhibited pulsing behavior. As an initial step, the source was set as a 1 ms pulse followed by 99 ms of no source neutrons being created. The MCNP program was then set up to provide five of these pulse sequences. Figure 5.6 shows the resulting volume flux tally for a 4 cm radius (~5 kg) uranium sphere enriched to 100 percent ^{235}U . Error bars are present, but generally smaller than the data points. Although the delayed neutrons are decaying between pulses, the cumulative effect of each pulse is consistently increasing the total delayed neutron population. However, the delayed neutron population will begin to reach a steady-state value over time, as seen in Figure 5.7. This will be true in the experimental case as well, and will have to be taken into account when neutron measurements are made.

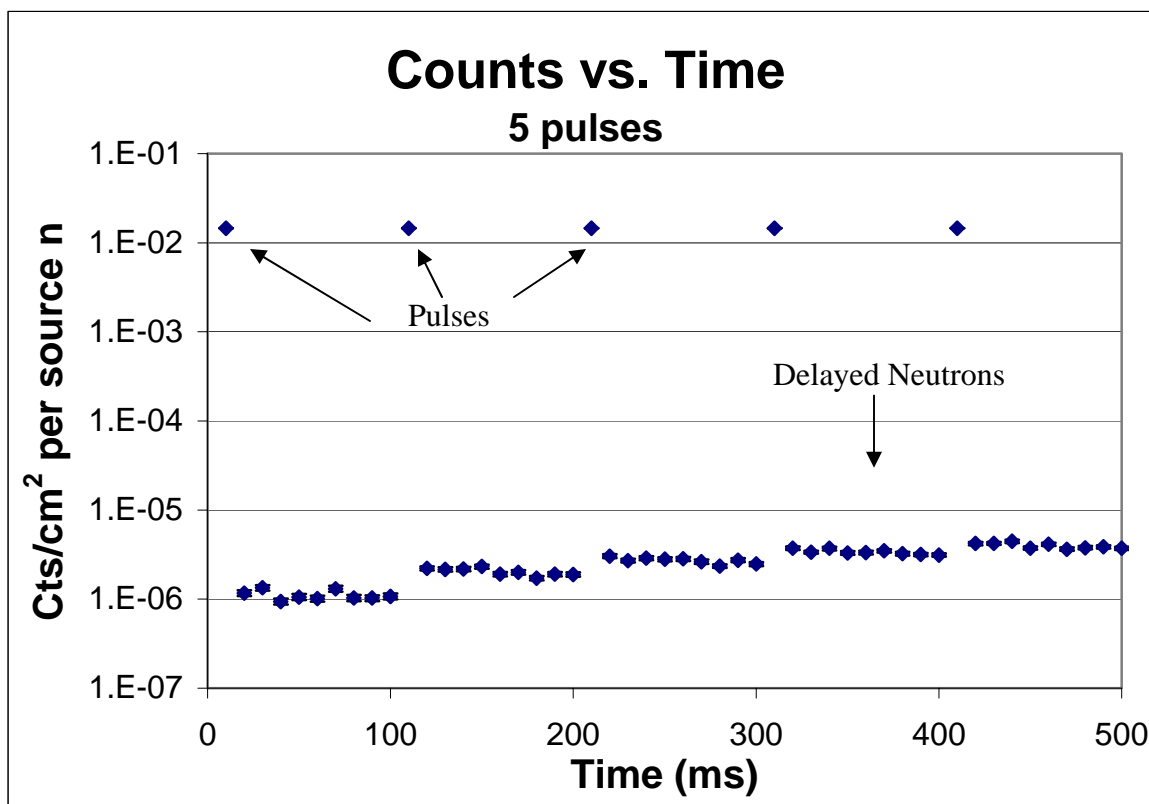


Figure 5.6: Calculated fluence for a series of 5 pulses in test case. Counts are normalized per source neutron and are taken in 10 ms bins.

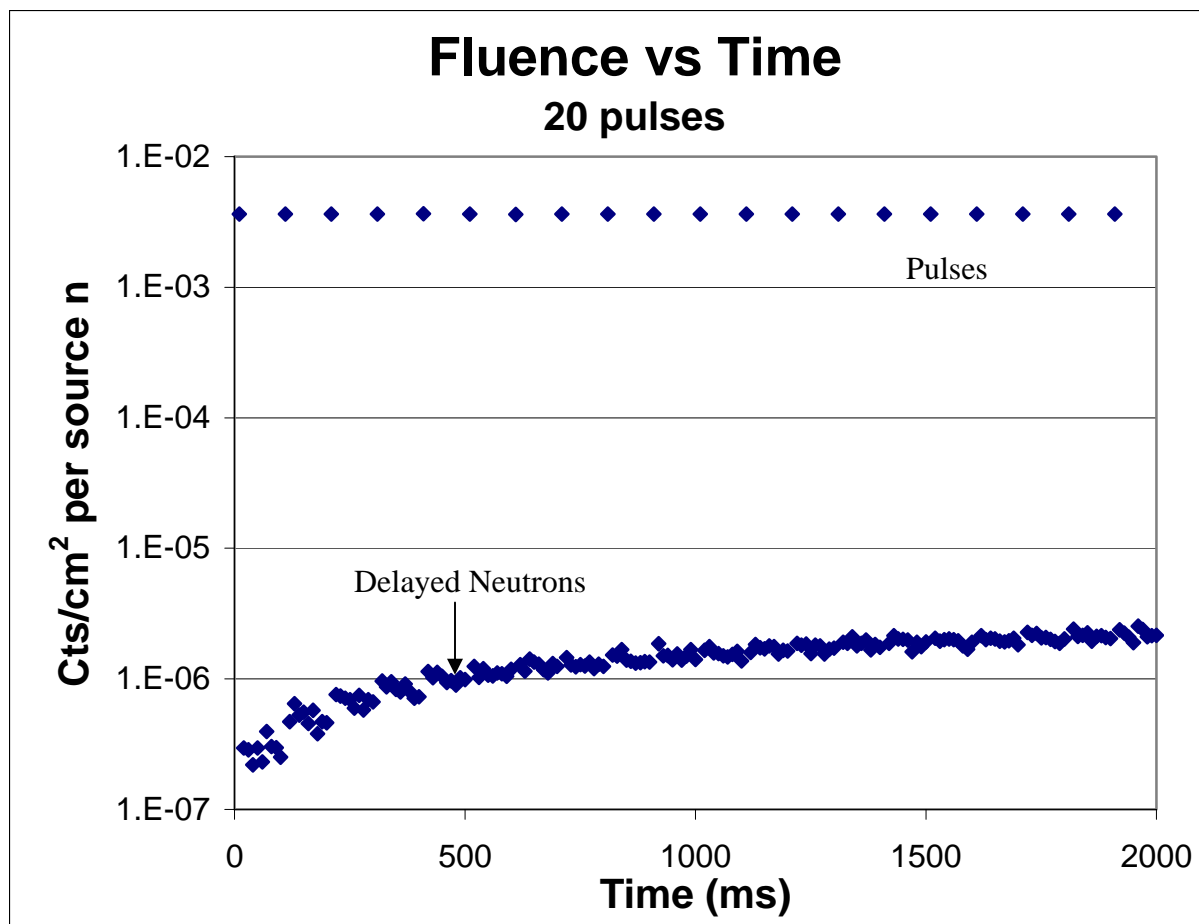


Figure 5.7: Calculated fluence for a series of 20 pulses in test case. Counts are normalized per source neutron and are taken in 10 ms bins.

As a final validation of MCNP5, and as an initial indicator of the validity of the IEC model, the enrichment of the bare sphere was varied from 100 percent down to natural enrichment. As shown in Figure 5.8, the delayed neutron levels are not directly related to the amount of fissile isotope in the irradiated sample, as was originally assumed. In this case, error bars were omitted for clarity. Due to this lack of linearity, the final model was designed using the actual enrichment of the experimental sample.

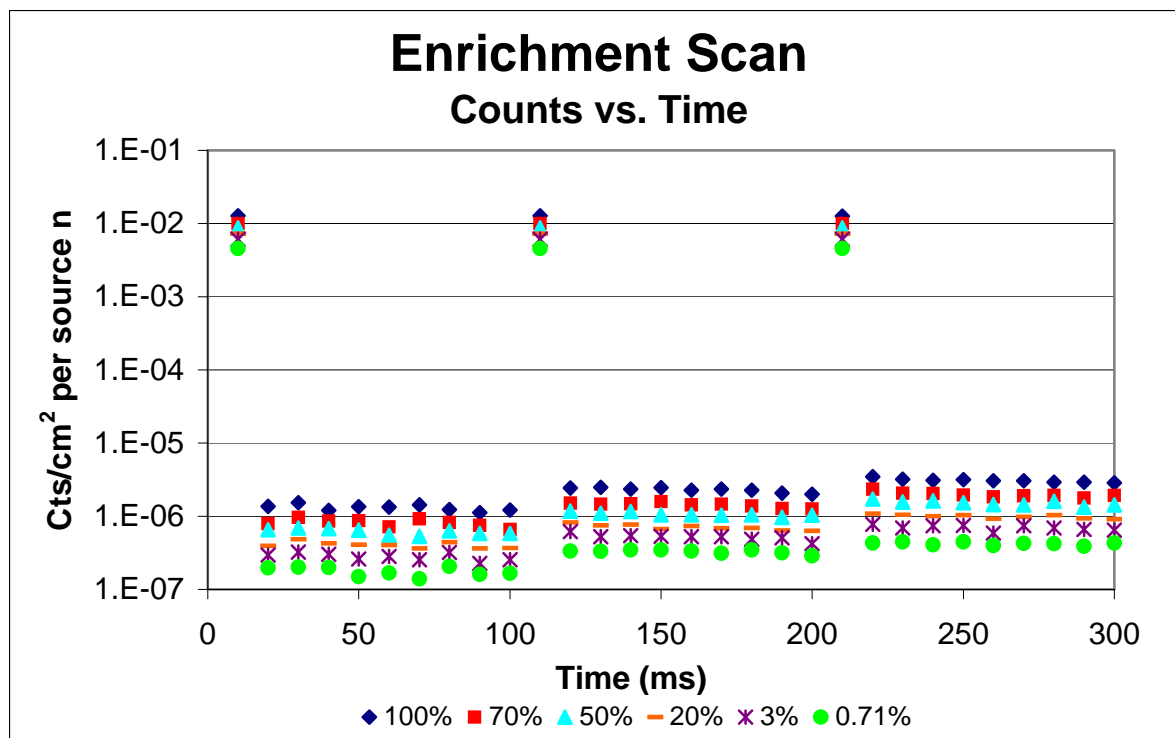


Figure 5.8: Calculated delayed neutron spectra for 3 pulses. The various colors represent different levels of ^{235}U enrichment. Counts are normalized per source neutron and are taken in 10 ms bins.

5.1.2 MCNP Model of the IEC

Once it was determined that MCNP5 was capable of properly modeling delayed neutrons with a pulsed neutron source in place, work was begun on a simple model of the IEC device. Figures 5.9 and 5.10 show a side and top view of the device with the HEU and detection module in place. This geometry was chosen to maximize the number of fission neutrons that survive to enter the ^3He detectors. It was also chosen due to the relative ease of construction. The detection unit is modeled after a modified long counter with the central detector replaced with a HEU sample. The actual detector system utilizes a neutron detector

gate to eliminate counts from room-scattered neutrons, so this model neglects the effects of the concrete walls in the room to drastically decrease computation time.

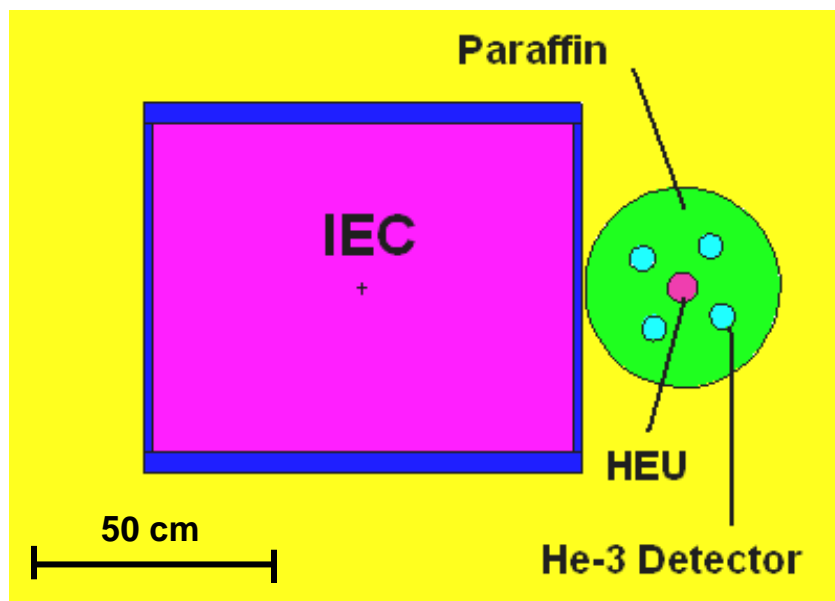


Figure 5.9: Side view of the HEU detection model in MCNP.

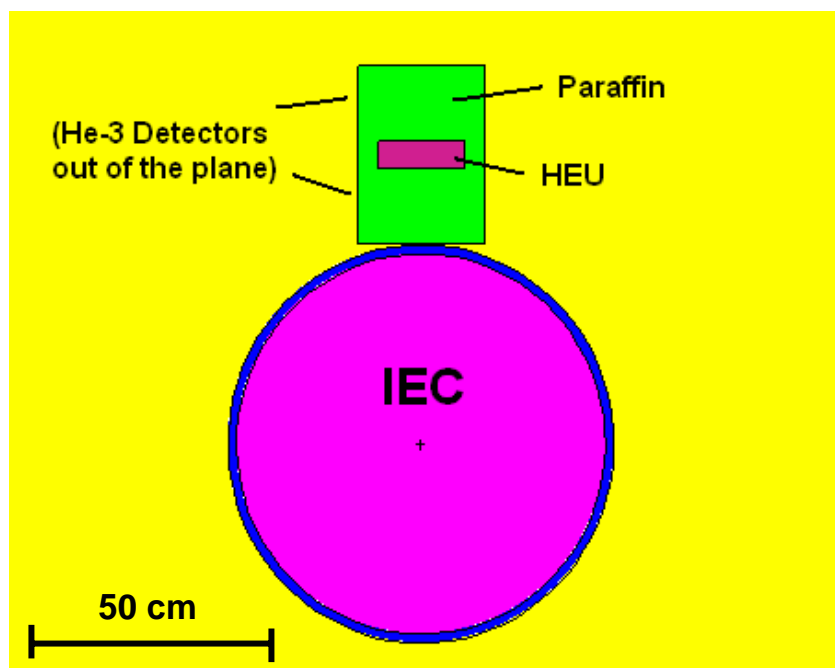


Figure 5.10: Top view of the HEU detection model in MCNP.

Since this model places a relatively small HEU sample relatively far from a point neutron source, the counting statistics were initially very poor. In fact, the source neutrons would seldom create delayed neutrons that made it to the detectors at all. A number of methods of variance reduction were employed to improve statistics and limit the amount of runtime required to achieve reliable results. First, the importances of the various cells were modified to increase the likelihood of neutrons being transported through the paraffin into the detectors. Next, the isotropic source was biased such that it only released neutrons in the direction of the detector. This was assumed to be a reasonable assumption as neutrons traveling in other directions would only contribute to wall-scattered thermal neutrons, which are absorbed by the cadmium shield. Finally, the source was designed to act as a series of pulses. This allowed the delayed neutron count between pulses to increase well above its value for single pulses without significantly increasing the runtime required to complete a run.

After completing these methods, results were obtained that had reasonable levels of error present in the delayed neutron counts. Figure 5.11 shows the average flux present in the ^3He detectors per source neutron. Error in the prompt neutrons is less than 0.1 percent. However, the error in the delayed neutrons is as high as 15 percent after the first pulse and is still ~7 percent at 1 second. Even with this error, the delayed neutron flux is clearly increasing with time and is approaching the steady-state delayed neutron value.

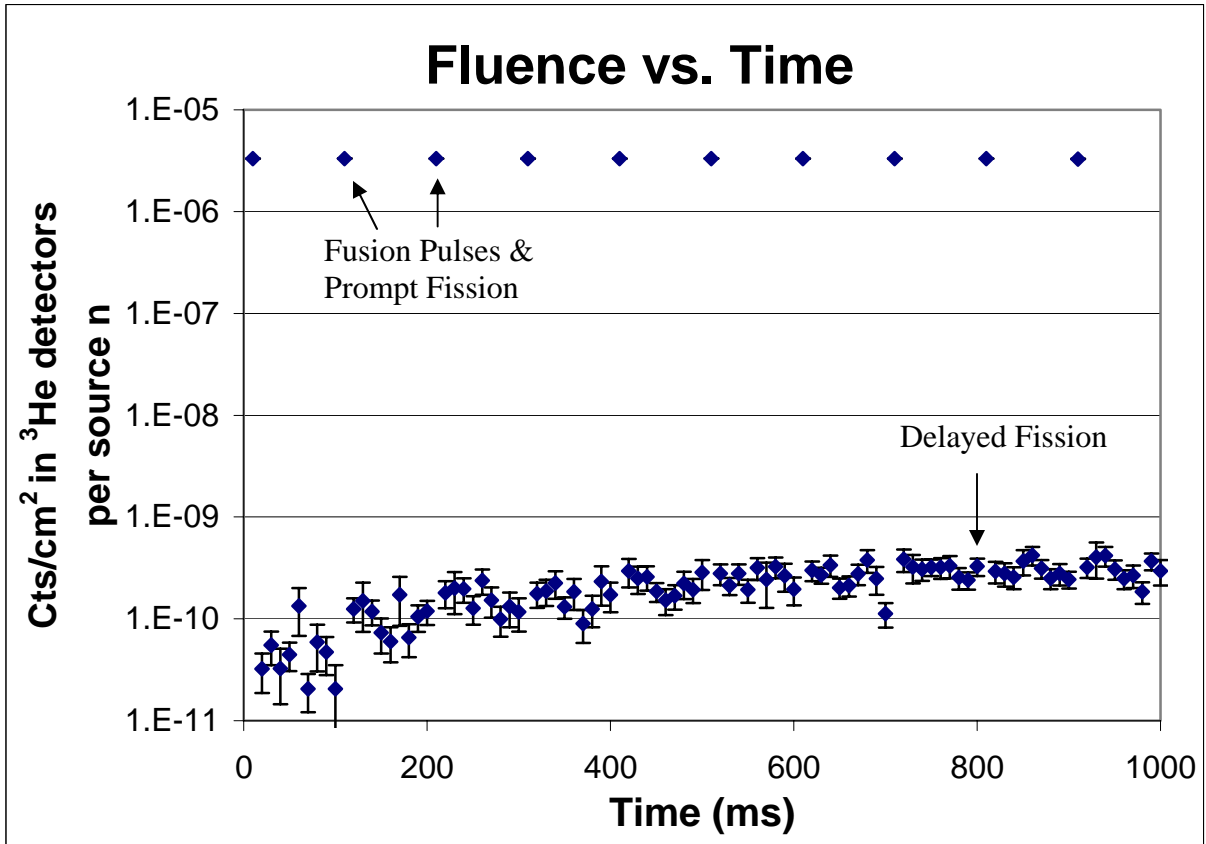


Figure 5.11: Calculated average neutron fluence in the ^3He detectors. Counts are normalized per source neutron and are taken in 10 ms bins.

These data were then used to determine the total number of reactions occurring in the detectors, and therefore the number of counts available for detection. A tally multiplier was added to the volume tallies corresponding to the detector tubes that performed the operation:

$$V \int \varphi(E) N \sigma(E) dE \quad (5.1)$$

where $\varphi(E)$ is the energy-dependent fluence (particles/cm²), N is the number density of the ^3He , $\sigma(E)$ is the energy-dependent absorption cross section and V is the volume of the detector assembly [1]. The resultant number of reactions plotted as a function of time is shown in Figure 5.12.

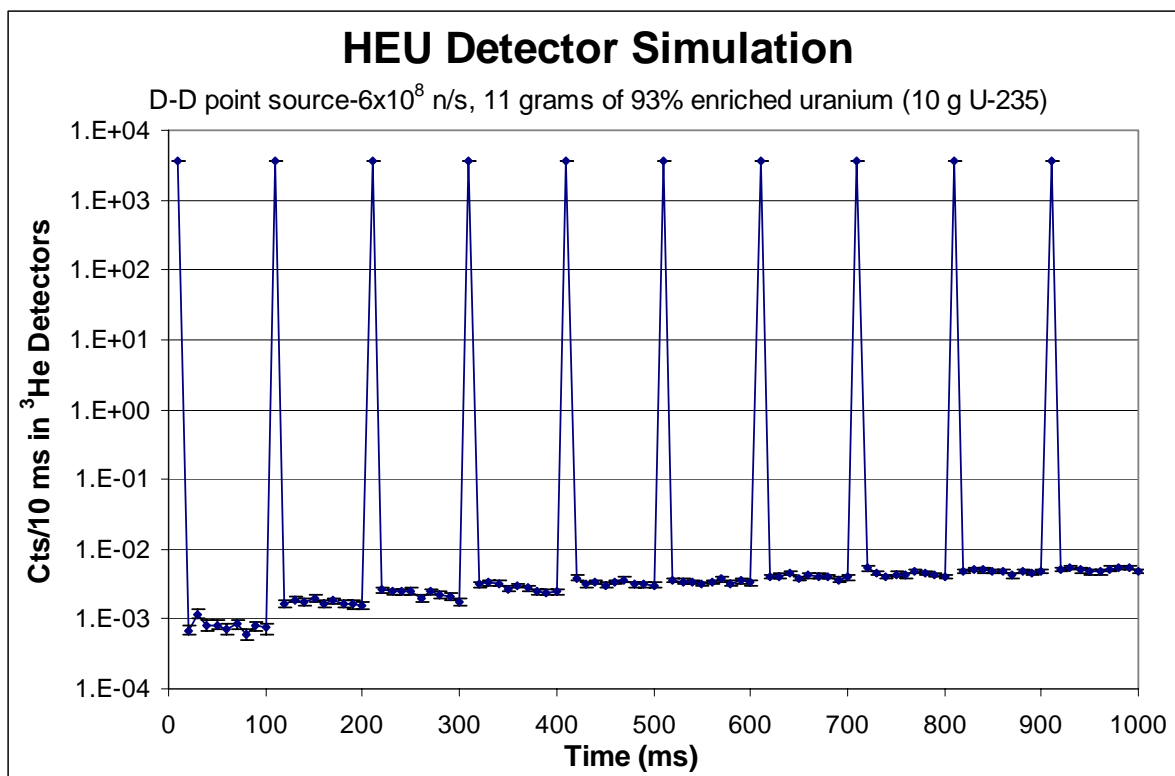


Figure 5.12: Calculated reaction rate within the ^3He detectors. Counts are taken in 10 ms bins. HEU sample is 50 cm from neutron source.

Figure 5.12 shows the results of an MCNP simulation of the UW-IEC device (as shown in Figure 5.9) during a HEU irradiation experiment. A point source of 2.45 MeV D-D neutrons was used in the model to replicate the 6.8×10^8 n/s fusion rate measured during an actual irradiation experiment. Since a gate is used to block counts during the first 20 ms after pulses in the experiment, the model assumes this as well. This MCNP model predicted that 1.04 counts/second should be measured by the ^3He tubes from delayed neutrons coming from the 11 gram sample of 93 percent enriched uranium (10 grams of uranium-235). When this experiment was performed in the laboratory, a rate of 1.2 counts/second was measured in the neutron detectors.

5.1.3 Neutron Scattering

In addition to predicting delayed neutron detection rates, MCNP was also used to model the behavior of the IEC fusion neutron pulse decay. This information was not only valuable for exploring the source of the thermal neutron decay, but it provides more insight into the “fall away” behavior of the background neutron population, which will be crucial for future investigations of the “Differential Die-Away” technique (DDA). Figure 5.13 shows the calculated decay behavior of a 1 ms D-D neutron pulse in the IEC hot cell. The neutron pulse decays rapidly for the first 0.5 ms after the fusion pulse. However, a slower decay behavior dominates after 0.5 ms. This decay appears to result from thermal neutrons as they scatter in the concrete walls and other materials in the room.

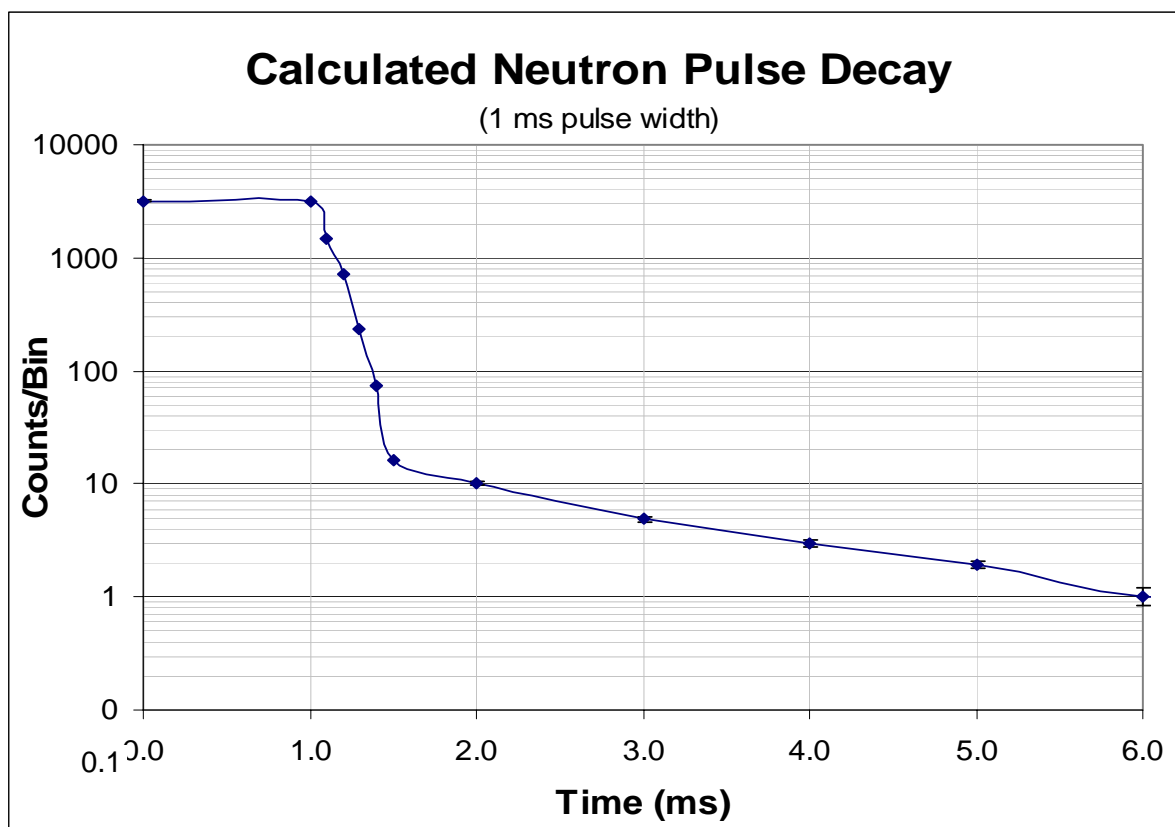


Figure 5.13: Calculated fusion neutron pulse decay. No uranium in system.

Figure 5.14 compares an MCNP pulse to data acquired in the IEC hot cell. The MCNP output was normalized to match the experimental data during the pulse. The decay behavior of the MCNP model matches well with the experimental data.

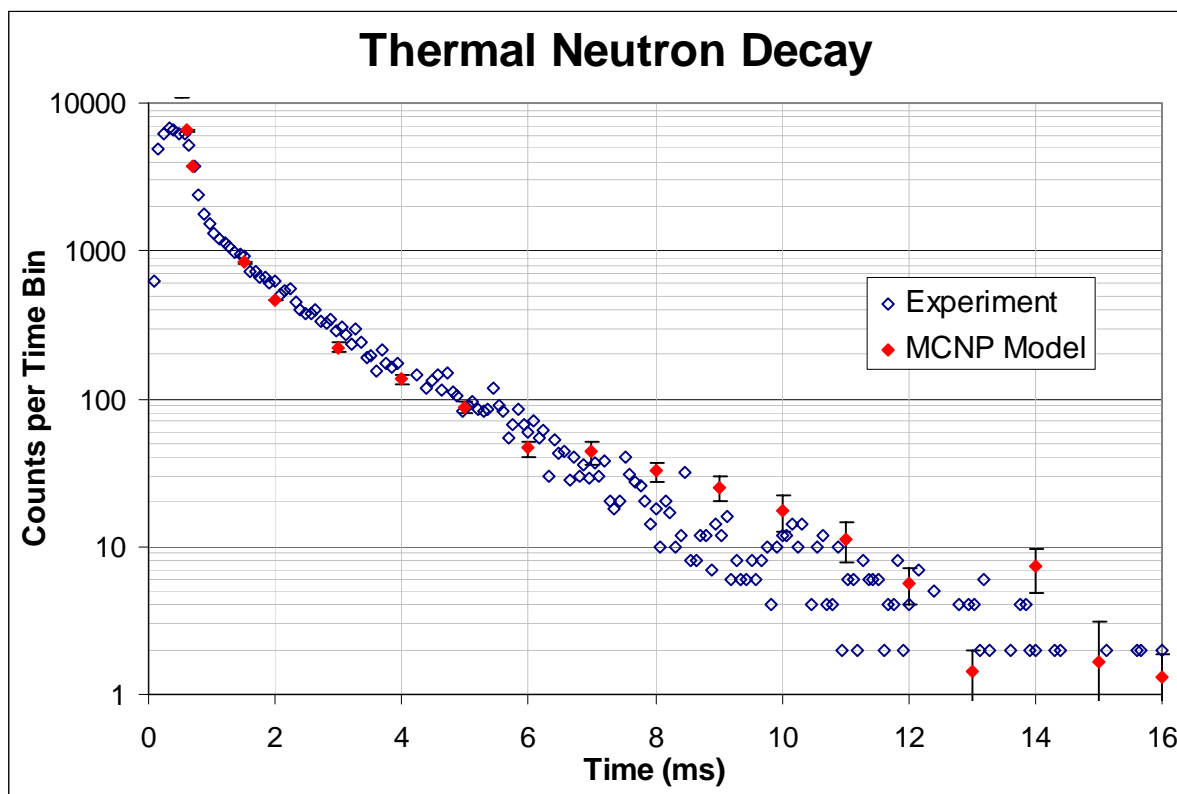


Figure 5.14: Thermal neutron decay for MCNP model and experimental data. MCNP output normalized to match experimental pulse height. No uranium in system.

5.2 Pulsed Neutron Source Development

5.2.1 Ion Source Region

Development and characterization of the ion source region of the IEC device began with examining the effect of various parameters on the ion emission current. As seen in Figure 5.15, the filament emission current is a strong function of the filament temperature. The filaments were therefore run at maximum temperature during most experiments to maximize emission current. Although it is known that operating the filaments at higher temperature shortens their lifespan, this effect has not yet been quantified for IEC operation.

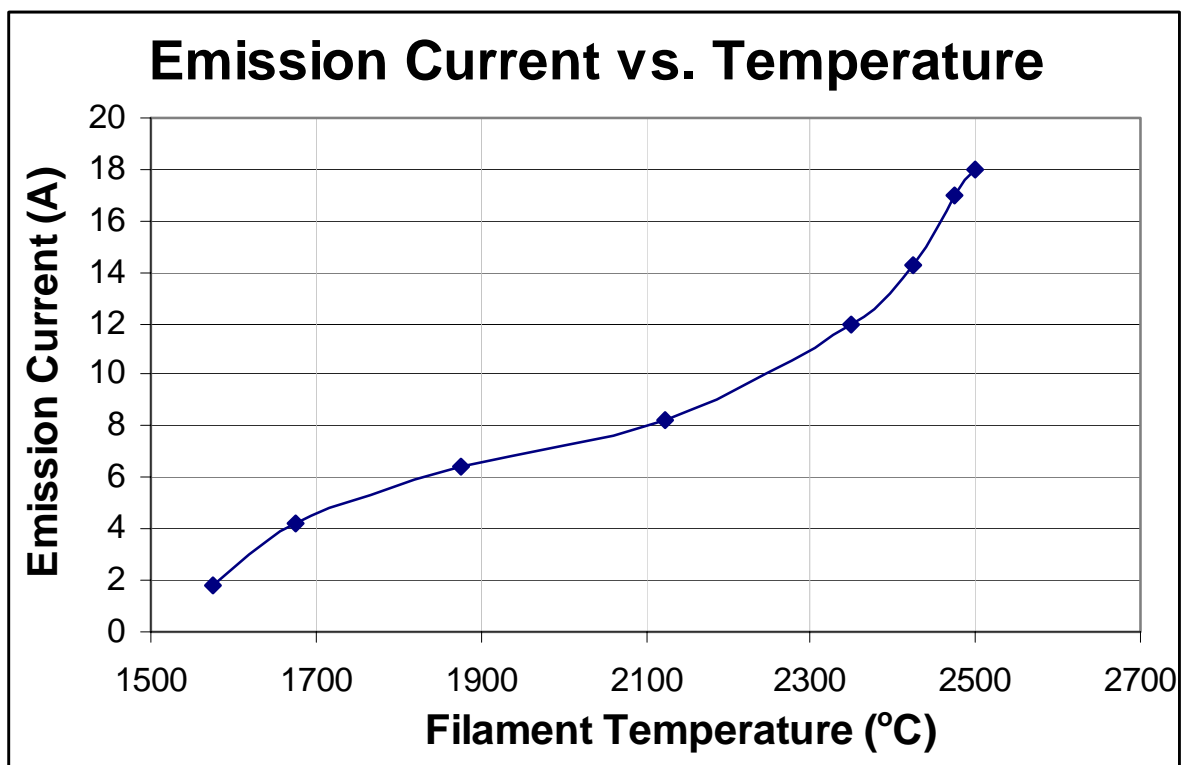


Figure 5.15: Emission current increases with increasing filament temperature.

The bias voltage on the filaments also plays a key role in determining the filament emission current. Figure 5.16 shows the emission current increasing linearly as the negative pulse bias is added to the filaments. Since the heater current on the filaments provides a negative bias, the filaments will emit with zero bias voltage. A positive bias of nearly 50 V is required to turn off filament emission. As the bias level approaches -300 V, it appears that the emission current level is beginning to saturate.

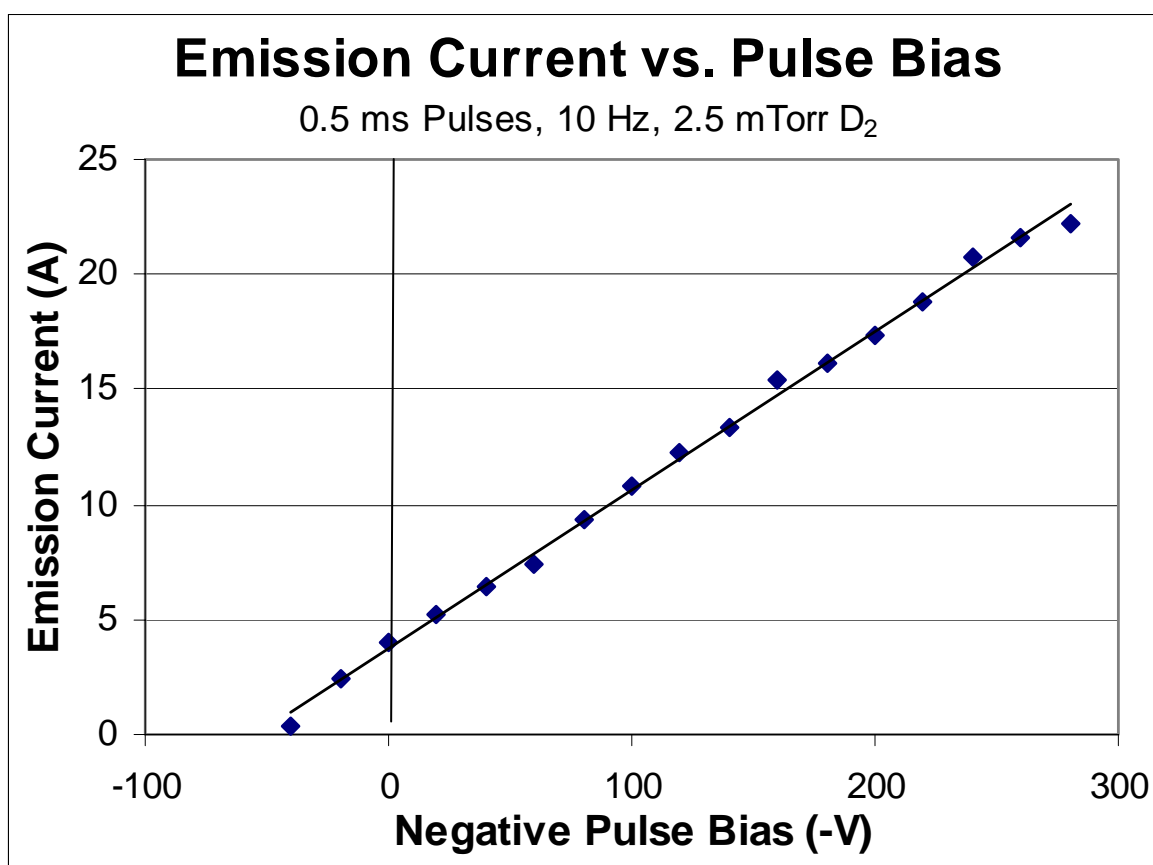


Figure 5.16: Emission current increases linearly with filament bias.

Deuterium gas pressure in the IEC chamber impacts both the filament emission current and the pulse current. Figure 5.17 shows the filament emission current as a function

of deuterium pressure. When no deuterium is present, the emission current is 3.5 A during the pulses. As deuterium is introduced, the emission current rapidly increases, reaching 19 A at 1 mTorr. The emission current continues to increase more slowly from 1-3 mTorr, and appears to be approaching a steady maximum value.

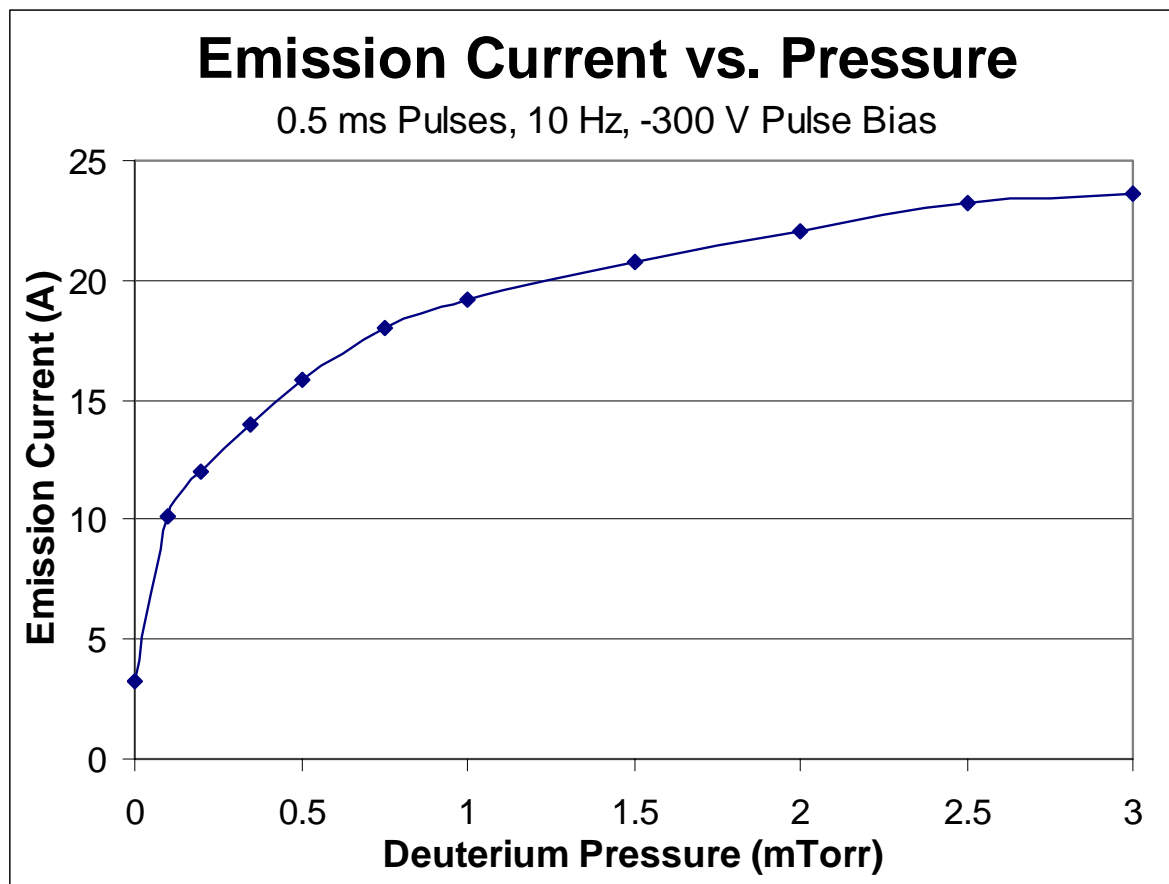


Figure 5.17: Emission current increases with increased deuterium pressure.

However, the pulse current behaves differently than the emission current as the deuterium pressure is increased. While the emission current is asymptotically approaching a maximum value between 1 and 3 mTorr, the pulse current is increasing nearly linearly. See Figure 5.18. Pulse current is largely generated by ions that drift from the source region into

the volume between the anode and cathode. The ion population in the source region is generated by electrons that bombard the background gas, so it is reasonable that the pulse current would increase roughly linearly with deuterium pressure.

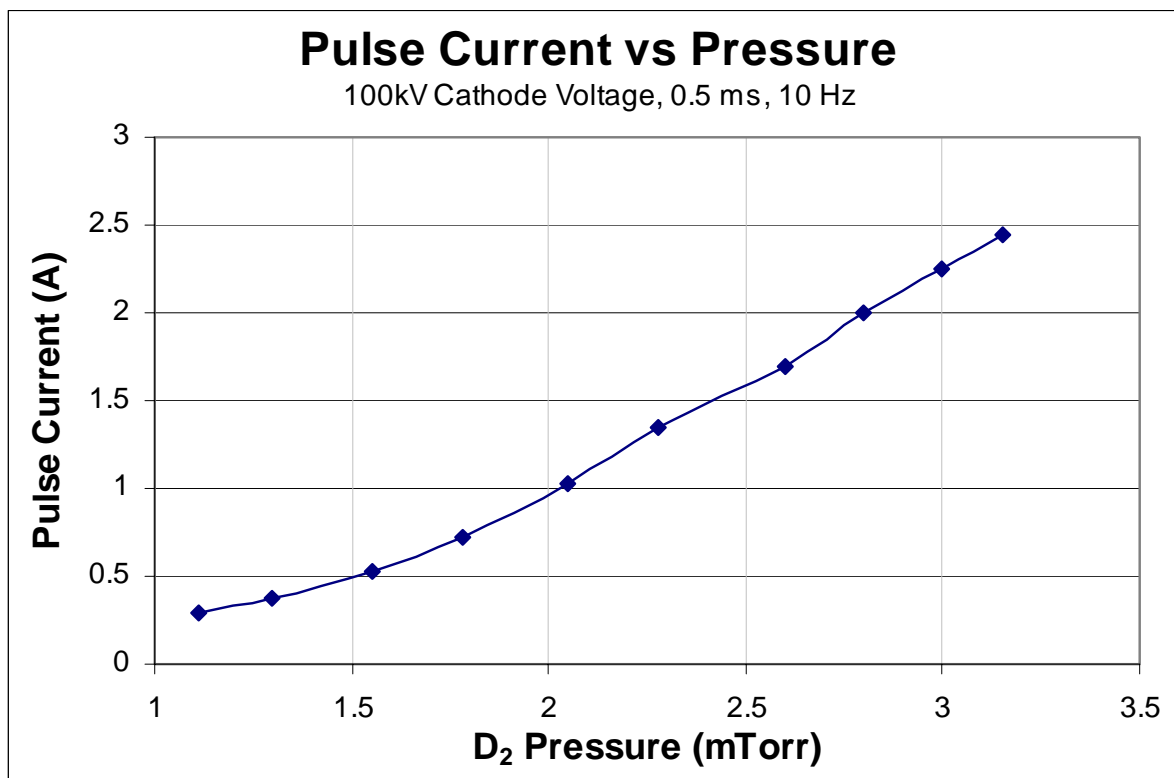


Figure 5.18: Pulse current increases with increased deuterium pressure.

5.2.2 Pulse Characteristics

Figure 5.19 shows a plot of the pulse current as a function of the filament emission current. The pulse current was found to be linearly dependent on the filament emission current at constant operational parameters.

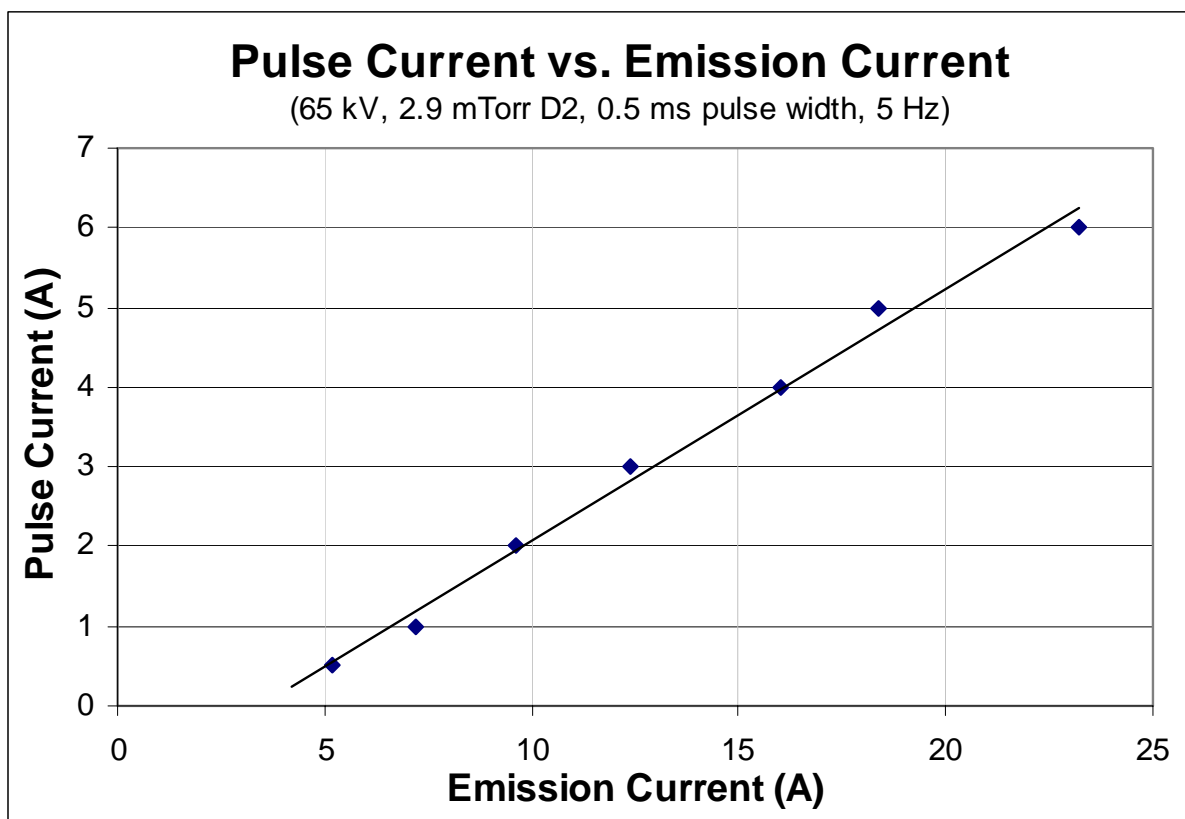


Figure 5.19: Pulse current scales linearly with filament emission current.

This relationship between pulse current and emission current is shown in Figure 5.20. The data in this plot were taken at constant ion source conditions. However, the pulse current that was drawn out of the source region varied linearly with the cathode voltage. This indicates that the plasma behaves approximately like a 23 k Ω resistor in this operating regime.

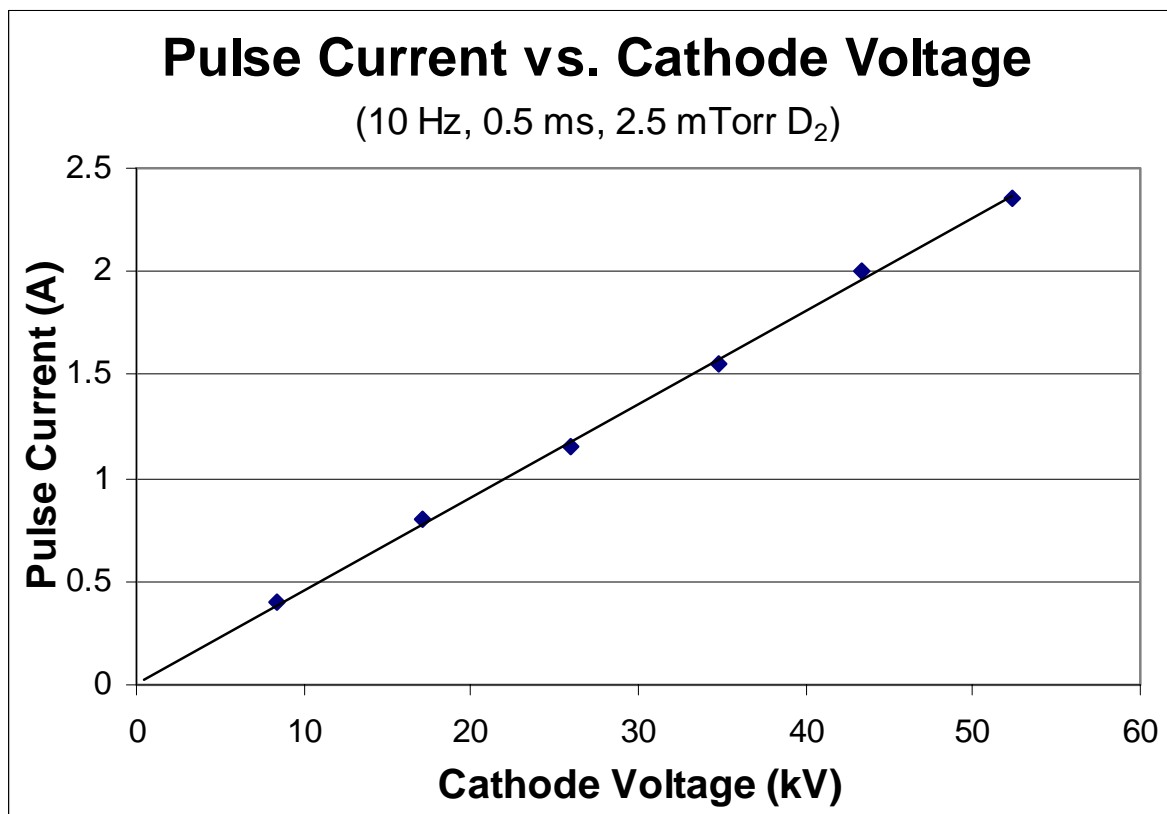


Figure 5.20: Pulse current scales linearly with cathode voltage.

The pulse width can be varied independently of other pulse parameters. Figure 5.21 shows current pulses with widths ranging from 0.1 to 1 ms. Since these pulses are not square, the widths are measured using the full width at half maximum (FWHM) and the amplitude is measured by averaging the values at each time step. The negative slope of the pulses is a result of sag on the capacitor that supplies current to the pulse. While this slope appears linear for the relatively short pulse widths shown in Figure 5.21, it is clearly exponential in the longer 5 ms pulse shown in Figure 5.22. This exponential behavior is consistent with simple RC circuit theory:

$$I = I_0 e^{-t/RC} \quad (5.2)$$

where R is the resistance of the circuit (~ 25 k-ohm), C is the capacitance (200 nF), and RC is the time constant of the discharging capacitor (~ 5 ms). This effect results in shorter pulses having higher average ion current and instantaneous neutron production, as discussed below. It is also noteworthy that as the pulse widths increase, the negative slope in the falloff of the discharge current increases as well, as shown in Figure 5.23.

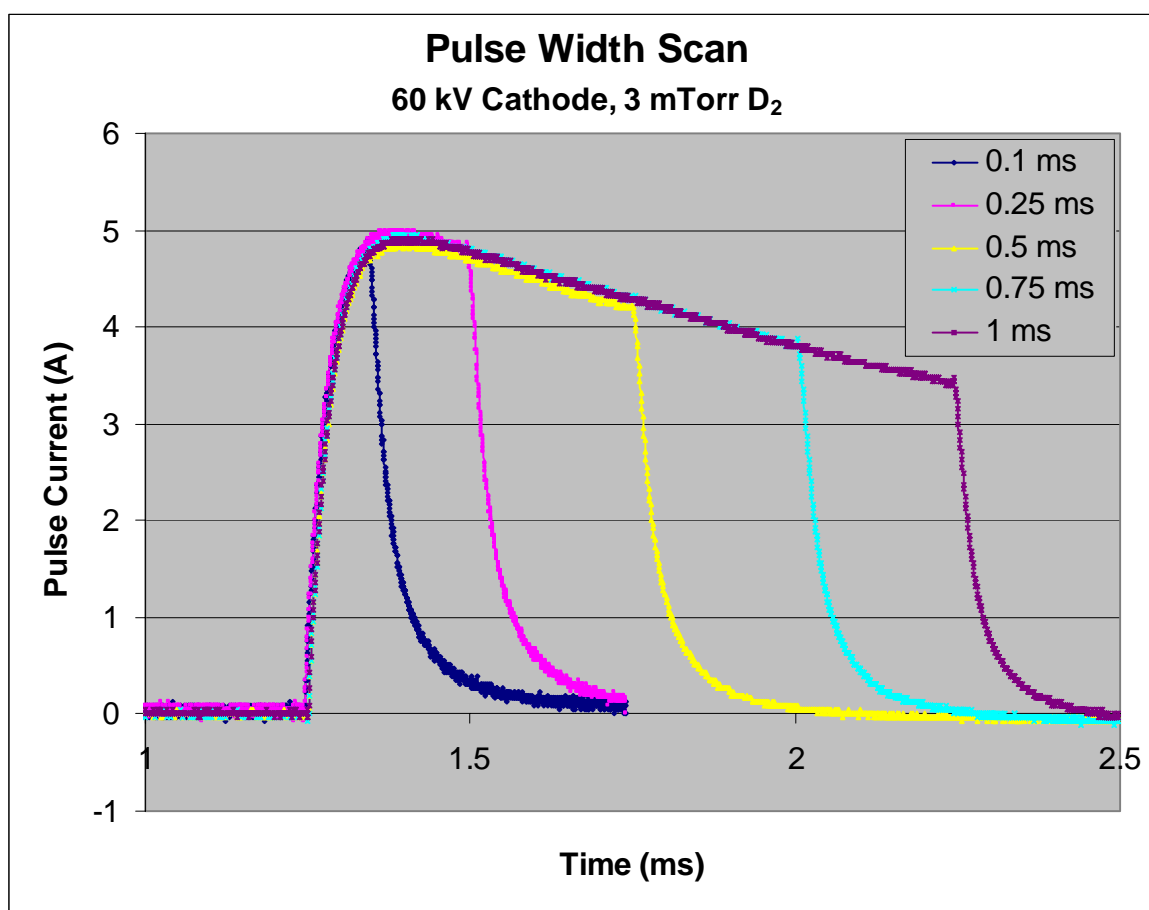


Figure 5.21: Shorter pulse widths yield higher average current.

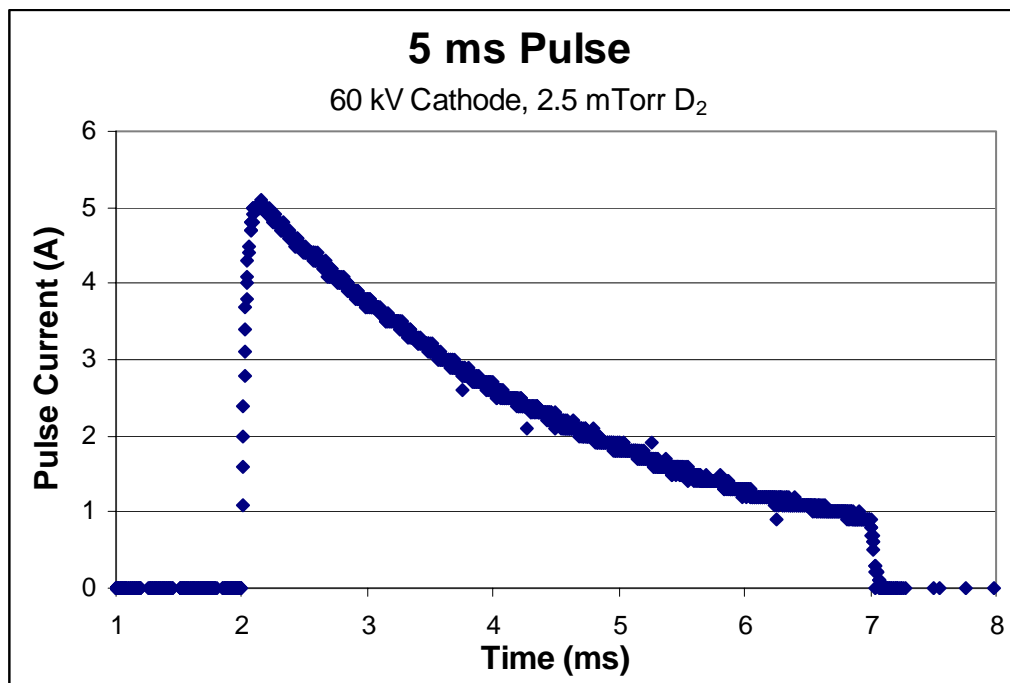


Figure 5.22: Exponential decay can be seen when pulse width is increased to 5 ms.

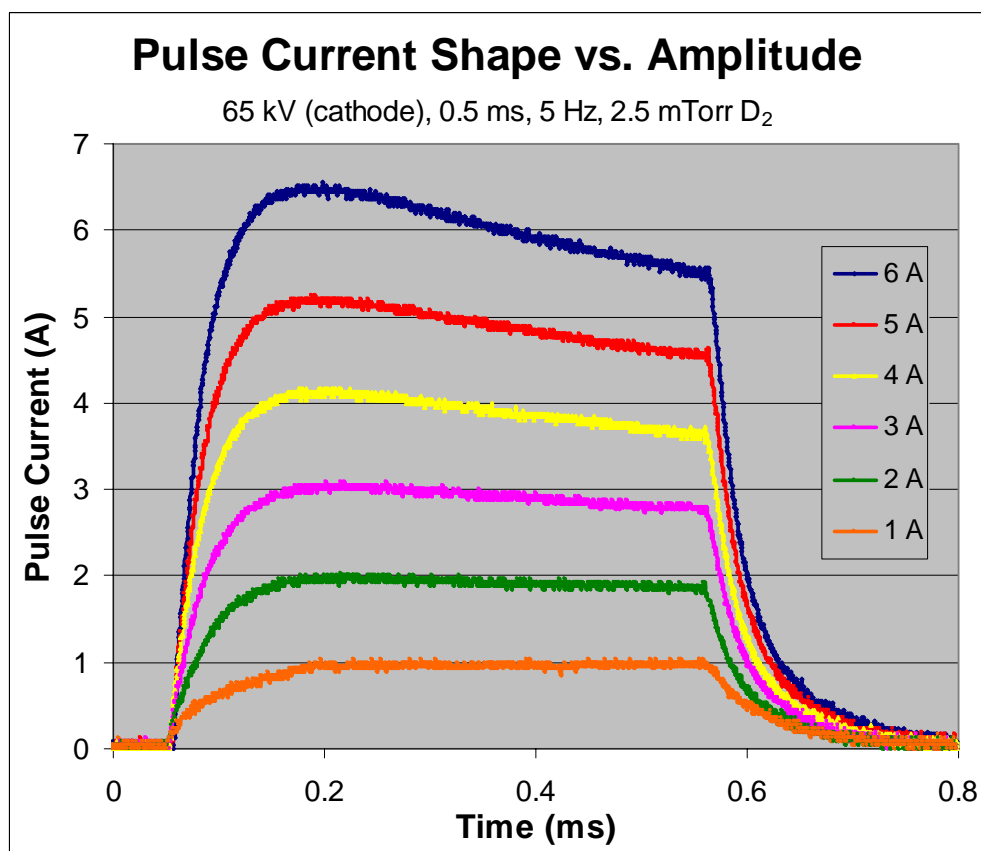


Figure 5.23: Measured pulse shapes at various pulse currents.

Varying the pulse frequency also had an effect on the pulse current. As shown in Figure 5.24, higher frequency pulsing resulted in less current during the pulses. This is again due to the high-voltage capacitor. After each pulse, the capacitor must be recharged by the power supply. However, as the frequency is increased, there becomes insufficient time for the capacitor to be fully charged between pulses. Therefore, most experiments were run at less than 10 Hz in order to allow the circuit to recover between pulses.

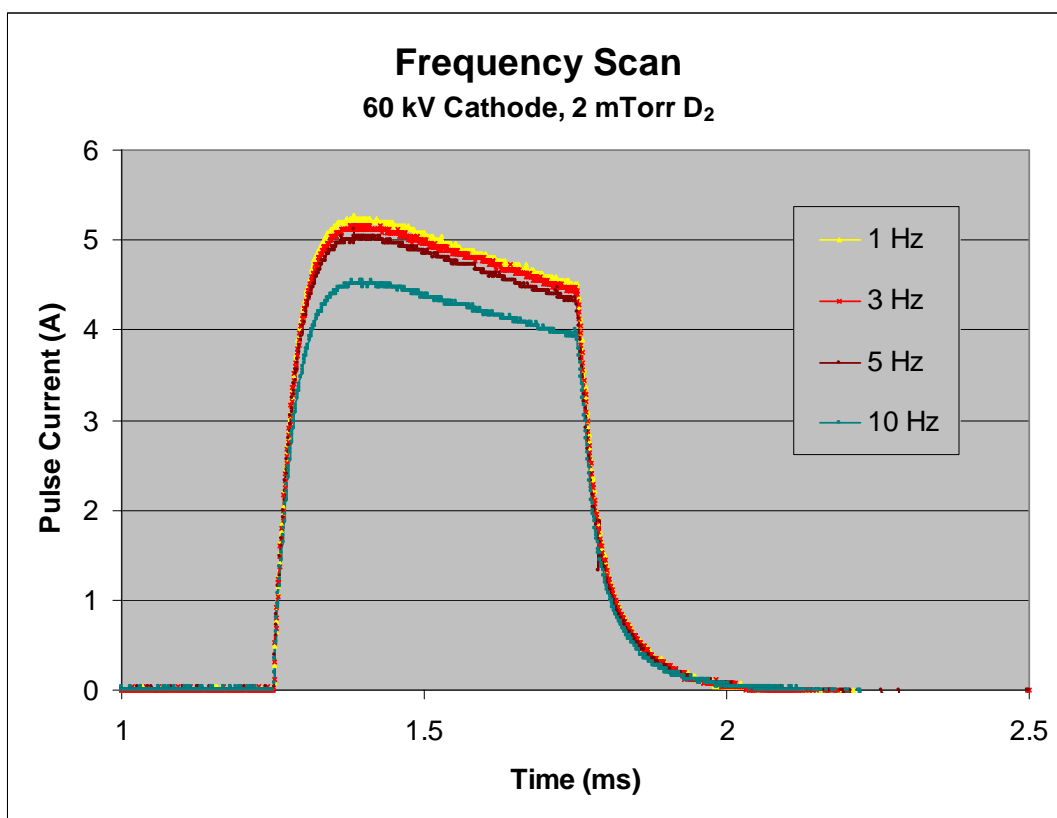


Figure 5.24: Pulse amplitude increases at lower frequencies.

5.2.3 Pulsed Neutron Production

Significant increases in the pulsed D-D neutron production rate have been made over the past two years on the Wisconsin IEC device. Numerous factors have led to the increased neutron production rate, including increased cathode voltage, increased pulse current, upgraded cathode/anode geometry, the introduction of a titanium coating, and shortened pulse widths. Each of these factors will be discussed in detail below.

The most significant factor that influences the neutron production rate is the cathode voltage. As shown in Figure 3.3, the D-D fusion cross section increases rapidly as the ion collision energy increases. Additionally, it was found that the maximum pulse current at given ion source conditions is directly proportional to the cathode voltage, as shown in Section 5.2.2. Much of the development work on this system went toward creating circuitry capable of stable operation at high voltage. Ultimately, cathode voltages as high as 120 kV were achieved during 500 μ s pulses at 5 Hz. Neutron rates are plotted as a function of cathode voltage for pulsed and steady state IEC operation in Figure 5.25. The pulsed neutron production rate increases in a manner similar to the steady-state neutron production rate.

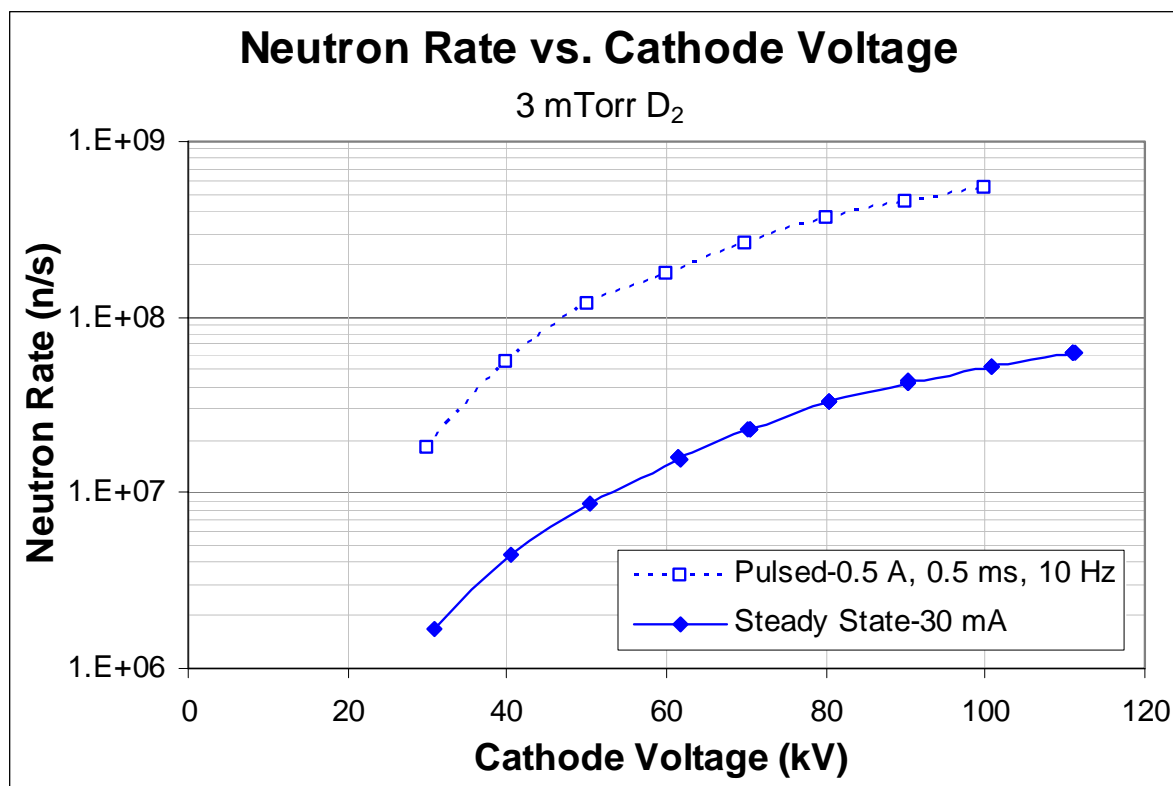


Figure 5.25: Pulsed neutron rate increases with cathode voltage in a manner similar to the steady-state neutron rate.

The ion current during the pulse also plays an important role in determining neutron rates. Steady-state experiments have shown the neutron rate exhibiting a linear dependence with cathode current, as shown in Figure 5.26. This behavior is consistent with the fusion generation being dominated by ion-neutral and fast charge-exchange neutral-neutral collisions.

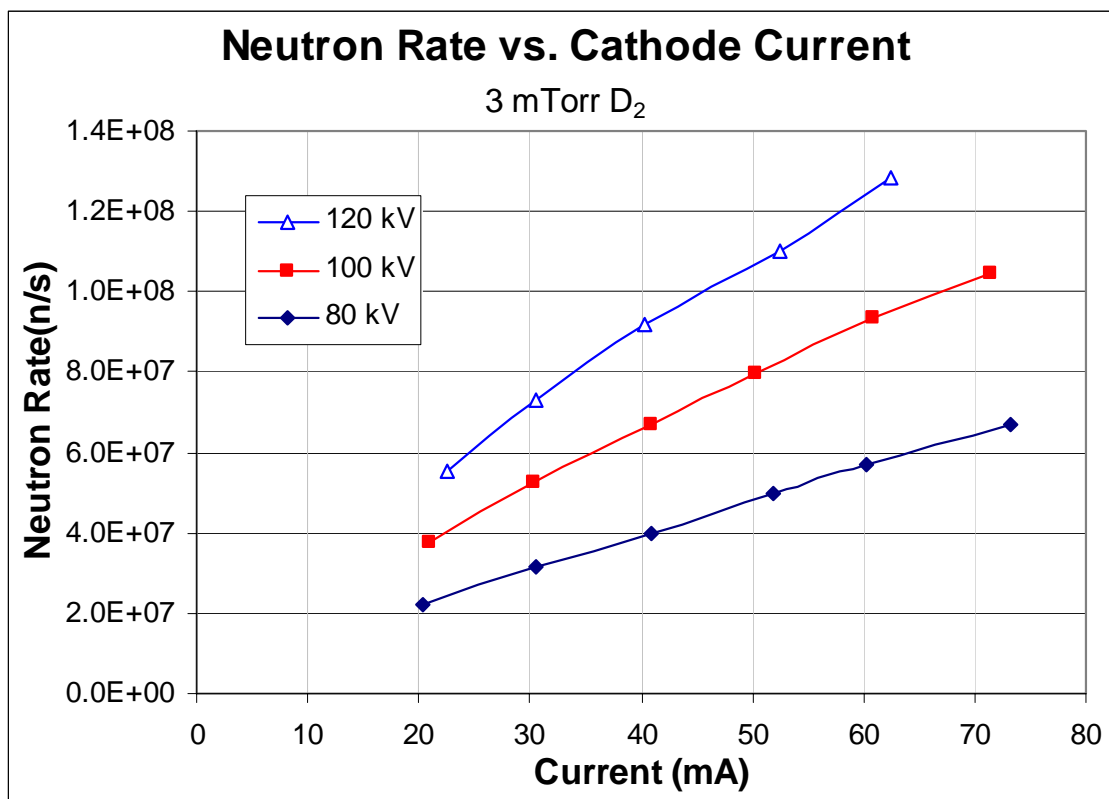


Figure 5.26: Steady-state neutron production rate increases linearly with cathode current.

At moderate current levels, pulsed IEC neutron rates exhibit similar behavior. Figure 5.27 shows the pulsed neutron rate plotted versus cathode current for two cathode voltages. As in the steady-state case, these neutron rates appear to increase roughly linearly with the cathode current. However, as the cathode current levels are increased further, there appears to be a loss mechanism. This less than linear increase is shown in Figure 5.28.

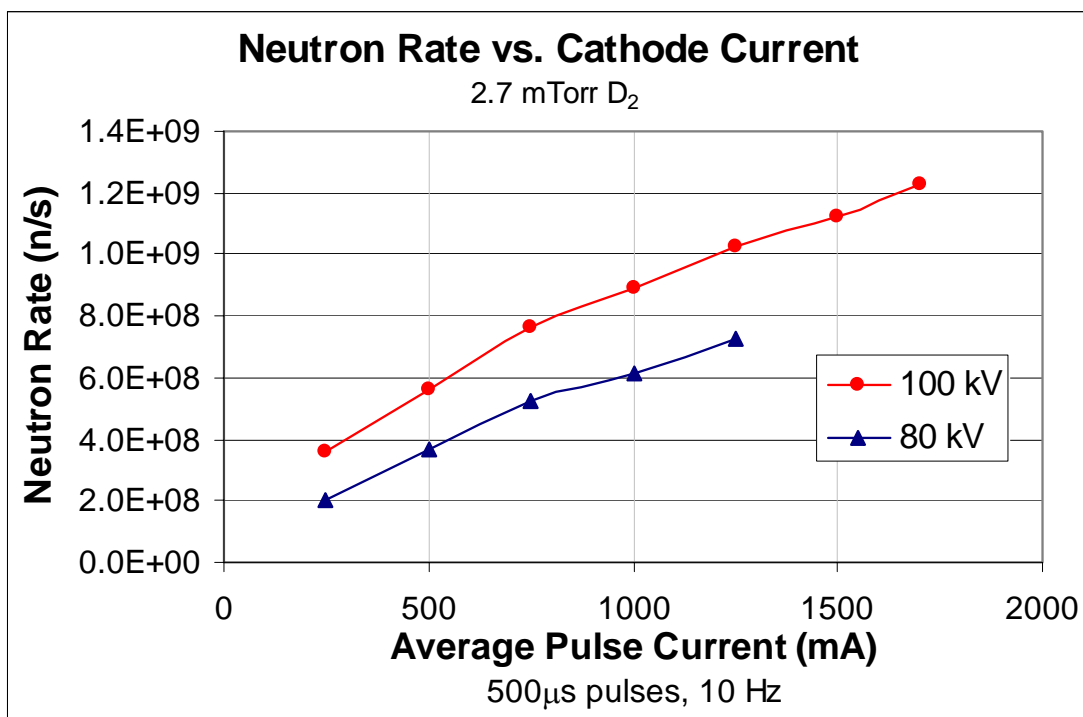


Figure 5.27: Measured pulsed neutron rate increases nearly linearly with cathode current at low pulse currents.

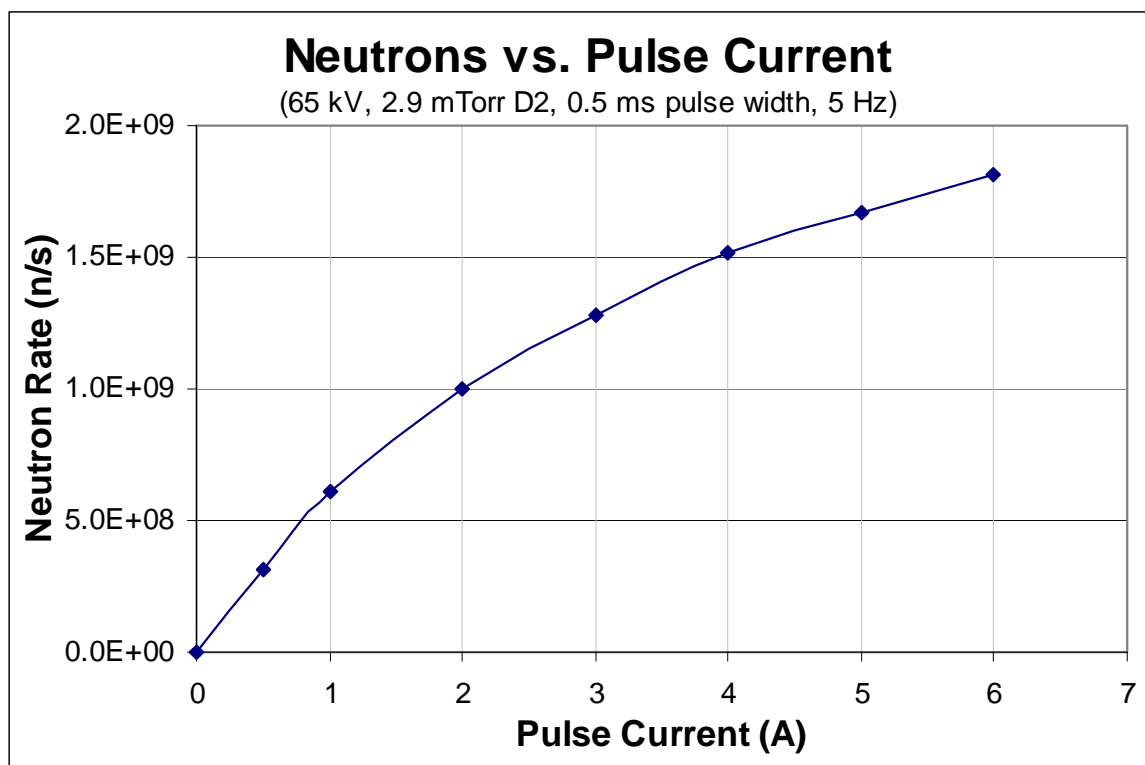


Figure 5.28: Measured pulsed neutron rate increases with cathode current.

As discussed in Section 4.1, the relative sizes of the cathode and anode were moved closer to each other in order to increase the steady-state neutron production rates. The motivation behind moving the cathode and anode closer together was to create a shorter path length for ions to travel while being accelerated to the cathode voltage. Since these ions experience parasitic charge-exchange reactions as they encounter background gas, shortening this path results in higher average ion energy at the cathode. This higher energy results in an increase of nearly a factor of two in neutron production rate at most cathode voltages, as shown in Figure 5.29. Using this cathode/anode configuration also increased the maximum steady-state D-D neutron production rate to 2.2×10^8 n/s. This neutron rate was recorded with a cathode voltage of 165 kV, a steady-state current of 68 mA, and a deuterium gas pressure of 3.1 mTorr.

A secondary advantage of moving the cathode closer to the anode is an increase of the Child-Langmuir space charge limit between the concentric spheres [3]. While this is not a factor for steady-state operation, the ion currents drawn during pulsed operation are approaching these limitations. Switching to the 20 cm cathode and 40 cm anode increased the maximum pulse current in the UW-IEC device.

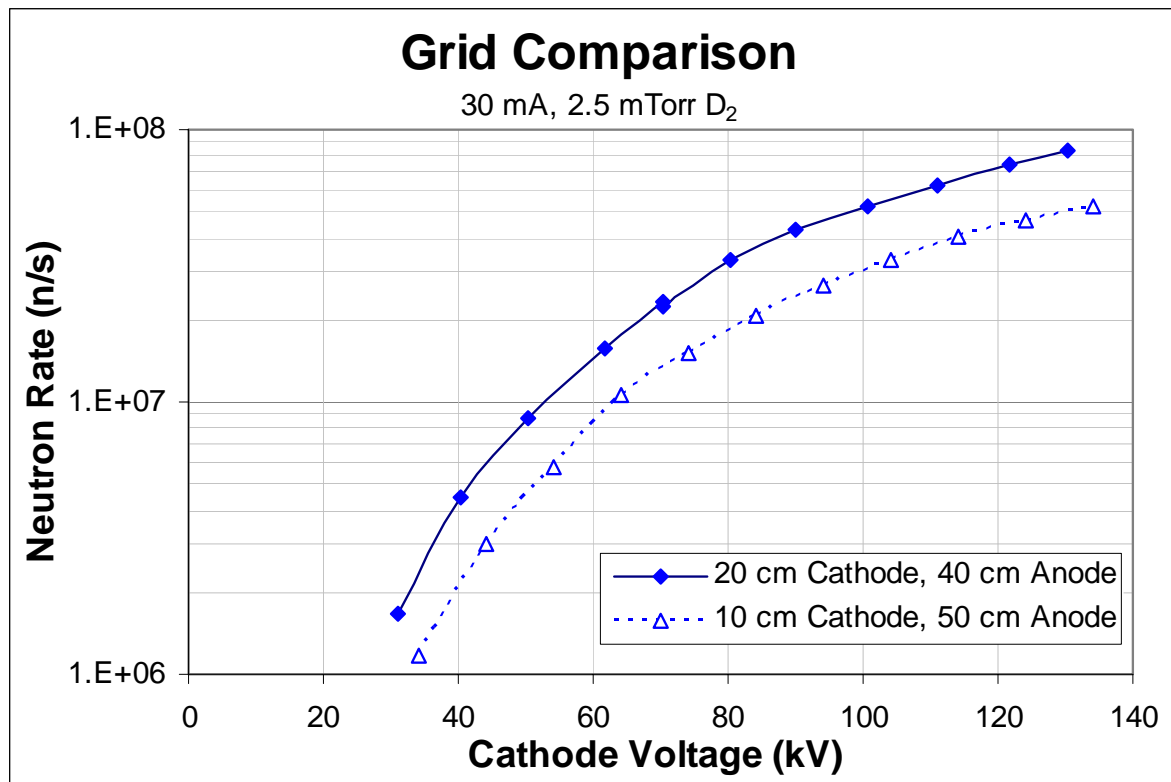


Figure 5.29: Measured neutron production rate of 20 cm cathode/40 cm anode configuration is nearly twice that of 10 cm cathode/50 cm anode.

A final factor observed to dramatically impact neutron rates was the pulse width. Figure 5.30 plots the neutron rate as a function of pulse width. The fusion rate increases as the pulse width is decreased because the average ion current is larger during the shorter pulses. This effect can also be seen in Figure 5.21 and is due to the sag on the high-voltage capacitor. Increasing the capacitance of this component would cancel out this effect and result in more uniform neutron production at varying pulse widths.

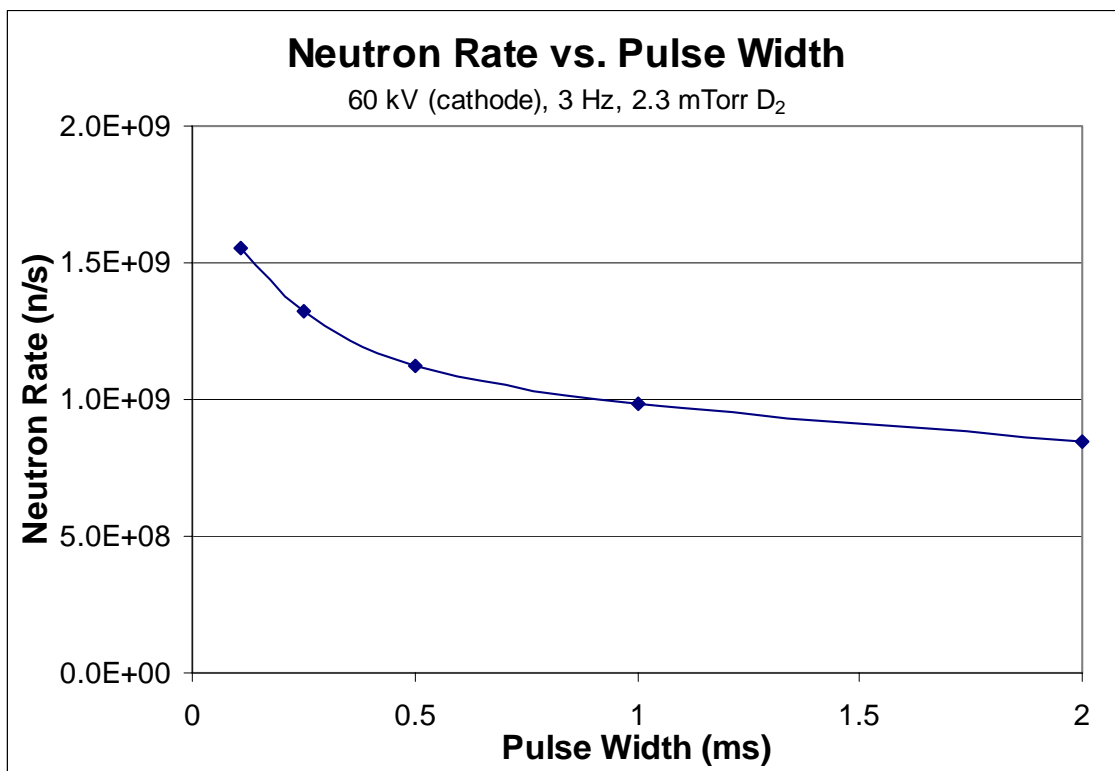


Figure 5.30: The measured instantaneous neutron production rate drops with increasing pulse width.

Each of these factors was optimized in order to generate the maximum neutron production rate possible in the UW-IEC device. Figure 5.31 shows a voltage scan where the ion source conditions are kept at maximum conditions, with an emission current of 32 A. Deuterium pressure was held at 2.5 mTorr. Pulses were generated at 5 Hz with a FWHM of 110 μ s. With these conditions, a maximum neutron production rate of 4.7×10^9 n/s was achieved at 94 kV and 4.8 A.

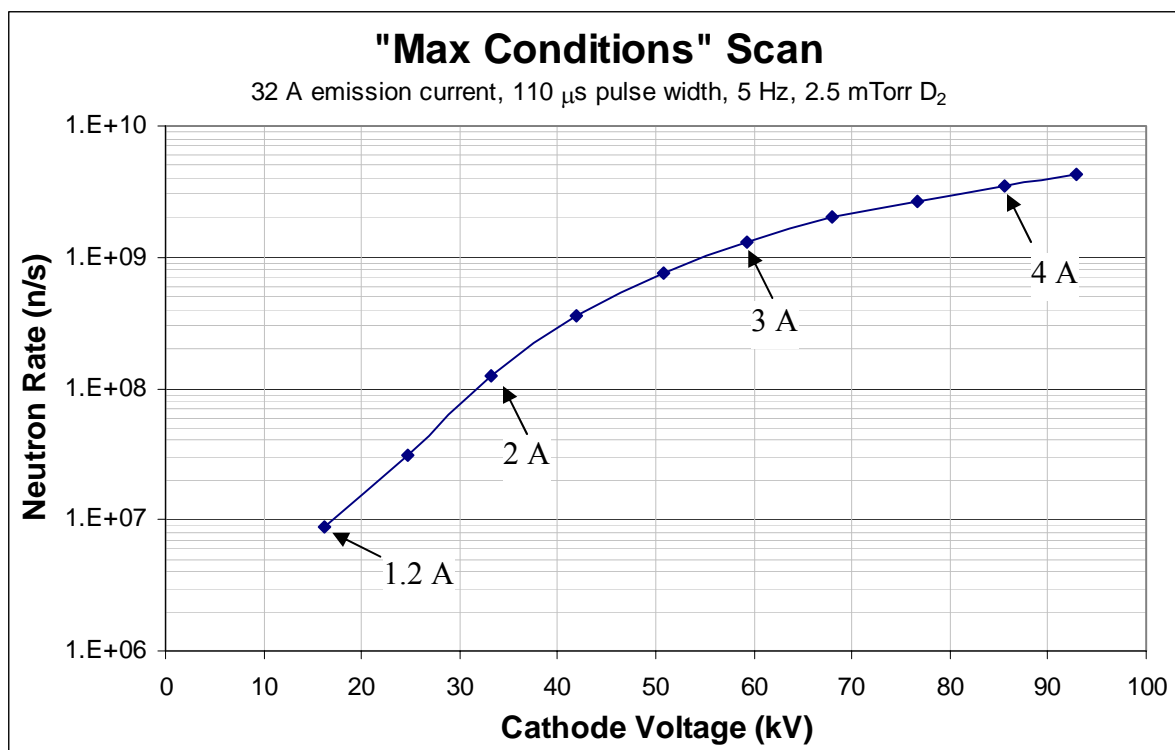


Figure 5.31: Neutron production rate versus cathode voltage at optimum conditions for neutron production. Note that pulsed current and neutron production increase with increasing cathode voltage.

One factor that has been implemented on the UW-IEC device during steady-state experiments, but has not yet been used for pulsed experiments, is the addition of a titanium coating on the anode grid and outer aluminum wall. Titanium was chosen for its ability to hold onto hydrogen species in its matrix. Preliminary experiments have been performed where a minimum of 0.3 μ m layer of titanium was deposited on the anode and wall surface. Deuterium gas was introduced during deposition to saturate the titanium. This trapped deuterium then acts as a target for fast neutral atoms resulting from charge exchange reactions. As shown in Figure 5.32, the addition of the titanium and trapped deuterium has

increased the steady-state fusion production between 35 and 70 percent, depending on the cathode voltage. It is expected that pulsed rates will increase in a similar manner.

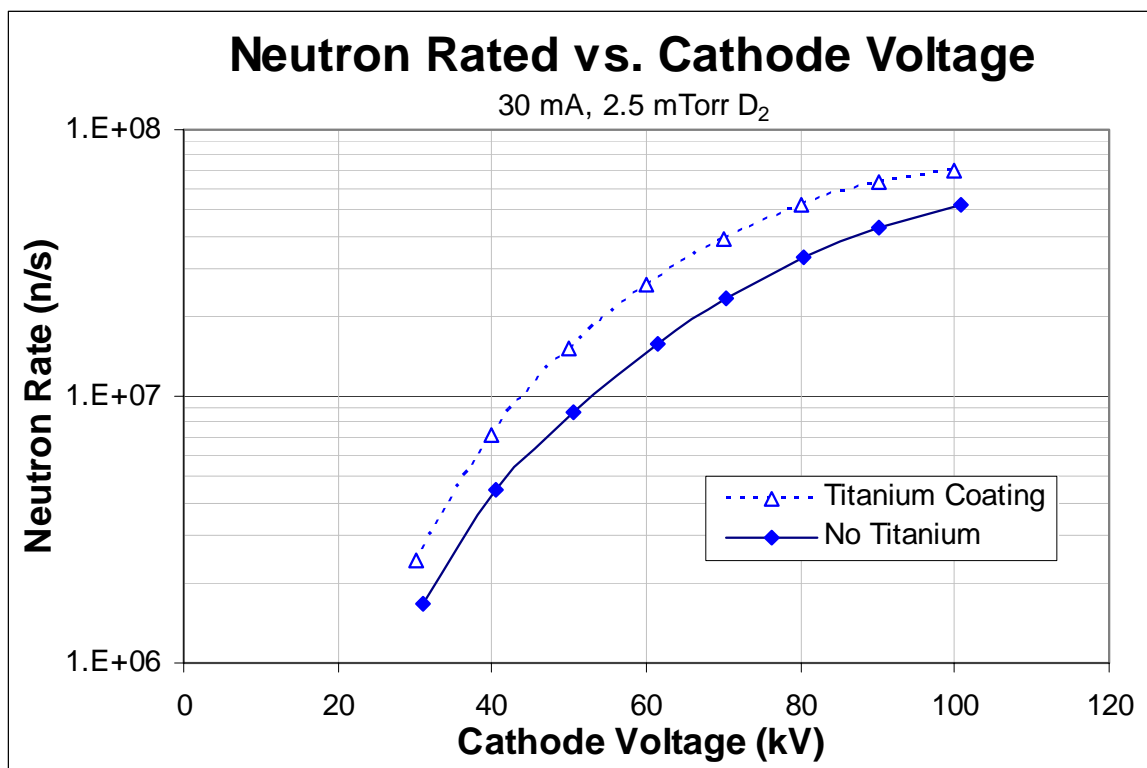


Figure 5.32: Using a Ti coating on the inner chamber surface increases the measured steady-state neutron production rate.

A final consideration for neutron production is fusion counts that occur between IEC pulses. Fusion reactions are possible because the cathode is held at high voltages between pulses. If the pressure is too high for the cathode voltage, any source of ionization, such as induced radioactivity or cosmic rays, in the IEC chamber will result in a cascade of ions and electrons known as a Paschen breakdown [4]. Although these neutrons are not counted when determining the pulsed fusion rates, they are a cause for concern with HEU detection, as discussed in Section 3.3. Therefore, great care was taken in determining which operating

regimes lead to high levels of these neutrons. Figure 5.33 shows the steady-state neutron production rate for an IEC device with a 20 cm cathode and 40 cm anode at 2.7 mTorr D_2 and no filaments as a function of cathode voltage. Neutron production was less than 6×10^2 n/s below 60 kV. However, above 60 kV the neutron production rate rises rapidly. This increase is due in part to the increased fusion cross-sections at higher energy. However, the primary factor is the high voltage on the cathode causing ionization cascades, resulting in fusion reactions. These cascades can be initiated by any ionization source, such as an arc or a cosmic ray, but the high voltage is needed to turn the single ionization event into a cascade.

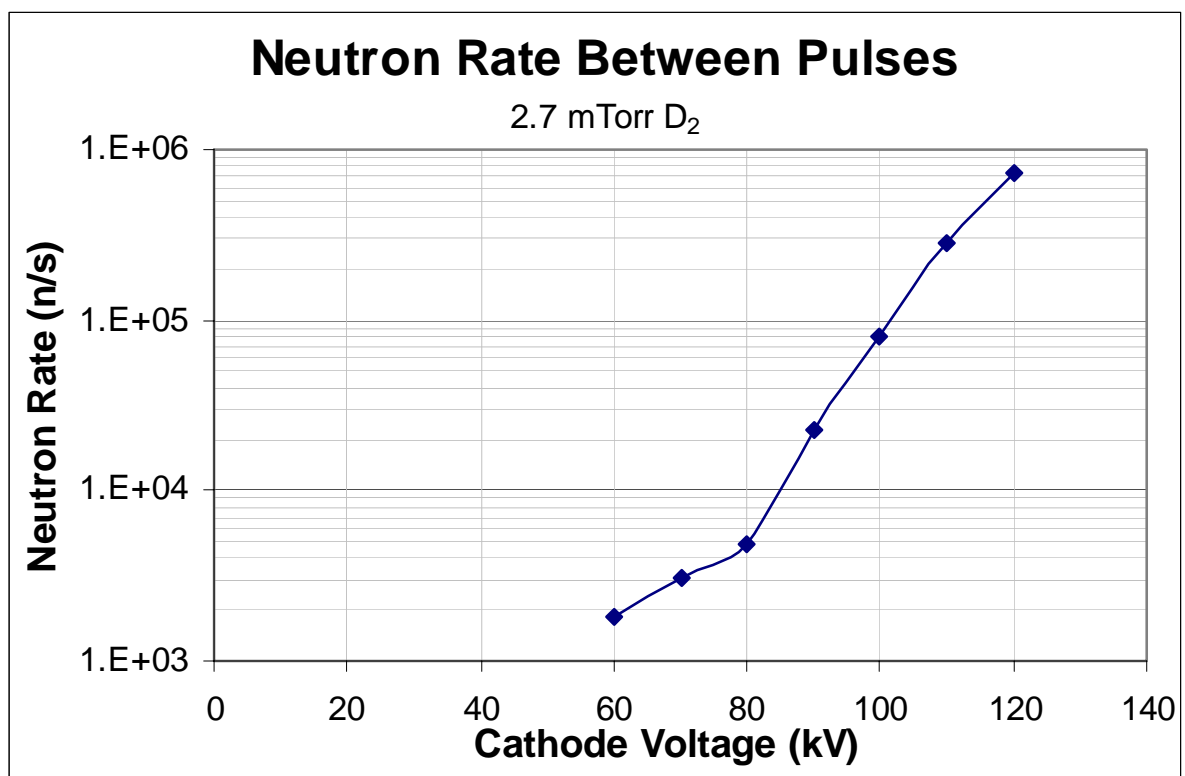


Figure 5.33: Measured steady-state neutron rate without filaments increases rapidly as cathode voltage is increased.

The cathode was then held constant at 100 kV with no filaments operating. As seen in Figure 5.34, the neutron rates below 3 mTorr D_2 were below 1×10^5 n/s (four orders of magnitude below the pulsed fusion rate at that voltage). However, by 3.25 mTorr the neutron rate jumps to 1×10^7 n/s as the IEC enters a “glow discharge” mode of operation. This “glow discharge regime requires no ionization source other than the high voltage on the cathode. In order to ensure these neutrons were kept as low as possible, all pulsed experiments were run below 3 mTorr.

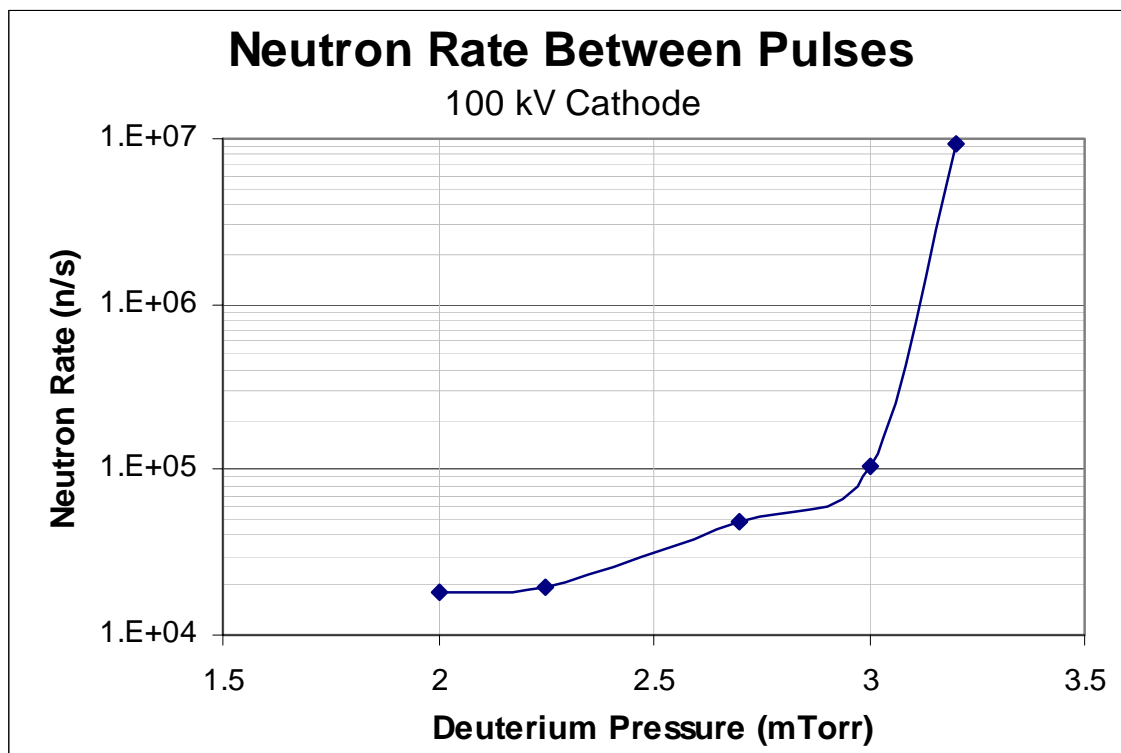


Figure 5.34: Measured steady-state neutron rate without filaments increases as deuterium pressure is increased.

5.3 Highly Enriched Uranium Detection

Initial experiments were performed by irradiating the HEU sample in the apparatus described in Section 4.2.2 with a steady-state neutron flux. Figure 5.35 shows neutron counts after shutdown for four cases [5]. In each case, the IEC device was run at 130 kV, 60 mA and 2.6 mtorr D₂, producing neutrons at $\sim 1.5 \times 10^8$ n/s. An 11 gram sample of 93 percent enriched uranium (10 grams U-235) was placed in the apparatus described in Chapter 4 approximately 50 cm from the center of the IEC device. As noted in the plot, the IEC device was run for 2 minutes, 1 minute, and 30 seconds with HEU present, and for 2 minutes with no HEU present in the system. After shutdown, neutron counts were recorded every 5 seconds. It is clearly seen that delayed neutron production increased as the total fusion neutron fluence was increased.

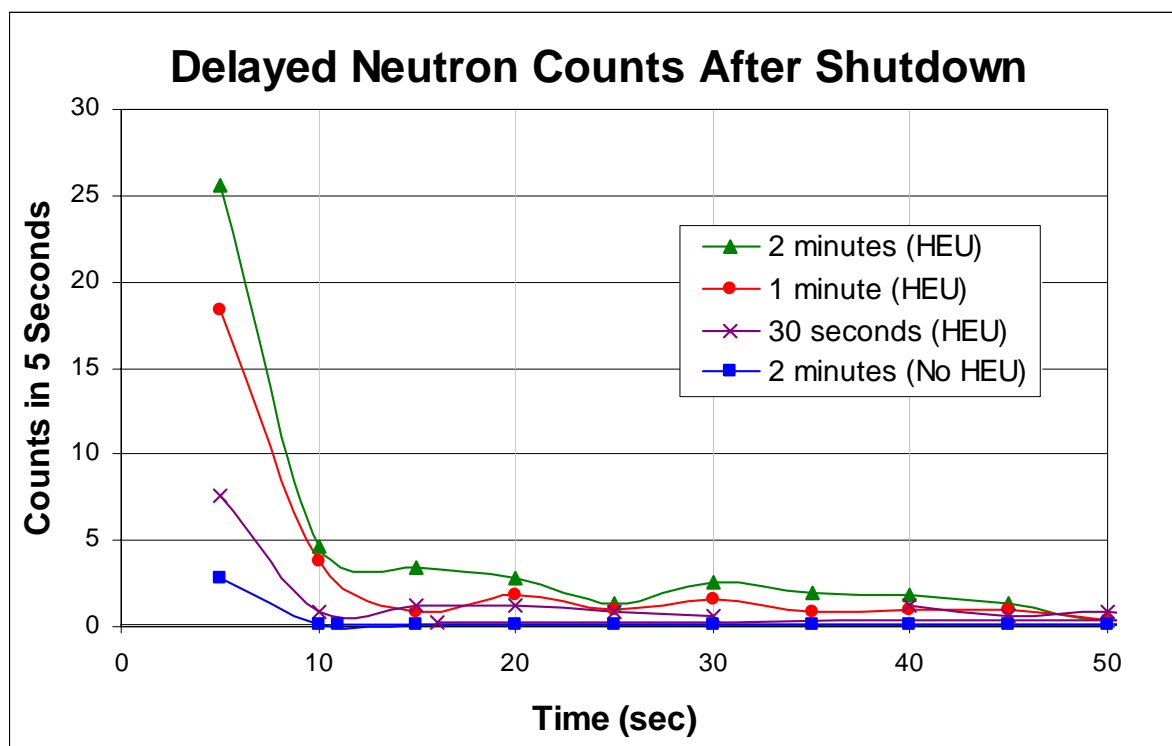


Figure 5.35: Delayed neutron counts after steady-state IEC operation [5].

When the initial experiments to detect delayed neutrons between fusion pulses were performed, it was found that a steady-state fusion level exists between pulses, as described in Section 5.2. The HEU detection hardware was then modified to lower the level of detected neutrons between pulses with no HEU present. A top-down view of this modification is shown in Figure 5.36. The two ^3He detectors are shielded against the fusion neutrons with multiple layers of borated polyethylene. This shielding configuration was experimentally verified to reduce detected neutrons by a factor of 10. The HEU sample has no borated material in front of it, but still has paraffin to moderate the fusion neutrons. A remotely-operated motor was used to insert or remove the HEU sample during irradiation experiments. This allowed continuous operation of the IEC device and a more consistent neutron flux.

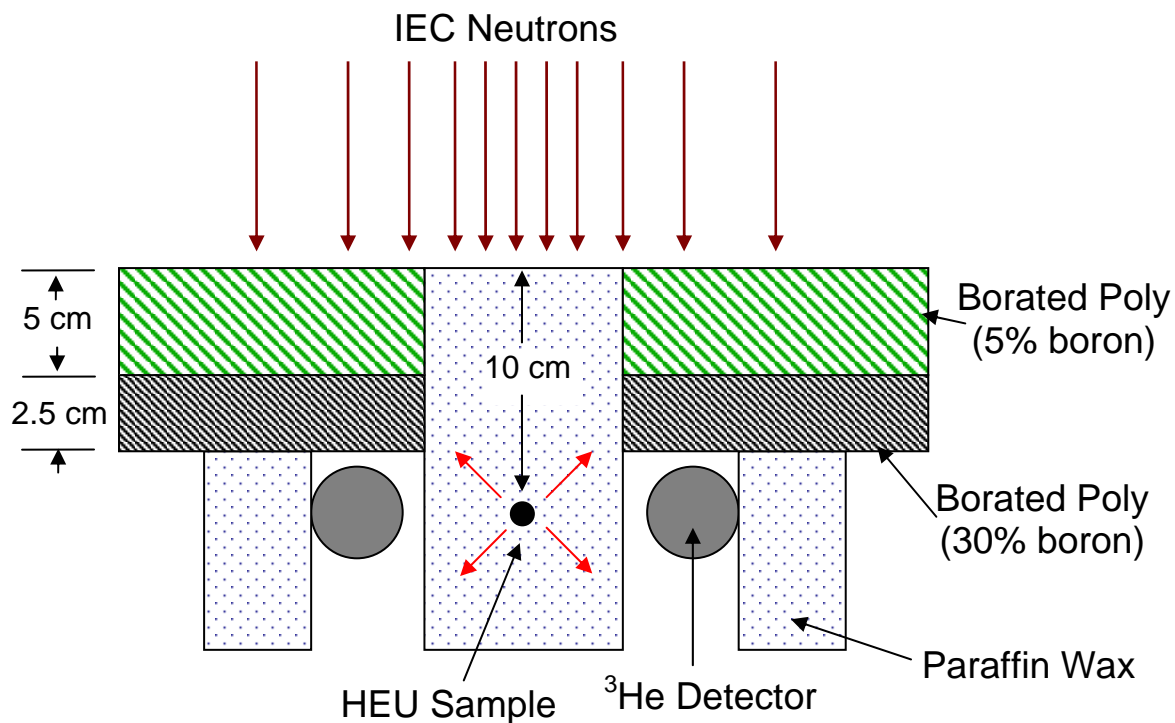


Figure 5.36: Modified HEU detection module (not to scale) shields detectors while allowing neutrons into HEU sample.

Using this detection apparatus, neutrons were counted during pulsed operation. Figure 5.37 shows neutron counts as a function of time during and between 10,000 0.5 ms IEC fusion pulses. The open circles represent counts without the HEU sample present, while the closed circles were taken with the HEU present. While there is some scatter in the data, the delayed neutron population is clearly elevated above the background counts.

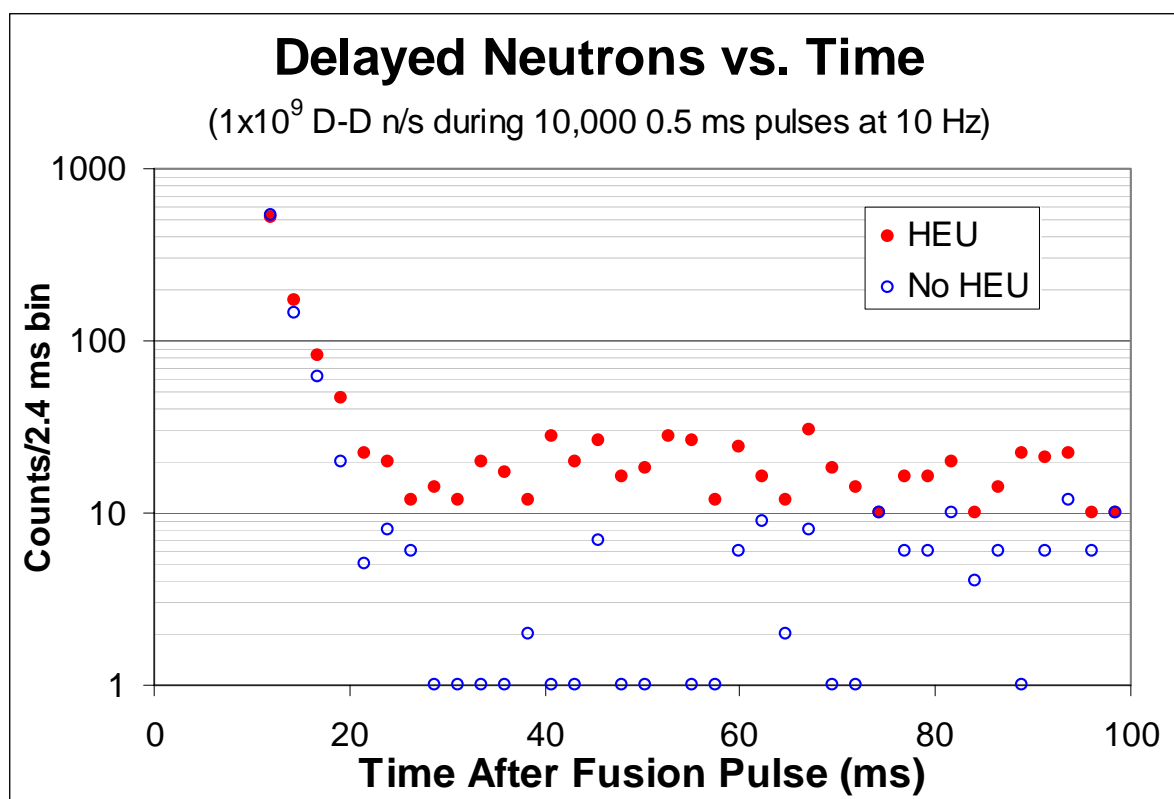


Figure 5.37: Increased levels of neutrons are measured when HEU is present.

While this type of plot provides visual evidence of the presence of HEU, it does not give quantitative information about the levels of HEU in the system. To acquire quantitative information from this data, the counts from 25 ms (after the thermal background subsides) to 100 ms were summed. This data can then be compared to background to make a determination as to whether HEU is present in the system.

Figure 5.38 shows this summed data for various pulsed fusion neutron rates. These neutrons were generated during 500 μs pulses at 10 Hz. As expected, there is a linear relationship between the fusion neutron population and the induced delayed neutron population. However, the trend does not fit through zero, as would be expected. This is likely due to the small sampling size and the manner of background subtraction used to collect the data. These data are re-plotted as a function of fusion neutron flux at the HEU sample in Figure 5.39. In this plot, the minimum flux needed to detect the 11 gram sample of 93 percent enriched uranium (10 grams U-235) with 2,000 IEC pulses is calculated to be $1.5 \times 10^4 \text{ n/cm}^2\text{s}$. Coincidentally, this corresponds to a minimum fluence of $1.5 \times 10^4 \text{ n/cm}^2$ at the HEU sample.

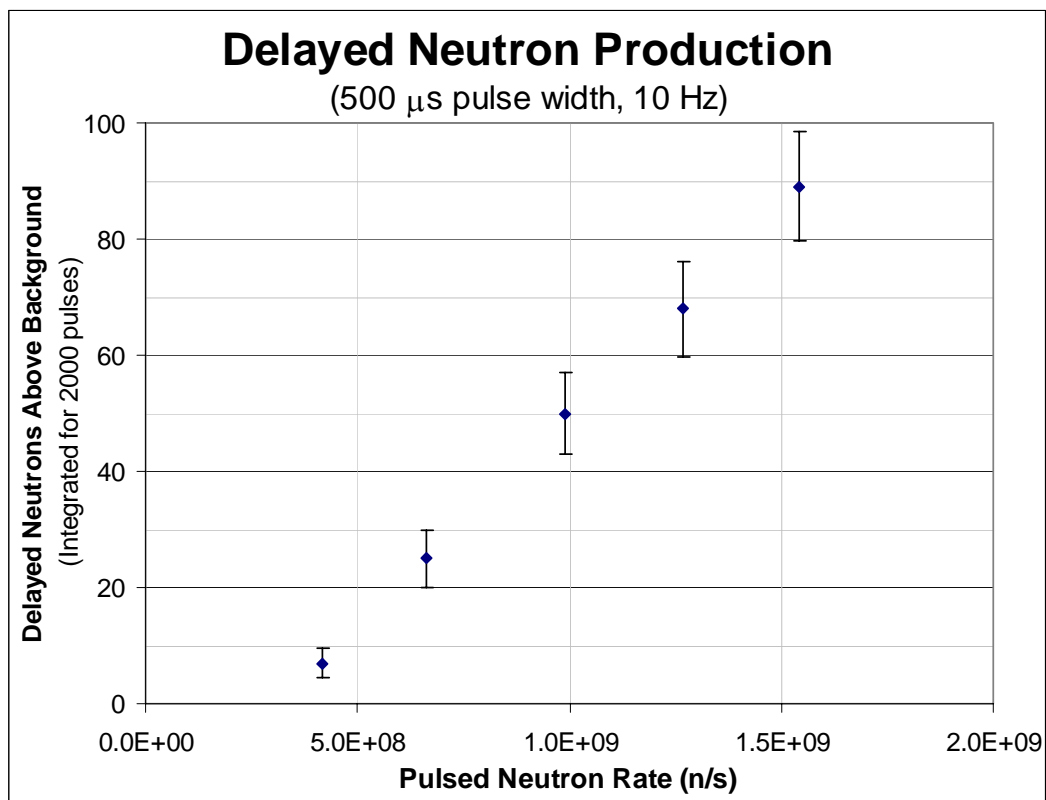


Figure 5.38: Delayed neutron production measured as a function of IEC neutron rate.

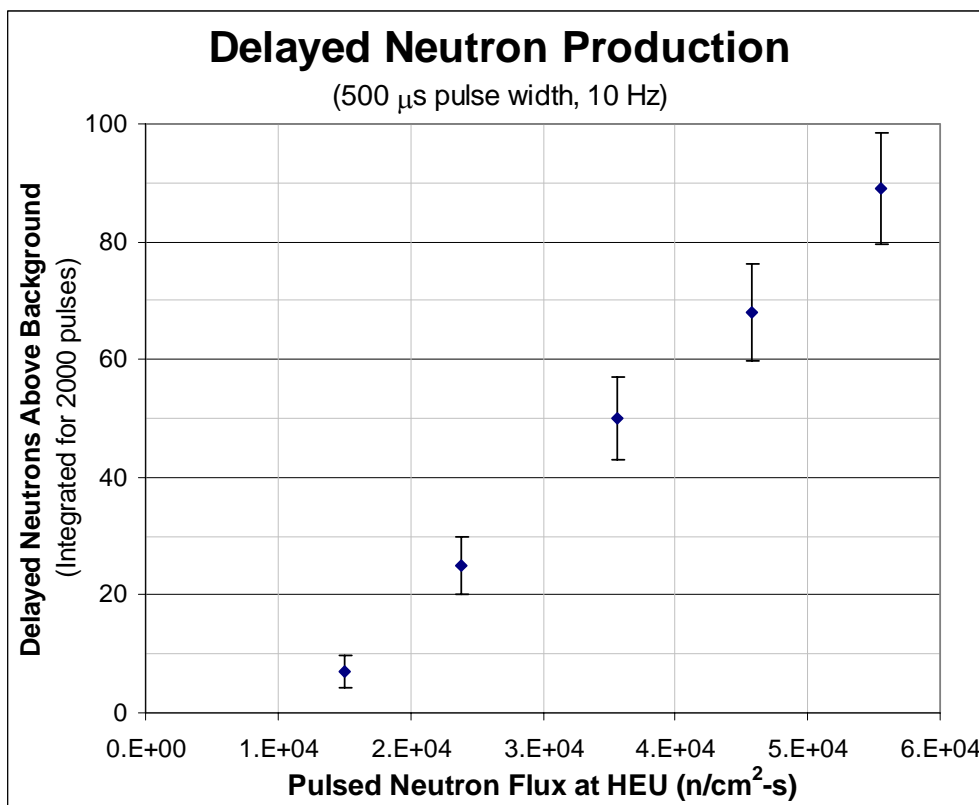


Figure 5.39: Delayed neutron production as a function of IEC neutron flux at the HEU.

Using this experimental data, the maximum distance from the IEC neutron source to the HEU samples was calculated for each neutron production level. This maximum distance of detection is plotted in Figure 5.40 as a function of pulsed D-D neutron rate for both the data taken during this experiment and for projected D-D rates that have been demonstrated using this device. For pulsed D-D neutron rates of 4.7×10^9 n/s, which is the current maximum production level, the maximum distance between the IEC device and the HEU sample that will provide detectable counts is 160 cm. However, this distance will change for different detector settings and geometries.

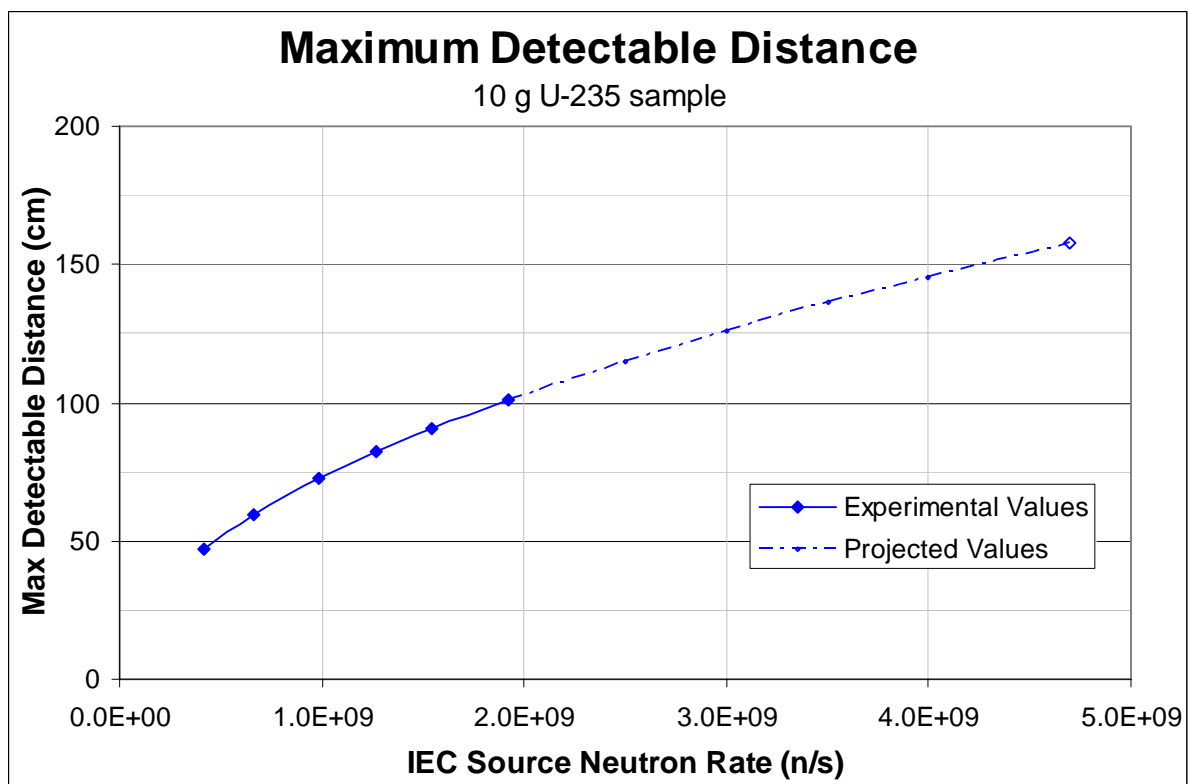


Figure 5.40: Maximum detectable distance from the IEC device to the HEU sample.

As shown in Figures 5.33 and 5.34, the present IEC neutron source generates a continuous background fusion rate as well as the pulsed fusion rate. This continuous neutron source acts as a significant source of noise in the detection system. The signal to noise (S/N) ratio for HEU data taken between 50 kV and 90 kV is plotted in Figure 5.41. At low voltages, the noise levels are very low. As the voltage is increased to 65 kV, the fusion neutron rate, and therefore the delayed fission neutron rate, increases faster than the background noise. Therefore the S/N increases rapidly, reaching as high as 6.2. However, since the background rate increases rapidly as the IEC cathode voltage is increased (as shown in Figure 5.33), the ratio of HEU neutron counts to background neutron counts decreases as

the cathode voltage increases above 65 kV. This increase in background is due not only to the increased fusion cross-sections at higher energy, but also to the constant high voltage on the cathode between pulses causing ionization cascades, resulting in fusion reactions between pulses. These cascades can be initiated by any ionization source between pulses, such as an arc or a cosmic ray, but the high voltage is needed to turn the single ionization event into a cascade. This effect has serious implications for future study in this area, and is discussed further in Chapter 6.

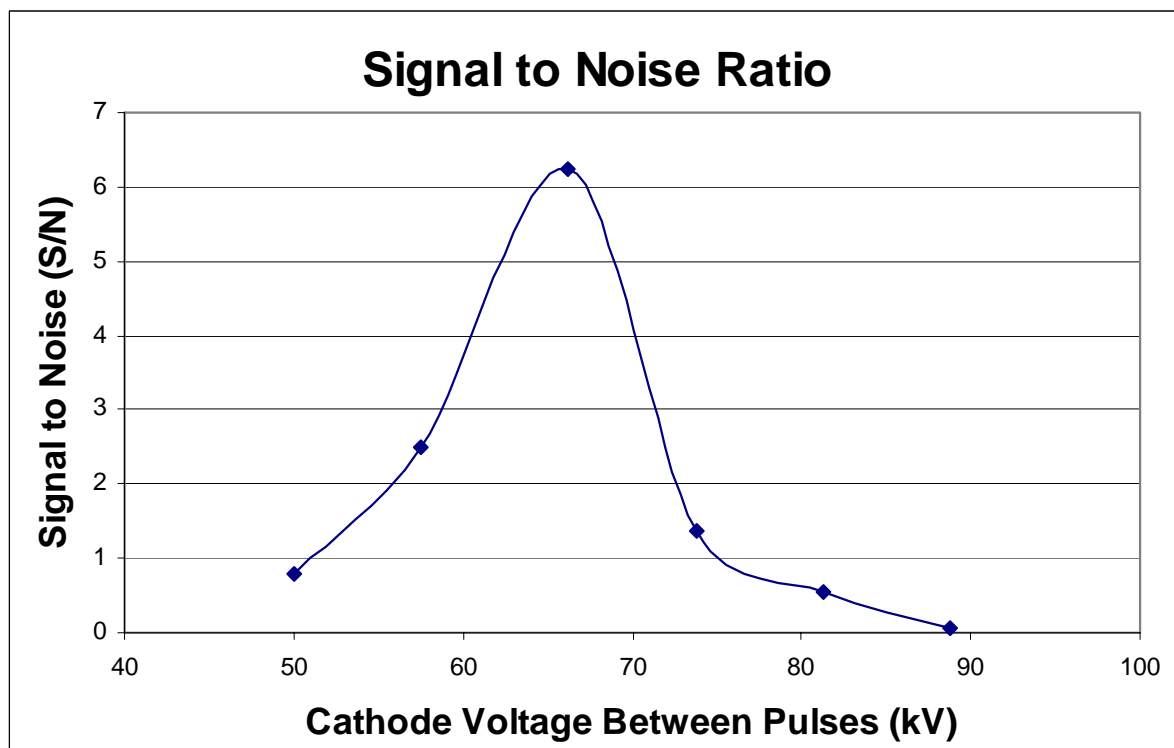


Figure 5.41: Signal to noise ratio of HEU counts taken between 50 kV and 90 kV.

5.4 Pulsed Helium Implantation in Tungsten

Previous work by Cipiti [6], Kulcinski [6,7], and Radel [7], including that discussed in Sections 5.5 and 5.6, has shown extensive surface damage resulting from steady-state implantation of helium on tungsten. However, ICF reactors will face a simultaneous bombardment of helium and hydrogen isotopes, which could affect the way helium damage occurs. These reactors will also be operating in a pulsed mode, with pulse widths of $\sim 10 \mu\text{s}$ and frequencies of $\sim 5 \text{ Hz}$ [8]. This thesis evaluates the effects of simultaneous helium and deuterium implantation and of performing helium implantation in a pulsed mode.

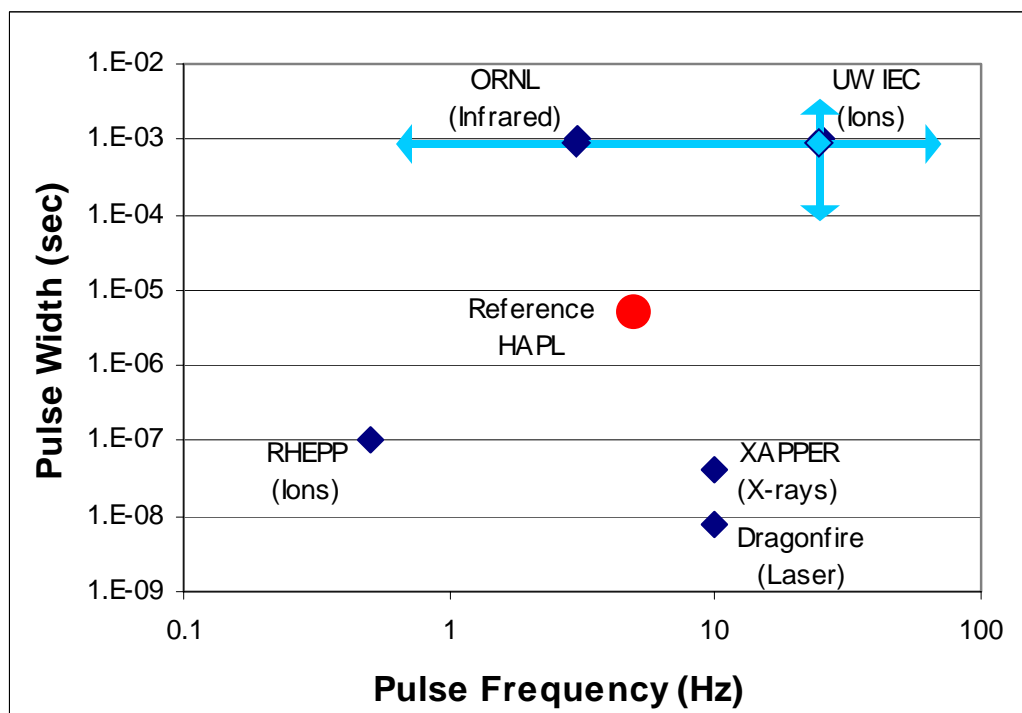


Figure 5.42: Pulse capabilities of selected HAPL experimental facilities.

As discussed in Chapter 1, this research was performed as part of the High Average Power Laser (HAPL) program. The HAPL program also incorporates other experiments that are studying the effects of pulsed irradiation on tungsten surfaces, including the RHEPP facility at Sandia National Laboratories [9], the XAPPER facility at Lawrence Livermore National Laboratory [10], the Dragonfire facility at the University of California-San Diego [11], and an infrared facility at Oak Ridge National Laboratory [12]. Figure 5.42 shows the pulse widths and frequencies for each of these experiments relative to the reference HAPL pulse characteristics. Initial IEC experiments at the University of Wisconsin operated at 1 ms pulse width with a 25 Hz frequency. However, subsequent experiments have indicated that operation at 200 μ s pulse widths with frequencies as low as 5 Hz are possible.

Pulsed helium implantation of polycrystalline tungsten was performed at 1,150°C using the UW-IEC device. Fluences of 1×10^{18} , 6×10^{18} , and 1×10^{19} He^+/cm^2 were delivered to the samples in 1 ms pulses at 25 Hz. Micrographs of these samples were then compared to previous steady-state results at the same fluences and temperatures.

Figure 5.43 shows results for both pulsed and steady-state irradiation to 1×10^{18} He^+/cm^2 . It is clear from this comparison that more damage has resulted from the pulsed irradiation. While the steady-state sample only has pores collecting at grain boundaries with a pore density of 1.2×10^9 pores/ cm^2 , the pulsed sample appears close to a saturation density with larger pore size.

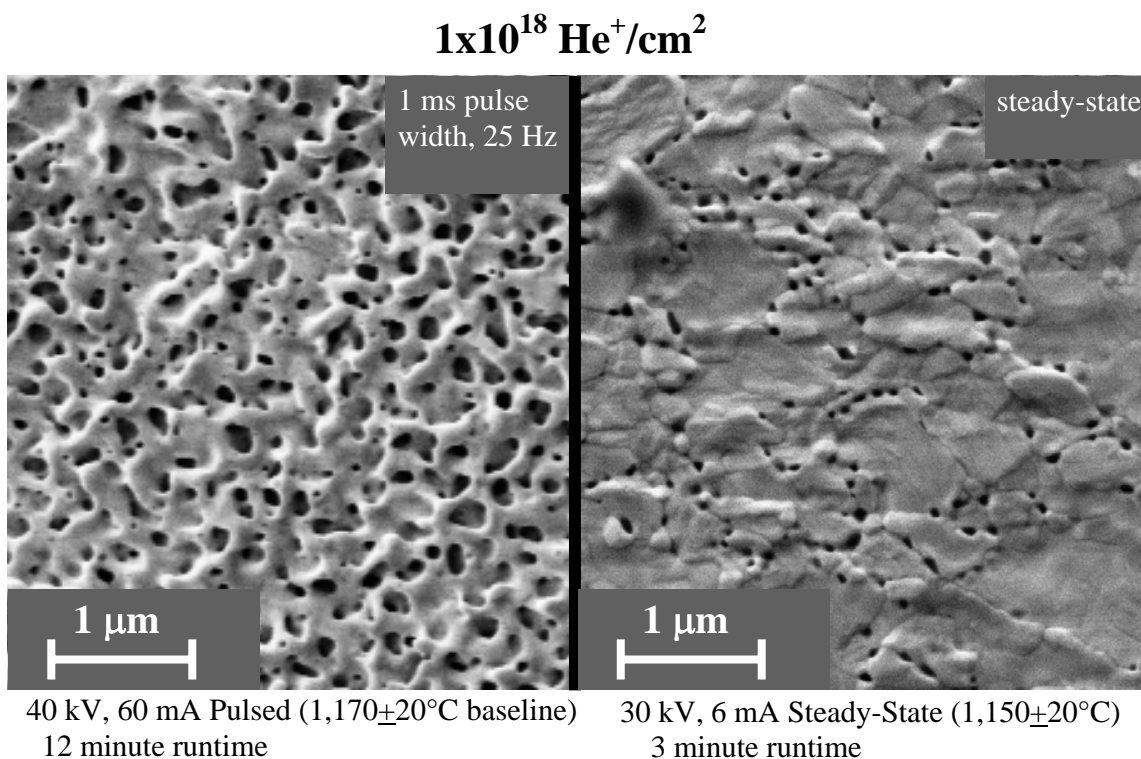


Figure 5.43: Pulsed and steady-state tungsten samples irradiated at $\sim 1,150^\circ\text{C}$ to $1 \times 10^{18} \text{ He}^+/\text{cm}^2$.

When the implanted helium fluence was increased to $6 \times 10^{18} \text{ He}^+/\text{cm}^2$ at $1,150^\circ\text{C}$, the pore density of the steady-state sample increased dramatically, reaching 3.7×10^9 pores/ cm^2 . In contrast, the pore density on the 6×10^{18} pulsed He^+/cm^2 sample did not significantly increase from the lower fluence, as shown in Figure 5.44. However, there does appear to be a change in the surface morphology at the grain boundaries. This change may indicate a shift toward a more macroscopic damage mechanism as the pulsed helium fluence is increased.

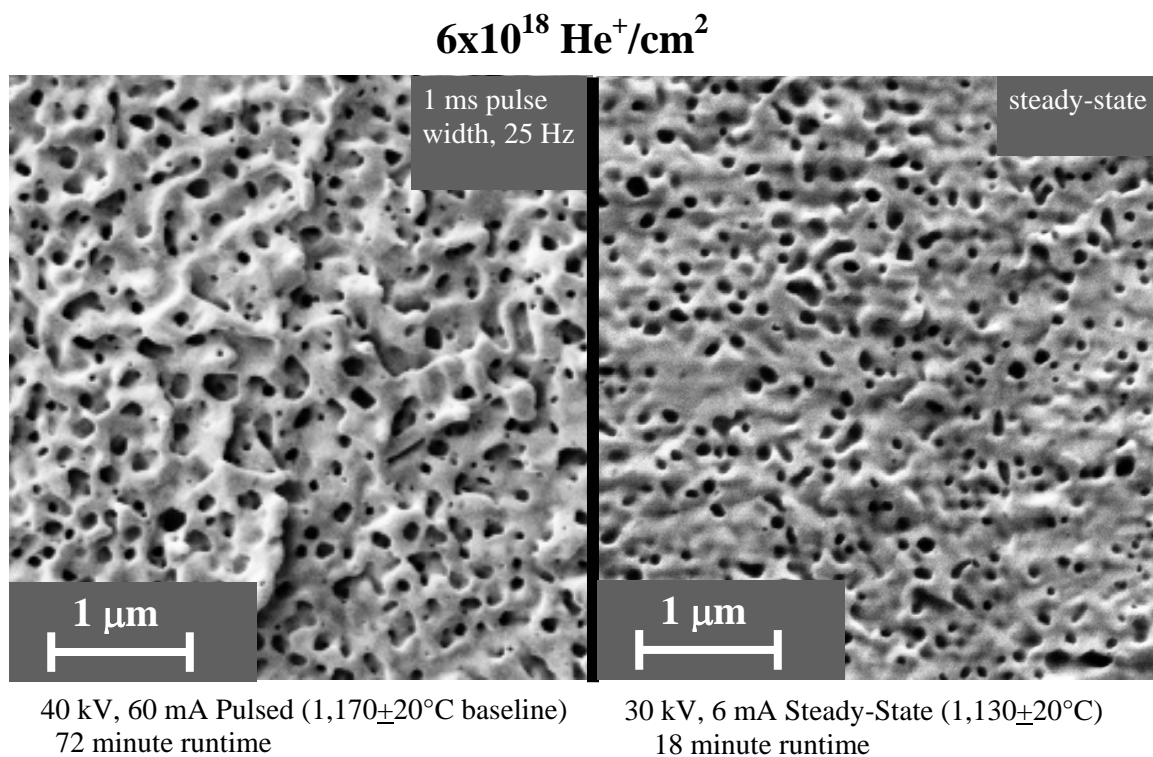


Figure 5.44: Pulsed and steady-state tungsten samples irradiated at $\sim 1,150^\circ\text{C}$ to $6 \times 10^{18} \text{ He}^+/\text{cm}^2$

When the steady-state implanted helium fluence was increased to $1 \times 10^{19} \text{ He}^+/\text{cm}^2$ at $1,150^\circ\text{C}$, the pore density decreased slightly to $1.9 \times 10^9 \text{ pores}/\text{cm}^2$, as shown in Figure 5.45. However, the surface appears to have roughened in a similar fashion to the pulsed sample at $6 \times 10^{18} \text{ He}^+/\text{cm}^2$. The pulsed sample, however, has been damaged to the point of having a coral-like structure in addition to the uniform pore density covering the surface.

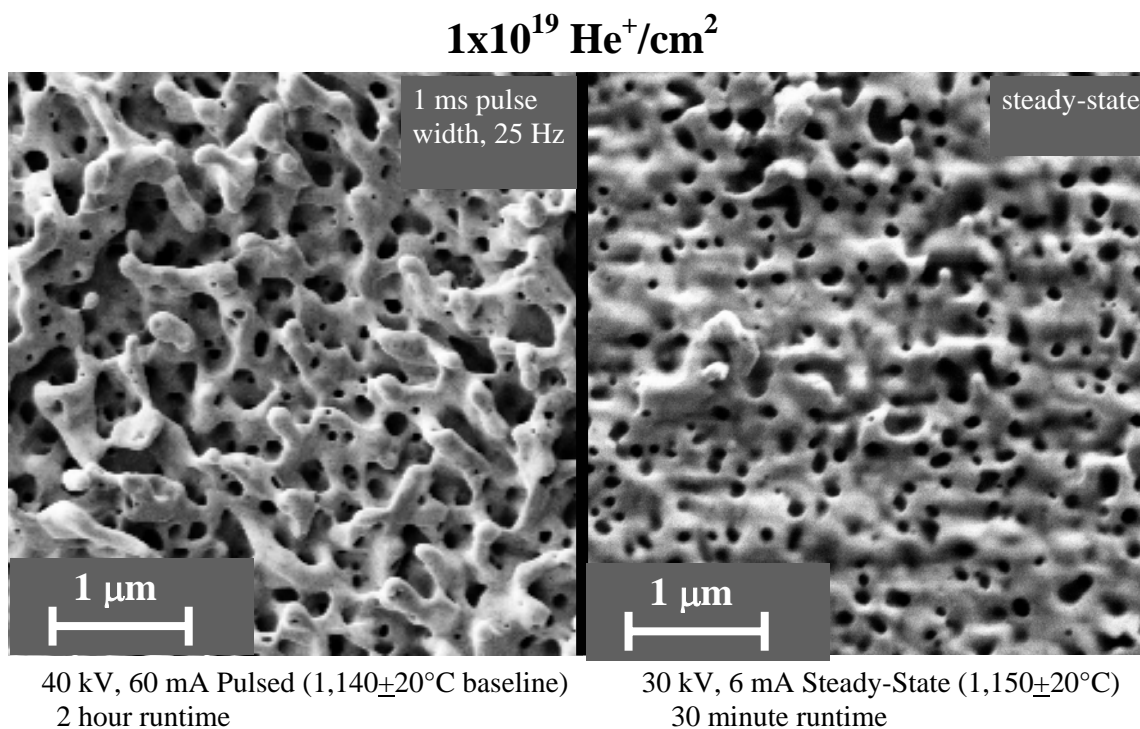
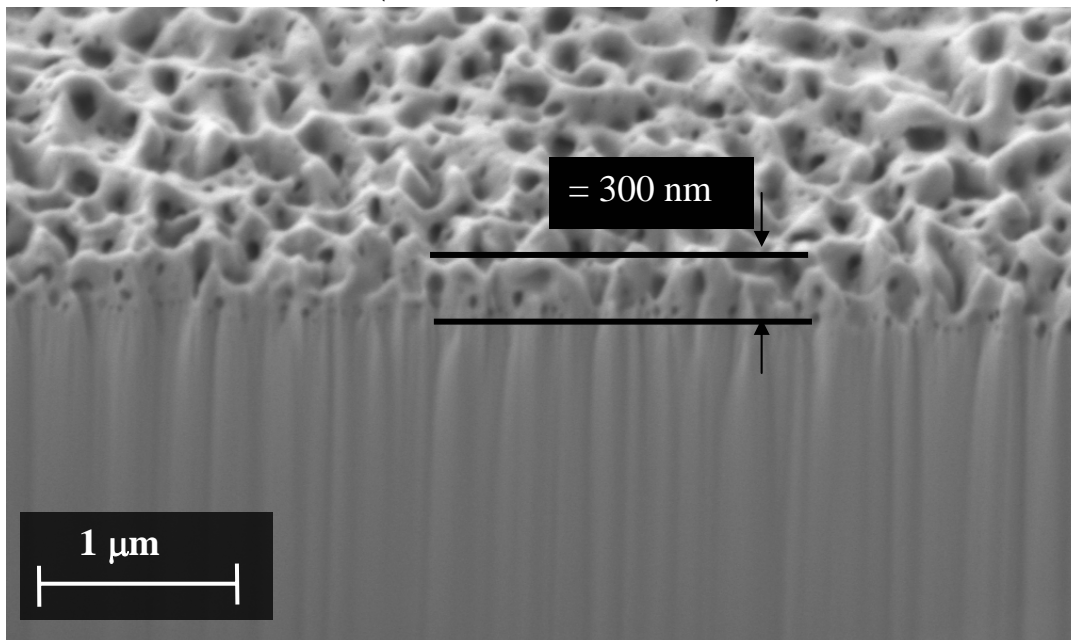


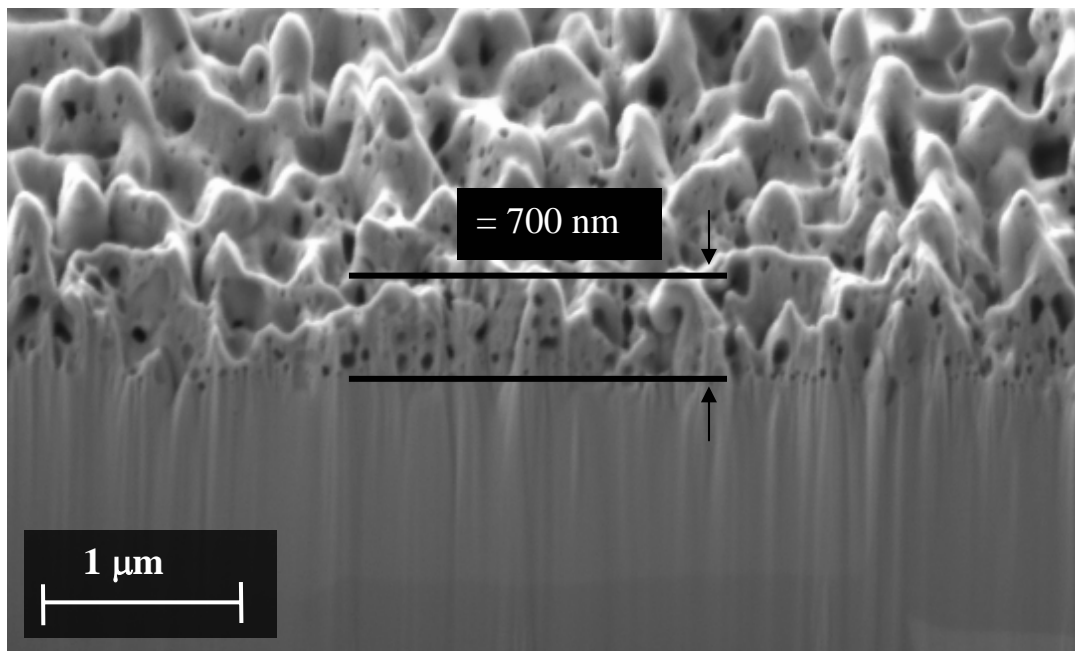
Figure 5.45: Pulsed and steady-state tungsten samples irradiated at $\sim 1,150^\circ\text{C}$ to $6 \times 10^{18} \text{ He}^+/\text{cm}^2$

Pulsed irradiation resulted not only in increased pore density on the surface, but also an increased semi-porous layer beneath the surface. Figures 5.46 and 5.47 show Focused Ion Beam (FIB) images of these surface layers at two fluences for both pulsed and steady-state implantation. As either steady-state or pulsed fluence is increased, the additional helium bubbles create and extend a semi-porous surface layer.

Pulsed (40 kV)
(1,150°C baseline)



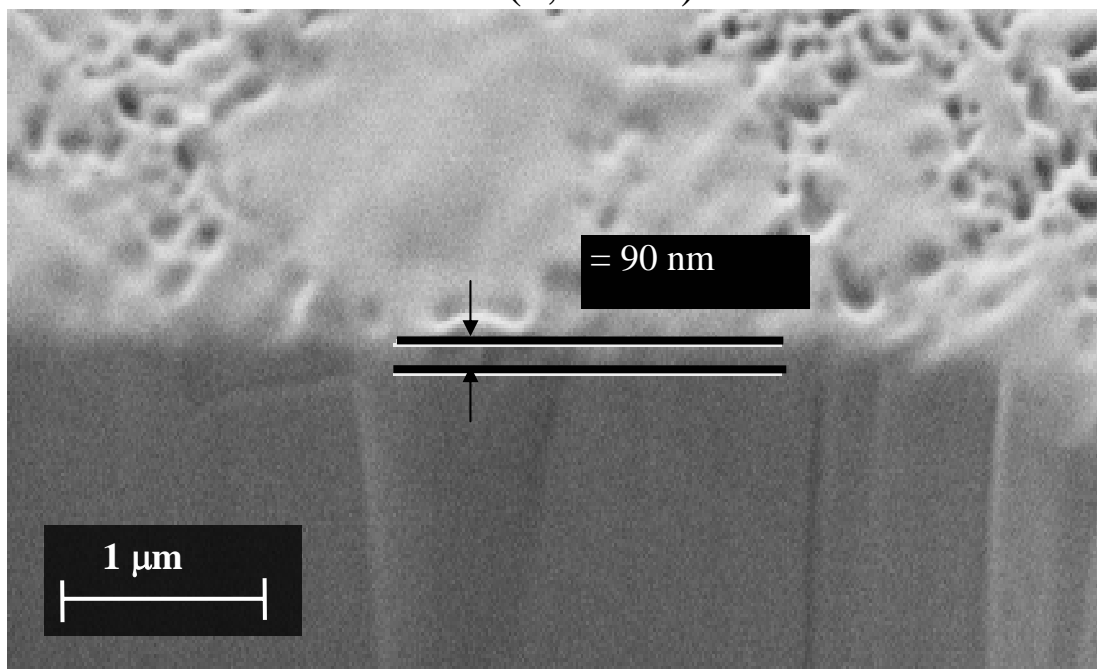
$10^{18} \text{ He}^+/\text{cm}^2$



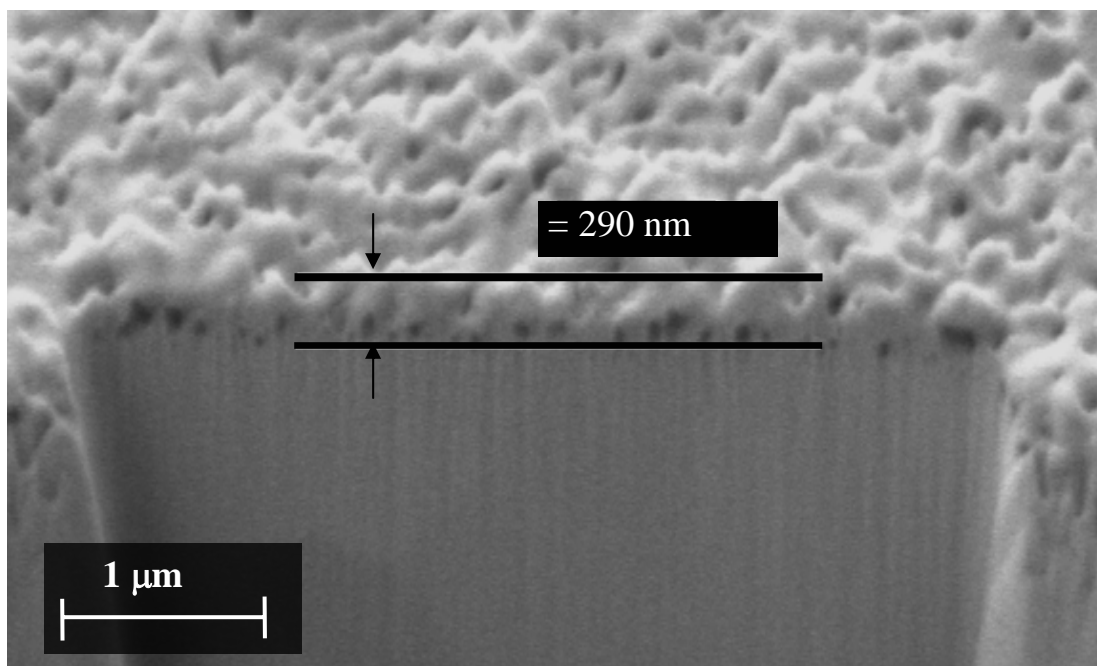
$10^{19} \text{ He}^+/\text{cm}^2$

Figure 5.46: Focused Ion Beam (FIB) images of tungsten irradiated with pulsed helium fluence

Steady-State (30 kV) (1,150°C)



$10^{18} \text{ He}^+/\text{cm}^2$



$10^{19} \text{ He}^+/\text{cm}^2$

Figure 5.47: Focused Ion Beam (FIB) images of tungsten irradiated with steady-state helium fluence

In addition to the morphological changes, the samples pulsed at 1,150°C also experienced a measurable change in mass. Theoretical calculations based on physical sputtering rates predict the sample would lose ~0.2 mg after 10^{19} He⁺/cm². However, the sample actually lost 4.2 mg, or roughly 1.1 μm uniformly from the surface, suggesting that other mechanisms of mass loss must be taking place. The mass losses for three samples subjected to pulsed helium implantation are summarized in Table 5.1.

	1×10^{18} He ⁺ /cm ²	6×10^{18} He ⁺ /cm ²	1×10^{19} He ⁺ /cm ²
Mass Loss (2 g sample)	0.5±0.1 mg	3.6±0.1 mg	4.2±0.1 mg
Thickness Loss	0.13±0.03 μm	0.93±0.03 μm	1.10±0.03 μm

Table 5.1: Mass loss for pulsed samples (1 ms pulse width, 25 Hz, 1,150°C)

One possible explanation for the higher-than-expected mass loss could be increased sputtering coefficients for non-perpendicular ion incidences. However, this would not increase the physical sputtering loss enough to account for the observed mass loss, even assuming the forward-sputtered material is not re-deposited on the sample [13]. Another possible explanation is the loss of the small protrusions during the irradiation process.

5.5 Polycrystalline Tungsten

Previous work by Cipiti, et al. investigated the effects of temperature, ion voltage, and fluence up to 10^{19} ions/cm² for deuterium and helium implantation in polycrystalline tungsten [6]. Recent work has expanded that investigation to 10^{20} ions/cm², examined the effects of simultaneous He⁺ and D⁺ implantation, and evaluated the effects of alloying tungsten with 25 percent rhenium. Table 5.2 provides a summary of the temperature, fluence, and post-irradiation pore density measured in these experiments.

Sample	Ions	Fluence (#/cm ²)	Mode	Temp (C)	Pore Density (pores/cm ²)
Poly-11	⁴ He ⁺	1×10^{20}	DC	~1150	2.8×10^9
Poly-1	⁴ He ⁺	1×10^{19}	DC	~1150	1.9×10^9
Poly-2	⁴ He ⁺	6×10^{18}	DC	~1120	3.7×10^9
Poly-3	⁴ He ⁺	3×10^{18}	DC	~1125	7.7×10^9
Poly-4	⁴ He ⁺	1×10^{18}	DC	~1150	1.2×10^9
Poly-5	⁴ He ⁺	6×10^{17}	DC	~1130	8.9×10^7
Poly-6	⁴ He ⁺ and D ⁺	1×10^{19}	DC	~1150	2.5×10^9
Poly-7	⁴ He ⁺ and D ⁺	6×10^{18}	DC	~1150	1.7×10^9
Poly-9	⁴ He ⁺ and D ⁺	3×10^{18}	DC	~1150	1.2×10^9
Poly-10	⁴ He ⁺ and D ⁺	1×10^{18}	DC	~1150	3.2×10^8
W-Re-1	⁴ He ⁺	1×10^{19}	DC	~1100	1.3×10^9
W-Re-2	⁴ He ⁺	6×10^{18}	DC	~1100	1.5×10^9
W-Re-3	⁴ He ⁺	3×10^{18}	DC	~1100	2.5×10^9
W-Re-4	⁴ He ⁺	1×10^{18}	DC	~1100	1.7×10^9
W-Re-5	⁴ He ⁺	6×10^{17}	DC	~1100	5.9×10^7

Table 5.2: Summary of irradiation history and pore density (P=polycrystalline, SC = single crystal, W-Re = W-25%Re). All samples were irradiated at 30 kV.

5.5.1 Simultaneous He⁺ and D⁺ Implantation

Simultaneous implantation of D⁺ and He⁺ was performed on tungsten samples at ~1,100°C. Previous experiments have indicated that deuterium irradiation alone does not induce pore formation [6]. Figure 5.48 compares polycrystalline tungsten samples irradiated

with helium alone and a helium-deuterium mixture. The first micrograph compares samples at a fluence of 1×10^{18} ions/cm². At this fluence, there appears to be a slight reduction of surface pore density from 1.2×10^9 to 3.2×10^8 pores/cm² on the sample run with He and D simultaneously. As the fluence is increased, however, this difference diminishes. At 10^{19} ions/cm² there appears to be no significant difference in pore density between the samples with and without simultaneously added deuterium.

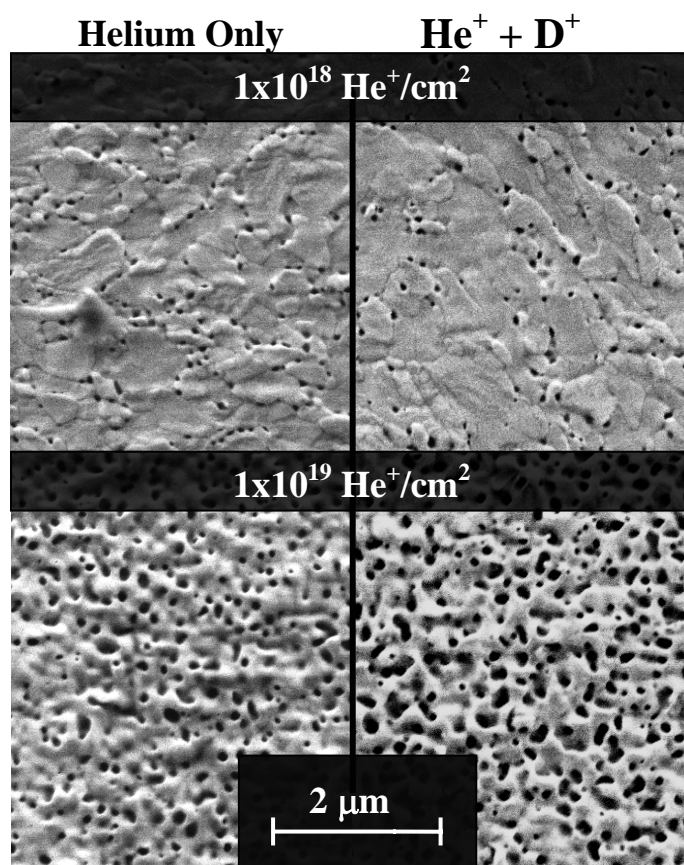


Figure 5.48: Tungsten samples irradiated at 1,150°C with He and He + D at 1×10^{18} and 1×10^{19} ions/cm².

5.5.2 W-25%Re Alloy

The effect of alloying tungsten with 25 percent rhenium was also studied in the IEC device. The W-25%Re alloy has a melting point 300°C lower than pure tungsten, but it exhibits more favorable mechanical properties [14]. The first pictures in Figure 5.49 compare pure and alloy samples irradiated to 1×10^{18} He⁺/cm². The pure tungsten sample appears to have just reached its threshold fluence, with pores beginning to collect at grain boundaries, while the alloy sample already has fairly uniform coverage with a pore density of 1.7×10^9 pores/cm². The second micrographs, each representing samples subjected to a fluence of 3×10^{18} He⁺/cm², indicate that both samples have achieved a uniform fluence, although the average pore diameter is larger on the W-25%Re sample, perhaps due to the material's lower melting point. Similarly, the samples that received fluences of 1×10^{19} ions/cm² also show uniform coverage of larger pores. Again, the W-25%Re alloy sample has an average pore diameter larger than the pure tungsten sample.

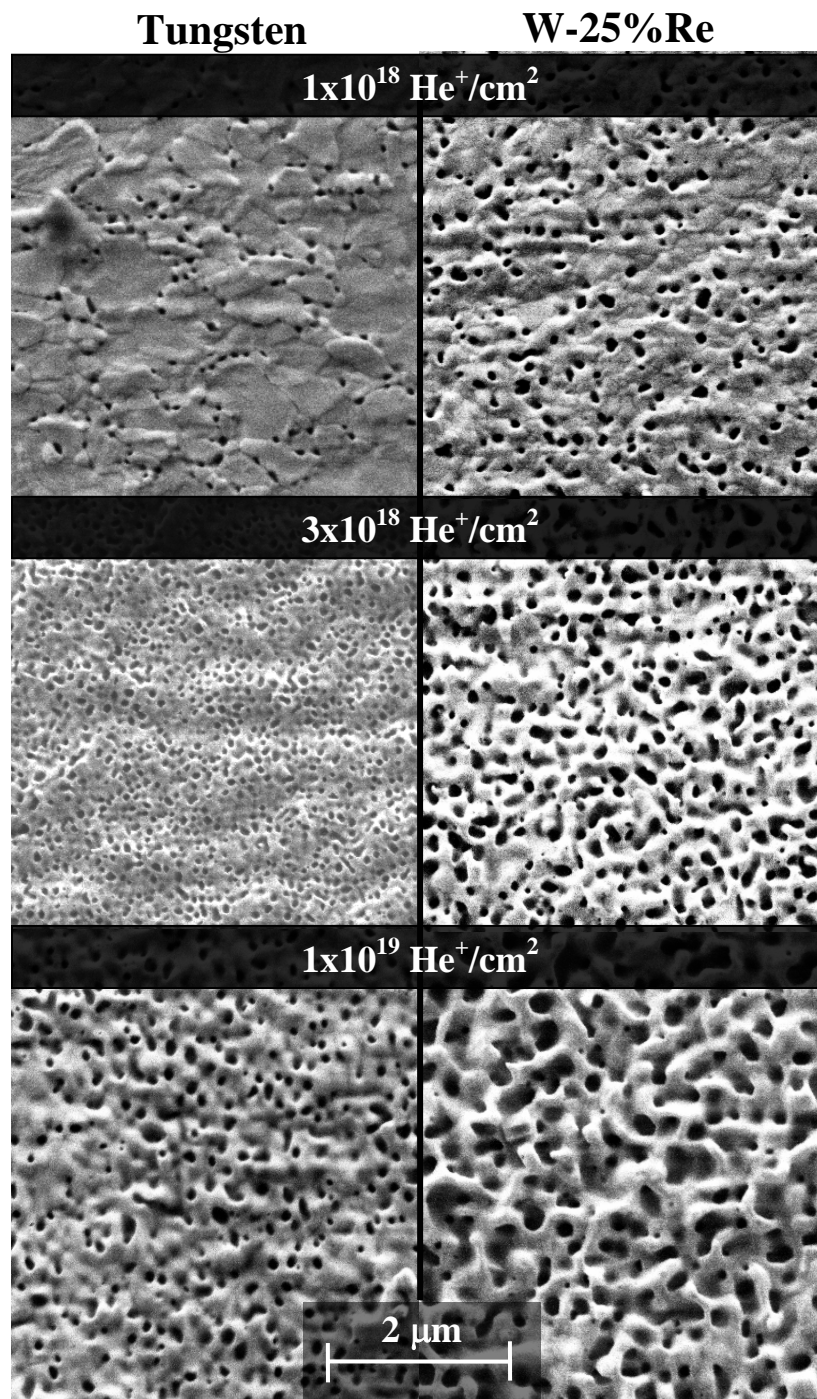


Figure 5.49: Pure tungsten and W-25%Re alloy samples irradiated with 30 keV He^+ at 1,150°C

5.5.3 Helium Retention

Polycrystalline samples were also evaluated with Elastic Recoil Detection (ERD) analysis in the University of Wisconsin Tandem Particle Accelerator Laboratory. The analysis was performed with 8 MeV (O^{4+}) oxygen. This oxygen was accelerated into the tungsten sample at a glancing angle, as depicted in Figure 5.50. It would then collide with the tungsten or helium atoms in the sample, and forward scatter some helium ions into a solid-state detector. Both the oxygen and helium ions will lose energy as they move through the tungsten sample, resulting in less energy deposited in the detector for helium embedded deeper in the sample. The energy spectra seen in the detector is then deconvolved to determine the concentration depth profile of helium in the sample.

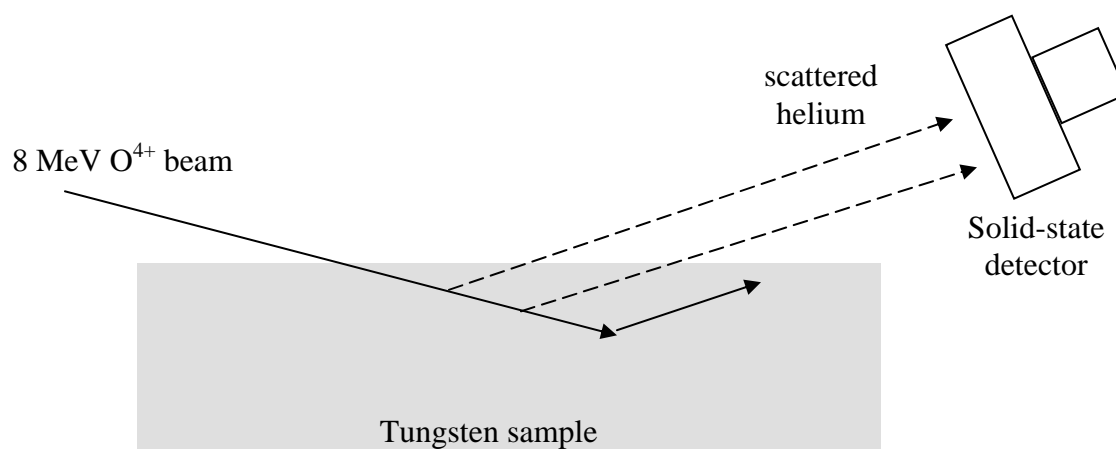


Figure 5.50: Elastic Recoil Detection is used to determine helium concentrations.

ERD analysis was used to evaluate tungsten samples that had been implanted with 30 keV helium to fluences of 10^{18} - 10^{19} He⁺/cm². Although helium atoms were predicted to be deposited as deep as 2,000 angstroms, as discussed in Chapter 3, this technique only allowed

the first 130 angstroms of surface to be examined. Figure 5.51 shows the results of an ERD analysis on a sample that had been irradiated to $1 \times 10^{19} \text{ He}^+/\text{cm}^2$. Helium diffusion resulted in low concentrations in the first 100 angstroms of the sample. However, the helium concentration very quickly reaches a steady level of 40 percent (atomic).

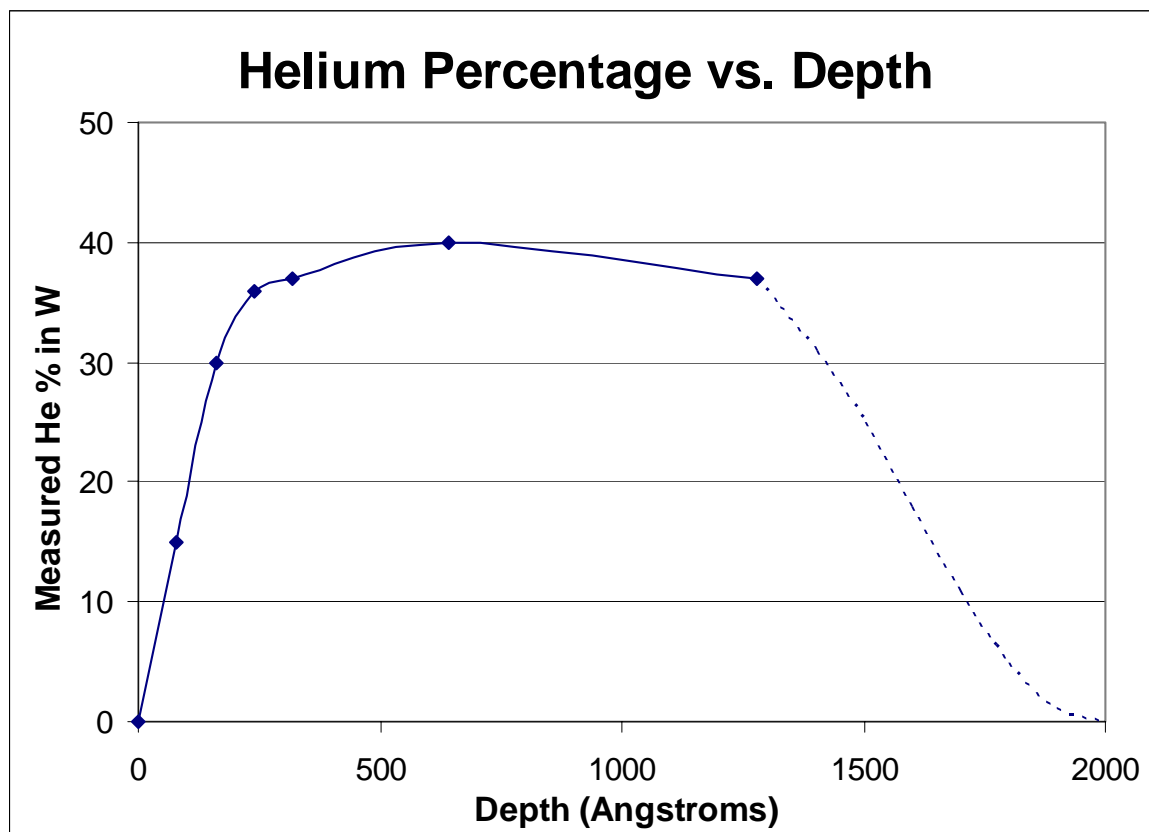


Figure 5.51: Helium concentration depth profile for $1 \times 10^{19} \text{ He}^+/\text{cm}^2$ sample.

To estimate the total amount of helium retained in each of the tungsten samples, it was assumed that the helium concentration dropped from its saturation value at 1,300 angstroms to zero at the maximum depth of 2,000 angstroms. The shape of the drop is derived from helium ion deposition theory. This concentration profile was then used to determine the helium retention of each sample. Figure 5.52 shows the helium retention in the

tungsten samples as a function of helium fluence. It is clearly seen that the retention saturates at $\sim 4 \times 10^{17}$ He⁺/cm². Therefore, as samples are subjected to higher fluences, this additional helium will be recycled back into the system. Figure 5.53 shows the retention ratio (retained helium/total helium fluence) as a function of incident fluence for polycrystalline tungsten irradiated at 1,150°C.

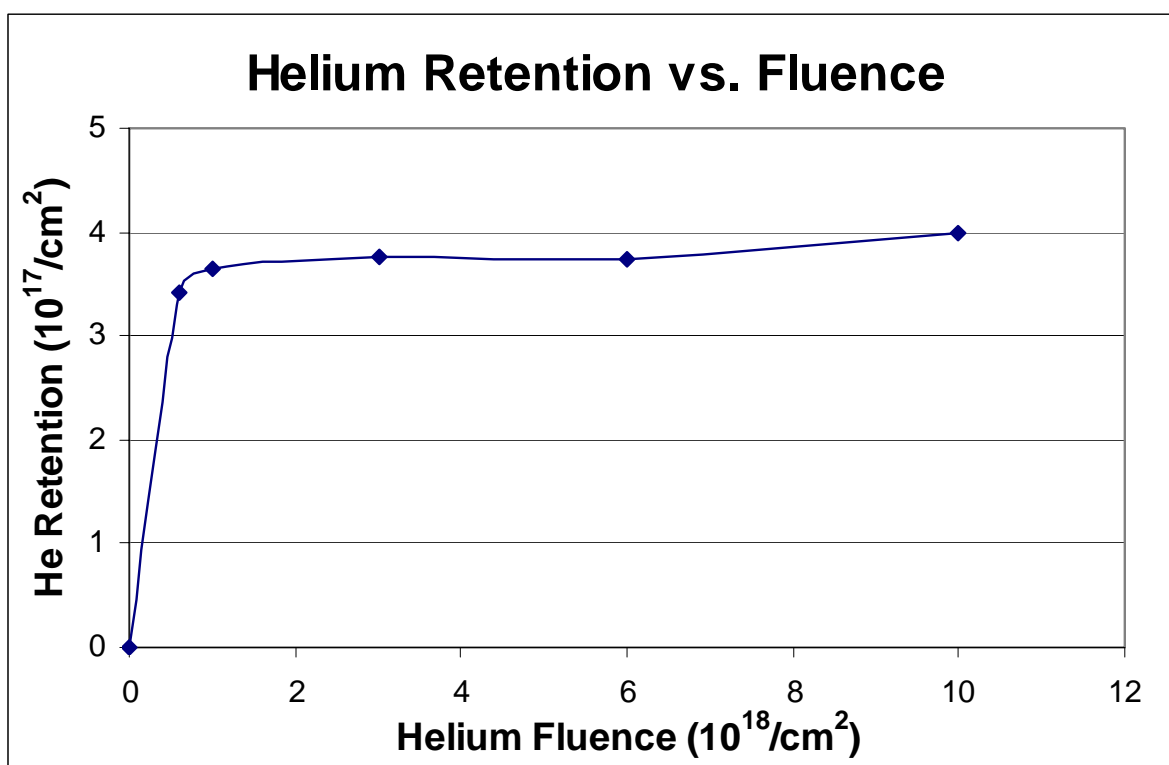


Figure 5.52: Helium retention saturates by 1×10^{18} He⁺/cm².

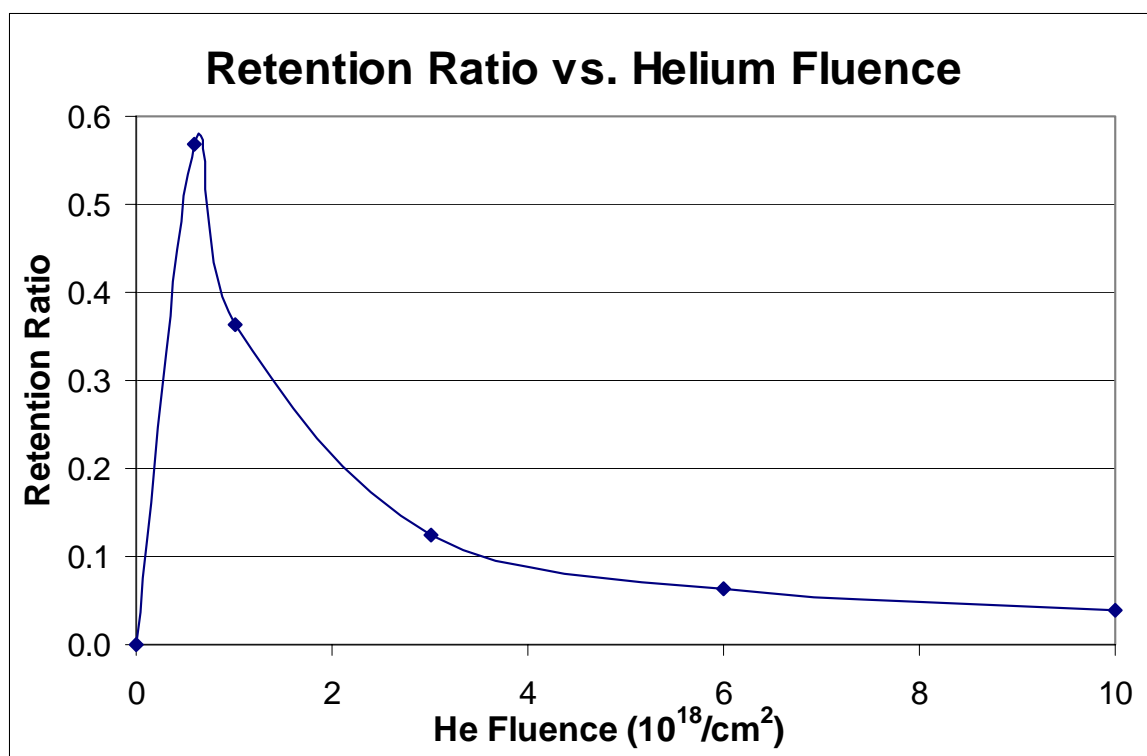


Figure 5.53: Helium retention ratio versus incident fluence.

5.5.4 Expanded Fluence

Increasing the helium fluence to 10^{20} ions/ cm^2 produced an increase in the pore density and a significant increase in surface roughness of the polycrystalline samples. Figure 5.54 shows the surface morphology of tungsten irradiated at $1,150^\circ\text{C}$ to 10^{18} , 10^{19} , and 10^{20} ions/ cm^2 . As the fluence is increased, the pore structure not only covers the entire sample, but additional damage begins to occur at grain boundaries. Additionally, the increased helium fluence creates and extends a semi-porous sub-surface layer, as shown in the FIB images at the bottom of Figure 5.54.

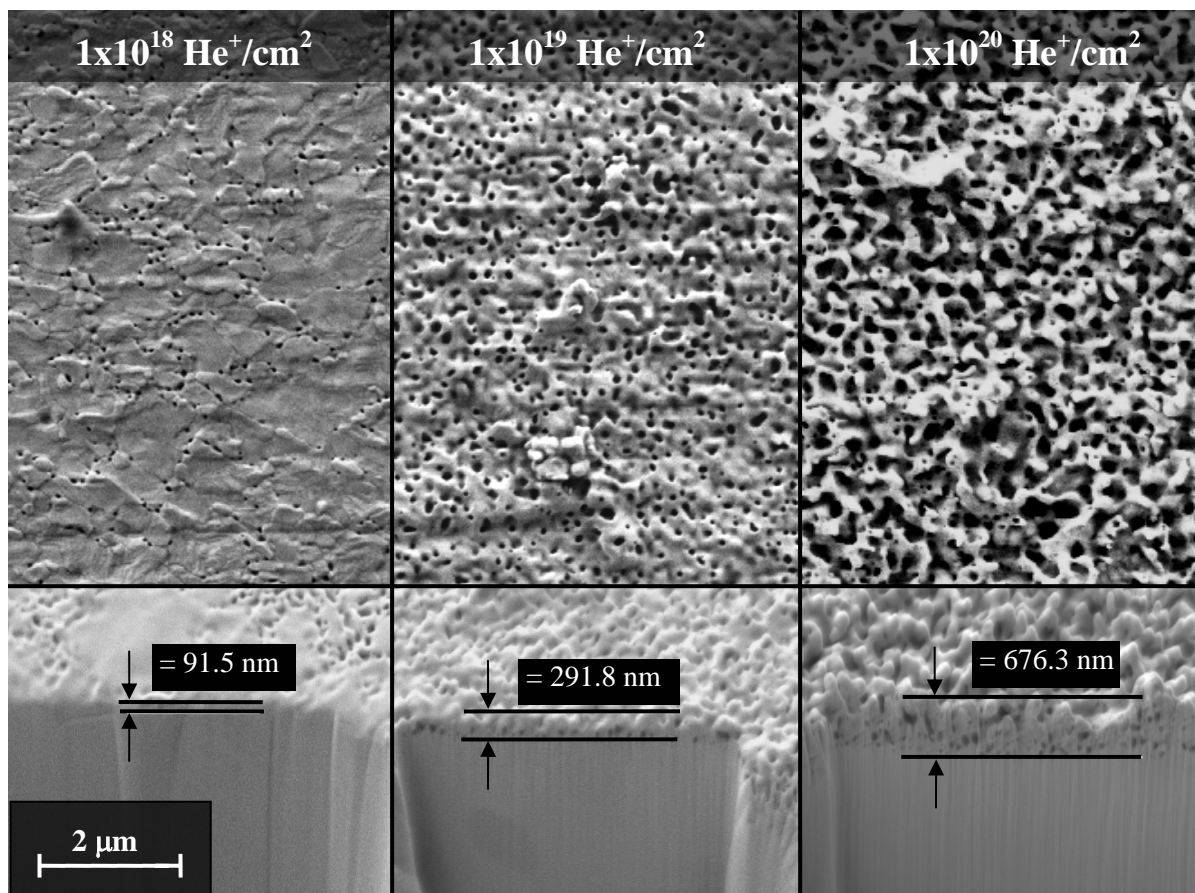


Figure 5.54: Polycrystalline tungsten samples irradiated with 30 keV He^+ at $1,150^\circ\text{C}$ to 10^{18} , 10^{19} , and 10^{20} He^+/cm^2 , respectively.

Changes in surface morphology on the 1×10^{20} He^+/cm^2 sample are shown at multiple magnifications in Figure 5.55. Though the sample had been polished prior to irradiation, increased damage at grain boundaries is clearly seen on the first micrograph. The second image indicates that different erosion behavior may be occurring at these grain boundaries. It appears as though material is being pushed into the boundary layer, creating ridges between

grains. At higher magnification, the surface can be seen to contain not only a high pore density, but many small protrusions are also jutting from the surface.

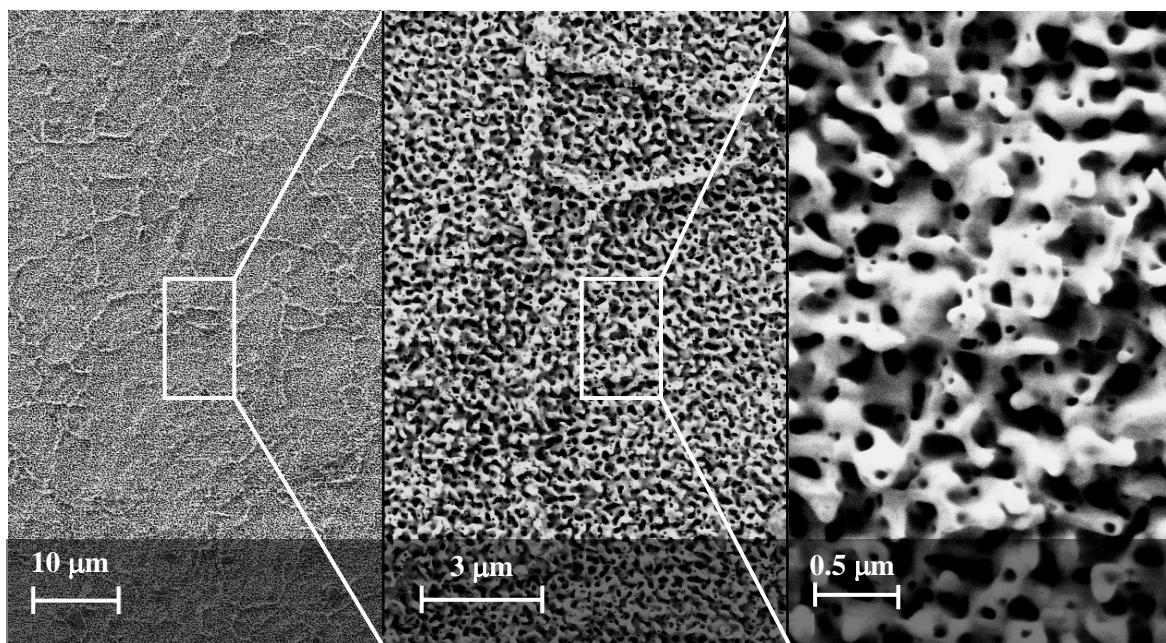


Figure 5.55: Polycrystalline tungsten sample irradiated with 30 keV He^+ at $1,150^\circ\text{C}$ to $10^{20} \text{He}^+/\text{cm}^2$. Each magnification of the tungsten sample reveals new surface features.

In addition to the morphological changes, this sample also experienced a measurable change in mass. Theoretical calculations based on physical sputtering rates predict the sample would lose $\sim 2.1 \text{ mg}$ after $10^{20} \text{He}^+/\text{cm}^2$. However, the sample actually lost 10.2 mg , or roughly $2.6 \mu\text{m}$ uniformly from the surface, suggesting that other mechanisms of mass loss must be taking place. One possible explanation would be increased sputtering coefficients for non-perpendicular ion incidences. However, this would not increase the physical sputtering loss enough to account for the observed loss, even assuming the forward-sputtered material is not re-deposited on the sample [13]. Another possible explanation is the loss of the small protrusions during the irradiation process.

5.6 Other Tungsten Forms

In addition to the polycrystalline tungsten discussed in the previous chapter, two additional forms of tungsten were studied during this project. The first is single crystal tungsten, which was investigated to determine the effects of grain boundaries on pore development and migration. The second is a tungsten-coated carbide foam developed by Ultramet. This material was proposed as an alternative to polycrystalline tungsten for ICF fusion first-wall applications, and was tested for that application by the HAPL project.

5.6.1 Single Crystal Tungsten

Previous work by Cipiti on the University of Wisconsin IEC device showed that polycrystalline tungsten samples began to experience pore formation at ion fluences of $1 \times 10^{18} \text{ He}^+/\text{cm}^2$ at $1,100^\circ\text{C}^*$ [6]. The pores would then migrate to the grain boundaries or be swept up by the moving grain boundaries during recrystallization, as can be seen in Figure 5.56. This work provided the motivation to test single crystal samples at similar conditions.

* Cipiti's fluence calculations were adjusted using a secondary electron coefficient of two ($\gamma=2$).

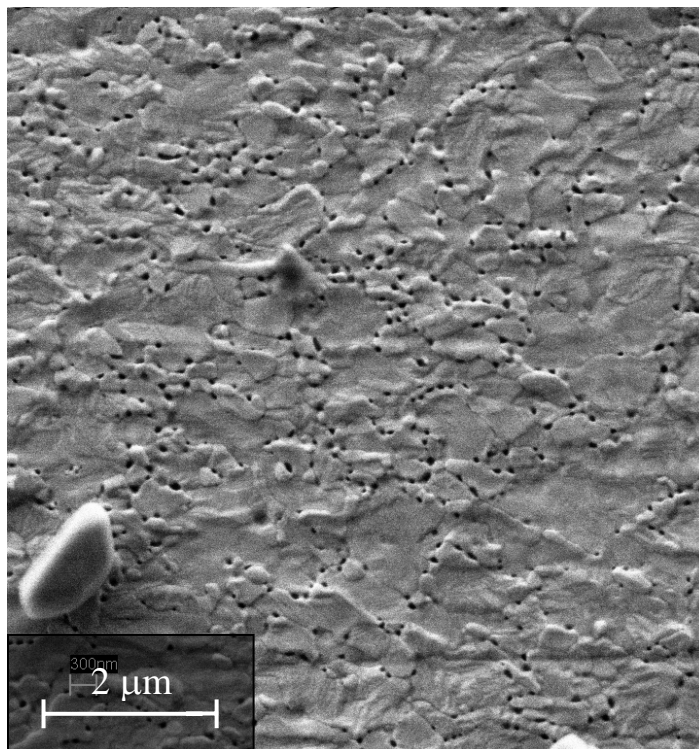


Figure 5.56: Polycrystalline tungsten sample irradiated with 30 keV helium at $\sim 1,100^{\circ}\text{C}$ to $1 \times 10^{18} \text{ He}^+/\text{cm}^2$.

The first single crystal tungsten sample in this study was irradiated with 30 kV He^+ ions to a fluence of $1 \times 10^{18} \text{ He}^+/\text{cm}^2$ at $\sim 1,100^{\circ}\text{C}$ [7]. As can be seen in Figure 5.57, dramatically fewer pores were formed compared to the polycrystalline sample in Figure 5.56. Since there were no grain boundaries, there seemed to be no preferential location for pore formation or migration.

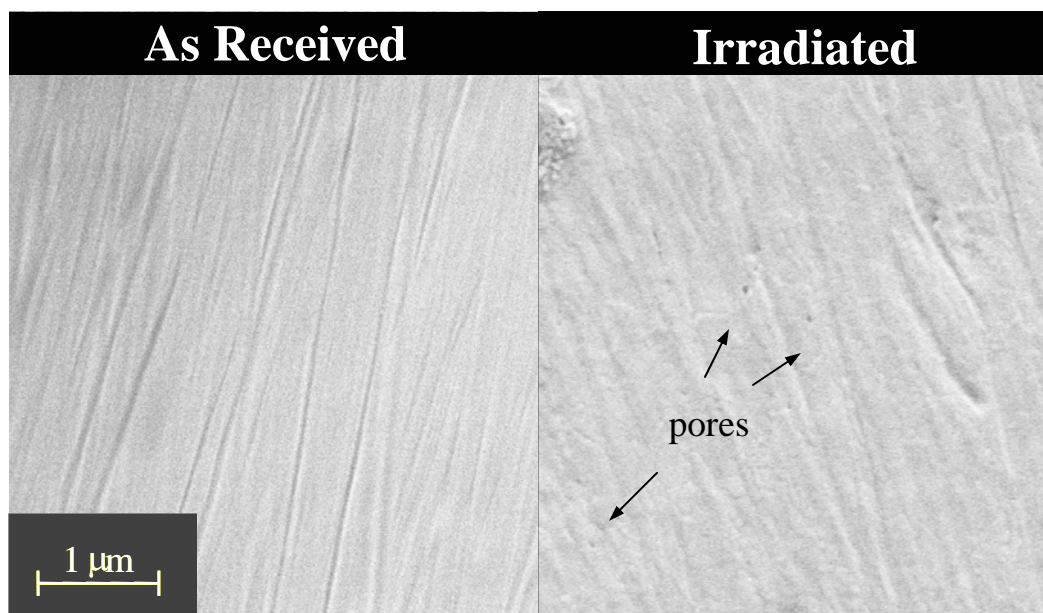


Figure 5.57: As-received and irradiated single crystal. The sample on the right was irradiated with 30 keV helium at 1,100°C to 1×10^{18} He^+/cm^2 .

When single crystal tungsten samples were subjected to higher fluences, they continued to exhibit lower damage rates than polycrystalline tungsten. Figure 5.58 shows micrographs of polycrystalline and single crystal tungsten samples irradiated to 3×10^{18} He^+/cm^2 at $\sim 1,100^\circ\text{C}$. The 5.8×10^9 pores/ cm^2 pore density on the polycrystalline sample is over twice that of the 2.3×10^9 pores/ cm^2 on the single crystal sample.

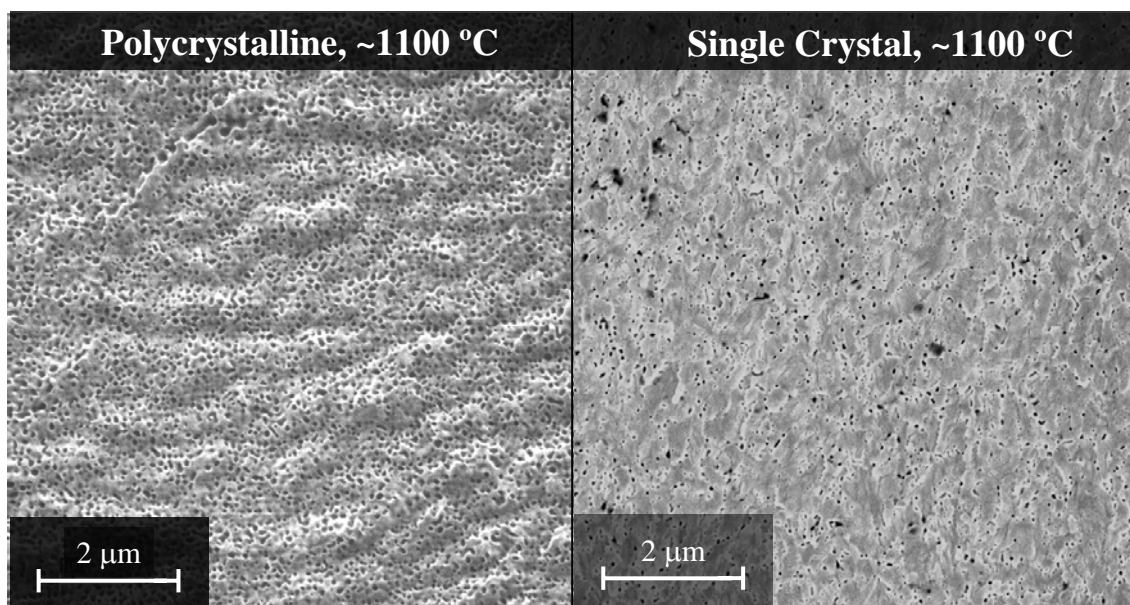


Figure 5.58: Polycrystalline and single crystal tungsten samples irradiated with 30 keV helium to $3 \times 10^{18} \text{ He}^+ / \text{cm}^2$.

5.6.2 Tungsten-Coated Foams

Tungsten-coated carbide samples were received from Ultramet, a manufacturer of tungsten-coated foam. SEM micrographs were taken of all samples both before and after irradiation in the IEC device. Figure 5.59 shows a view of the foam samples prior to irradiation. A typical foam sample has a surface area of $\sim 4 \text{ cm}^2$.

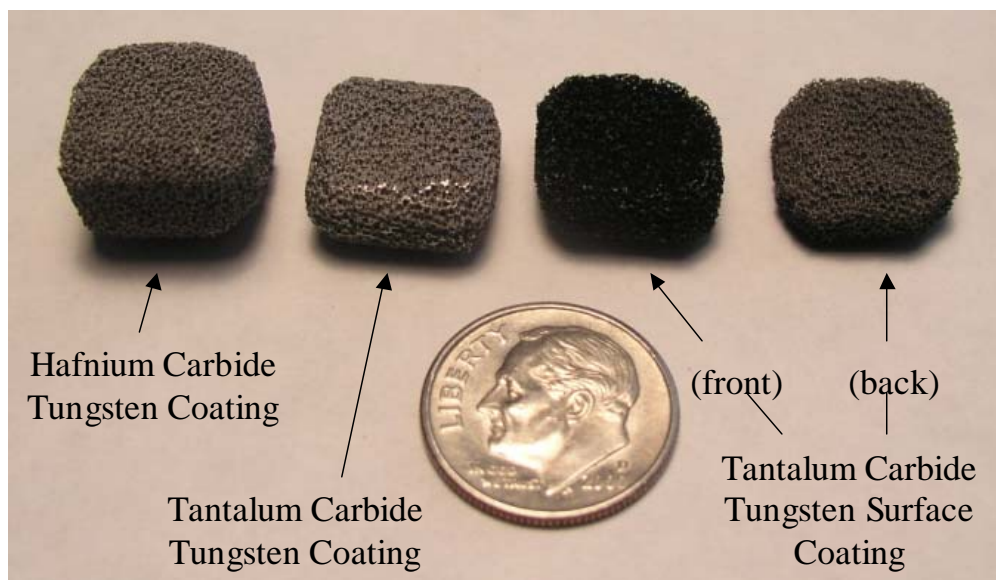


Figure 5.59: As-received foam samples.

As shown in Figure 5.60, the Ultramet foam samples are composed of a hollow tantalum carbide or hafnium carbide cores with a chemical vapor infiltration technique used to coat the cores with large or medium grain tungsten [15]. The “high ϵ ” foam has an extra layer of fine grain dendritic tungsten particles coating one side of the sample, as seen in Figure 5.59.

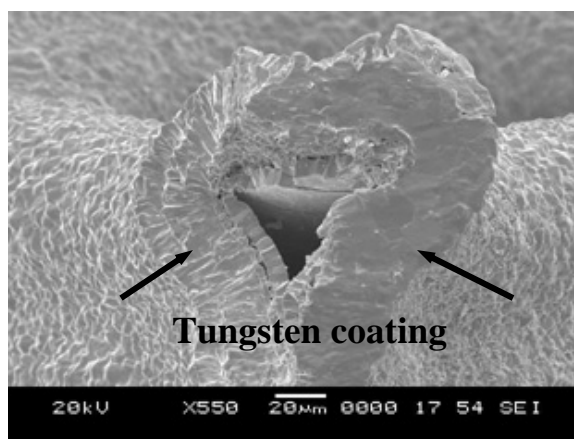


Figure 5.60: Cross section of TaC sample (Courtesy of Ultramet).

The series of micrographs in Figure 5.61 of an as-received tungsten-coated TaC sample shows the complex structure of the Ultramet foam. The three types of foams appear similar at low magnification (the first micrograph in Figure 5.61), but can vary significantly at higher magnification, as seen later in this chapter.

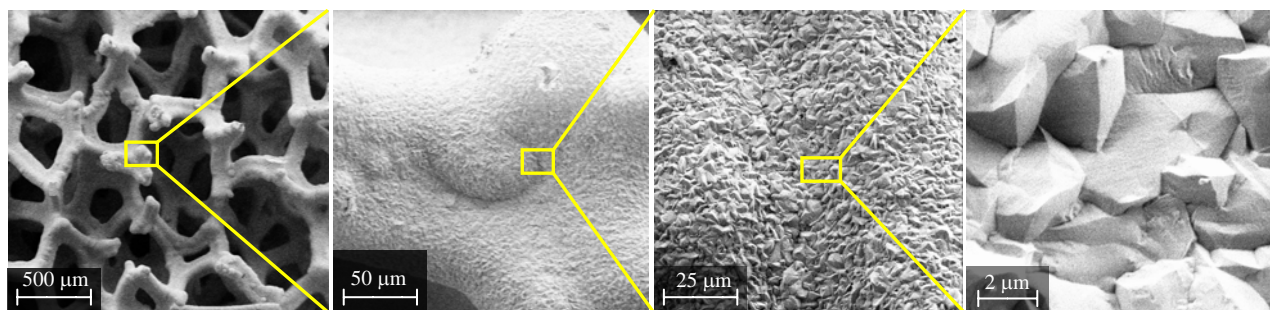


Figure 5.61: SEM micrographs of HfC foam samples coated with tungsten. The final picture reveals the small-scale structure of the tungsten coating.

Each of the samples was then mounted in the IEC device and irradiated to various fluence levels at temperatures ranging from 700 to 1100 °C. Temperatures were measured using a Raytek[®] Marathon two-color MR pyrometer. A summary of the fluence history of the samples used in this set of experiments can be seen in Table 5.3. Note that many of the samples were not irradiated in the IEC device, but were instead vacuum annealed outside of the device at 1,200°C for 30 minutes. These annealed control samples were used to distinguish damage caused by heating from that due to the irradiation process.

Sample	Ions	Fluence (#/cm ²)	Temp (°C)	Energy (kV)
TaC-1	D ⁺	~10 ¹⁸	>1,100	up to 50
TaC-2	⁴ He ⁺	6x10 ¹⁷	~1,100	30
TaC-4	---	---	1,200	---
HfC-1	⁴ He ⁺	6x10 ¹⁷	~1,100	30
HfC-4	---	---	1,200	---
TaC-ε-1	⁴ He ⁺	6x10 ¹⁷	varied	30
TaC-ε-4	---	---	1,200	---
Single Crystal	⁴ He ⁺	4x10 ¹⁶	~1,100	30

Table 5.3: Summary of experiments performed on alternative tungsten materials.

Irradiation times in the IEC device ranged from roughly 20 seconds to 30 minutes. Temperature, pressure, voltage, and current were constantly monitored during irradiation to maintain constant fluxes. After each sample was irradiated in the IEC device, SEM micrographs were again taken to observe the surface morphology changes that occurred due to ion bombardment.

Figure 5.62 shows SEM micrographs of a large grain tungsten-coated TaC sample before and after being vacuum annealed at 1,200°C for 30 minutes. Note that while the micrographs are of the same sample, they are not of the exact same location. The annealing process had little effect on the surface morphology, aside from a slight roughening of the surface.

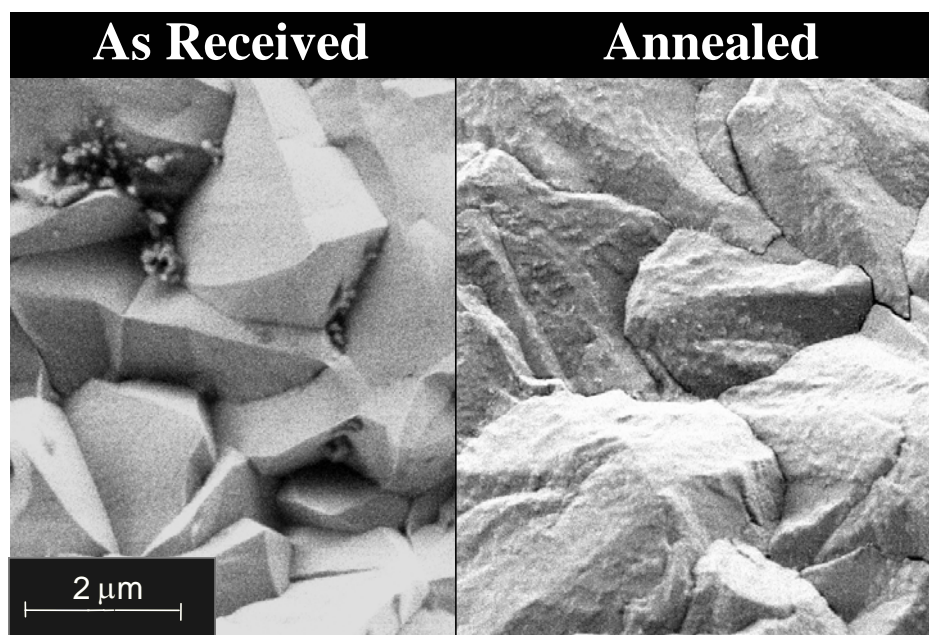


Figure 5.62: Large grain tungsten-coated TaC sample before and after vacuum annealing.

When subjected to D^+ and He^+ fluences in the UW-IEC device, the two types of large grain tungsten-coated foam samples (TaC and HfC) studied were observed to respond very similarly. As discussed above, both types of tungsten-coated foam are coated with a relatively thin (30-50 μm) tungsten layer of similar composition. However, the fast ions have a range of less than 100 nm, leaving the carbide substrate unaffected by the irradiation.

The first large grain tungsten-coated sample was irradiated with 30 keV deuterium at $\sim 1,100^\circ\text{C}$ with approximately a $\sim 10^{19} D^+/\text{cm}^2$ fluence. As can be seen in Figure 5.63 below, the surface was significantly smoothed, presumably from the combined high temperature and sputtering environment.

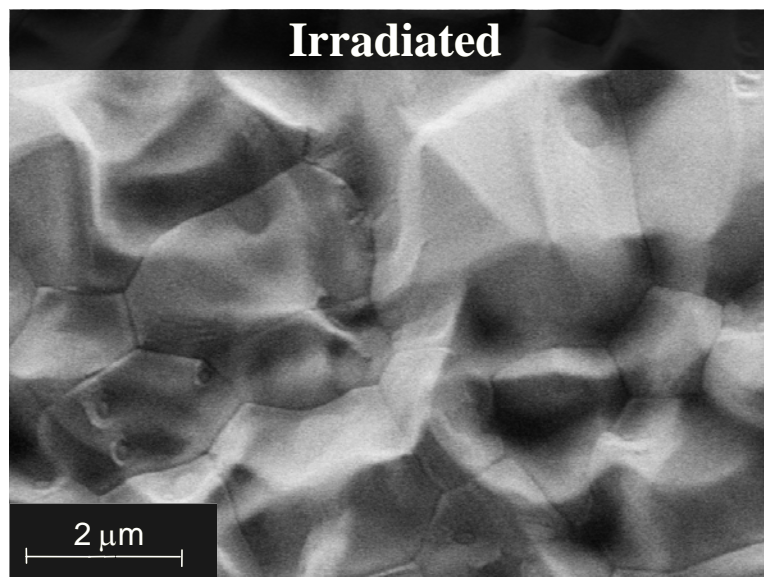


Figure 5.63: Large grain tungsten-coated TaC sample. This sample was irradiated with 30 keV deuterium at $\sim 1,100^{\circ}\text{C}$ with $\sim 10^{19} \text{ D}^+/\text{cm}^2$ fluence

Figure 5.64 shows SEM micrographs of a tungsten-coated HfC sample before and after being vacuum annealed at $1,200^{\circ}\text{C}$ for 30 minutes. As in the TaC sample, the annealing process had little effect on the surface morphology. The tungsten-coated HfC sample pictured in Figure 5.66 was irradiated at $\sim 1,100^{\circ}\text{C}$ with a $6 \times 10^{17} \text{ He}^+/\text{cm}^2$ fluence. When the foam samples were subjected to this He^+ fluence, a very different phenomenon was observed than the D^+ case. Figure 5.65 shows the dramatic effects on the surface morphology of the target. Not only did this sample experience a smoothing effect much like the D^+ irradiated sample, but also it showed extensive pore formation at the surface of the sample.

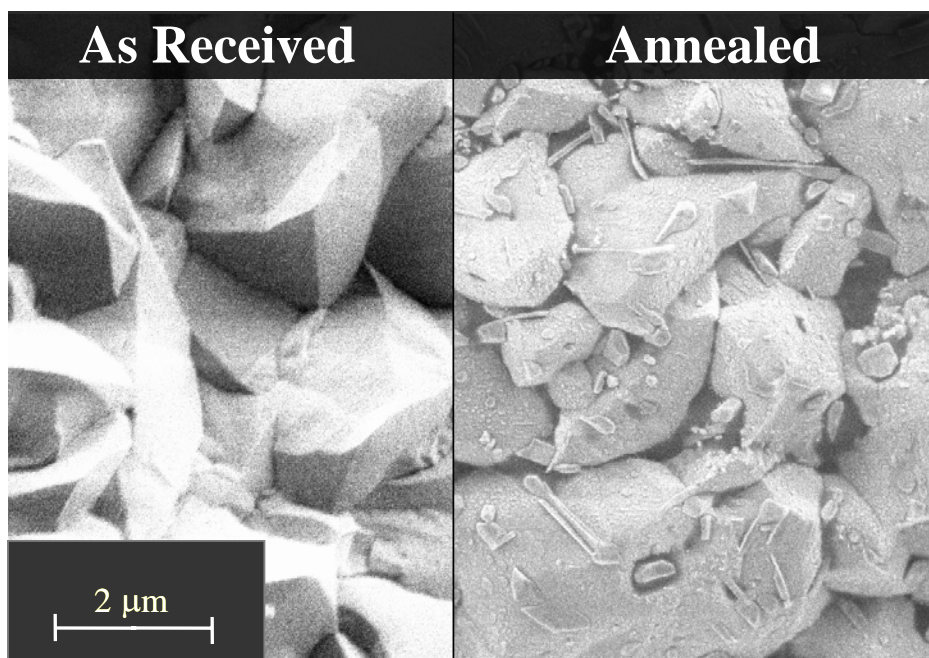


Figure 5.64: Large grain tungsten-coated HfC sample before and after vacuum annealing.

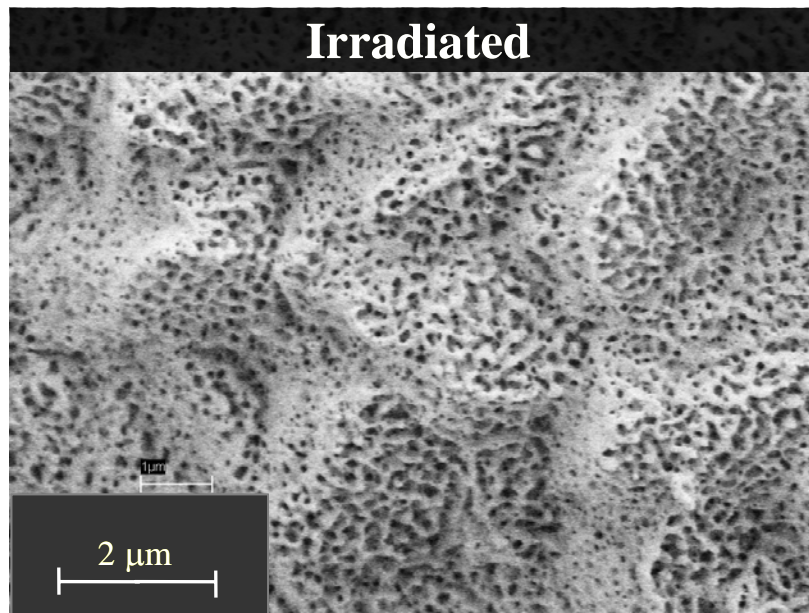


Figure 5.65: Large-grain tungsten-coated HfC sample. This sample was irradiated with 30 keV helium at $\sim 1,100^{\circ}\text{C}$ to $1 \times 10^{19} \text{ He}^+/\text{cm}^2$.

The final foam sample evaluated had a chemical vapor infiltration medium grain tungsten coating similar to that of the first two samples. However, one side of the sample was then coated with an additional layer of fine grain tungsten dendrites. These small particles act to increase the emissivity of the foam, so this sample will be referred to as the “high- ϵ sample”.

SEM micrographs of the medium and fine grain tungsten-coated samples before and after being vacuum annealed at 1,200°C for 30 minutes are shown in Figures 5.66 and 5.67. The medium-grain side of the sample seemed to react similarly to the large grain tungsten-coated TaC and HfC samples, while the side with the fine grain tungsten appears to have experienced some recrystallization.

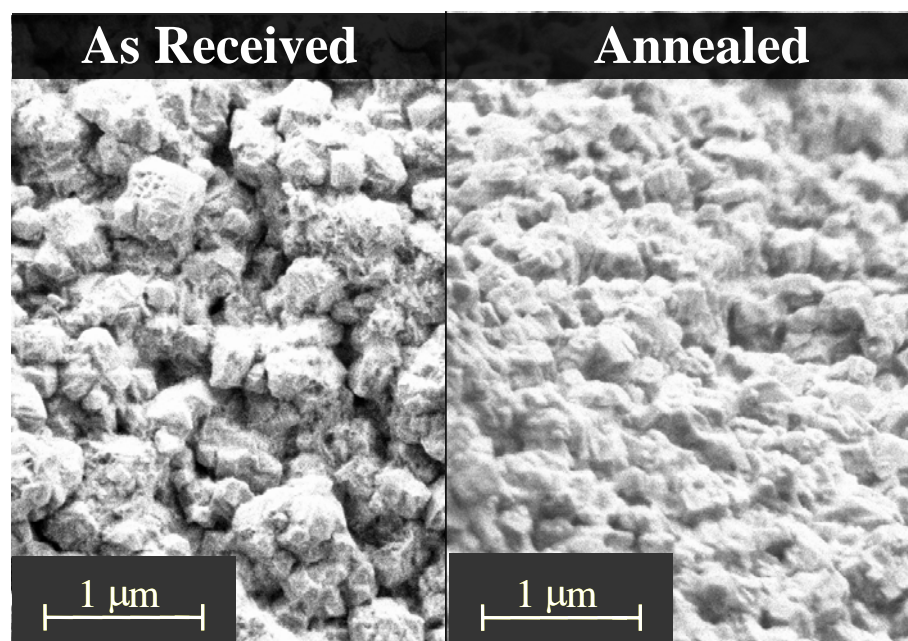


Figure 5.66: Medium-grain side of the “high ϵ ” sample before and after vacuum annealing (1,200°C for 30 min).

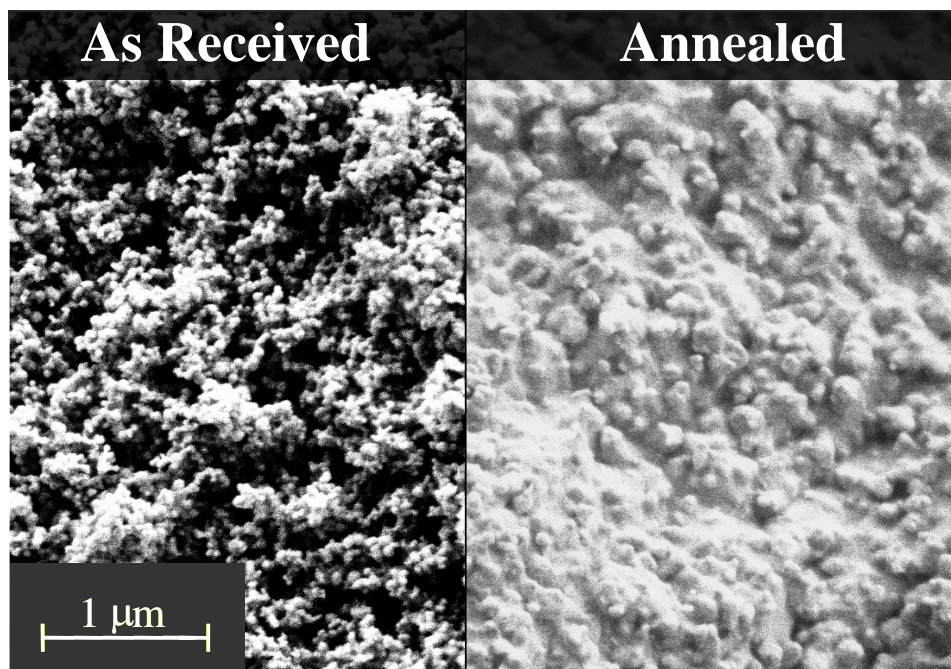


Figure 5.67: Fine-grain tungsten side of the “high ϵ ” sample before and after vacuum annealing (1,200°C for 30 min).

The spherical symmetry of the IEC device provided a relatively uniform 1×10^{19} He^+/cm^2 fluence across both sides of the sample. As seen in Figure 5.68, the medium grain tungsten side exhibited a uniform pore density similar to those seen in the tungsten-coated TaC and HfC samples. The fine grain tungsten-coated side of the “high ϵ ” foam experienced a very different phenomenon during irradiation, as seen in Figure 5.69. The “black” tungsten dendrites applied to the foam appeared to grow after irradiation. There also seemed to be a reduced pore density on the tungsten surface.

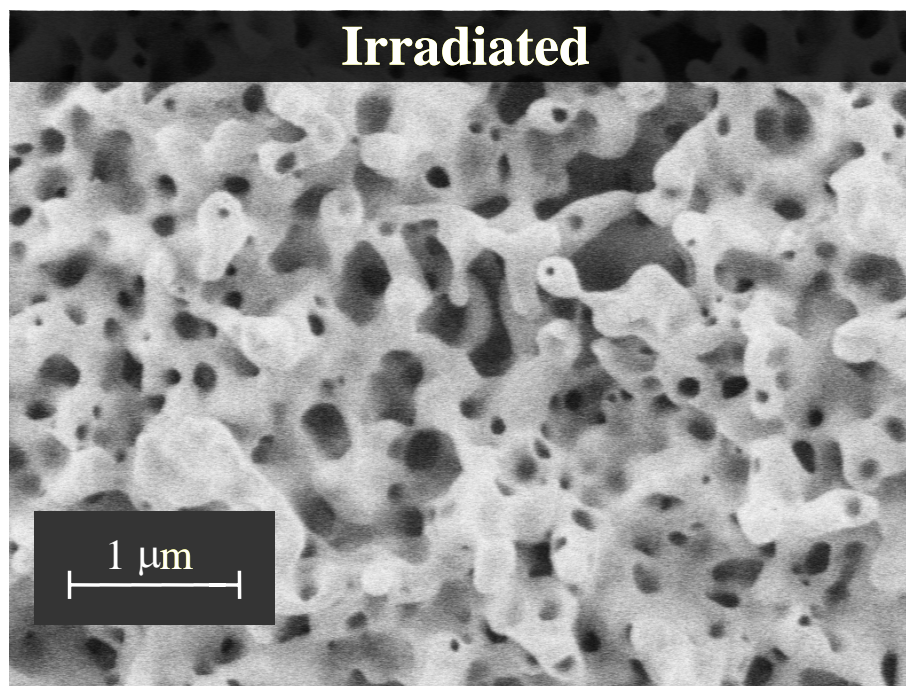


Figure 5.68: Medium grain side of the "high ε" sample.
Irradiated with 30 keV helium to $1 \times 10^{19} \text{ He}^+/\text{cm}^2$.

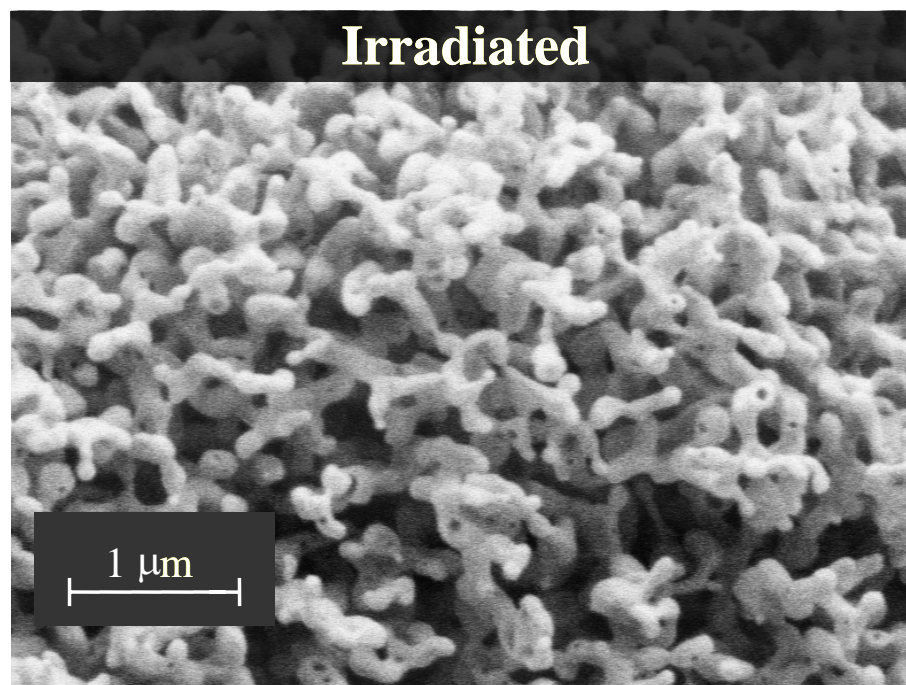


Figure 5.69: Fine grain side of the "high ε" sample.
Irradiated with 30 keV helium to $1 \times 10^{19} \text{ He}^+/\text{cm}^2$.

5.7 References

- [1] X-5 Monte Carlo Team, MCNP — A General Monte Carlo N-Particle Transport Code, Version 5, Vol. II: User's Guide (Revised 6/30/04)
- [2] Werner, C.J, "Simulation of Delayed Neutrons Using MCNP" *Progress in Nuclear Energy*; Vol. 41, No. 1-4, pp. 385-389, 2002
- [3] I. Langmuir and K. Blodgett, "Currents Limited by Space Charge Between Concentric Spheres," *Physical Review*, Vol. 24, p. 49-59, 1924
- [4] D.H. Hale, "The Breakdown of Gases in High Frequency Electrical Fields," *Physical Review*, Vol. 33, No. 9, 1943
- [5] R.F. Radel and G.L. Kulcinski, "Detection of Highly Enriched Uranium Using a Pulsed D-D Fusion Source," accepted for publication in *Fusion Science and Technology*
- [6] B.B. Cipiti and G.L. Kulcinski, "Helium and Deuterium Implantation in Tungsten at Elevated Temperatures," *Journal of Nuclear Materials*, Vol. 347, Issue 3, p. 255, 2005
- [7] R.F. Radel and G.L. Kulcinski, "Implantation of D and He in W-coated Refractory Carbides," *Fusion Science and Technology*, Vol. 47, Issue 4, p. 1250, 2005
- [8] J.D. Sethian, et. al. "Fusion Energy with Lasers, Direct-Drive Targets, and Dry Wall Chambers," *Nuclear Fusion*, Vol. 43, p. 1963, 2003
- [9] T. Renk, et al, "Chamber wall materials response to pulsed ions at power-plant level fluences," *Journal of Nuclear Materials*, Vol. 347, Issue 3, p. 255, 2005
- [10] J.F. Latkowski, et al, "Effect of multi-shot X-ray exposures in IFE armor materials," *Journal of Nuclear Materials*, Vol. 347(3), p. 255, 2005
- [11] A.R. Raffray, et al, "Progress Towards Realization of a Laser IFE Solid Wall Chamber," *Fusion Engineering and Design*, 81, Issues 8-14, p. 1627, 2006
- [12] S.B. Gilliam, et al, "Retention and Surface Blistering of Helium Irradiated Tungsten as a First Wall Material," *Journal of Nuclear Materials*, Vol. 347(3), p 289-297, 2005
- [13] M. Kaminsky, *Atomic and Ionic Impact Phenomena on Metal Surfaces*. p.p. 159-163, Springer-Verlag, Berlin, 1965
- [14] Goodfellow Corporation online database, "W and W-Re properties," <http://www.goodfellow.com/csp/active/gfHome.csp>
- [15] B.E. Williams (Ultramet Corporation), Private Communication, September, 2004

Chapter 6: Discussion

This thesis encompasses work performed in numerous areas of study. In each area, the work described pushed the limits of knowledge in the field and required the development of state-of-the-art IEC technology. The major achievements reported in this thesis include:

1. Steady-state IEC D-D neutron production of 2.2×10^8 n/s
2. Pulsed IEC D-D neutron production of 4.7×10^9 n/s
3. Pulsed IEC operational parameters increased:
 - a. Steady-state cathode voltages as high as 165 kV
 - b. Pulsed cathode voltages as high as 120 kV
 - c. Pulse currents in excess of 6 A
4. An MCNP model capable of predicting delayed neutron counts from uranium-235
5. Detection of delayed fission neutrons with both steady-state and pulsed neutron fluxes from an IEC device
6. Pulsed helium implantation in tungsten that revealed increased surface damage, subsurface porous structure, and mass loss
7. Measurements of helium retention values saturating at 40 percent (atomic) from 30 keV He^+ in tungsten at 1100 °C
8. Evaluation of alternative forms of tungsten, such as tungsten-coated TaC foams, single-crystal tungsten, and a tungsten-rhenium alloy, were evaluated for use as ICF fusion first-wall materials

All of these observations and achievements were discussed somewhat in Chapter 5. Additional discussions in this chapter will focus on items 2, 3, 5 and 6 above.

6.1 Pulsed IEC

Significant increases in the pulsed D-D neutron production rate have been made over the past two years on the University of Wisconsin IEC device. Figure 6.1 shows the pulsed D-D neutron production rate plotted as a function of time for the past two years. Numerous factors have led to the increased neutron production rate, including increased cathode voltage, increased pulse current, upgraded cathode/anode geometry, the introduction of a titanium coating, and shortened pulse widths. Each of these factors was discussed in detail in Section 5.2.

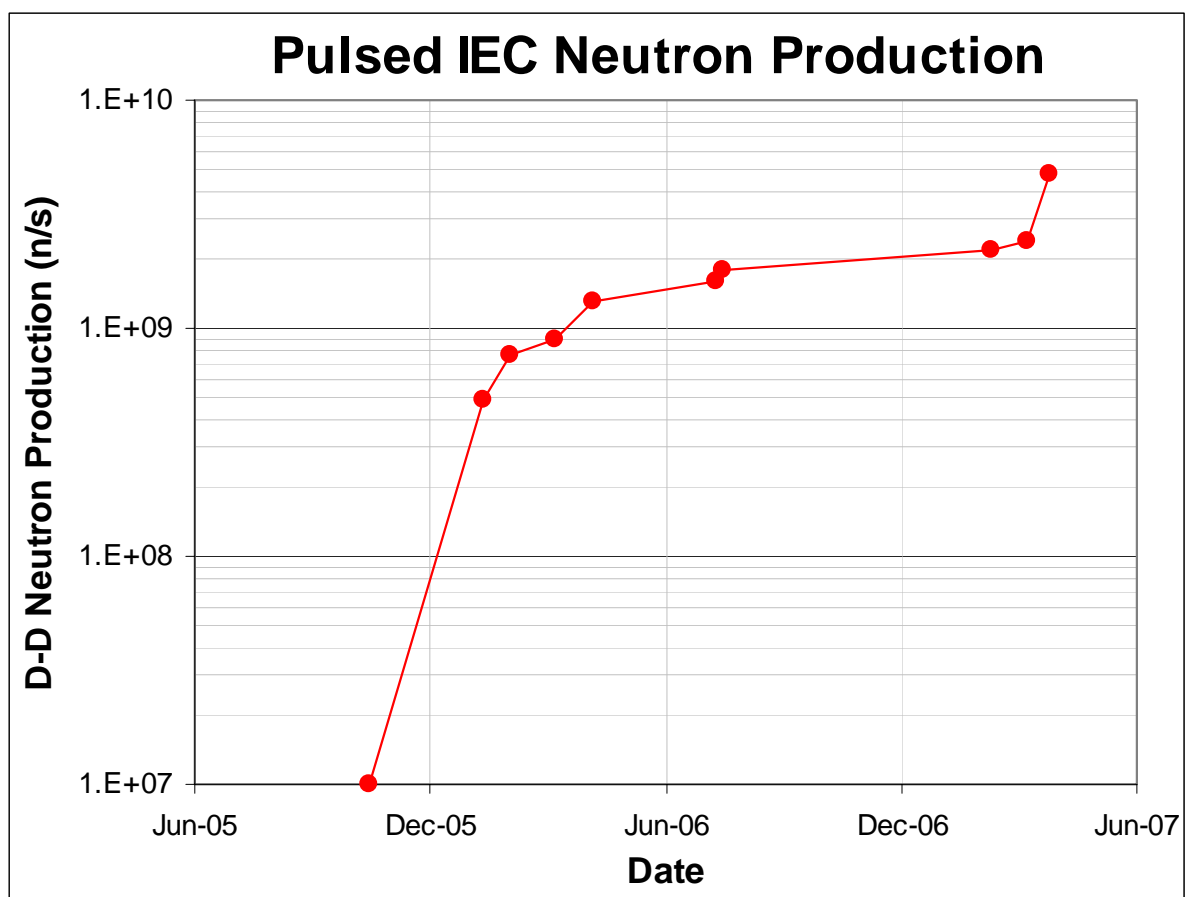


Figure 6.1: The pulsed D-D neutron production rate of the UW-IEC device has increased by a factor of 500 in the past two years.

To put this improvement in perspective, some of the indicators of IEC performance and near-term applications studied at various universities are compared in Table 6.1. Steady-state neutron production levels at the University of Wisconsin are well above levels produced at other universities. This is due, in part, to our ability to operate at higher cathode voltages and our use of advanced alloys for the cathode.

The pulsed neutron production level at the UW is at similar levels to the highest rates produced at the Tokyo Institute of Technology (see Table 6.1), but with much longer pulse widths. Also, the cathode voltage at which the UW-IEC device is able to operate is considerably higher than any other university. Finally, the University of Wisconsin is the only IEC group currently investigating HEU detection methods as well as conducting work on explosives detection.

	Steady-State D-D Neutron Rate (Cathode Voltage)	Pulsed D-D Neutron Rate (Pulse Width)	Maximum Pulse Voltage	HEU Detection	Explosives Detection
University of Wisconsin	2.2x10 ⁸ n/s (165 kV)	4.7x10 ⁹ n/s (110 μs)	120kV	x	x
Kansai University [1]	2.3x10 ⁶ n/s (60 kV)	6x10 ⁷ n/s (10 μs)	45 kV	-	x
Tokyo Institute of Technology [2]	2.1x10 ⁶ n/s (60 kV)	6.8x10 ⁹ n/s (20 μs)	70 KV	-	x

Table 6.1: Comparison of UW-IEC to other known pulsed IEC systems operated with deuterium fuels.

6.2 HEU Detection Approach

As discussed in Section 5.2, the pulsed IEC device continuously produces low levels of neutrons between pulses. Although these neutrons are not counted when determining the pulsed fusion rates, they are a cause for concern with HEU detection, as discussed in Section 3.3. The low level but continuous neutron production rate was shown to be a very strong

function of cathode voltage. This effect was due not only to the increased fusion cross-sections at higher ion energy, but to the fact that increased electric fields that are held constant between pulses produce ionization cascades, particularly as the deuterium pressure is increased. These cascades can be initiated by any ionization source between pulses, such as an arc or a cosmic ray, but the high voltage is needed to turn the single ionization event into a cascade. No mode of operation producing high levels of pulsed neutrons was found in this work that eliminated this continuous low-level neutron source.

Establishing operating modes that generate maximum levels of pulsed neutrons while minimizing this noise signal will be a top priority when designing a commercial SNM detection system. Large signal to noise ratios with these systems will allow for shorter scanning times and fewer false signals. The pulsed IEC neutron generator system described in this thesis is well suited for generating high fluxes during pulses, but it may produce too much noise between pulses in the current configuration for applications in the field.

However, since a commercial IEC neutron source will likely use the D-T reaction, this problem may be avoided. Due to the higher cross-sections at lower ion energy, the D-T reaction does not require cathode voltages as high as the D-D reaction. This will allow high intensity neutron pulses to be generated with lower cathode voltages. As shown in Figure 5.33, this may prevent an IEC discharge from initiating between pulses and therefore dramatically reduce the number of neutrons generated between pulses. In addition, if the Differential Die-Away (DDA) technique [3] is used to detect HEU in the future, it is much less sensitive to the continuous background neutron levels generated between pulses.

6.3 Helium Implantation in Tungsten

The damage mechanisms on tungsten surfaces resulting from the helium irradiation experiments described in this thesis are consistent with the types of damage observed in other refractory alloys by Kaminski [4], Erents [5], and others. This damage includes blistering, pore formation, and the development of subsurface porous structures. One phenomenon not seen by this early work is the development of a coral-like structure at higher fluences. The mechanism that creates this structure is unknown, but it has been observed during both pulsed and steady-state irradiation in this work and recently by Tokunaga [6].

6.3.1 Implications of Helium Implantation in Tungsten

The changes in surface morphology resulting from pulsed helium implantation have a number of serious implications for both inertial confinement fusion (ICF) first walls and IEC cathodes. For the case of ICF first walls, the HAPL reference chamber will be used as a basis for calculations. The reference HAPL chamber is a 10.5 meter radius steel sphere with a 250 μm coating of tungsten. The device operates with a rep rate of 5 Hz and target yield of 365 MJ. The fusion products are assumed a point source originating at the center of the sphere. The helium portion of the ion energy spectra is shown in Figure 2.18.

Based on the mass loss observed on the tungsten sample irradiated to $1 \times 10^{19} \text{ He}^+/\text{cm}^2$ (which corresponds to 8.5 days of operation in the HAPL reference design), the extrapolated wall thickness loss to the reference HAPL design would be 47 μm per full power year (FPY) due to low energy (<180 keV) helium alone. As seen in Figure 2.18, these low energy ions account for only a fraction of the total helium ion population. If the higher energy helium

ions result in similar wall material loss, this would correspond to 200 $\mu\text{m}/\text{FPY}$ due to all helium ions. Physical sputtering from other light ions (H^+ , D^+ , T^+) could contribute another 6 $\mu\text{m}/\text{FPY}$. Additional damage from carbon and heavier ions could further increase this loss. All told, these processes could result in the formation of $\sim 5,500$ kg/FPY of radioactive tungsten dust in the 10.5 m radius chamber. This radioactive dust will not only contaminate the chamber, but could work its way into beam lines (coating mirrors) and pumping systems. In addition to the erosion and dust concerns, the high density of small pores could act as nucleation sites for cracks under repeated shock loading.

In the IEC tungsten-rhenium cathodes, the sharp points created by pore formation may cause high voltage breakdown problems. It has been observed that operating the IEC device with ^3He fuel for extended periods of time leads to a degradation of high voltage performance of the cathodes.

In addition to the surface damage, the helium retention measurements also have serious implications for IEC performance for $\text{D}-^3\text{He}$ reactions. The high density of helium measured in the tungsten matrix indicates that a high density helium target is present in the cathode grid wires. This observation is consistent with fusion source region experiments, which revealed that the majority of $\text{D}-^3\text{He}$ reactions in the IEC device are occurring in the cathode grid wires. The time to saturation of $\text{D}-^3\text{He}$ reactions is also consistent with the time for the helium fluence to reach the levels of helium saturation in the tungsten matrix.

In summary, this work has significantly expanded the envelope of operational parameters in IEC devices. This, in turn, has uncovered new problems not foreseen at the start of this work. Future research will be required to resolve these issues and discover new solutions to phenomena identified in this work.

6.5 References

- [1] K. Yamauchi et al, "Pulsed Operation of a Compact Fusion Neutron Source Using a High-Voltage Pulse Generator Developed for Landmine Detection" (to be published in *Fusion Science and Technology*)
- [2] K. Yamauchi et al, "Performance of Neutron/Proton Source Based on Ion-Source-Assisted Cylindrical Radially Convergent Beam Fusion," *IEEE Trans. FM*, Vol. 126, No. 8, 2006
- [3] J.T Caldwell et al, "The Los Alamos Second Generation System for Passive and Active Neutron Assays of Drum-Size Containers," LANL Document LA-10774-MS, 1986
- [4] S.K. Das and M. Kaminsky, "Radiation Blistering in Metals and Alloys," Proceedings of the "Symposium on Radiation Effects on Solid Surfaces," *Advances in Chemistry Series*, 1975
- [5] S.K. Erents and G.M. McCracken, "Blistering of Molybdenum under Helium Ion Bombardment," *Radiation Effects*, Vol. 18, p. 191, 1973
- [6] K. Tokunaga et al, "Synergistic Effects of High Heat Loading and Helium Irradiation of Tungsten," *Journal of Nuclear Materials*, Vol. 329–333 (1), p. 757-760, 2004

Chapter 7: Conclusions

The conclusions listed in this chapter are arranged to match the order of their appearance in the Results chapter (Chapter 5). Only the major conclusions are listed here. Refer to Chapter 5 for more details.

MCNP

- An MCNP model was developed that accurately models the time-dependent behavior of pulsed IEC neutron production and the associated HEU detection hardware.
- This model was able to predict the number of delayed neutron counts collected in the ^3He detectors to within ± 13 percent.

Pulsed IEC

- It was found that filament temperature and bias play a major role in determining the emission current of the pulsed deuterium ion source. Deuterium pressure plays a lesser role in the 1-3 mTorr range.
- Numerous improvements were made to the pulsed IEC device, allowing pulsed neutron production rates of 4.7×10^9 n/s during 110 μs pulses at 5 Hz. This corresponds to fusion rates of 9.4×10^9 s $^{-1}$.
 - High voltage pulsing circuitry was built and operated at voltages up to 120 kV.
 - Pulsed ion currents in excess of 6 amperes were achieved.
 - A new 20 cm cathode was built and operated with a 40 cm anode to increase fusion production by nearly a factor of two and allow higher pulsed current.
 - Pulse width studies revealed increased neutron production at shorter pulse widths.

- Experimental parameters were optimized to operate with pulsed neutron production levels at least 10^5 times higher than steady-state neutron production between pulses.

HEU Detection

- The UW-IEC device running at 130 kV, 60 mA, and 2.6 mTorr D_2 to produce *steady-state* neutrons at $\sim 1.5 \times 10^8$ n/s was used to detect delayed neutrons with a Signal/Noise ratio of 8.7 from a 10 gram sample of uranium-235.
- *Pulsed* D-D neutron production rates as low as 4×10^8 n/s generated in the UW-IEC were used to detect the presence of a 10 gram sample of uranium-235.
 - Delayed neutron production was found to increase linearly with fusion neutron rates.
 - Signal-to-noise ratios as high as 6.2 were found to exist when 65 kV remained on the cathode between fusion pulses.

Pulsed Implantation of Polycrystalline Tungsten

- The IEC fusion device at the University of Wisconsin has been modified and is able to perform both steady-state and pulsed irradiation experiments.
 - This device is capable of generating 0.2-2 ms helium ion pulses of up to 1 ampere at rep rates ranging from 1-25 Hz.
- Pulsed helium implantation of polycrystalline tungsten was performed at $1,150^\circ\text{C}$ using the University of Wisconsin IEC device. Fluences of 1×10^{18} , 6×10^{18} , and 1×10^{19} He^+/cm^2 were delivered to the samples in 1 ms pulses at 25 Hz.

- Micrographs of these samples revealed increased surface damage at all fluences compared to steady-state irradiation.
 - At 1×10^{18} He^+/cm^2 , the steady-state sample only exhibits pores collecting at grain boundaries with a pore density of 1.2×10^9 pores/ cm^2 , while the pulsed sample appears close to a saturation density with larger pore size.
 - When the steady-state implanted helium fluence was increased to 1×10^{19} He^+/cm^2 at $1,150^\circ\text{C}$, the pore density decreased slightly to 1.9×10^9 pores/ cm^2 . The pulsed sample, however, was damaged to the point of having a coral-like structure form in addition to the uniform pore density covering the surface.
- Tungsten samples pulsed at $1,150^\circ\text{C}$ to fluences ranging from 10^{18} - 10^{19} He^+/cm^2 experienced a measurable change in mass. The 10^{19} He^+/cm^2 sample lost 4.2 mg, or roughly $1.1 \mu\text{m}$ uniformly from the surface.

Steady-State Implantation of Polycrystalline Tungsten

- Simultaneous implantation of deuterium and helium ions was performed on tungsten samples at $\sim 1,100^\circ\text{C}$.
 - At 1×10^{18} ions/ cm^2 , there appears to be a slight reduction of surface pore density (from 1.2×10^9 to 3.2×10^8 pores/ cm^2) on the sample irradiated with He^+ and D^+ simultaneously as compared to samples irradiated with helium alone.
 - At 10^{19} ions/ cm^2 there appears to be no significant difference between the samples with and without simultaneously added deuterium.

- The effect of alloying tungsten with 25 percent rhenium was studied in the IEC device.
 - The W-25%Re alloy has a lower fluence threshold for extensive pore formation.
 - With a helium fluence above $3 \times 10^{18} \text{ He}^+/\text{cm}^2$, the average pore diameter is larger on the W-25%Re sample than the pure tungsten sample
- Elastic Recoil Detection (ERD) analysis revealed the saturated helium retention level to be 40 percent (atomic) up to depths of at least 1300 Angstroms in polycrystalline tungsten when exposed to 30 keV He^+ at 1,100°C.
- Increasing the steady-state helium fluence to $10^{20} \text{ He}^+/\text{cm}^2$ on polycrystalline tungsten at 1100 °C further degraded the surface morphology and extended the subsurface porous layer to a depth of ~700 nm. The sample lost roughly 2.6 μm uniformly from its surface during irradiation.

Steady-State Implantation of Other Tungsten Forms

- Single crystal tungsten samples were irradiated at ~1,100°C with 30 keV helium ions.
 - Single crystal tungsten requires a higher fluence for the development of pores.
 - At fluences above $3 \times 10^{18} \text{ He}^+/\text{cm}^2$, single crystal tungsten developed a lower pore density than polycrystalline tungsten.
- Tungsten-coated carbide foams were irradiated in the IEC device with steady-state deuterium and helium ions.
 - D^+ implantation at $\sim 10^{19} \text{ ions}/\text{cm}^2$ and ~1,100°C on large grain tungsten-coated TaC and HfC foam showed no pore formation or change in morphology.

- When subjected to a 1×10^{19} He⁺ fluence at ~1,100°C, both large grain tungsten-coated TaC and HfC samples showed pore formation similar to polycrystalline samples.
- At fluences of 1×10^{19} He⁺/cm², the medium grain tungsten-coated TaC foam showed significant changes in its surface morphology
- At fluences of 1×10^{19} He⁺/cm², the fine grain “high ε” tungsten-coated foam showed growth of tungsten dendrites and a reduced pore formation

The pulsed IEC fusion device developed at the University of Wisconsin is a versatile piece of equipment. It has been used both to detect clandestine special material and as an irradiation facility for fusion first-wall materials research.

Chapter 8: Recommendations

8.1 Pulsed Inertial Electrostatic Confinement

Significant progress has been made in the past two years toward improving pulsed neutron rates, but the current configuration has by no means reached an optimum condition. The high-voltage hardware currently installed is rated for operation up to 200 kV, and has been tested up to 180 kV. Increasing the maximum operating voltage will require additional operating time, and possibly some study of the detailed pulse behavior, but it should dramatically increase the neutron production rate. Not only do higher voltages yield higher fusion cross sections, but pushing the cathode voltages higher will also increase the pulsed ion current (as discussed in Section 5.2).

As discussed in Section 5.2, switching from a 10 cm diameter cathode with a 50 cm anode to a 20 cm cathode with a 40 cm anode increased the neutron production rate by nearly a factor of two. While this new combination of cathode and anode diameters was not chosen at random, it may not be the optimum combination. A campaign to evaluate the effects of changing the grid sizes would likely yield increased neutron rates and increased pulse currents. Additionally, these scans will provide valuable information about fundamental IEC physics.

Another way to increase pulse current would be to add magnetic cusp fields at the IEC walls. Currently, electrons born at the filaments quickly find their way to walls and are lost to the system. Adding permanent magnets arranged in the proper orientation on the walls will increase the average lifetime of the electrons and therefore increase the intensity of

the ionization source. One potential downside to this configuration could be spontaneous ionization of the background gas between pulses.

8.2 Highly Enriched Uranium Detection

One way to quickly and easily improve the HEU detector assembly described in this thesis would be to add a layer of cadmium over a layer of paraffin over the ^3He detectors. Cadmium will absorb thermal room-return neutrons while allowing the higher energy delayed neutrons through. The paraffin inside the cadmium will then moderate the delayed neutrons, increasing the chance that the ^3He detectors will detect them. The major effect of this change will be to remove the room-return neutron counts that overwhelm the counting system for the first 20 ms after the pulse. This will allow for cleaner and more accurate counting of the delayed neutron population, and will allow the system to be run at a higher frequency, since less time will be needed between pulses to get the same statistics.

The work described in this thesis has resulted in a system capable of performing HEU detection using a delayed neutron analysis technique. However, this system has not been tested under conditions that are realistic in the field. For example, small mockups of shipping containers could be constructed and filled with various shielding materials to replicate the diversity found in actual shipping containers. These mockups could then be placed next to the detection system and irradiated with and without the uranium sample present. The results of these experiments would also be valuable to benchmark more detailed MCNP codes.

Coupling the pulsed ionization source described in this thesis with a pulsed cathode would be an effective way to eliminate the signal-to-noise issues discussed in Chapters 5 and 6. This would also allow operation at higher pressures, since there would be no need to worry about a discharge developing between pulses. Higher pressure operation would result in higher pulse current and therefore higher neutron rates. It would be particularly useful if the cathode/anode studies described above find that higher pressure operation is better with a different cathode and anode configuration.

While delayed neutron detection is a proven method for identifying fissile material, there are other techniques that may be better suited for use with pulse IEC neutron generators. The most applicable technique is known as differential die-away (DDA). With this technique, a moderating detection cavity is used to contain cadmium-clad ^3He detectors. Short pulses of fast neutrons are injected into the system, and then decay in time. When no fissile material is present, the system will exhibit die-away behavior with half-lives in the tens of microseconds. When fissile material is present, the prompt fission neutrons will induce additional generations of fissions, which will extend the die-away half-life to 100s of microseconds. The DDA technique has been shown to be a powerful screening tool, capable of detecting fissile material at milligram levels. Exploring the applicability of this technique to a pulsed IEC-based detection system should become a high priority for the Wisconsin IEC group.

8.3 Tungsten Implantation Studies

A significant increase of surface damage, subsurface porous structure development, and mass loss were observed when helium irradiation was changed from steady-state to pulsed. However, the pulse width during the irradiation experiments is a factor of 100 times

longer than the anticipated ICF pulses. The IEC device does not currently have the ability to reach the 5 μs needed to match a HAPL pulse. However, it can investigate pulse widths down to 100 μs ; 10 times shorter than the pulses discussed in this thesis. Evaluating the surface morphology changes and mass loss as a function of pulse width should provide insight into helium damage mechanisms.

The current pulse setup does not provide a significant change in temperature during the pulse. Adding a temperature increase during the ion pulses will add much realism to the experiment, and may dramatically change the damage effects. Flash lamps or high intensity lasers could be coupled with the IEC device to provide the proper temperature profile.

Significant progress has been made in these projects in the past few years. Through improvement of pulse power capability and implementation of advanced diagnostic techniques, more success is yet to come.

Appendix A: MCNP Input Files

Simulation of HEU detection with IEC - 3 detector case

(resulting plot shown in Figure 5.12)

c

c

c

c Cell cards

c

cell#	Mat#	Dens	Surface combinations	Description
1	0		1	\$ rest of world
2	0		1 -2	\$ Wall
3	4	-.001225	-1 #4 #5 #6 #7 #8 #10 #11 #12 #13	\$ in hotcell
5	3	-2.7	-9 8 -6	\$ top of chamber
6	3	-2.7	-10 11 -6	\$ bottom of chamber
7	3	-2.7	-6 7 -8 10	\$ wall of chamber
8	7	-.00000001	-7 -8 10	\$ inside chamber
11	5	-.9	14 -13 3 15 16 6 -18	\$ det moderator
10	6	-.0049	-14	\$ He-3 tube A
12	6	-.0049	-15	\$ He-3 tube B
13	6	-.0049	-16	\$ He-3 tube C
4	2	-18.95	-3	\$ Uranium

c Surface cards

c

c wall components

1 RPP -200 200 -100 200 -75 200

c 2 RPP -300 300 -200 300 -200 300

c

c chamber components

6 cz 45

7 cz 43

8 pz 33

9 pz 37

10 pz -33

11 pz -37

c

c Detector Components

3 1 RCC -0.23 -8.5 0 0.58 0 0 0.564 \$ accurate Uranium

13 1 RCC -11 0 0 22 0 0 22 \$ moderator

14 1 RCC -10 -8.5 5 20 0 0 2.5 \$ det A

15 1 RCC -10 -3 0 20 0 0 2.5 \$ det B

16 1 RCC -10 -8.5 -5 20 0 0 2.5 \$ det C

18 py 70

c Data Cards

c

c transformations

```

TR1 0 60 0
c
c Materials
c m1 1001 1 8016 2 20040 2 $ Concrete
m2 92235 93.16 92238 6.84 $ 93.16% enriched Uranium
m3 13027 1 $ Aluminum
m4 8016 21 7014 78 $ Air
m5 1001 52 6012 25 $ wax
m6 2003 1 $ 3-He
m7 8016 1 $ vacuum
C
C Number of Particles
nps 10000000000
C
c Source
SDEF ERG=2.45 TME=D1 VEC=0 1 0 DIR=D2
SI1 H 0 1e5 100e5 101e5 200e5 201e5 300e5 301e5 400e5 401e5 500e5
501e5 600e5 601e5 700e5 701e5 800e5 801e5 900e5 901e5 1000e5
SP1 0 1 0 1 0 1 0 1 0 1 0
1 0 1 0 1 0 1 0 1 0
SI2 H .866 1
SP2 0 1
c
PRINT 110
C
c Importances
Imp:n 0 1 .5 .5 .5 1 3 9 9 9
c
c Include delayed neutrons
totnu
c Tallies
F4:n (10 12 13)
T4 1e6 98i 100e6
FM4 -1.473e10 6 (-1) (-2) $ 1E8 n/s, 1/8 correction for n, V for 3 detectors
F14:n (10 12 13)
T14 1e6 98i 100e6
c Time cutoff
CUT:n 100e6
FQ4 T E
FQ14 T E

C End

```

Time-Dependent Thermal Flux Model

(resulting plot shown in Figure 5.14)

c

c

c Cell cards

cell#	Mat#	Density	Surface combinations	Description
1	0		2	\$ rest of world
2	1	-2.4	1 -2	\$ Wall
3	4	-.000001	-1 3 #5 #6 #7 #8 #9	\$ inside room
4	5	-.9	-3	\$ power supply
5	1	-.9	-9	\$ tally cell
6	5	-.9	-10 9	\$ moderator
7	1	-.9	-8	\$ capacitor
8	1	-.9	-11	\$ HV barrel #1
9	1	-.9	-12	\$ HV barrel #2

c Surface cards

c wall components

1 RPP -210 210 -210 210 -120 200
 2 RPP -300 300 -300 300 -200 300

c Room Components

3 RPP 110 209 110 209 -119 60
 8 RCC -100 160 -119 0 0 140 22.5
 11 RCC -20 160 -119 0 0 140 35
 12 RCC 55 160 -119 0 0 140 35
 9 RPP -103 -97 77 82 -7 7
 10 RPP -110 -90 70 89 -10 10

c Data Cards

c Materials

m1 1001 1 8016 2 20040 2 \$ Concrete
 m4 8016 21 7014 78 \$ Air
 m5 1001 5 6012 1 \$ wax
 nps 100000000

c Source

SDEF ERG=2.45 TME=D1 POS=-100 20 0

SI1 H 0 1e5 1e7

SP1 0 1 0

PRINT 110

Imp:n 0 1 1 1 2 1.5 1 1 1

c Tallies

F4:n 5

T4 0 19i 20e5

CUT:n 1e7

C End